

Modelling of atmospheric electricity phenomena in
the atmospheres of Venus, Earth, Jupiter and
Saturn



Universidad de Granada

Francisco Javier Pérez Invernón
Department of Solar System
Instituto de Astrofísica de Andalucía
Programa de Doctorado en Física y Ciencias del Espacio

A thesis submitted for the degree of

Philosophiæ Doctor (PhD)

March 2018

Editor: Universidad de Granada. Tesis Doctorales
Autor: Francisco Javier Pérez Invernón
ISBN: 978-84-9163-862-9
URI: <http://hdl.handle.net/10481/51164>

Examination date: March 22, 2018

Thesis supervisors:

Dr. D. Francisco J. Gordillo Vázquez Dr. D. Alejandro Luque Estepa

© Francisco Javier Pérez Invernón

Cover design: Francisco Javier Pérez Invernón

Cover picture: Upward lightnings. Oscar Van der Velde, acquired on
February 21, 2015.

1. Reviewer:

2. Reviewer: Day of the defense: March 22, 2018

Signature from the head of the PhD committee:

Abstract

In this doctoral thesis we describe the development and results of several models to study electricity phenomena in the atmospheres of Venus, Earth, Jupiter and Saturn. In addition, in the context of the future launch of ASIM (ESA) in 2018 and TARANIS (CNES) in 2019, we present two methods to analyze the optical signals emitted by Transient Luminous Events (TLEs) from space-based photometers.

We have developed two electrodynamical models to simulate the inception and evolution of halos and elves in planetary atmospheres. These models have been coupled with different sets of chemical reactions to describe TLEs in the upper atmospheres of Venus, Earth, Jupiter and Saturn. The terrestrial versions of these models have allowed us to quantify the local chemical impact of halos and elves in the atmosphere of the Earth. We have used these results together with the TLE occurrence rate reported by ISUAL (NSPO) to estimate the global impact of these events in the chemistry of the terrestrial mesosphere. We have also investigated the similarities and differences between elves triggered by different types of lightning discharges, such as cloud-to-ground (CG) discharges, Compact Intracould Discharges (CIDs) and Energetic In-cloud Pulses (EIPs). Finally, the model of halos has been used to calculate the quasiaelectrostatic field produced by this type of TLE at ground level. We

have compared this result with measurements of electric fields from thunderstorms.

The existence of lightning in Venus is still unclear. We have investigated the possibility of detecting Venusian TLE as an indirect evidence of the existence of Venusian lightning discharges. The Venusian versions of the TLEs models has been useful to predict the possible inception of halos and elves in Venus. According to our results, these Venusian TLEs could emit light in a wide range of frequencies of the optical spectrum. Some of these optical emissions would be produced in the 557 nm line. The Akatsuki spacecraft (JAXA), currently orbiting Venus since December 2015, could detect bursts of light in this spectral line.

In the case of Jupiter and Saturn, the three-dimensional version of the elve model have enabled us to study the shape and intensity of the predicted optical emissions in the upper atmosphere of the giant gaseous planets depending on the latitude, lightning channel inclination and upper atmospheric composition. In addition, we have concluded that the optical flashes in the Saturnian and Jovian atmosphere detected by several spacecraft as the Voyagers (NASA) and Cassini (NASA, ESA and ASI) come from lightning rather than from elves. However, it is possible that TLEs in the giant planets are triggered by the lightning activity in the atmospheres of Saturn and Jupiter. The models developed in this thesis could help unveil such new optical transient events in coordination with future dedicated instruments to search for such phenomena.

We have used a Full Wave Method to investigate the propagation of Very Low Frequency (VLF) waves through planetary atmospheres. In the case of Earth, we have calculated the transfer

function of the curved Earth-ionosphere waveguide. This transfer function is useful to analyze distant sources of electromagnetic pulses. This model has also been particularized to the case of whistler wave propagation through the Venusian atmosphere. The comparison of our results with signals reported by the Pioneer Venus Orbiter (PVO) of NASA and Venus Express (VEX) ESA has allowed us to derive the rate of occurrence and energy released by hypothetical Venusian lightning radiating electromagnetic waves.

Finally, we have used the simulated optical emissions of halos and elves to develop two methods to analyze the emitting source from signals recorded by space-based photometers onboard the future space missions ASIM and TARANIS to study atmospheric electricity in the Earth atmosphere. These methods can be used to obtain the temporal evolution of the number of photons emitted by elves and to deduce the reduced electric field in halos and elves. We have applied one of these methods to the signals reported by GLIMS (JAXA).

Resumen

En esta tesis doctoral se describen el desarrollo y los resultados de varios modelos para el estudio de fenómenos eléctricos en las atmósferas de Venus, la Tierra, Júpiter y Saturno. En el contexto del futuro lanzamiento de ASIM (ESA) en 2018 y TARANIS (CNES) en 2019, presentamos dos métodos para el análisis de la señal óptica emitida por fenómenos luminosos transitorios o “Transient Luminous Events (TLEs)” y detectadas por fotómetros situados en el espacio. Estos fenómenos transitorios se producen en la alta atmósfera terrestre como consecuencia de la actividad eléctrica en la troposfera.

Se han desarrollado dos modelos electrodinámicos para simular el comienzo y la evolución de halos y elves (dos de los más frecuentes tipos de TLEs) en atmósferas planetarias. Estos modelos han sido acoplados con diferentes conjuntos de reacciones químicas para describir TLEs en las capas altas de las atmósferas de Venus, la Tierra, Júpiter y Saturno. Las versiones terrestres de estos modelos nos han permitido cuantificar el impacto químico local de halos y elves en la atmósfera de la Tierra. Hemos utilizado estos resultados junto a la tasa de ocurrencia global de TLEs observada por ISUAL (NSPO) para estimar el impacto químico global de estos eventos en la atmósfera terrestre. Además, hemos investigado las similitudes y diferencias entre los elves producidos por diferentes tipos de descargas eléctricas

troposféricas, como los rayos nube-suelo o las impulsivas descargas que se producen entre nubes. Finalmente, se ha utilizado el modelo de halos para calcular el campo cuasiestático producido por este TLE a nivel del suelo. Hemos comparado este resultado con algunas medidas de campo eléctrico producido en tormentas con actividad eléctrica.

La existencia de rayos en Venus es todavía una incógnita. Hemos investigado la posibilidad de detectar TLEs venusianos como una evidencia indirecta de la existencia de rayos en ese planeta. Las versiones venusianas de los modelos de TLEs han sido útiles para predecir la posible existencia de halos y elves en Venus. De acuerdo a nuestros resultados, estos TLEs venusianos emitirían luz en un amplio rango de frecuencias del espectro óptico. Algunas de esas emisiones ópticas se producirían en la línea de 557 nm. La nave Akatsuki (JAXA), que actualmente orbita Venus desde el mes de diciembre de 2015, podría detectar destellos de luz en esa línea espectral.

En el caso de Júpiter y Saturno, la versión tridimensional del modelo de elves nos ha permitido predecir la forma e intensidad de las emisiones ópticas que se producirían en la alta atmósfera de esos planetas dependiendo de la latitud, la inclinación del canal del rayo y la composición de la alta atmósfera. Además, hemos determinado que los destellos de luz detectados en las atmósferas de Saturno y Júpiter por naves espaciales como las Voyager (NASA) y Cassini (NASA, ESA y ASI) son probablemente producidos por rayos en lugar de por elves. Sin embargo, la aparición de TLEs en las atmósferas de Saturno y Júpiter es posible según nuestros modelos. Estos resultados podrían servir para revelar estos nuevos TLEs en coordinación con futuros instrumentos dedicados a buscar estos fenómenos.

Por otra parte, hemos usado un método de propagación de ondas “Full Wave Method (FWM)” para investigar la propagación de ondas de muy baja frecuencia “Very Low Frequency (VLF)” a través de atmósferas planetarias. En el caso de la Tierra, hemos calculado la función de transferencia de la guía de ondas curvada formada por la Tierra y la ionosfera. Dicha función de transferencia es útil para analizar los pulsos electromagnéticos emitidos por fuentes lejanas. También hemos particularizado este modelo para el caso de la propagación de ondas “whistler” (de silbido) a través de la ionosfera de Venus. Hemos comparado los resultados calculados con las señales obtenidas por las sondas Pioneer Venus Orbiter (PVO) de NASA y Venus Express (VEX) de ESA, deduciendo tanto la tasa de ocurrencia global de rayos en Venus como la energía media por descarga necesarias para producir las detecciones obtenidas por las citadas naves.

Finalmente, hemos utilizado las emisiones ópticas simuladas con los modelos de halos y elves para desarrollar dos métodos que nos permitan analizar las señales ópticas reales de TLEs obtenidas con fotómetros desde el espacio. Estos métodos pueden ser utilizados para obtener la evolución temporal del número de fotones emitidos por elves y para deducir el campo eléctrico reducido en el interior de halos y elves. Hemos aplicado uno de esos métodos a señales de elves obtenidas por GLIMS (JAXA).

To Ángela

Acknowledgements

Me gustaría dedicar este trabajo a mi familia más cercana y a Ángela. El esfuerzo diario de mis padres, Paloma Invernón y Francisco Pérez, me han dado la posibilidad de llegar hasta donde he querido. Ángela ha sido la persona más importante de mi vida, la que siempre ha estado a mi lado incluso durante los largos viajes y me ha enseñado tantas cosas. Mi hermano Pedro, mis abuelos, tíos, primos y especialmente mi hermano Sergio siempre han tenido mucho interés por lo que hago y me han apoyado. Y finalmente, mi hermana Mihret (D.E.P.), posiblemente la persona que más cosas me ha enseñado en menos tiempo. A todos ellos, gracias.

Gracias también a mis amigos más cercanos: Antonio, Víctor, Lucas, Rafa, Pablo, Irene, Fran y Ana Belén. Algunos de ellos llevan desde la guardería conmigo.

First and foremost, I would like to thank my supervisors Dr. Francisco J. Gordillo Vázquez and Dr. Alejandro Luque for their support throughout this project. Their patience, motivation, enthusiasm, immense knowledge and continuous guidance have helped me in finishing this thesis and growing as a scientist. Their work and dedication were a great example to me. Thank you to the TRAPPA group for their support and scientific talks, specially to María Passas and Francisco Parra, who helped me from the first moment, and to Alejandro Malagón.

I would like to give thanks to the Gamma-ray flashes team from the University of Bergen, specially to Dr. Nikolai Lehtinen, who supported me during my stay at the Birkeland Centre for Space Science. His invaluable help and immense knowledge made it possible for me to learn a lot. Thank you also to Dr. Andrey Mezentsev, an excellent scientist and hard worker with whom I had the pleasure of collaborating. I am also thankful to Dr. Anne Smith and the ACOM division, who shared with me their knowledge about climate models during my stay at NCAR (Boulder).

I would also like to thank my colleagues of the Institute for Astrophysics of Andalusia (Granada), specially to Antonio Lorenzo, Eulalia Gallegos and Francisco Nogueras, with whom I shared and office for several years. The everyday work was really nice with them.

I would like to acknowledge the University of Granada for allowing me to get a Ph.D. in the Physics and Space Science program.

I acknowledge the JEM-GLIMS science team members for providing the elve data for research purposes.

This work has been made possible with the financial assistance of the Spanish Ministry of Science and Innovation, MINECO (previously MICINN) under projects ESP2013-48032-C5-5-R, FIS2014-61774-EXP, 09-RNP-101 (LESC) (European Networking Foundation - Research Networking Programmes), ESP2015-69909-C5-2-R, ESP2017-86263-C4-4-R, H2020-MSCA-ITN-2016 (Marie Curie Innovation Training Networks - ITN) and the EU through the FEDER program.

Also, I acknowledge the European Science Foundation (ESF) Thunderstorm Effects on the Atmosphere-ionosphere System (TEA-

IS) network, to the University of Alicante (UA), to the German Aerospace Center (DLR) and to the European Space Agency Centre (ESA-C) for funding my attendance to scientific meetings.

Contents

List of Figures	xi
List of Tables	xxxv
1 Introduction	1
1.1 Lightning	1
1.2 Transient Luminous Events	10
1.2.1 Elves	12
1.2.2 Halos and sprites	14
1.2.3 Blue jets	15
1.2.4 Gigantic Jets	16
1.2.5 Other TLEs	17
1.3 Electrical phenomena in other planets	17
1.3.1 Giant Gaseous Planets	19
1.3.2 Venus	22
1.3.3 Other planets	25
1.4 Motivation	26
1.5 Content	28
2 Electrodynamical models	31
2.1 Introduction	31
2.2 Model of halos	33
2.3 Models of elves	37
2.3.1 Two-dimensional model	38

2.3.2	Three-dimensional model	44
3	Electrical phenomena in the atmosphere of the Earth	49
3.1	Transient Luminous Events: Halos and elves	49
3.1.1	Introduction	49
3.1.2	Electric breakdown in the mesosphere	50
3.1.3	Description of models	58
3.1.3.1	Simulations of halos and elves	58
3.1.4	Results and discussion	66
3.1.4.1	Electromagnetic fields and conductivity in the lower ionosphere	67
3.1.4.2	Chemical impact of halos and elves	71
3.1.4.3	Optical signature of halos and elves	80
3.1.4.4	Quasielectrostatic field created by a halo	90
3.2	Very Low Frequency wave propagation through the Earth- ionosphere waveguide	97
3.2.1	Introduction	97
3.2.2	Transfer function of the Earth-ionosphere waveguide	98
4	Analysis of optical signals emitted by TLEs	111
4.1	Introduction	111
4.2	Methods for the analysis of light emissions from TLEs	112
4.2.1	Deduction of the reduced electric field	112
4.2.2	Treatment of the signal emitted by an elve	115
4.2.2.1	Observed signal	115
4.2.2.2	Inversion of the signal	121
4.3	Results	126
4.3.1	Analysis of the signals obtained with the halo and elve models	126
4.3.1.1	Reduced electric field in halos	126
4.3.1.2	Reduced electric field in elves	131
4.3.1.3	Emitting source of elves	133

4.3.2	Analysis of signals recorded from space	137
4.3.2.1	Deduction of the source of an elve reported by GLIMS	138
4.3.2.2	Remarks about the possibility of applying the inversion method to signals reported by other space missions	146
5	Signature of possible lightning from the Venusian atmo- sphere	149
5.1	Introduction	149
5.2	The atmosphere of Venus: Mesosphere and ionospheric plasma conditions	151
5.2.1	Electric breakdown in the nightside lower ionosphere of Venus	152
5.2.2	Model of a cloud discharge in the atmosphere of Venus	156
5.2.3	Plasma conditions in the ionosphere of Venus	162
5.3	Optical signature of possible Venusian TLEs	170
5.3.1	Description of the models	170
5.3.2	Results	173
5.3.2.1	Venusian Halos	173
5.3.2.2	Venusian Elves	182
5.3.2.3	Comparison with previous measurements	189
5.3.2.4	Feasibility of detecting Venusian TLEs from present and future orbiters	191
5.4	Electromagnetical signatures of possible Venusian lightning: Whistler waves	193
5.4.1	Particularization of the model for the atmosphere of Venus	193
5.4.2	Results: Characteristic of whistler waves traveling through the Venusian ionosphere	199

CONTENTS

5.4.2.1	Power spectral density based on the electric field	200
5.4.2.2	Power spectral density of the magnetic field	204
5.4.2.3	Transfer function of the Venusian ionosphere	206
5.4.2.4	Remarks about the comparison between calculated and reported signals	208
6	Elves produced in Giant Gaseous Planets	211
6.1	Introduction	211
6.1.1	Model of TLEs in Jupiter and Saturn	212
6.2	Results	218
6.2.1	Reduced electric field and electron density in the lower ionosphere	218
6.2.2	Optical emissions	221
6.3	Conclusions	223
7	Summary	227
7.1	Summary	227
8	Conclusions	231
8.1	Conclusions	231
9	Future work	233
9.1	Future work	233
Appendix A	Chemical schemes	235
A.1	Kinetic model for terrestrial TLEs	235
A.2	Kinetic model for Venusian TLEs	248
	References	253

List of Figures

1.1	Global electric circuit. The surface of the Earth is charged negatively and the air is charged positively. The vertical electric field in fair weather is about 100 V m^{-1} . Adapted from <i>Pierce (1974)</i> and <i>Rakov and Uman (2003)</i>	2
1.2	Charge distribution inside a thundercloud in New Mexico (<i>Krehbiel, 1986; Rakov and Uman, 2003</i>).	3
1.3	Cloud to ground lightning discharge impacting over a building. Photo taken by José Luis Escudero Gallegos in Málaga (Spain) in 2017.	4
1.4	Different types of lightning. Courtesy of the British Encyclopedia.	6
1.5	Lightning flash density in flashes per second and per squared kilometer (flashes/s km^2) around the globe from 1995 to 2003. Observations by the Optical Transient Detector (OTD) and the Lightning Imaging Sensor (LIS) (<i>Christian et al., 2003</i>).	7
1.6	Transverse and longitudinal resonances in the Earth-ionosphere cavity (<i>Nickolaenko and Hayakawa, 2002</i>).	10
1.7	First scientifically documented image of a TLE (a sprite) in 1989 (<i>Franz et al., 1990</i>).	12
1.8	Types of Transient Luminous Events (TLEs). Courtesy of María Passas Varo.	13
1.9	An elve observed by ISUAL (<i>Chern et al., 2014</i>).	14

LIST OF FIGURES

1.10	Sprites and halos captured by María Passas operating GRASSP from Almería (Spain) in 2013 (<i>Passas et al.</i> , 2014).	15
1.11	First image of a Blue Jet before their official discovery. Taken by Tudor Williams in Queensland (Australia) in 1968.	16
1.12	A Blue Jet emerging from the top of a thundercloud. This image was taken over the Bay of Bengal from the International Space Station (<i>Chanrion et al.</i> , 2017).	17
1.13	First recorded Gigantic Jet extending from the cloud tops to the lower ionosphere (<i>Pasko et al.</i> , 2002).	18
1.14	Some lightning flashes from a Jovian storm recorded by the Galileo Solid State Imager (SSI) onboard the NASA Galileo orbiter (<i>Little et al.</i> , 1999).	20
1.15	Polar lightning discharges recorded by the Long Range Reconnaissance Imager (LORRI) onboard the New Horizons spacecraft (<i>Baines et al.</i> , 2007).	21
1.16	A lightning flash from a Saturnian thunderstorm taken by the Cassini spacecraft. Courtesy of NASA.	22
1.17	Cloud layer structure in Saturn showing where lightning activity can take place. Despite different pressures, the sketch is similar in the Jovian atmosphere (<i>Fischer et al.</i> , 2008). . .	23
1.18	Structure of the Venusian atmosphere, courtesy of Pearson Education, Inc. The pressure at ground level is ninety times greater than the terrestrial surface pressure.	25
2.1	Discretization of the time derivatives. This scheme illustrate the “leapfrog” updating of the electric and magnetic fields (<i>Inan and Marshall</i> , 2011).	38

2.2	Yee cell in the two-dimensional cylindrical coordinate system showing the discretization of the spatial derivatives. The space is discretized in a grid formed by a given number of cells. Derivatives with respect to the angular coordinate are set to zero as a consequence of the cylindrical symmetry. This sketch is taken from <i>Inan and Marshall</i> (2011). In this spatial discretization, we locate the components of the current density vector \mathbf{J} in entire subindex points (i, k) (<i>Lee and Kalluri, 1999</i>).	40
2.3	Yee cell in the three-dimensional Cartesian coordinate system showing the discretization of the spatial derivatives. The space is discretized in a grid formed by a given number of cells. This sketch is taken from <i>Inan and Marshall</i> (2011). In this spatial discretization, we locate the components of the current density vector \mathbf{J} in entire subindex points (i, j, k) (<i>Lee and Kalluri, 1999</i>).	45
3.1	Distribution of electrical charges in a cloud during the inception of a -CG lightning discharge. The negative charge -60 C is removed from the cloud. Sketch taken from <i>Pasko et al.</i> (2012).	50
3.2	Total ionization and attachment rates as a function of the reduced electric field with the chemical scheme detailed in Appendix A.1. These rates have been calculated with BOL-SIG+ (<i>Hagelaar and Pitchford, 2005</i>) in air.	53
3.3	Maxwell relaxation and effective ionization times at different reduced electric field under the chemical scheme detailed in Appendix A.1.	55
3.4	Most important species at equilibrium conditions. Dashed lines correspond to most abundant species. The H_2O concentration is set constant to $1.6 \times 10^9 \text{ cm}^{-3}$	61

LIST OF FIGURES

3.5	Snapshots showing the reduced electric field and the electron concentration in the upper atmosphere 1 ms and 3 ms after the onset of three vertical CG lightning discharges. The lightning channel is always located at $r = 0$ and between the ground and an altitude of 7 km. Each column show results for lightning discharges with different CMCs.	68
3.6	Snapshots of the reduced electric fields and densities of $N_2(C^3\Pi_u, v = 0)$ in the upper atmosphere produced by two different vertically oriented CG lightning discharges. The CMC value of each discharge is 560 C km and 800 C km. The lightning discharge that triggers these electric fields start at 0 ms. . .	69
3.7	Snapshots of the reduced electric field, E_r and E_z electric field components and the density of $N_2(C^3\Pi_u, v = 0)$ in the upper atmosphere produced by CIDs and EIPs. The lightning discharge that triggers these electric fields start at 0 ms.	70
3.8	Variation (with respect to ambient values) of the density of some neutrals in the atmosphere of the Earth 3 ms after the beginning of a CG lightning discharge with a CMC of 560 C km. We show the total number of molecules created by the halo in the lower right corner of each subplot.	72
3.9	Density (with respect to ambient values) variation of some ions in the atmosphere of the Earth 3 ms after the onset of a CG lightning discharge with a CMC of 560 C km. We show the total number of molecules created by the halo in the lower right corner of each subplot.	73
3.10	Temporal evolution of the density of the emitting species $N_2(C^3\Pi_u(v = 0))$ (top panels) and the reduced electric field (bottom panels) in a vertical column above the lightning discharge. Panels in the first and second column correspond to two different lightning discharges with CMCs of 140 C km and 560 C km, respectively.	74

3.11 Variation of the density of some neutrals in the atmosphere of the Earth 1 second after the beginning of a CG lightning discharge producing a CMC of 560 C km producing a bright halo. We show the total number of molecules created by the halo in the lower right corner of each subplot. 76

3.12 Evolution of the density of electrons and O^- in the atmosphere of the Earth during 1 second after the onset of a CG lightning discharge with a CMC of 560 C km producing a bright halo. The first and the last rows show the initial and final profiles, respectively. The second, third and fourth rows show the increase in the density at different times since the beginning of the lightning discharge. 79

3.13 Temporal evolution of the total emitted photons per second (for the main spectral bands) from halos. This figure shows results for two halos triggered by two CG lightning discharges with total CMCs of, respectively, 350 C km and 560 C km. As can be seen in the legend box, some lines have been multiplied by different factors in an effort to plot all of them together. LBH, SP, FP and FN correspond to the Lyman-Birge-Hopfield band, second positive, first positive and first negative systems of molecular nitrogen, respectively. 80

3.14 Temporal evolution of the total emitted photons per second (for the main spectral bands) from elves. This figure shows results for two elves triggered by two CG lightning discharges producing total CMCs of 560 C km (154 kA) and 800 C km (220 kA). As in figure 3.13, some lines have been multiplied by different factors in an effort to plot all of them together. LBH, SP, FP and FN correspond to the Lyman-Birge-Hopfield band, second positive, first positive and first negative systems of the molecular nitrogen, respectively. . . 81

LIST OF FIGURES

- 3.15 Temporal evolution of the total emitted photons per second (for the main spectral bands) from elves produced by CIDs and EIPs. As in figure 3.13, some lines have been multiplied by different factors in an effort to plot all of them together. LBH, SP, FP and FN correspond to Lyman-Birge-Hopfield band, second positive, first positive and first negative systems of molecular nitrogen, respectively. 82
- 3.16 Calculated spectra of halos for different spectral bands. The first and the second rows show different moments of the emission spectra at the source, while the third row shows the predicted observed spectra at 3 km (red solid line) and 275 m (green dashed line) over the sea and at an horizontal distance of 350 km (between the halo and the observer). We plot the intensity of the bands in arbitrary units, normalizing each subplot to the stronger transition in each band. The numbers in the boxes correspond to photons per second in the case of emission spectra, and photons per second and squared meters in the case of the predicted observed spectra. 85
- 3.17 Calculated spectra of elves produced by a CG lightning discharge of 1000 C km (276 kA) for different bands. The first and the second rows show the emission spectra at the source, while the third row shows the predicted observed spectra at 3 km (red solid line) and 275 m (green dashed line) over the sea and at an horizontal distance of 350 km. We plot the intensity of the bands in arbitrary units, normalizing each subplot to the stronger transition in each band. The numbers in the boxes correspond to photons per second in the case of emission spectra, and photons per second and squared meters in the case of the predicted observed spectra. 86

3.18 Calculated spectra of elves produced by a CID for different bands. The first and the second rows show the emission spectra at the source, while the third row shows the observed spectra at 275 m (red solid line) and 3 km (green dashed line) over the sea and at an horizontal distance of 350 km. We plot the intensity of the bands in arbitrary units, normalizing each subplot to the stronger transition in each band. The numbers in the boxes correspond to photons per second in the case of emission spectra, and photons per second and squared meters in the case of the predicted observed spectra. 87

3.19 Calculated spectra of elves produced by an EIP for different bands. The first and the second rows show the emission spectra at the source, while the third row shows the observed spectra at 275 m (red solid line) and 3 km (green dashed line) over the sea and at an horizontal distance of 350 km. We plot the intensity of the bands in arbitrary units, normalizing each subplot to the stronger transition in each band. The numbers in the boxes correspond to photons per second in the case of emission spectra, and photons per second and squared meters in the case of the predicted observed spectra. 88

3.20 Calculated spectra of the (A) first positive system of N_2 and (B) second positive system N_2 for halos and elves produced by different atmospheric discharges as seen by an observer located at an altitude of 3 km and a horizontal distance of 350 km. The magenta circles correspond to the sprite spectrum observed by *Kanmae et al.* (2007). The observation of this sprite was performed from an altitude of 3.25 km and at horizontal distance of 350 km, and the observed region of the sprite was between 84 and 86 km of altitude. The normalization of the spectra of the FP and the SP systems of the N_2 spectra were done with respect to the (2,0) and the (0,1) transitions, respectively. We have selected the spectra at the moment of maximum emission of each TLE. 90

3.21 Sequence of mirror charges as a consequence of a charge located between two perfect conductors of electricity. Charge $+Q_1$ corresponds to the electrical charge accumulated by a lightning stroke on clouds at altitude h . Both $-Q_2$ and $-Q_3$ are the mirror charges of $+Q_1$ with respect to the ground and the ionosphere, respectively. The charge $+Q_4$ corresponds to the mirror charge of $-Q_2$ with respect to the ionosphere. This sequence of mirror charges respect to ground and ionosphere layers can be extended to an infinite number of charges. . . . 93

3.22 Vertical component of the electric field at ground level divided by its causative charge Q . We show two evaluations of equation (3.14) (dashed lines) where the ionosphere is represented by a planar, perfect conductor placed at $L = 90$ km and $L = 70$ km as well as the outcome of two simulations (coincident solid lines). For the simulations, we plot the electric field 10 ms after the start of the discharge. We also provide an arbitrarily placed reference line to illustrate the slope of a r^{-3} decay (*Pérez-Invernón et al.*, 2016a). 94

3.23 In the upper panels we can see the space charge density induced in the lower ionosphere by the thundercloud charge Q_{\max} produced by (a) a weak discharge of $hQ_{\max} = 175 \text{ C km}$ and (b) a strong discharge of $hQ_{\max} = 560 \text{ C km}$ causing a halo. The corresponding total accumulated charge in the lower ionosphere calculated by spatial integration after 10 ms is (a) $Q_i = -2.56 \text{ C}$ and (b) $Q_i = -8.15 \text{ C}$. In the lower panel we plot the difference between E/Q_{\max} at ground level for two different discharges for different times. We can see the influence of the halo in the first kilometers causing a sign change in the difference (*Pérez-Invernón et al., 2016a*). 96

3.24 Inclination of the geomagnetic field in degrees in 2015. This map has been developed by NOAA/NGDC and CIRES. . . . 99

3.25 Schematic procedure to obtain the EIWG transfer function of a curved Earth with a tilted geomagnetic field using the FWM. 100

3.26 EIWG transfer functions at ground level in decibels for a flat Earth (upper panel) and a curved Earth (lower panel). The horizontal axis corresponds to the distance between the radiating source and the point of detection. The values of the EIWG transfer functions are calculated for frequencies between 500 Hz and 20 kHz with a frequency step of 500 Hz. Both calculations have been performed using the 2-D FWM version under summer day conditions and in the presence of a vertically oriented geomagnetic field. 102

LIST OF FIGURES

- 3.27 Panels in the upper row show the decay of a signal with 16 kHz over the distance for a flat and a curved Earth, respectively. The background magnetic field vertical to the ground in both cases. The left panel in the lower row shows the positions of each signal peak for the flat and the curved case after establishing a one-to-one correlation. The differences in amplitude of each peak pair over the peak position is plotted in the right panel of the lower row. 104
- 3.28 Electric field at ground level for the flat case (blue), curved case (green) and corrected case (red), for a frequency of 16 kHz and with a vertical geomagnetic field. Both the blue and the green signals are calculated with the 2-D FWM version, while the red signal is obtained after applying the described transform method to the blue signal. The electric field is expressed in Vm^{-1} units and is produced by a dipole current of 1 A·m 108
- 3.29 Electric field at ground level for a propagating wave with a frequency of 16 kHz in the flat case calculated with the 3-D FWM (upper panel) and in the case with curvature after applying the transform method (lower panel). The electric field is expressed in Vm^{-1} units and is produced by a dipole current of 1 A·m located at 13 km of altitude and in the center of the x-y coordinate system shown. 109

4.1 Geometry for calculating the observed signal from ASIM. The elve and the spacecraft are located at altitudes h_0 and h_1 from the ground, respectively. $I(t)$ and $i(t)$ are the temporal evolution of the observed and emitted intensities, respectively. The center of the elve, denoted as O , is located at an horizontal distance l from ASIM. $R(t)$ corresponds to the temporal dependence of the elve radius, that is radially symmetrical. The blue line (s) represents the path of an observed photon emitted from the elve at a point given by (R, θ) 116

4.2 Value of the kernel (equation (4.16)) for an arbitrary value of τ . There are two vertical asymptotes in t_{inf} and t_{sup} as a consequence of the singularities of equation (4.14). 119

4.3 Piecewise-constant $i(t)$ 120

4.4 Approximation of an elve as a succession of thin rings. $I(t)$ corresponds to the signal observed from ASIM, while $\hat{I}(t)$ would be the observed signal observed if all the emissions were focused in an instantenous and, consequently, thin ring. 121

4.5 Difference between the quenching and the radiative decay rates of each vibrational state $N_2(a^1 \Pi_g, v = 0, \dots, 12)$ for different altitudes in $cm^{-3}s^{-1}$ multiplied by a scale factor. The altitude at which the quenching rate is similar to the radiative decay rate is called the quenching altitude. The quenching of each state can be neglected for altitudes significantly above the quenching altitude. These rates have been calculated using the Appendix??. 128

LIST OF FIGURES

4.6	Temporal evolution of the maximum reduced electric field inside a halo. The blue line corresponds to the maximum reduced electric field according to the halo model. The rest of the lines correspond to the inferred reduced electric field using the ratios of the observed First and Second Positive Systems of N_2 and the First Negative Systems of N_2^+ following subsection 4.2.1.	130
4.7	Temporal evolution of the maximum reduced electric field producing an elve. The blue line corresponds to the maximum reduced electric field according to the elve model. The rest of the lines correspond to the inferred reduced electric field using the ratios of the observed First Positive System, Second Positive System, First Negative System and LBH band of the N_2 following subsection 4.2.1.	132
4.8	Optical emissions in different wavelengths of an elve simulated in chapter 3 and triggered by a lightning with a current peak current of 220 kA.	133
4.9	Optical emissions in different wavelengths of an elve simulated in chapter 3 and triggered by a lightning with a current peak current of 220 kA convolved with their corresponding decay function.	134
4.10	Received signals from an elve at a spacecraft located at an altitude of 410 km and at a horizontal distance from the center of the elve of 80 km. We have assumed that the photometer has a FOV of 55° , an observation frequency of 20 kHz and a circular aperture with a total area of 0.04 m^{-2}	135
4.11	Signals of figure 4.10 (solid line) and signals after adding an artificial noise (dots).	136
4.12	Result of inverting the signals plotted in figure 4.10 (Orange points). We also plot the emitted signal given by the FDTD elve model (blue line).	136

4.13 Same as figure 4.12, but considering a larger FOV of 90° 136

4.14 Image data obtained by the broadband 768 nm - 830 nm filter (LSI-1) (first row) and by the narrowband 760 nm - 775 nm filter (LSI-2) (second row) for an event reported by GLIMS at a time of 16.28.04 (UT) on December 13, 2012. The temporal separation between each frame is about 33 ms. 138

4.15 Photometer data for an event reported by GLIMS at a time of 16.28.04 (UT) on December 13, 2012. The characteristics of each photometer are shown in table 4.1. 139

4.16 Expansion of the elve wavefront and the elve radius during a time of $\tau = \tau_2 - \tau_1$. Lightning and elve are located at altitudes of $h_{lightning}$ and h_0 , respectively. The elve wavefront propagates at the velocity of light. 141

4.17 The horizontal axis corresponds to the time since the beginning of the parent lightning. In the vertical axis we plot the advance of the wavefront and the radius of the elve during 0.1 ms before the corresponding time plotted in the horizontal axis. 142

4.18 Photons received by GLIMS in the 150 nm - 280 nm band from an elve. 143

4.19 Signal plotted in figure 4.18 after the application of the Wiener deconvolution in order to approximate the elve as a thin ring. 144

4.20 Emitting source for an instantaneous thin ring. 144

4.21 Source plotted in figure 4.20 after the convolution with the corresponding decay function in order to obtain the emitting source. This source emits photons with wavelengths between 150 nm and 280 nm. 145

4.22 Comparison between the source intensity derived using the inversion method and the simulated intensity emitted by an elve triggered by a CG lightning discharge with current peak of 83 kA. The simulated emitted intensity has been calculated using the FDTD elve model developed in chapter 3. 146

5.1 Ambient equilibrium daytime (solid lines) and nighttime (dashed lines) concentrations of (a) neutrals CO₂ (black line), N₂ (green line), O₂ (blue line), O (red line) and CO (yellow line), (b) positive ions CO₂⁺ (black line), O₂⁺ (blue line) and O⁺ (red line), and (c) electrons in the mesosphere of Venus as a function of the altitude (*Pérez-Invernón et al.*, 2016b). 154

5.2 Total ionization and attachment rates for a Venusian atmosphere as a function of the reduced electric field. These rates have been calculated with BOLSIG+ (*Hagelaar and Pitchford*, 2005). 155

5.3 Electron mobility (solid line) and conductivity (dashed line) ($\sigma = e\mu_e N_e$) of nighttime electrons in the mesosphere of Venus assuming $E/N = 0$ Td(ambient conditions) (*Pérez-Invernón et al.*, 2016b). 157

5.4 Maxwell relaxation times for $E/N = 0$ (ambient conditions) (dashed blue line), $E/N = 80$ Td (dashed green line) and $E/N = 2 E_k/N$ (dashed red line). Effective ionization times for $E/N = 80$ Td (solid green line) and $E/N = 2 E_k/N$ (solid red line). (*Pérez-Invernón et al.*, 2016b). 158

- 5.5 Time evolution of the applied electric field components due to an in-cloud discharge with a released energy of 10^{10} J calculated according to equation (3.2). The left panel shows the value of the field components at 100 km vs time, while the right panel shows the maximum value of each reduced electric field component at different altitudes for a discharge with a characteristic time of 0.1 ms. We do not take into account the effect of the ionosphere in this plots. 161
- 5.6 Representation of the propagation of ducted and unducted whistler waves through the magnetosphere of the Earth. The direction of the background magnetic field is also represented. The unducted whistler wave can be reflected when its frequency is equal to the local lower hybrid resonance frequency. 164
- 5.7 Structure of the magnetic field vector induced in the atmosphere of Venus by solar winds in the \mathbf{X} and \mathbf{Y} directions. R_V denotes distances in terms of the planetary radius. Data are folded into a single $+\mathbf{Z}$ hemisphere. Each panel represents a Z position range of $\pm 0.075 R_V$. These magnetic fields have been obtained by PVO measurements near the solar maximum. The vector labelled as 10 nT represent a magnetic field vector with a module of 10 nT. Adapted from *Phillips et al.* (1986). 165
- 5.8 Clemmow-Mullay-Allis (CMA) diagram for two-component (electron and ion) plasma. This diagram demonstrates different plasma wave modes at given frequency ω , depending on electron gyrofrequency Ω_e and electron plasma frequency ω_{pe} . Taken from (*Stix*, 1992, p. 27). 168

5.9 Time evolution of the reduced electric field E/N in the atmosphere of Venus under different cloud lightning discharges with total released energy of 10^{10} J, 2×10^{10} J and 10^{11} J. Four snapshots are shown for each energy. The discharge length of the cloud discharge channel in this case is 10 km, and the radius of the spheres (acting as clouds) that contain the charges is set to 2.5 km (*Pérez-Invernón et al.*, 2016b). Note that the reduced breakdown field in the Venusian atmosphere is ~ 75 Td. 174

5.10 Time evolution of the electron density in the atmosphere of Venus under different cloud lightning discharges with total released energy of 10^{10} J, 2×10^{10} J and 10^{11} J. Four snapshots are shown for each energy (*Pérez-Invernón et al.*, 2016b). 175

5.11 Total number of photons per second emitted by the entire halo up to 1 ms due to the radiative decay $O(^1S) \rightarrow O + h\nu$ (557 nm). The considered cloud discharges release a total energy of 10^{10} J (top panel), 2×10^{10} J (middle panel) and 10^{11} J (bottom panel) (*Pérez-Invernón et al.*, 2016b). 177

5.12 Total number of photons per second emitted by the entire halo up to 1 ms due to the radiative decays $N_2(B^3\Pi_g \text{ (all } v')) \rightarrow N_2(A^3\Sigma_g^+ \text{ (all } v'')) + h\nu$ (550 nm - 1.2 μm) and $N_2(C^3\Pi_u \text{ (all } v')) \rightarrow N_2(B^3\Pi_g \text{ (all } v'')) + h\nu$ (250 - 450 nm). The considered cloud discharges release a total energy of 10^{10} J (top panel), 2×10^{10} J (middle panel) and 10^{11} J (bottom panel) (*Pérez-Invernón et al.*, 2016b). 178

5.13 Total number of photons per second emitted by the entire halo up to 1 ms due to the radiative decays $N_2(W^3\Delta_u (v' = 0)) \rightarrow N_2(X^1\Sigma_g^+ (v'' = 5)) + h\nu$ (208 nm) and $N_2(W^3\Delta_u (v' = 0)) \rightarrow N_2(B^3\Pi_g (v'' = 0)) + h\nu$ (136.10 μm). The considered cloud discharges release a total energy of 10^{10} J (top panel), 2×10^{10} J (middle panel) and 10^{11} J (bottom panel) (*Pérez-Invernón et al.*, 2016b). 179

5.14 Total number of photons per second emitted by the entire halo up to 1 ms due to the radiative decays $N_2(a^1\Pi_g (\text{all } v')) \rightarrow N_2(X^1\Sigma_g^+ (\text{all } v'')) + h\nu$ (120 - 280 nm) and $N_2(a^1\Pi_g (v' = 0)) \rightarrow N_2(a^1\Pi_g (v'' = 0)) + h\nu$ (8.25 μm). The considered cloud discharges release a total energy of 10^{10} J (top panel), 2×10^{10} J (middle panel) and 10^{11} J (bottom panel) (*Pérez-Invernón et al.*, 2016b). 180

5.15 Emission brightness in Rayleigh from the radiative decay $O(^1S) \rightarrow O(^1D)$ (557 nm) along different positions of the glowing disc and for different times after the beginning of the IC discharge: 0.5 ms (black line), 0.75 ms (red line) and 1 ms (blue line). The considered cloud discharges release a total energy of 10^{10} J (top panel), 2×10^{10} J (middle panel) and 10^{11} J (bottom panel) (*Pérez-Invernón et al.*, 2016b). 181

5.16 Time evolution of the $\text{CO}_2(001)$ density in the center of the halo created by cloud lightning discharges with total released energy of (a) 10^{10} J, (b) 2×10^{10} J and (c) 10^{11} J (*Pérez-Invernón et al.*, 2016b). 183

5.17 Reduced electric field E/N in the atmosphere of Venus created by lightnings with several inclinations. We show snapshots at two different times after the beginning of the discharge with two total released energies: 2×10^{10} J and 10^{11} J. We plot results for three different channel inclinations (*Pérez-Invernón et al.*, 2017b). 185

- 5.18 Main optical emission brightness, in Rayleigh, in the atmosphere of Venus 0.3 ms after the initiation of a lightning discharge with a total released energy of 10^{11} J. The plots show optical emissions produced by radiative decay of $O(^1S)$ (557 nm), $N_2(B^3\Pi_g)$ (all v') (550 nm - 1.2 μm), $N_2(C^3\Pi_u)$ (all v') (250 - 450 nm), $N_2(a^1\Pi_g)$ (all v') (120 - 280 nm) and $N_2(a^1\Pi_g)$ ($v' = 0$) (8.25 μm). The shown optical emissions correspond to the nadir direction from an orbiting probe without considering atmospheric and geometric attenuation (*Pérez-Invernón et al.*, 2017b). 188
- 5.19 Some optical emission brightness, in Rayleigh, in the atmosphere of Venus 1 ms after the initiation of lightning discharges with total released energies of 2×10^{10} J and 10^{11} J and three inclinations. The direction of the horizontal and oblique channels in the xy plane is of 45° . The shown optical emissions correspond to the radiative decay of $O(^1S)$ (557 nm) and $N_2(B^3\Pi_g)$ (all v') (550 nm - 1.2 μm). The optical emissions shown correspond to the nadir direction from an orbiting probe without considering atmospheric and geometric attenuation (*Pérez-Invernón et al.*, 2017b). 190
- 5.20 Geometrical scheme in cylindrical coordinates and ambient concentration of electrons in the nightside of Venus (red line) (*Borucki et al.*, 1982; *Bauer et al.*, 1985; *Pérez-Invernón et al.*, 2016b). Lightning channels can be vertical (red) or horizontal (blue). We calculate lightning-produced electromagnetic fields at detection levels (green dashed lines) to compare with observations. The background magnetic field is vertical to ground everywhere (*Pérez-Invernón et al.*, 2017a). 197

5.21 Maximum power spectral density (PSD) in $(\text{V/m})^2\text{Hz}^{-1}$ calculated from the E_x and E_y components at different altitudes and resulting from a lightning rate of 1 stroke per second for horizontal discharges (first row) and vertical discharges (second row). The x-axis represent the background magnetic field and the y-axis corresponds to the ionospheric hole magnitude, defined as the reduction of the electron density compared to the background value (n_{e0}) which peaks at around $3 \times 10^4 \text{ cm}^{-3}$. This definition of the x-axis alludes explicitly to the holes detected by PVO. We plot results for background magnetic fields greater than 1 nT (*Pérez-Invernón et al., 2017a*). 200

5.22 Time averaged electromagnetic field and Poynting vector components produced by a vertical discharge in the ionosphere of Venus under a background magnetic field of 20 nT and a reduction of 5 orders of magnitude in the electron and ion densities. The vertical lightning discharge is located at 45 km of altitude and produces a wave with a frequency of 100 Hz. This plot shows atmospheric regions above an altitude of 100 km (*Pérez-Invernón et al., 2017a*). 202

5.23 Time averaged electromagnetic field and Poynting vector components produced by a horizontal discharge in the ionosphere of Venus under a background magnetic field of 20 nT and a reduction of 5 orders of magnitude in the electron and ion densities. In this case, The horizontal lightning discharge is a dipole located at 45 km of altitude and contained in the plane x-z. The source produces a wave with a frequency of 100 Hz. As in figure 5.22, this plot shows atmospheric regions above an altitude of 100 km (*Pérez-Invernón et al., 2017a*). 203

5.24 (left) Power spectral density at 250 km of altitude in $(\text{nT})^2\text{Hz}^{-1}$ calculated at 40 Hz from the B_x and B_y components at different altitudes and resulting from a lightning rate of 1 stroke per second for vertical discharges. The axes are the same as in figure 5.21. We also plot results for background magnetic fields greater than 1 nT. (right) Calculated power spectral density for different frequencies and a fixed intermediate background magnetic field of 15 nT, where the numbers in the inset indicate the order of magnitude of the reduction in the electron and ion density peak, n_{e0} . The spectrum recorded in the nightside of Venus by VEX is also shown (dashed line) (*Russell et al.*, 2013). Results below 24 Hz could change with the inclusion of the planetary curvature as a consequence of the Schumann resonances (*Pérez-Invernón et al.*, 2017a). 205

5.25 Attenuation of the electromagnetic signal (in dB) at 100 Hz after traversing the Venusian ionosphere from 75 km to 250 km altitude under a background magnetic field greater than 3 nT. The axes are the same as in Figure 5.21. Here we plot values of the transfer function for different orders of magnitude in the reduction of the electron and ion density peak (*Pérez-Invernón et al.*, 2017a). 207

6.1 Structure of the Jovian (left) and Saturnian (right) atmospheres. Lightning discharges take place in the cloud layers. The altitude of 0 km is conventionally defined at the level where the pressure is 1 bar in each planetary atmosphere. Adapted from Pearson Prentice Hall, Inc. (2011). 213

6.2 Weighted ionization and attachment rates as a function of the reduced electric field in the Jovian atmosphere. These rates have been calculated with BOLSIG+ (*Hagelaar and Pitchford*, 2005). 215

6.3 Approximated quasi-static, induction, and radiation-reduced electric fields in the atmospheres of Jupiter and Saturn as a consequence of a lightning discharge with a CMC of 10^5 C km and a characteristic discharge time of 100 μ s. In these plots *Luque et al.* (2014) do not take into account the effect of the ionospheric electrons in the electric field. Adapted from (*Luque et al.*, 2014). 216

6.4 Reduced electric field E/N and electron density perturbation in the atmosphere of Saturn created between 4.8 ms and 5 ms after the beginning of a lightning discharge with a CMC of 10^5 C km and different channel inclinations and initial electron density profiles (with and without a CH_x layer). Subplots show results in the y-z plane for a latitude of 35° . The total energy released by the considered lightning is 10^{12} J. In the case of the vertical discharge, the channel is a straight line with coordinates $x = y = 0$, while in the case of the horizontal discharge, its coordinates are $x=z=0$. The oblique channel, contained in the y-z plane, forms an angle of 45° with the y axis. The background magnetic field at this latitude forms an angle of 35° with the vertical axis, and is contained in the plane x-z (*Pérez-Invernón et al.*, 2017b). 218

6.5 Reduced electric field E/N and electron density perturbation in the upper atmosphere of Jupiter as seen 3 ms after the beginning of a Jovian lightning discharge with different inclinations with charge moment changes of 10^4 and 10^5 C km. The subplots show results in the y-z plane for a latitude of 35° with the initial electron density profile measured at ingress of Voyager 2 (V2N). The total energy released by the considered lightning is 10^{12} J. In the case of the vertical discharge, the channel is a straight line with coordinates $x = y = 0$, while in the case of the horizontal discharge, its coordinates are $x = z = 0$. The background magnetic field at this latitude forms an angle of 35° with the vertical axis, and is contained in the plane x-z (*Pérez-Invernón et al., 2017b*). 220

6.6 Reduced electric field E/N in the upper atmosphere of Jupiter created 3 ms after the onset of a horizontal lightning discharge with a CMC of 10^5 C km as seen at different latitudes (first and second panels). The last panel shows the difference between the second and the first panel. These results correspond to the case of the V2N electron density profile. The total energy released by the considered lightning is 10^{12} J (*Pérez-Invernón et al., 2017b*). 221

6.7 Integrated flux of total emitted photons from the radiative decays of $\text{H}_2(\text{d}^3\Pi_u)$ and $\text{H}_2(\text{a}^3\Sigma_g^+)$ between 4.8 ms and 5 ms after a lightning discharge on Saturn with different CMCs of 10^5 C km and 10^6 C km. Different channel inclinations are shown in each column, while each row corresponds to two different initial electron densities. The total energy released by the considered lightning discharges are 10^{12} J and 10^{13} J. The total number of emitted photons shown corresponds to the nadir direction from an orbiting probe without considering atmospheric and geometric attenuation. Lightning channel and background magnetic field inclinations are as in figure 6.4. (*Pérez-Invernón et al.*, 2017b). 225

6.8 Integrated flux of total emitted photons from the radiative decays of $\text{H}_2(\text{d}^3\Pi_u)$ and $\text{H}_2(\text{a}^3\Sigma_g^+)$ 3 ms after Jovian lightning discharges with different charge moment changes. Vertical and horizontal channel inclinations are shown in each column. These results correspond to the case of the V2N electron density profile. The total energy released by lightning is 10^{12} J. The total number of emitted photons shown corresponds to the nadir direction from an orbiting probe without considering atmospheric and geometric attenuation. Lightning channel and background magnetic field inclinations are as in figure 6.5. (*Pérez-Invernón et al.*, 2017b). 226

LIST OF FIGURES

List of Tables

3.1	Coefficients of the transform equation (3.20). This equation transforms the EIWG transfer function for a flat Earth to the case with curvature.	107
4.1	Optical characteristic of the photometers onboard ISUAL (<i>Chern et al.</i> , 2003), GLIMS (<i>Sato et al.</i> , 2015; <i>Adachi et al.</i> , 2016), ASIM (<i>Neubert et al.</i> , 2006) and TARANIS (<i>Blanc et al.</i> , 2007) It is also indicated the observation mode of each photometer.	137
5.1	Total number of emitted photons for cloud lightnings with total released energy of 10^{10} J, 2×10^{10} J and 10^{11} J one millisecond after the onset of the halo (<i>Pérez-Invernón et al.</i> , 2016b).	176
5.2	Total number of emitted photons and approximate optical energy released from the lower ionosphere for cloud lightning discharges on Venus with total released energy of 10^{10} J (<i>Pérez-Invernón et al.</i> , 2017b). Transitions are as in table 5.10.186	
5.3	Total number of emitted photons and approximate optical energy released from the lower ionosphere for cloud lightning discharges on Venus with total released energy of 2×10^{10} J (<i>Pérez-Invernón et al.</i> , 2017b). Transitions are as in table 5.10.186	

5.4 Total number of emitted photons and approximate optical energy released from the lower ionosphere for cloud lightning discharges on Venus with total released energy of 10^{11} J (*Pérez-Invernón et al.*, 2017b). Transitions are as in table 5.10.187

6.1 Total number of emitted photons and approximated optical energy released from the Saturnian ionosphere between 4.8 ms and 5 ms after the onset of a cloud discharge. CH_x corresponds to an electron density profile in the presence of a hydrocarbon layer, while non CH_x corresponds to an electron density profile without a hydrocarbon layer. Charge moment change (CMC) are in C km. Null values are below our numerical precision, while - corresponds to not calculated cases. Emissions are produced by radiative decay of $\text{H}_2(\text{d}^3\Pi_u)$ and $\text{H}_2(\text{a}^3\Sigma_g^+)$ molecules (*Pérez-Invernón et al.*, 2017b). 222

6.2 Total number of emitted photons and approximated optical energy released from the Jovian ionosphere 3 ms after a cloud lightning. V2N corresponds to an electron density profile measured at ingress of Voyager 2, while V2X corresponds to measurements at egress. Charge moment change (CMC) are in C km. Null values are below our numerical precision. Emissions are produced by radiative decay of $\text{H}_2(\text{d}^3\Pi_u)$ and $\text{H}_2(\text{a}^3\Sigma_g^+)$ molecules (*Pérez-Invernón et al.*, 2017b). 223

A.1 Ionization and dissociative ionization processes. 237

A.2 Electronical and vibrational excitation processes by electron impact, including those in which dissociation can occur. . . . 237

A.3 Attachment processes. 238

A.4 Electron detachment processes. 238

A.5 Electron-ion recombination processes. 239

A.6 Ionic kinetics. 242

A.7 Electron impact dissociation processes producing ground state species. 242

A.8 Neutral kinetics. 245

A.9 Vibrational-Translational (VT) Vibrational-Vibrational (VV) processes. 246

A.10 Electronic quenching. 246

A.11 Vibrational redistribution. 247

A.12 Energy pooling reactions. 247

A.13 Intersystem collisional transfer (ICT). 247

A.14 Radiative decay processes. 247

A.15 Species considered in the basic kinetic model providing ambient nighttime electron density profiles in Venus between 70 km and 125 km of altitude. We do not include here the species whose density remains constant in time. 248

A.16 Basic kinetic scheme of the model providing ambient nighttime electron density profiles in Venus between 70 km and 125 km of altitude. The gas temperature (T) is in K. The electron temperature is $T_e = T$. References are as follows: [1] *Viggiano et al.* (2005); [2] *Gordillo-Vázquez* (2008); [3] *Brasseur and Solomon* (2005); [4] *Chen and Nagy* (1978); [5] *Upadhyay and Singh* (1990); [6] *Schunk and Nagy* (1980); [7] *Nordheim et al.* (2015); [8] *Chen and Nagy* (1978). Note that for photoionization mechanisms (37)-(40) reactions rates (in $\text{cm}^{-3} \text{s}^{-1}$) rather than rates ($\text{cm}^3 \text{s}^{-1}$) are shown. The values of the reaction rate k and of the nondimensional magnitudes $\eta_i = N_i/N$ (with $\eta_1 = 0.9$, $\eta_2 = 0.1$, $\eta_3 = 10^{-6}$, $\eta_4 = 10^{-6}$) are obtained from *Nordheim et al.* (2015) and *Chen and Nagy* (1978), respectively. 249

A.17 Species considered in the 2D electric discharge model between 70 km and 125 km of altitude. 250

A.18 Basic kinetic scheme of the 2D electric discharge model between 70 km and 125 km of altitude in the mesosphere of Venus. The gas temperature (T) is in K. The electron temperature (T_e) dependence of some rates is transformed into a reduced electric field (E/N) dependence using $T_e(\text{eV}) = 2\bar{\epsilon}/3$ where the mean electron energy ($\bar{\epsilon}$) is obtained from BOLSIG+. References are as follows: [1] *Viggiano et al.* (2005); [2] *Gordillo-Vázquez* (2008); [3] *Brasseur and Solomon* (2005); [4] *Chen and Nagy* (1978); [5] *Upadhyay and Singh* (1990); [6] *Schunk and Nagy* (1980); [9] *Itikawa* (2002); [10] *Itikawa* (2006); [11] *Phelps* (2005); [12] *Laher and Gilmore* (1990); [13] *Pagnon et al.* (1995); [14] *Erdman and Zipf* (1987); [15] *Atkinson and Welge* (1972); [16] *Filseth et al.* (1970); [17] *Parra-Rojas et al.* (2014); [18] *Dagdikian et al.* (1988); [19] *Rayment and Moruzzi* (1978); [20] *Rapp and Briglia* (1965); [21] *Capitelli et al.* (2000); [22] *Gilmore et al.* (1992). Note that reactions No. 1 through 7 together with reactions 16 and 19 are the same as in Table 2. 251

A.19 Vibrational-Translational (VT) and Vibrational-Vibrational (VV) processes. The rates shown are defined as $k_{co2} = g \times h \times \exp(i/T + j/T^2)$ in cm^3s^{-1} with the gas temperature (T) in Kelvins. The rates of the return processes are calculated multiplying the direct reaction rate by $\exp(-E/\kappa_B T)$, where E is the energy emitted/absorbed during the process and κ_B stands for the Boltzmann constant. References are as follows: [23] *Lepoutre et al.* (1977); [24] *López-Valverde* (1990); [25] *Orr and Smith* (1987) 252

Chapter 1

Introduction

1.1 Lightning

The atmosphere of the Earth, mainly composed by molecular nitrogen and oxygen, can be seen as a global electric circuit where numerous electrical phenomena contribute to separate, transport and recombine electrical charges, as firstly investigated by Lemonnier (*Kasemir*, 1959). Lightning is the most powerful mechanism of discharge that takes place in this circuit. Despite the complexity of the channels and the stages that compound a lightning discharge, they can be defined as a fast movement of charge taking place between two regions. Depending on the nature of these regions, lightning can be either cloud-to-ground discharges (CG) or cloud discharges, which are subdivided into intra-cloud (IC) and cloud-to-cloud (CC).

The study of lightning began around the time of Benjamin Franklin, when he carried out his investigations about the electricity on clouds. He described and probably performed the so-called “Kite Experiment”, storing electrical charge in a Leyden jar from a thunderstorm (*Cohen*, 1941). The investigations about the charge distribution inside clouds by the 1927 Nobel Prize winner C.T.R. Wilson entailed another historical contribution to the study of lightning (*Wilson*, 1916, 1921). Since then, the improvement of technology has led to a better knowledge of the physics and chemistry behind

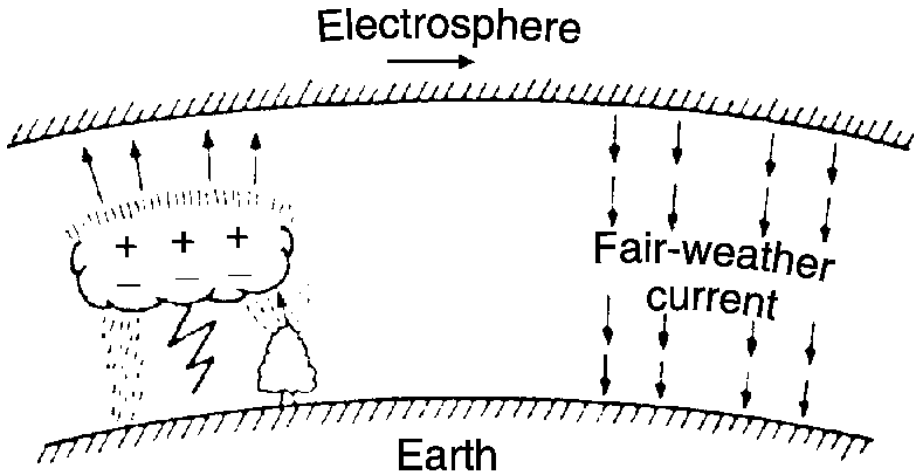


Figure 1.1: Global electric circuit. The surface of the Earth is charged negatively and the air is charged positively. The vertical electric field in fair weather is about 100 V m^{-1} . Adapted from *Pierce (1974)* and *Rakov and Uman (2003)*.

lightning discharges and other related atmospheric electrical phenomena.

Lightning discharges are triggered in the troposphere by a cloud electrification process. Most lightnings is produced in cumulonimbus, although they can also be triggered in other types of clouds, such as stratiform clouds, pyrocumulus, volcanic clouds or sandstorms. Electrification occurs in the region of the cloud placed between 0°C and -40°C , where water can coexist in different phases. In that region, liquid water, graupel and ice particles are transported either upward by convection or downward by the action of gravity. Although the cloud electrification mechanism is complex and not fully understood, it is accepted that collisions between graupel and ice particles provide each of them with opposite net charge, accumulating the positively charged ice and the negatively charged graupel in different places of the cloud. The final distribution of charges determines the type and polarity of the resultant lightning discharge.

Despite the complexity of the real charge distribution structure, the charged layer inside clouds are usually simplified as shown in figure 1.2.



Figure 1.2: Charge distribution inside a thundercloud in New Mexico (*Krehbiel, 1986; Rakov and Uman, 2003*).

The negative charge is often accumulated in the middle part of the cloud, while the positive usually locates both at the top and at the bottom. The total charge at the main positive and negative parts of the cloud can be of the order of tens of coulombs, while only ~ 10 C are accumulated at the secondary positive charged part, located at the lower part of the cloud (*Rakov and Uman, 2003*). This accumulation of electrical charge produces an electric field in the cloud that can trigger the inception of a discharge. Electrical breakdown occurs in air when an intense voltage ionizes the gas, causing the air to behave as a conductor of electricity. This process is known as conventional electrical breakdown, while the threshold value of the electric field that triggers the process is called breakdown field. According to measurements, the electric field created in thunderclouds is lower than 2×10^5 V m⁻¹, while breakdown field is $\sim 10 \times 10^6$ V m⁻¹. This apparent contradiction keeps the lightning initiation mechanism not well established. Some theories propose relativistic runaway processes together with conven-

1. INTRODUCTION

tional dielectric breakdown as the cause of lightning initiation (*Gurevich et al.*, 1992; *Gurevich and Zybin*, 2001; *Dwyer et al.*, 2005). Cosmic-ray background electron would be accelerated by the applied electric field producing secondary electrons after the collision with air molecules. However, according to recent observations by *Rison et al.* (2016) only fast positive breakdown processes could trigger many or all-lightning discharges.

After the breakdown, the discharge emerges in the form of streamers forming part of a streamer corona. Streamers are formed by an ionization front followed by a conductive plasma filament. Streamers can heat the air up to the so-called streamer-to-leader transition. A leader is a highly conductive plasma channel that can transport charge and heat the air to temperatures of thousands of kelvins.



Figure 1.3: Cloud to ground lightning discharge impacting over a building. Photo taken by José Luis Escudero Gallegos in Málaga (Spain) in 2017.

As mentioned above, lightning can be either cloud-to-ground or cloud discharges. There exist some differences in the stages of these two types of lightning. Cloud-to-ground lightnings, which represent $\sim 20\%$ of the total lightning discharges and have a characteristic time of several milliseconds, are often initiated between the negative and the lower positive charge layers inside clouds. After the breakdown, a stepped leader starts its path and

surpasses the lower charged region of the cloud. Afterwards, the leader keeps descending down to the ground with a velocity of about $2 \times 10^5 \text{ m s}^{-1}$. In case of a negative leader, it propagates in consecutive discrete steps every 10-50 μs , while positive leaders propagate in faster time steps. When the stepped leader approaches the charge accumulated near the ground, a channel is formed between clouds and ground. This connection triggers a violent and luminous flow of charge that can transport tens to hundreds of coulombs producing currents of tens of kiloamperes. This stage of the discharge is known as return stroke, and can be repeated several times after the end of the first discharge process. The temperature inside the channel can increase up to more than 10000 K, triggering a cascade of chemical reactions that can produce an important amount of NO molecules and other species. About 90% of all CG lightning discharges have negative polarity, while the remaining flashes are positive. Electric currents produced by positive CG lightning discharges are often three times higher than those produced in negative discharges. Furthermore, a continuous current forms an important part of the positive lightning discharge that can favor the occurrence of Transient Luminous Events (TLEs) and wildfires.

Cloud discharges are $\sim 80\%$ of the total global lightning discharges and have characteristic times of microseconds. They are often less powerful than CG lightning discharges. Therefore, detection and characterization of cloud discharges is more difficult and they are less understood than CG lightning discharges, since they do not have a return stroke phase. They are often initiated between the two main charged regions of a cloud or between two clouds, and are formed by two different stages. The first stage is known as active stage and begins when a leader extend from one of the charged regions to the other with a velocity of about 10^5 m s^{-1} (*Rakov and Uman, 2003*). During the final stage a small amount of charge is transported to the location where the flash began. Cloud discharges can neutralize tens of coulombs of charge and are capable of producing currents of hundreds

1. INTRODUCTION

of amperes. Figure 1.4 shows the different types of lightning and the cloud regions where they often start and end.

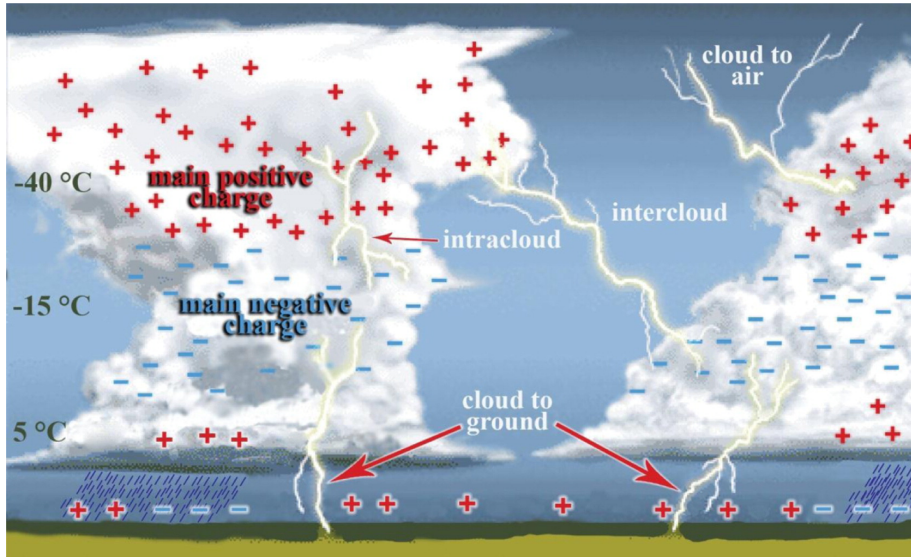


Figure 1.4: Different types of lightning. Courtesy of the British Encyclopedia.

The high temperatures reached in the lightning channel can trigger a cascade of chemical reactions producing an important amount of molecules of different species. In addition, the lightning channel can damage buildings, technological devices, vehicles, forests or even humans. For this reason, a good knowledge of the spatial and temporal global lightning occurrence and its relation with climatic or meteorological variables becomes very important to prevent damage.

The occurrence of lightning discharges around the globe has been estimated thanks to space-based optical observations. The Optical Transient Detector (OTD) and the Lightning Imaging Sensor (LIS), onboard the Tropical Rainfall Measuring Mission (TRMM) satellite, recorded the temporal and geographical occurrence rates of lightning around the globe, plotted in figure 1.5. According to these observations, around 44 lightning flashes could take place every second all around the world. As can be seen in the

map, most flashes are produced in the tropical continental regions between 60°S and 60°N, where the atmospheric convection is stronger. Furthermore, OTD/LIS data reveals that the season with most lightning occurrence is the Northern Hemisphere summer. It has been recently estimated that lightning flash frequency could enhance due to global warming by about ~ 5 flashes per second for each degree of increase in temperature (*Romps et al.*, 2014).

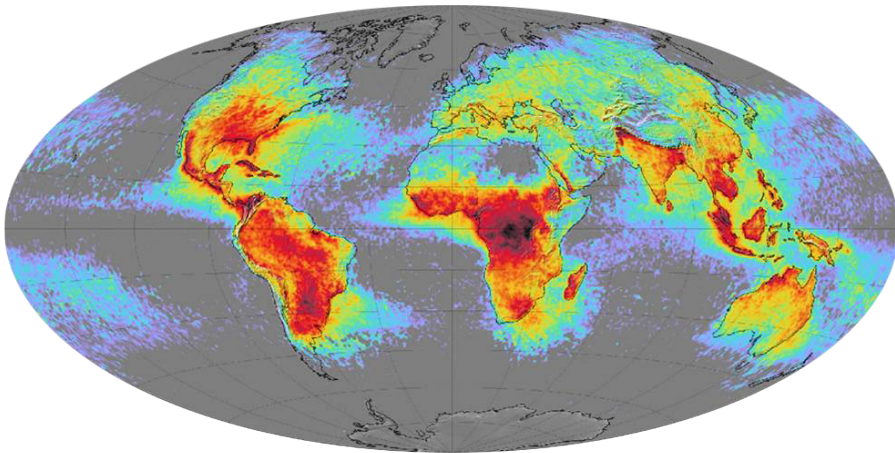


Figure 1.5: Lightning flash density in flashes per second and per squared kilometer (flashes/s km²) around the globe from 1995 to 2003. Observations by the Optical Transient Detector (OTD) and the Lightning Imaging Sensor (LIS) (*Christian et al.*, 2003).

Nowadays, lightning discharges produce 10% of the tropospheric $\text{NO}_x = \text{NO} + \text{NO}_2$. However, they were one of the most important sources of NO_x in the pre-industrial period. Furthermore, lightning discharges are small sources of other trace gases, such as N_2O , HNO_2 , H_2O_2 , HO_2 , CO and O_3 (*Schumann and Huntrieser*, 2007).

The inclusion of lightning occurrence in global or regional atmospheric models needs a good knowledge of the relation between some meteorological quantities and lightning. In 1992, Price and Rind proposed one of the first lightning parameterizations, finding an empirical relation between the cloud top height and the lightning flash density data (*Price and Rind*, 1992). Since

1. INTRODUCTION

then, many authors have proposed new lightning parameterizations looking for other relations between observed meteorological variables and lightning occurrence (*Tost et al.*, 2007).

There are numerous ground-based and space-based lightning detection systems currently in operation over the globe, known as Lightning Location Systems (LLS) (*Nag et al.*, 2015). The objective of these systems is twofold. On the one hand, they provide valuable scientific information about lightning characteristics. On the other hand, remote measurements of electrical activity are essential to minimize the risks involved in severe weather. The quasiolelectrostatic field created by lightning discharges in thunderstorms decays as the inverse of the third power of distance to the source. On the other hand the radiation field or pulses emitted by the rapidly varying currents of the lightning discharge decays with the inverse of the distance. For this reason, lightning detection systems often rely on the measurement of the emitted pulses at different spectral bands rather than on the quasiolelectrostatic field. Some of the most important networks are the World Wide Lightning Location Network (WWLLN), the U.S. National Lightning Detection Network (NLDN), the Canadian Lightning Detection Network (CLDN), the European lightning detection network (LINET) and the Vaisala Global Lightning Data set GLD360. Some low-Earth orbiting satellites, as OTD/LIS, have provided useful information about lightning characteristics (*Christian et al.*, 2003). The block of four satellites known as Geostationary Operational Environmental Satellite R-series (GOES-R) *Goodman et al.* (2013), operating since 2016, will also provide useful information about lightning using different instruments.

The most distant measurement of lightning-emitted waves is often done in the Extremely Low Frequency (ELF), the Very Low Frequency (VLF) or Low Frequency (LF) ranges of the radiation spectrum (*Nag et al.*, 2015). A portion of the lower frequency lightning-emitted radiation waves travels through the cavity formed by the Earth ground and the ionosphere, which acts as a waveguide. Lightning can excite and generate transverse

resonances or the so-called longitudinal Schumann resonances, detected as several peaks in the ELF part of the electromagnetic spectrum. These resonances were predicted by Winfried Otto Schumann in 1952 (*Schumann, 1952*) and later discovered in the early 1960s. The remaining lightning-emitted energy is either absorbed by the atmosphere or transmitted out of the Earth in the form of whistler waves, a Very Low Frequency (VLF) wave that propagates through the ionosphere interacting with inospheric electrons and ions (*Helliwell, 1965*). In 1999, the radio and plasma wave science (RPWS), onboard the Cassini spacecraft, reported VLF waves during its Earth flyby at an altitude of 1186 km (*Kurth et al., 2001*). Measurements in other spectral bands, such as in the High Frequency (HF), in the Very High Frequency (VHF) or even in the near InfraRed (IR) or optical ranges are usually done in the line of sight between the detection system and the thunderstorm (*Nag et al., 2015*).

There exist other tropospheric electrical discharges that could be closely related with CG and cloud lightning discharges and have characteristic times of several microseconds. One of them is the so-called Compact Intracloud Discharges (CID). According to recent results, these positive and impulsive discharges could be part of the beginning of all lightning discharges *Rison et al. (2016)*. Furthermore, there are other impulsive electrical discharges known as energetic in-cloud pulses (EIPs) that could be involved in the production of Terrestrial Gamma-ray Flashes (TGF) (*Cummer et al., 2014; Lyu et al., 2015; Watson and Marshall, 2007; Liu et al., 2017*). These high energy photons were discovered in 1994 by the NASA “Burst and Transient Source Experiment” (BATSE) (*Fishman et al., 1994*). Both CIDs and EIPs are often formed by currents with peaks higher than 400 kA and can emit High Frequency (HF) radiation.

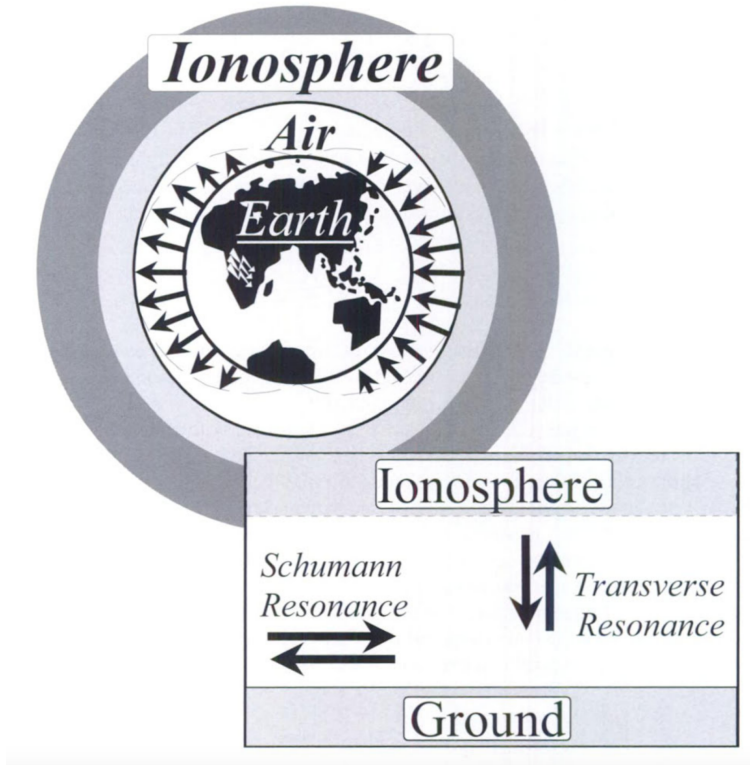


Figure 1.6: Transverse and longitudinal resonances in the Earth-ionosphere cavity (*Nickolaenko and Hayakawa, 2002*).

1.2 Transient Luminous Events

While the existence of optical flashes produced by lightning has always been known, in 1886 Mackenzie described for the first time some optical flashes taking place above a thunderstorm (*Mackenzie and Toynbee, 1886*). Later in the 20th century similar observations were reported by ground-based observer and pilots (*Everett, 1903; Boys, 1926; Malan, 1937*). Although the nature of these events was still unknown, nowadays we know that they were probably the first reported observations of Transient Luminous Events (TLEs).

C.T.R. Wilson, the winner of the Nobel Prize in Physics in 1927, was the first scientist who related thunderstorms and upper atmospheric optical

emissions. In 1924 he proposed the electric field created by a thunderstorm as the triggering mechanism of upper atmospheric ionization (*Wilson, 1925*). According to his theory, the thundercloud-produced electric field applied to the low-density air present in the mesosphere would trigger an ionization process driven by electron collisions producing an electrical discharge above clouds.

Since the theory of Wilson, there were other reports of flashes above thunderclouds (*Ashmore, 1950; Burch et al., 1958; Vaughan Jr. and Vonnegut, 1989*), while some scientists attempted to detect and document them scientifically without success (*Vonnegut et al., 1989*).

Despite the efforts of Bernard Vonnegut and Otha H. Vaughan to prove the existence of the discharges predicted by Wilson, these Transient Luminous Events were accidentally discovered by a group of scientists headed by J. R. Winkler in 1989 (*Franz et al., 1990*). They were performing investigations of Rayleigh scattering using the SKYFLASH Experiment when they recorded the first scientifically documented TLEs.

Since 1989, TLEs have been widely modeled and observed from planes, ground-based detectors, such the GRANada Sprite Spectrograph and Polarimeter (GRASSP), and space-based instrumentation (*Kanmae et al., 2007; Gordillo-Vázquez, 2008; Sentman et al., 2008; Pasko et al., 2012; Chern et al., 2014*). Nowadays we know about the existence of several kind of TLEs, while the physical production mechanisms behind some of them and their global chemical impact in the terrestrial atmosphere is still a subject of study.

The instrument “Imager of Sprites and Upper Atmospheric Lightning” (ISUAL), onboard the FORMOSAT-2 satellite of the National Space Organization (NSPO), detected TLEs from its orbit from May 2004 to July 2013 (*Chern et al., 2014*). ISUAL was the first instrument in space dedicated to the observation of TLEs. The Global Lightning and sprite MeasurementS (GLIMS) of the Japan Aerospace Exploration Agency (JAXA) also contributed to the knowledge of terrestrial TLEs. Other missions, such as the



Figure 1.7: First scientifically documented image of a TLE (a sprite) in 1989 (*Franz et al.*, 1990).

“Atmosphere-Space Interactions Monitor” (ASIM) (*Neubert et al.*, 2006) of the European Spatial Agency (ESA) and the “Tool for the Analysis of RAdiations from lightNING and Sprites” (TARANIS) (*Blanc et al.*, 2007) of the Centre National d’Études Spatiales (CNES), will be devoted to the observation of these events from space during the next years (2018-2022).

1.2.1 Elves

The most common TLEs are the so-called elves (Emission of Light and Very low frequency perturbations due to Electromagnetic pulse Sources). Approximately 73% of TLEs observed by ISUAL were elves (*Chern et al.*, 2014).

When lightning-emitted electromagnetic pulses (EMP) reach the lower ionosphere, they can heat electrons. These electrons produce molecular

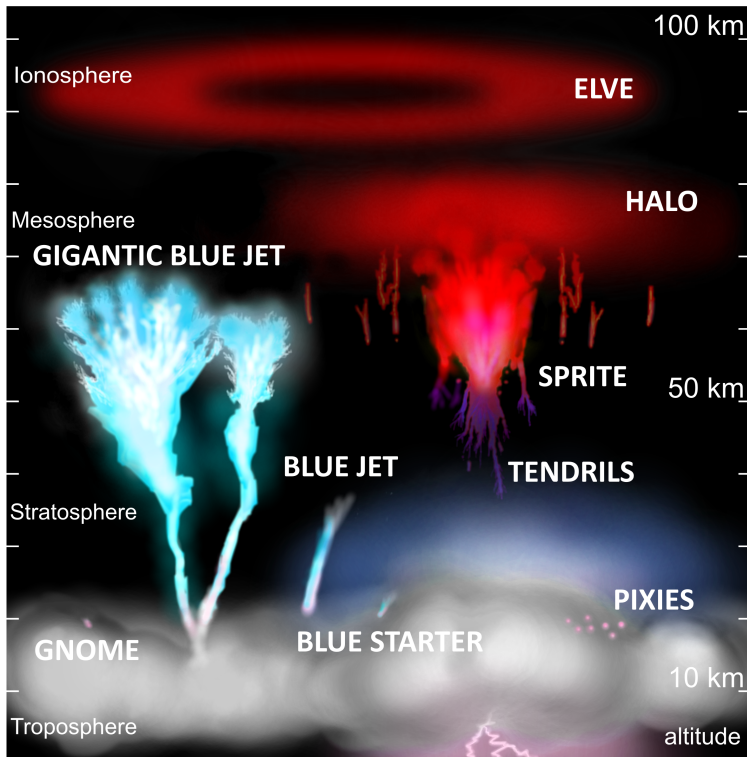


Figure 1.8: Types of Transient Luminous Events (TLEs). Courtesy of María Passas Varo.

excitation and fast red optical emissions known as elves, lasting less than 1 millisecond.

This TLE is usually observed in a thin layer located at altitudes around 88 km (*van der Velde and Montanyà, 2016a*), with a lateral extension of more than 200 km. Two lobes that expand from the lightning channel center in the horizontal direction form the vertically oriented CG lightning-radiated emission pattern. This expansion causes the ring-shaped emissions known as elves. When elves are caused by lightning discharges with a non-vertical orientation, they can be seen as a solid disc.

The first observation of elves from spacecraft was accomplished by the Space Shuttle (*Boeck et al., 1992*). The study of these events from space

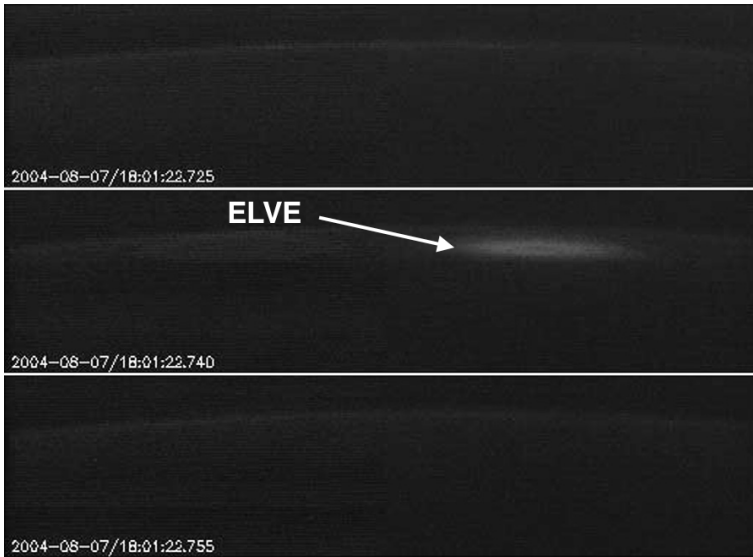


Figure 1.9: An elve observed by ISUAL (*Chern et al.*, 2014).

allows to obtain information about the shorter emitted wavelengths that are highly absorbed by the lower atmosphere.

1.2.2 Halos and sprites

Approximately 6% of TLEs observed by ISUAL were halos and 6.5% were sprites (*Chern et al.*, 2014), both of them red coloured TLEs. Halos are red disc-shaped emissions at altitudes between 75 km and 80 km. However, differently from elves, halos are a consequence of the quasi-electrostatic field produced by the lightning-charged accumulated on clouds. On the other hand, sprites are seen as a large and complex structure of thousands of streamers that can extend from 40 km up to 85 km of altitude.

When the electric field reaches the breakdown value in the lower ionosphere, ionization is triggered. Free electrons collide with atoms and molecules producing electronical and ro-vibrational excitation of some species, especially N_2 molecules. Then, an important amount of these excited species emit optical radiation after suffering radiative decay, while the rest are de-excited by other mechanisms, such as collisional quenching.

When the ionization front spreads diffusively causing a glow-discharge, the resultant TLE is a halo. However, if ionization is focused on streamer tips, a sprite traveling downward is produced.

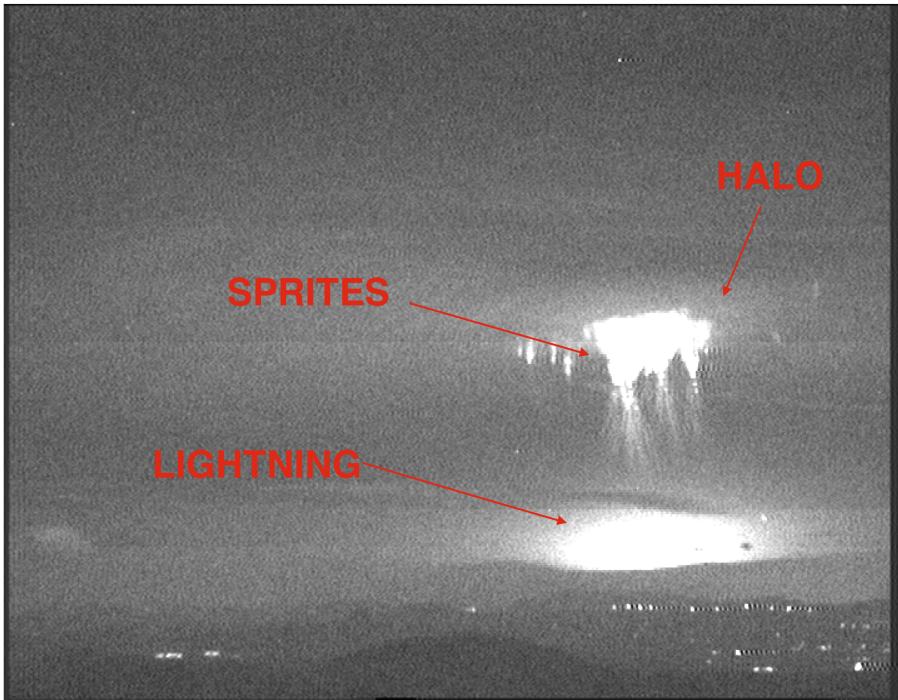


Figure 1.10: Sprites and halos captured by María Passas operating GRASSP from Almería (Spain) in 2013 (*Passas et al.*, 2014).

Halos and sprites are usually associated with cloud-to-ground (CG) lightning discharges.

1.2.3 Blue jets

Blue Jets are a type of TLE that emerge from cloud tops in the form of a leader surrounded by streamers. They represent $\sim 13\%$ of TLEs observed by ISUAL (*Chern et al.*, 2014) and can reach altitudes of 40 km. Blue Jets could produce an important amount of N_2O and NO molecules in the stratosphere (*Winkler and Notholt*, 2015).



Figure 1.11: First image of a Blue Jet before their official discovery. Taken by Tudor Williams in Queensland (Australia) in 1968.

Blue Jets, officially discovered in 1994 (*Wescott et al.*, 1996), are an upwards discharge consequence of the imbalance of charge produced on cloud tops by a strong lightning discharge. However, the physical mechanism behind these events is still poorly understood. *Krehbiel et al.* (2008) proposed a model based on quasi-electrostatic fields formed as an imbalance of charge on cloud tops to predict Blue Jet inception. After a lightning discharge, a charged layer can remain near the storm top. Krehbiel found that Blue Jets can be triggered by electrical breakdown near this charged layer.

1.2.4 Gigantic Jets

Gigantic Jets are believed to be upward-negative lightning discharges that start their development on clouds. They can extend up to 90 km of altitude, connecting the troposphere with the lower ionosphere. Therefore, Gigantic

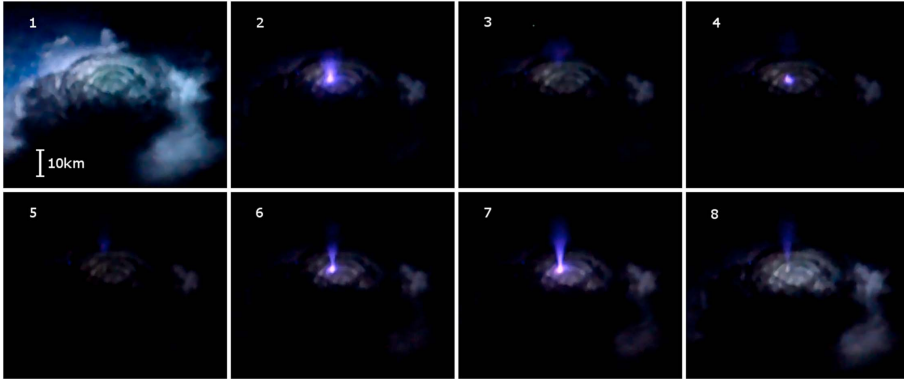


Figure 1.12: A Blue Jet emerging from the top of a thundercloud. This image was taken over the Bay of Bengal from the International Space Station (*Chanrion et al.*, 2017).

Jets could play an important role in the global circuit. According to the ISUAL statistic, only $\sim 0.3\%$ of TLEs are Gigantic Jets (*Chern et al.*, 2014).

Gigantic Jets were discovered in 2001 by a group headed by Dr. Victor P. Pasko (*Pasko et al.*, 2002). They are formed by a complex structure of a leader surrounded by a group of streamers moving upward with velocities of the order of 10^5 m s^{-1} .

1.2.5 Other TLEs

There exist other types of TLEs with lower occurrence frequency. Some of them, such as the Trolls, Gnomes and Palm Trees are upward discharges quite similar to Blue Jets. The Smooth Crawlers are also upward emissions. However, they do not seem to be associated with clouds. Finally, other considered TLEs, called pixies, are often observed from the top of the clouds as 100 m sized dots of light.

1.3 Electrical phenomena in other planets

Lightning and possibly TLEs are not exclusively terrestrial phenomena (*Yair et al.*, 2008; *Yair*, 2012). Since the discovery of lightning in Jupiter in 1979

1. INTRODUCTION

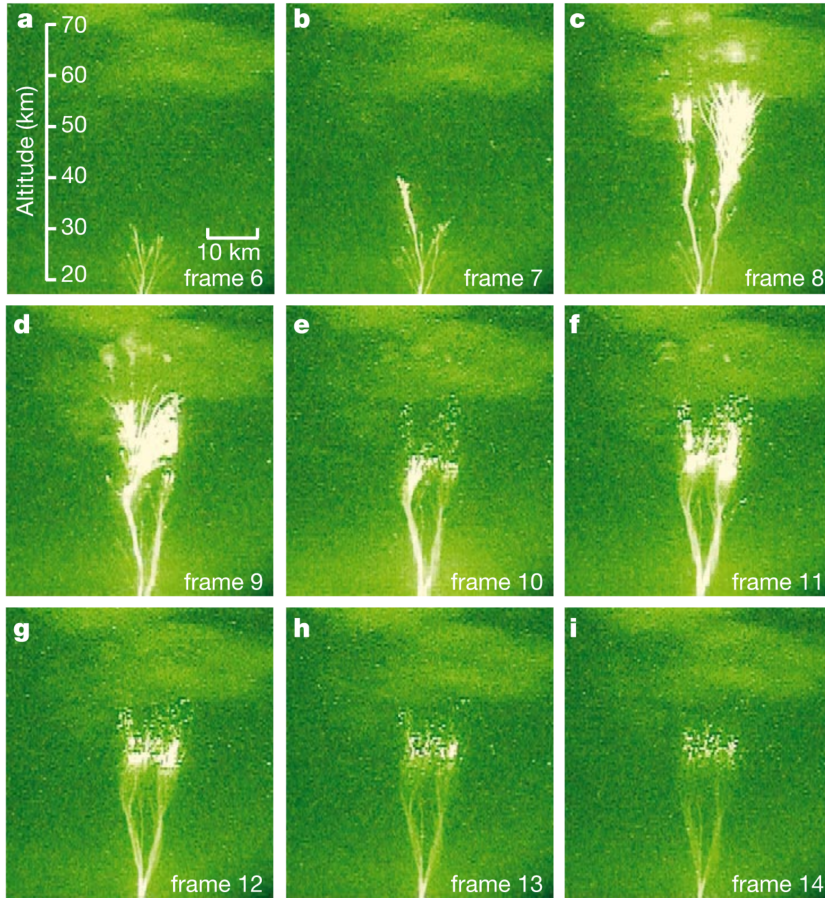


Figure 1.13: First recorded Gigantic Jet extending from the cloud tops to the lower ionosphere (*Pasko et al.*, 2002).

by the Voyager 1 (NASA), other planets have been added to the list of worlds with atmospheric electrical activity. Nowadays, the existence of lightning has already been reported in Jupiter, Saturn, Uranus and Neptune. Furthermore, there are some evidence of electrical activity in the atmospheres of Mars and Venus, although it has not been completely demonstrated. The existence of lightning discharges in exoplanets has also been proposed.

Investigation of electrical activity in other planets is a key point in the science of planetary atmospheres. The lack or existence of lightning in a planet is an indication of some of their atmospheric characteristics, such

as convection, composition, atmospheric plasma or coupling with the space weather. In addition, the information provided by the study of extraterrestrial lightning can provide valuable information about the nature of electrical discharges themselves.

1.3.1 Giant Gaseous Planets

NASA launched the Voyager 1 spacecraft on September 5, 1977. Some of their scientific goals were the study of the giant gaseous planets.

The spacecraft arrived to Jupiter in January 1979 and took images for the first time of extraterrestrial lightning flashes (*Cook et al.*, 1979). Furthermore, also in 1979, this spacecraft measured the first lightning-generated radio waves from that planet (*Gurnett et al.*, 1979). One year later, the Voyager 1 continued its journey across the Solar System visiting another giant gaseous planet, Saturn. During one of its flybys over Saturn in 1980, the Voyager 1 detected high frequency (HF) pulses from electrical discharges taking place in the atmosphere of the planet. These signals are known as Saturn Electrostatic Discharges, or simply SEDs (*Warwick et al.*, 1981). The Voyager 2 spacecraft, launched 16 days after the Voyager 1 by NASA, also recorded electromagnetic signals from electrical discharges in the atmospheres of Jupiter and Saturn. This spacecraft detected whistler waves produced by Saturnian lightning.

Apart from detecting lightning signatures on Jupiter and Saturn, the Voyagers measured lightning electromagnetic signals from Uranus and Neptune (*Zarka and Pedersen*, 1986; *Gurnett et al.*, 1990; *Kaiser et al.*, 1991), confirming the existence of lightning discharges as a common feature of the giant gaseous planets. After the Voyagers, the Galileo spacecraft, launched in 1989 to study the Jovian system, visited Jupiter. This spacecraft provided more information about some of the Jovian lightning characteristics (*Little et al.*, 1999).

The recently deactivated Cassini spacecraft also played an important role in the investigations of giant gaseous planets atmospheric electricity. This

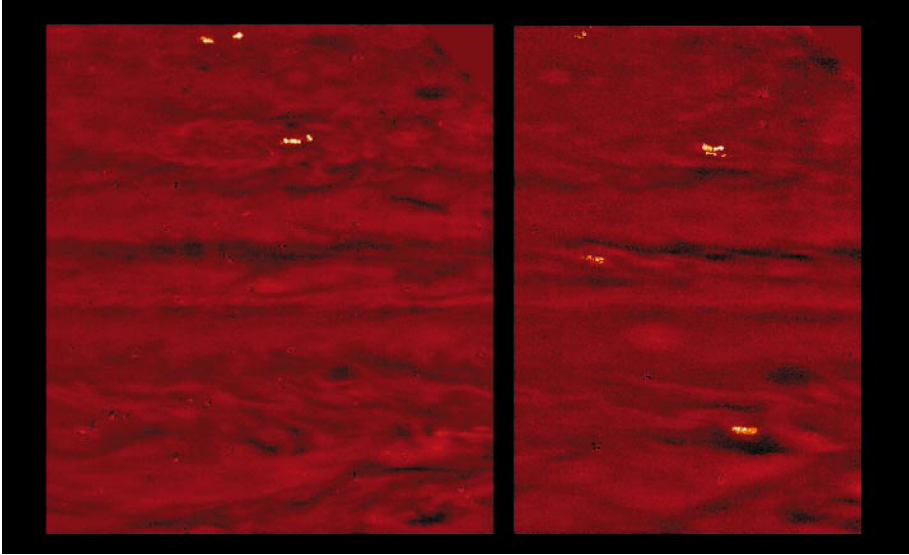


Figure 1.14: Some lightning flashes from a Jovian storm recorded by the Galileo Solid State Imager (SSI) onboard the NASA Galileo orbiter (*Little et al., 1999*).

mission was launched by NASA, ESA and ASI in 1997. Cassini arrived to Jupiter in 2000, detecting once again the existence of electrical activity in the Jovian atmosphere (*Zarka et al., 2004; Dyudina et al., 2004*). Afterwards, Cassini traveled to Saturn, where it could detect electromagnetic signals from lightning discharges and, for the first time, optical lightning flashes (*Fischer et al., 2008; Dyudina et al., 2010, 2013*).

Since the first detections of lightning in the gaseous planets by the Voyagers and Cassini, other spacecraft have sent us valuable data on extraterrestrial lightning from the Jovian orbit, as is the case of the New Horizons (*Baines et al., 2007*) and the Juno spacecraft (*Bolton and The Juno Science Team, 2010*). For instance, New Horizons discovered that Jovian lightning are not only confined in the Great Red Spot storm, but can also take place at polar latitudes (*Baines et al., 2007*). However, no ground-based optical detection of lightning on giant gaseous planets has been achieved to date (*Luque et al., 2015*).

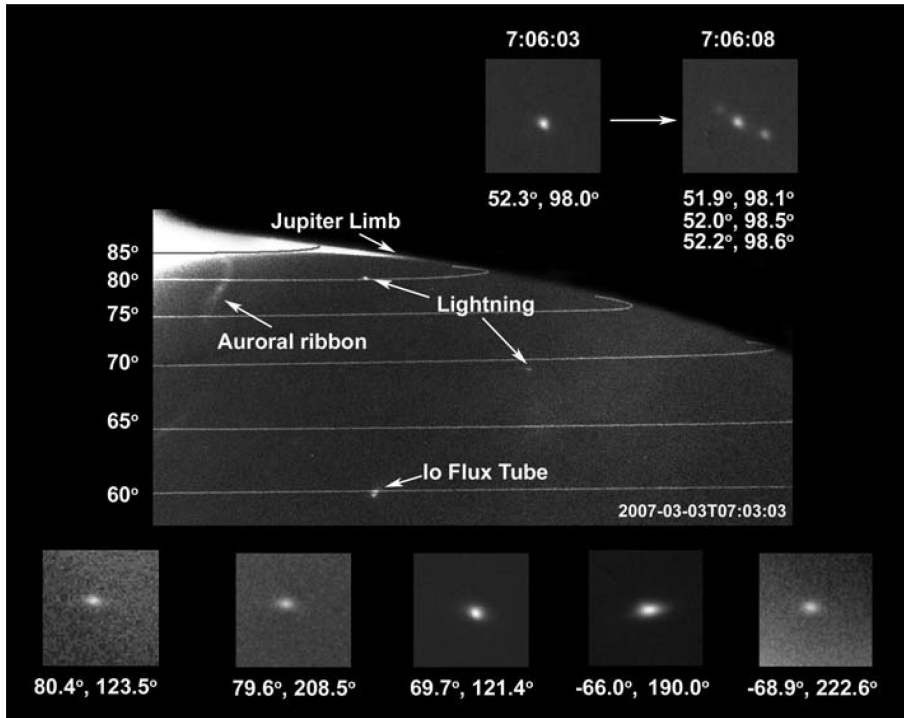


Figure 1.15: Polar lightning discharges recorded by the Long Range Reconnaissance Imager (LORRI) onboard the New Horizons spacecraft (*Baines et al.*, 2007).

The atmospheres of Jupiter and Saturn are mainly formed by hydrogen and helium. Clouds in such planets are a combination of ammonia (NH_3), ice particles, ammonium hydrosulfide (NH_4SH) and water (H_2O) droplets. The energy that feeds atmospheric convection on gaseous giant planets comes from the inner part of the planet instead of from the Sun. All these features lead to several differences between lightning produced in giant gaseous planets and terrestrial lightning. For instance, it is estimated that Jovian and Saturnian lightning strokes could be 4 orders of magnitude more powerful than the terrestrial atmospheric discharges.

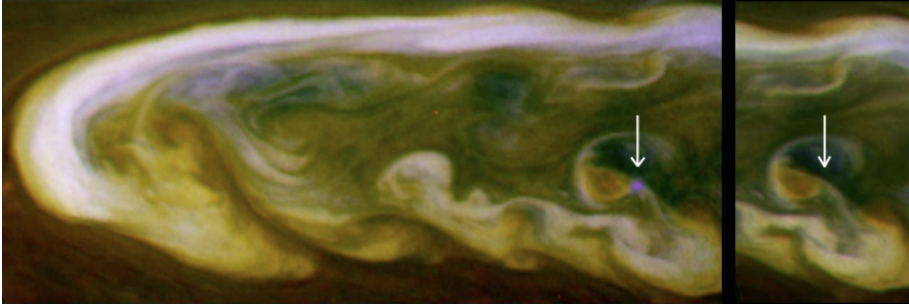


Figure 1.16: A lightning flash from a Saturnian thunderstorm taken by the Cassini spacecraft. Courtesy of NASA.

1.3.2 Venus

The search of lightning in the Venusian atmosphere began in 1956, when an interferometer antenna at the Ohio State University detected radio signals of an impulsive nature from Venus (*Kraus, 1956*). It is today known that those radio signals were produced by the highly heated planetary surface. However, it was initially hypothesized that they were originated from Venusian lightning discharges. Nowadays the existence of lightning on Venus is still a controversial subject due to the lack of optical evidence.

In the 1960s and 1970s the soviet probes of the Venera series carried out optical and electromagnetic observations of the Venusian atmosphere. In 1975, the Venera 9 recorded several optical bursts over a storm in that planet (*Krasnopolsky, 1980*). Three years later both the Venera 11 and 12 descended through the Venusian atmosphere detecting bursts of very low frequency (VLF) pulses that could be produced by lightning (*Ksanfomaliti et al., 1979; Ksanfomaliti, 1980*). The same year the Pioneer Venus Orbiter (PVO) of NASA reported whistler waves in several flybys over the planet. Those signals were very similar to whistler waves emitted by terrestrial lightning (*Scarf et al., 1980; Strangeway et al., 1993; Strangeway, 1995, 2003*).

These optical bursts and electromagnetic signals suggested the existence of Venusian lightning. However, some studies claimed that they could be

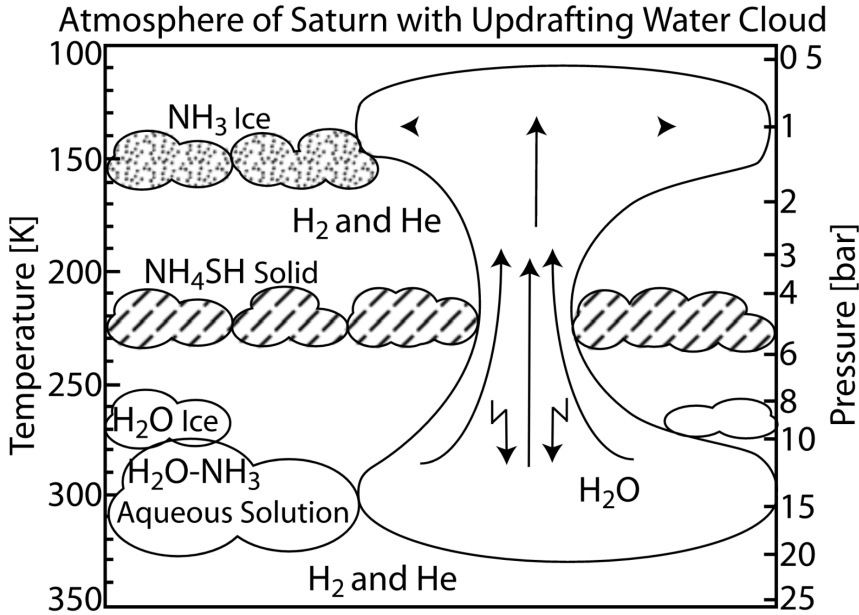


Figure 1.17: Cloud layer structure in Saturn showing where lightning activity can take place. Despite different pressures, the sketch is similar in the Jovian atmosphere (*Fischer et al.*, 2008).

due to plasma instabilities rather than lightning discharges (*Cole and Hogeny*, 1997). For this reason, other missions, such as the soviet Vega balloons, Galileo (NASA) and Cassini, attempted to collect more evidence of lightning on Venus. However, these missions did not report any definitive evidence of electromagnetic or optical signature of lightning discharges in their observations of the Venusian atmosphere (*Gurnett et al.*, 1991, 2001).

In 1995, a ground-based telescope detected seven flashes from the atmosphere of Venus (*Hansell et al.*, 1995). It is unclear if these flashes were due to lightning or to the interaction of cosmic rays with the camera. Other ground-based observations did not succeed in their search of Venusian lightning (*García Muñoz et al.*, 2013). However, *Krasnopolsky* (2006) could detect an important amount of NO in the lower atmosphere of Venus operating the “Texas Echelon Cross Echelle Spectrograph” (TEXES). The source of

1. INTRODUCTION

these NO molecules remains unknown, although it has been hypothesized that they could be a product of lightning activity.

The Venus Express (VEX), an ESA probe, was equipped with a fluxgate magnetometer able to detect electromagnetic signals from the Venusian orbit. This spacecraft, launched in 2005, arrived to Venus one year later. The spacecraft flew over several storms, detecting whistler waves at different frequencies (*Russell et al.*, 2013). However, its optical detector did not record any optical flash (*Cardesín Moineiro et al.*, 2016).

This combination of negative and positive results in the search of lightning on Venus together with the lack of unambiguous optical detections keep unclear the existence of Venusian lightning discharges. One of the purposes of the Japanese Akatsuki spacecraft (JAXA) (*Takahashi et al.*, 2008; *Peralta et al.*, 2016), orbiting Venus since 2015, is to shed light over the open question of the existence of lightning on Venus. One of the instruments onboard Akatsuki is a high temporal resolution instrument, the so-called Lightning and Airglow Camera (LAC), capable of detecting fast emissions in the atomic oxygen 777 nm line of the spectrum, where the hypothetical Venusian lightning are expected to emit light (*Borucki and McKay*, 1987). Despite the high capabilities of this camera to confirm or discard the existence of lightning, some engine problems during the probe orbital injection caused the spacecraft to remain at an orbital distance larger than planned.

The atmosphere of Venus is primarily composed by carbon dioxide (CO₂) and molecular nitrogen (N₂). Venusian clouds are formed by a mixture of sulfuric acid (H₂SO₄), droplets and water vapor. These clouds are located at approximately 50 km above the ground, where the pressure is about 1 bar. This high altitude cloud location together with the high pressures at surface level would favor the occurrence of cloud discharges rather than cloud-to-ground.

The observation of Venusian lightning signature from space or ground-based telescopes is a serious challenge. Clouds are very dense and opaque, possibly difficulting optical flashes to be seen from space. The absence of

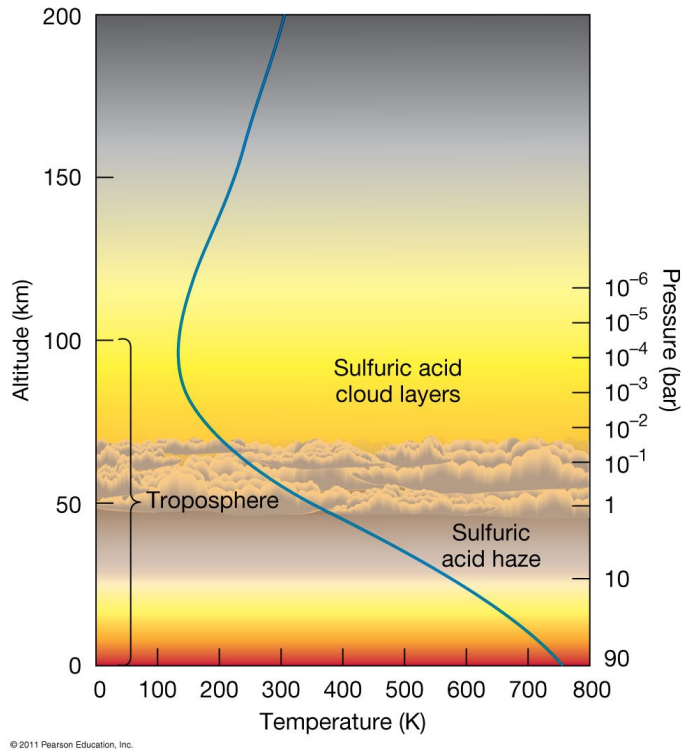


Figure 1.18: Structure of the Venusian atmosphere, courtesy of Pearson Education, Inc. The pressure at ground level is ninety times greater than the terrestrial surface pressure.

a geomagnetic field produced by the inner core of Venus causes a strong dependence of the ionospheric plasma behavior with the solar winds, which can influence the propagation of possible lightning-generated electromagnetic pulses out of the planet.

1.3.3 Other planets

Apart from the evidences of lightning in the previously discussed planets, the existence of atmospheric electrical discharges in other planets has been proposed. The dust storms taking place in our nearest neighbor, Mars, are good candidates to produce electrical discharges. As in the case of the Earth, saltation processes (wind-driven transport of dust material from the

surface to the air) contribute to the accumulation of dust in the Martian atmosphere (*Barth et al.*, 2016). Dust particles in the Martian atmosphere become electrically charged when they contact each other exchanging charge (triboelectric effect), as in the case of the terrestrial “dust devils”. On Earth, measurements indicate that these atmospheric structures can produce electric fields of the order of several tens of kilovolts (*Jackson and Farrell*, 2006). The probed existence of dust devils in Mars points to the possibility of the occurrence discharges between the charged regions inside these dust devil structures (*Barth et al.*, 2016).

Lightning discharges could also exist beyond the Solar System. As proposed by *Helling et al.* (2013) and *Vorgul and Helling* (2016), the existence of clouds formed by mineral dust, ice and liquid particles in extra solar planets or brown dwarfs could be electrified triggering lightning discharges.

1.4 Motivation

The physics and chemistry behind all the previously described atmospheric electrical phenomena is still not fully understood. Among others, there are still some open questions about the local and global chemical impact and the optical emissions of TLEs. We have developed two electrodynamic models that simulate the inception and evolution of halos and elves. We have revised the literature to couple this electrodynamic models with an extensive set of chemical reactions capable of predicting the local impact and optical signature of these two types of TLEs. Thanks to these models, we have obtained for the first time the spectra of elves triggered by CIDs and EIPs. In addition, we have quantified the production of some important species, such as NO and N₂O, by halos.

The upcoming launch of two new missions devoted to the study of TLEs and TGFs, such as ASIM (ESA) and TARANIS (CNES), has motivated us to develop some methods to analyze the optical signature of elves. The fast and spatially large development of elves implies the necessity of developing

new algorithms for the analysis of recorded optical data in order to determine the characteristics of the emitting source. Comparison between the light observed from a TLE at different wavelengths can provide information about some of the physical quantities involved in the event, such as the reduced electric field.

The characteristics of detected radio waves emitted by lightning discharges and other electrical phenomena can be used as a tool to investigate atmospheric electricity. For instance, radio emissions from thunderstorms where TGFs have been reported could contain information about their inception. However, the characteristics of the emitted electromagnetic radiation are modified across its journey through the Earth-ionospheric waveguide. We have used the Full-Wave-Method (FWM) developed by *Lehtinen and Inan* (2008) to describe the change of VLF wave properties from the source to a ground-based observer located up to 4000 km away from the wave source.

The chemical impact of lightning in the atmosphere is not negligible, as it is estimated to produce 10% of the total NO_x deposited in the atmosphere yearly. Due to this important contribution to the atmospheric chemistry, different lightning parameterizations are often included in global and regional atmospheric models. Recent investigations estimate an increase in the global lightning occurrence, which would lead to an enhancement in the tropospheric NO_x . In connection to this, we have tested different lightning parameterizations in the Whole Atmosphere Community Climate Model (WACCM) developed at the National Center for Atmospheric Research (NCAR). The use of this model has allowed us to investigate the similarities and differences in the lightning occurrence and NO_x production predicted by each parameterization. Furthermore, we have quantified for the first time the global impact of Blue Jets on the global atmospheric chemistry.

The controversy involved around the existence of Venesian lightning discharges and the presence of the Akatsuki probe in Venus have motivated

us to investigate their possible detection from space. On the one hand, we have adapted our developed models of terrestrial halos and elves to the atmosphere of Venus. We have proposed a set of chemical reactions that could take place in the lower ionosphere of Venus under the influence of a lightning-produced electromagnetic field. Using these models, we have computed both the amount of photons and the energy emitted by possible Venusian TLEs. On the other hand, we have adapted the FWM developed by *Lehtinen and Inan* (2008) to the case of Venus. We have used this model to investigate the lightning-produced whistler wave propagation through the ionosphere of Venus up to a spacecraft orbiting the planet.

The detection of optical flashes from the atmosphere of Jupiter and Saturn demonstrated the existence of electrical phenomena in the atmosphere of the giant gaseous planets. Some characteristics of the ionosphere of these planets are still unknown, such as their amount of electrons, ions and hydrocarbons. The knowledge of some of the Jovian and Saturnian lightning characteristics could be useful to estimate their atmospheric composition or how they are coupled with the outer space. Despite the observation of optical flashes, it was not observationally determined if the detected photons were produced by lightning discharges or by possible TLEs. We have applied our elve model to the case of Jupiter and Saturn in order to compare the predicted optical emissions with the reported flashes. Thanks to this model, we have also studied the influence of the atmospheric composition and the background magnetic field in the optical emissions due to possible elves.

1.5 Content

We have divided the content of this thesis in different chapters. We have chosen to present the electrodynamical models of halos and elves in a general version in Chapter 2. We present in Chapter 3 the modelling of electrical phenomena in the atmosphere of Earth. Some of these results have been

published in *Pérez-Invernón et al. (2016a)* and *Mezentsev et al. (2018)*. Chapter 4 is devoted to the analysis of optical signals emitted by TLEs. In Chapter 5 we discuss the modelling of Venusian TLEs and lightning-emitted electromagnetic waves from the troposphere of Venus. We have published these results in *Pérez-Invernón et al. (2016b)*, *Pérez-Invernón et al. (2017b)* and *Pérez-Invernón et al. (2017a)*. Chapter 6 describes the results of the modelling of elves in the atmospheres of Jupiter and Saturn, also published in *Pérez-Invernón et al. (2017a)*. Finally, Chapters 7 and 8 are devoted to the summary and conclusions of our work.

1. INTRODUCTION

Chapter 2

Electrodynamical models

2.1 Introduction

This chapter details the developed general electrodynamic models for halos and elves. In the following chapters, these models will be particularized for different planetary atmospheres, as well as for different types of lightning discharges. Furthermore, they will be coupled with different sets of kinetic reactions (Appendix A) in order to describe the evolution of halos and elves in different planets.

As introduced in subsection 1.2.5, halos are red disc-shaped emissions at altitudes between 75 km and 85 km consequence of the quasi-electrostatic field created by a lightning discharge. The purpose of the developed halo model is to calculate the quasi-electrostatic field in the atmosphere and its interaction with different species, mainly electrons and ions. The use of a two-dimensional scheme allows us to compute the local chemical influence of the halo in an extensive region, describing the event in a self-consistent way. Section 2.2 of this chapter describes the two-dimensional model of halos in cylindrical coordinates, based on the same assumptions considered in previous models by, for instance, *Luque and Ebert (2009)*; *Neubert et al. (2011)*; *Qin et al. (2014)*; *Liu et al. (2015)*. We have implemented the model in several subroutines using the Fortran and Python programming

2. ELECTRODYNAMICAL MODELS

languages.

Elves are fast ring-shaped emissions located at altitudes around 88 km (*van der Velde and Montanyà, 2016a*), with a lateral extension of more than 200 km. They are a consequence of the interaction between the lightning-radiated ElectroMagnetic Pulses (EMP) and the charged region of the upper atmosphere. The calculation of the quasi-electrostatic field produced by lightning is not enough to describe the EMPs. On the contrary, our elve model calculates the propagation of the lightning emitted waves by computing all the electromagnetic field components. We have developed and described two different elve models in subsections 2.3.1 and 2.3.2. Both of them are based on a Finite-Difference Time Domain (FDTD) scheme. This scheme has been previously used by other authors to simulate elves (*Inan et al., 1991; Taranenko et al., 1993; Kuo et al., 2007; Marshall et al., 2010; Inan and Marshall, 2011; Luque et al., 2014; Marshall et al., 2015; Liu et al., 2017*). Our first elve model is two-dimensional using cylindrical coordinates, while the second one is a three-dimensional model in Cartesian coordinates. We have implemented both models in Fortran and Python. The main differences between the two developed models are the different computational costs of their implementation and the capability of including non-symmetrical phenomena. The numerical implementation of the two-dimensional model produces a less-computationally costly code, while the three-dimensional model is capable of including different lightning channel inclinations, as well as the natural background magnetic field of each planet at different latitudes.

The simulations of halos and elves are carried out in a CSIC computer cluster in Madrid called “Trueno”. The computer cluster located at IAA-CSIC in Granada has also been used in order to test the codes.

2.2 Model of halos

This section details the general electrodynamical model of halos. This numerical scheme can be applied to different atmospheres as well as to vertical CG and cloud lightning discharges.

The electrodynamical model of halos computes the quasi-electrostatic field produced by lightning in planetary atmosphere using a cylindrically symmetrical scheme. The time evolution of the electric field is coupled with the transport of charged particles near the ionosphere, such as electrons and ions. Finally, the whole electrodynamical model is coupled with a set of chemical reactions particularized for each planetary atmosphere (Appendices A.1 and A.2).

This model takes as inputs the lightning discharge characteristics, i.e., the type of discharge (CG or cloud discharge), the temporal dependence of the charge $Q(t)$ accumulated by the electric current, the lightning channel length h , the altitude of the discharge center z_p located in the axis of symmetry of the cylindrical coordinates, the radius of the sphere that contains the charge r_{sp} and the spatial domain limits and spatial steps. In the case of CG lightning discharges, the accumulated charge is deposited in a cloud region, causing the appearance of a mirror charge with opposite sign below the ground, which acts as a perfect electrical conductor (PEC). On the contrary, cloud discharges accumulate the same amount of charge but with opposite sign in two separated regions of the cloud, forming a dipole.

The quasi-electrostatic field created by the charge $Q(t)$ resulting from the lightning electric current at a given time is calculated using FISHPACK (*Sweet, 1977*), a 2-D Poisson solver in cylindrical coordinates that solves the equation

$$\nabla^2 \phi = -\frac{\rho}{\epsilon_0}, \quad (2.1)$$

where ϕ is the electric potential, ϵ_0 is the permittivity of vacuum and ρ is the charge density located in the integration domain. This quantity

2. ELECTRODYNAMICAL MODELS

includes both the lightning-accumulated charge in the troposphere and the induced charge in the mesosphere.

The resultant electric field induces electron and ion transport in the mesosphere and lower ionosphere, separating charge of opposite sign. The transport of the charged species i is determined by the advection-diffusion flux \mathbf{J}_i , whose components in the vertical and radial directions (z and r) are given, in the case of electrons, by

$$J_{e,z} = -D_e \frac{\partial N_e}{\partial z} - \mu_e E_z N_e \quad (2.2a)$$

$$J_{e,r} = -D_e \frac{\partial N_e}{\partial r} - \mu_e E_r N_e, \quad (2.2b)$$

while in the case of ions we can neglect diffusion and write these equations as

$$J_{i,z} = -v_{i,z} N_i, \quad (2.3a)$$

$$J_{i,r} = -v_{i,r} N_i, \quad (2.3b)$$

where D_e , μ_e and N_e are, respectively, the electron diffusion coefficient, mobility and density, while v_i and N_i are the ion velocities and densities. The electron diffusion coefficient and mobility depend on the gas composition and the electric field, and, therefore, are unique of each planetary atmosphere. In the case of ions with mass m_i , their velocity in the presence of a high reduced electric field is given by (*Fahr and Müller, 1967; Pancheshnyi, 2013*)

$$v_i = \sqrt{\frac{2\theta_z}{\pi m_i}}, \quad (2.4)$$

where θ_z is the kinetic energy of the ion in the presence of an electric field E , given by *Fahr and Müller (1967); Pancheshnyi (2013)* as

$$\theta_z = q_e E \lambda_i, \quad (2.5)$$

where q_e is the negative elementary electric charge and λ_i is the mean free path of particles in the gas between successive collisions, calculated as a function of the air density N (*Chapman and Cowling, 1970*)

$$\lambda = \left(\sqrt{2}\pi d^2 N \right)^{-1}, \quad (2.6)$$

where d is the average diameter of molecules in air.

In the case of fluxes of charged particles fluxes produced by glow discharges as halos, where the quasi-electrostatic field remains high for several milliseconds, numerical oscillations can appear as a consequence of large density gradients. For this reason, equations (2.2) and (2.3) are solved using a Koren limiter function (*Montijn et al., 2006*) to obtain the charged species fluxes. Then, we can write the continuity equation of the species i including kinetics and transport as

$$\frac{\partial N_i}{\partial t} + \nabla \cdot \mathbf{J}_i = P_i - L_i, \quad (2.7)$$

where P_i and L_i are the production and loss rates of the species i , determined by the kinetic scheme. We solve this equation using an explicit Runge-Kutta method of order 5 with step size control based on the Dormand and Prince algorithm (*Dormand and Prince, 1980*). We solve this equation exclusively where the plasma density is important.

Equations (2.1)-(2.7) are discretized in a cylindrical grid with a spatial resolution given by Δz and Δr , that are inputs of the model. We use an adaptive time step Δt . For the Poisson equation (2.1), we use boundary conditions of the Neumann type at the domain limit, undetermined in the axis of symmetry and of the Dirichlet type in the upper (ionosphere) and lower (ground) boundaries assuming that both of them behave as PECs. In the case of the transport equations (2.2) and (2.3) we use Neumann type boundary conditions.

2. ELECTRODYNAMICAL MODELS

After analyzing the model, we noted that the resolution of the Poisson equation to obtain the quasi-electrostatic field is one of the most computational costly stages of the complete process. For this reason, we have developed an automatic procedure to accelerate the computation. This procedure determines the number of steps in which the quasi-electrostatic field can be assumed to stay constant. The evolution of the lightning-produced electric field is influenced by the total transferred charge during roughly the first millisecond. After that time, the impulsive stage of the lightning discharge ends and the rhythm of charge accumulation on the clouds decreases. Therefore, the field-induced electron currents determine the main change of the quasi-electrostatic field in the lower ionosphere, with time scales approximately given by the Maxwell relaxation time (ϵ/σ) at each altitude level. Then, the time derivative of the quasi-electrostatic field will decrease progressively as the field is screened at highest altitude. We take advantage of this fact and implement a method to progressively decrease the computational cost of our simulation. We include a parameter p in the code that calculates the maximum time derivative of the reduced electric field at a given time t' by computing the difference between the field at that time and at the previous step ($t'-\Delta t$):

$$p(t') = \max \left(\frac{\frac{\partial E(r,z,t')}{N(r,z)}}{\partial t'} \right) = \max \left(\frac{\frac{E(r,z,t') - E(r,z,t' - \Delta t)}{N(r,z)}}{\Delta t} \right). \quad (2.8)$$

This parameter gives us the maximum absolute variation of the reduced electric field per second. Using p we can then estimate the total number of time steps n that are necessary to see a maximum absolute change of 0.1 Td as

$$n\Delta t = \frac{0.1}{p}. \quad (2.9)$$

If n is greater than one, we deactivate the Poisson equation solver for that number of following time steps, keeping the electric field and its effects

constant. This allows us to exclusively solve the equations related to the chemistry and the charged particles transport assuming a maximum relative error in the electric field of less than 0.1 Td.

We have implemented the complete halo model in several Fortran and Python subroutines. As mentioned before, we have used the numerical packet FISHPACK (*Sweet, 1977*) for the resolution of the 2-D Poisson equation. In addition, we have considered the Dormand and Prince algorithm-based (*Dormand and Prince, 1980*) Python integrator “dopri5” for the computation of the time derivatives. The code is parallelized with a shared-memory approach based on Open MP using 12 CPUs.

2.3 Models of elves

This section details a general two-dimensional electrodynamical elve model and its extension to three dimensions. Both models are based on a Finite-Difference Time Domain (FDTD) scheme (*Inan et al., 1991; Taranenko et al., 1993; Lee and Kalluri, 1999; Kuo et al., 2007; Marshall et al., 2010; Inan and Marshall, 2011; Luque et al., 2014; Marshall et al., 2015; Liu et al., 2017*) and can be coupled with any set of chemical reactions (as those listed in Appendix A).

In these FDTD schemes both the time and the spatial derivatives are discretized. In the case of the time derivatives, it is done using a “leapfrog” updating procedure, shown in figure 2.1. Following this staggered in time scheme, the components of the magnetic fields are calculated at half time steps, while the components of the electric field are defined at integer time steps. The discretization of spatial derivatives depends on the coordinate system and will be described in the following subsections 2.3.1 and 2.3.2. In both cases, spatial derivatives are evaluated using a simple two-point centered difference method (*Lee and Kalluri, 1999; Inan and Marshall, 2011*).

2. ELECTRODYNAMICAL MODELS

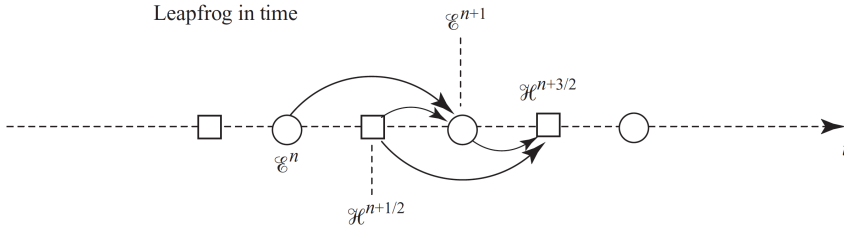


Figure 2.1: Discretization of the time derivatives. This scheme illustrates the “leapfrog” updating of the electric and magnetic fields (*Inan and Marshall, 2011*).

2.3.1 Two-dimensional model

This section details the general two-dimensional electrodynamic model for elves. We use a FDTD scheme to solve the Maxwell equations in a cylindrical 2-D grid, obtaining the lightning-produced electromagnetic wave propagation (vectors \mathbf{E} and \mathbf{H}). The vertically oriented radiation source current can be either a CG lightning discharge, a CID or an EIP. We use a modified Ohm’s equation to calculate the current density induced by the electric fields on the upper atmosphere (*Lee and Kalluri, 1999; Luque et al., 2014*). This electrodynamic scheme can be coupled with a set of kinetic reactions (as those listed in Appendix A), updating the species concentrations N_i at each time step. The complete set of equations is given by

$$\nabla \times \mathbf{E} = -\mu_0 \frac{\partial \mathbf{H}}{\partial t}, \quad (2.10)$$

$$\nabla \times \mathbf{H} = \epsilon_0 \frac{\partial \mathbf{E}}{\partial t} + \mathbf{J}, \quad (2.11)$$

$$\frac{d\mathbf{J}}{dt} + \nu \mathbf{J} = \epsilon_0 \omega_p^2(\mathbf{r}, t) \mathbf{E} + \omega_b(\mathbf{r}, t) \times \mathbf{J}, \quad (2.12)$$

$$\frac{\partial N_i}{\partial t} = G_i - L_i. \quad (2.13)$$

We solve Maxwell equations (2.10) and (2.11), where ϵ_0 and μ_0 are the permittivity and permeability of free space, using a two-dimensional FDTD model in a cylindrical grid using the Yee algorithm (Yee, 1966) with a space step Δd shorter than the minimum characteristic wavelength of the source electric current in each case and with a time step shorter than $\Delta d/\sqrt{3}c$ (Inan and Marshall, 2011). Figure 2.2 shows one of characteristic cells that compose the two-dimensional cylindrical mesh according to the Yee algorithm. The election of a cylindrically symmetrical mesh implies that the derivatives with respect to azimuthal angle are zero (i.e., $\partial/\partial\phi = 0$). We can write the Maxwell equations (2.10) and (2.11) in a 2-D cylindrically symmetrical mesh distinguishing between the Transverse Magnetic (TM) and the Transverse Electric (TE) modes as (Inan and Marshall, 2011)

$$\frac{\partial H_r}{\partial t} = \frac{1}{\mu_0} \left[\frac{\partial E_\phi}{\partial z} \right] \quad (2.14)$$

$$\frac{\partial E_\phi}{\partial t} = \frac{1}{\epsilon_0} \left[\frac{\partial H_r}{\partial z} - \frac{\partial H_z}{\partial r} - J_\phi \right] \quad (2.15)$$

$$\frac{\partial H_z}{\partial t} = -\frac{1}{\mu_0 r} \left[\frac{\partial}{\partial r} (r E_\phi) \right], \quad (2.16)$$

and

$$\frac{\partial E_r}{\partial t} = -\frac{1}{\epsilon_0} \left[\frac{\partial H_\phi}{\partial z} - J_r \right] \quad (2.17)$$

$$\frac{\partial H_\phi}{\partial t} = \frac{1}{\mu_0} \left[\frac{\partial E_z}{\partial r} - \frac{\partial E_r}{\partial z} \right] \quad (2.18)$$

$$\frac{\partial E_z}{\partial t} = \frac{1}{\epsilon_0 r} \left[\frac{\partial}{\partial r} (r H_\phi) \right] - \frac{1}{\epsilon_0} J_z, \quad (2.19)$$

respectively. As explained by Inan and Marshall (2011), TE and TM modes are completely uncoupled from one another. They are identified on the basis of whether the wave has a nonzero electric or magnetic field

2. ELECTRODYNAMICAL MODELS

component in the third dimension. These modes do not correspond to the classic guided electromagnetic waves.

The term \mathbf{J} contains current densities, i.e., lightning channel current density and electron current density induced by electric fields in the lower ionosphere. In this cylindrically symmetrical approach with $\partial/\partial\phi = 0$, the lightning channel current density is a purely vertically oriented vector located in the axis of symmetry, i.e., at $r = 0$ coordinates.

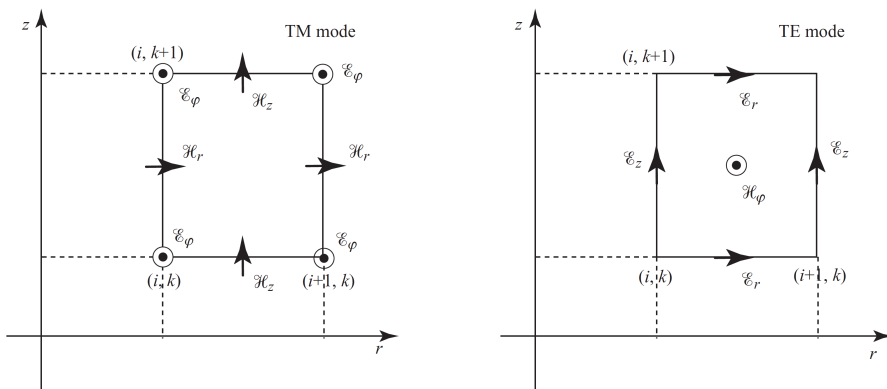


Figure 2.2: Yee cell in the two-dimensional cylindrical coordinate system showing the discretization of the spatial derivatives. The space is discretized in a grid formed by a given number of cells. Derivatives with respect to the angular coordinate are set to zero as a consequence of the cylindrical symmetry. This sketch is taken from *Inan and Marshall* (2011). In this spatial discretization, we locate the components of the current density vector \mathbf{J} in entire subindex points (i, k) (*Lee and Kalluri*, 1999).

The use of a FDTD scheme entails a finite calculation domain. The existence of spatial limits makes necessary the use of boundary conditions. The ground can be approximated as a perfect electrical conductor (PEC), where the vertical component of the electric field E_z is set to zero. However, the use of this boundary condition in the upper and lateral limits would cause an unrealistic wave reflexion when the pulse reached the spatial limits. For that reason, we use Convolutional Perfectly Matched Layers (CPML) followed by a PEC near the upper and lateral domain limits (*Inan and*

Marshall, 2011). This approach is based on the definition of a number of non-physical absorbing layers covering a region between the physics domain and a PEC boundary. In these regions, both the non-physical electrical and magnetical conductivities are set to absorb the propagating wave, preventing undesired reflexion.

The modified Ohm's equation (2.12) is only solved at altitudes where the electron density becomes important. At these regions, usually near the ionosphere, the electron conductivity is orders of magnitude higher than the ion conductivity, hence we can neglect the ion current density contribution. We use the same notation that *Lee and Kalluri* (1999); *Luque et al.* (2014), where $\nu = e/\mu m_e$ is the effective collision frequency between electrons and neutrals, dependent on electron charge magnitude e and mass m_e , and on electron mobility μ . The term $\omega_p = (e^2 n_e / m_e \epsilon_0)^{1/2}$ corresponds to the plasma frequency for electrons and depends on the electron density n_e . Finally, $\omega_b = e \mathbf{B}_0 / m_e$ is the electron gyro frequency, where \mathbf{B}_0 is the background magnetic field, considered zero in this two-dimensional approximation. We can express equation (2.12) in a 2-D cylindrically symmetrical system as

$$\begin{bmatrix} \frac{dJ_r}{dt} \\ \frac{dJ_\phi}{dt} \\ \frac{dJ_z}{dt} \end{bmatrix} = \mathbf{\Omega} \begin{bmatrix} J_r \\ J_\phi \\ J_z \end{bmatrix} + \epsilon_0 \omega_p^2 \begin{bmatrix} E_r \\ E_\phi \\ E_z \end{bmatrix} \quad (2.20)$$

where we have defined $\mathbf{\Omega}$ following *Lee and Kalluri* (1999) as

$$\mathbf{\Omega} = \begin{bmatrix} -\nu & -\omega_{bz} & \omega_{b\phi} \\ \omega_{bz} & -\nu & \omega_{br} \\ \omega_{b\phi} & \omega_{br} & -\nu \end{bmatrix}. \quad (2.21)$$

The natural position of the electrical current density in the Yee cell is the same as the position of the electric field components. However, maintaining the same accuracy in the finite differences approximation of equation (2.12) than in Maxwell equations would require a higher order central differences scheme (*Lee and Kalluri*, 1999). To overcome these difficulties, we follow *Lee and Kalluri* (1999) by placing \mathbf{J} in the center of the cells. *Lee and*

2. ELECTRODYNAMICAL MODELS

Kalluri (1999) performed both a Laplace transform and an inverse Laplace transform to equation (2.20) to finally obtain

$$\mathbf{J}(t) = \mathbf{A}(t)\mathbf{J}_0(t) + \epsilon_0\omega_p^2\mathbf{K}(t)\mathbf{E} \quad (2.22)$$

where

$$\mathbf{A}(t) = \exp[\mathbf{\Omega}t] \quad (2.23)$$

and

$$\mathbf{K}(t) = \mathbf{\Omega}^{-1}(\exp[\mathbf{\Omega}t] - \mathbf{I}), \quad (2.24)$$

and where \mathbf{I} correspond to the identity matrix.

Equation (2.13) describes the evolution of each component's density as a function of its gains G_i and losses L_i , determined by each different chemical scheme. This equation will be particularized for each chemical species and will be coupled with equations (2.10), (2.11) and (2.12) as a consequence of the electric field dependence of some reaction rates. We solve this equation using a forward Euler method choosing a time step smaller than the Maxwell relaxation time, the fastest chemical reaction characteristic time and $\Delta d/\sqrt{3}c$.

Let us now describe the discretization of equations (2.14)-(2.19) and (2.12) in the two-dimensional grid with cylindrical symmetry. As previously mentioned, the time derivatives are discretized according to the leapfrog scheme (figure 2.1), while the spatial derivatives are discretized following the Yee algorithm (figure 2.2). The discretized equations (2.14)-(2.16) corresponding to the TM mode are given by (*Lee and Kalluri, 1999; Inan and Marshall, 2011*)

$$H_r|_{i,k+1/2}^{n+1} = H_r|_{i,k+1/2}^{n+1} - \frac{\Delta t}{\mu_{i,k+1/2}} \left[\frac{E_\phi|_{i,k+1}^n - E_\phi|_{i,k}^n}{\Delta z} \right] \quad (2.25)$$

$$E_\phi|_{i,k}^{n+1} = E_\phi|_{i,k}^{n+1} + \frac{\Delta t}{\epsilon_{i,k}} \left[\frac{H_r|_{i,k+1/2}^{n+1/2} - H_r|_{i,k-1/2}^{n+1/2}}{\Delta z} - \frac{H_z|_{i+1/2,k}^{n+1/2} - H_z|_{i-1/2,k}^{n+1/2}}{\Delta r} \right] \quad (2.26)$$

$$H_z|_{i+1/2,k}^{n+1} = H_z|_{i+1/2,k}^{n+1} - \frac{\Delta t}{\mu_{i+1,k}} \left[\frac{r_{i+1}E_\phi|_{i+1,k}^n - r_iE_\phi|_{i,k}^n}{r_{i+1/2}\Delta r} \right], \quad (2.27)$$

while equations (2.17)-(2.19) for the TE mode are discretized as (*Lee and Kalluri, 1999; Inan and Marshall, 2011*)

$$E_r|_{i+1/2,k}^{n+1} = E_r|_{i+1/2,k}^n - \frac{\Delta t}{\epsilon_{i+1/2,k}} \left[\frac{H_\phi|_{i+1/2,k+1/2}^{n+1/2} - H_\phi|_{i+1/2,k-1/2}^{n+1/2}}{\Delta z} \right] - \frac{\Delta t}{2\epsilon_{i+1/2,k}} \left[J_r|_{(i+1,k)}^{n+(1/2)} + J_r|_{(i,k)}^{n+(1/2)} \right] \quad (2.28)$$

$$H_\phi|_{i+1/2,k+1/2}^{n+1} = H_\phi|_{i+1/2,k+1/2}^{n+1} + \frac{\Delta t}{\mu_{i+1/2,k+1/2}} \left[\frac{E_z|_{i+1,k+1/2}^n - E_z|_{i,k+1/2}^n}{\Delta r} - \frac{E_r|_{i+1/2,k+2}^n - E_r|_{i+1/2,k}^n}{r_i\Delta r} \right] \quad (2.29)$$

$$E_z|_{i,k+1/2}^{n+1} = E_z|_{i,k+1/2}^{n+1} + \frac{\Delta t}{\epsilon_{i,k+1/2}} \left[\frac{r_{i+1/2}H_\phi|_{i+1/2,k+1/2}^{n+1/2} - r_{i-1/2}H_\phi|_{i-1/2,k+1/2}^{n+1/2}}{r_i\Delta z} \right] - \frac{\Delta t}{2\epsilon_{i+1/2,k}} \left[J_z|_{(i,k+1)}^{n+(1/2)} + J_z|_{(i,k)}^{n+(1/2)} \right]. \quad (2.30)$$

On the axis of cylindrical symmetry ($r = 0$), the azimuthally symmetric E_z component can be written as (*Inan and Marshall, 2011*)

$$E_z|_{0,k+1/2}^{n+1} = E_z|_{0,k+1/2}^{n+1} + \frac{4\Delta t}{\epsilon_{0,k+1/2}\Delta r} H_\phi|_{1/2,k+1/2}^{n+1/2}. \quad (2.31)$$

2. ELECTRODYNAMICAL MODELS

Finally, the Ohm's modified equation 2.12 is discretized as (*Lee and Kalluri, 1999*)

$$\begin{bmatrix} J_r|_{i,k}^{n+1/2} \\ J_\phi|_{i,k}^{n+1/2} \\ J_z|_{i,k}^{n+1/2} \end{bmatrix} = \mathbf{A}(\Delta t) \begin{bmatrix} J_r|_{i,k}^{n-1/2} \\ J_\phi|_{i,k}^{n-1/2} \\ J_z|_{i,k}^{n-1/2} \end{bmatrix} + \frac{\epsilon_{i,k}}{2} \omega_p^2|_{i,k}^n \mathbf{K}(\Delta t) \begin{bmatrix} E_r|_{i+1/2,k}^n + E_r|_{i-1/2,k}^n \\ 0 \\ E_z|_{i,k+1/2}^n + E_z|_{i,k-1/2}^n \end{bmatrix} \quad (2.32)$$

As in the case of the halo model, we have developed this method in several Fortran subroutines, compiling them to create Python modules. The code is parallelized with a shared-memory approach based on Open MP. We run each parallelized simulation using 12 CPUs.

2.3.2 Three-dimensional model

In this section we extend the previous two-dimensional model of elves in cylindrical coordinates to a three-dimensional model in Cartesian coordinates. Maxwell equations (2.10) and (2.11) are now solved in Cartesian coordinates discretizing the spatial derivatives in a Cartesian grid. The characteristic cells that are part of this grid are shown in figure 2.3.

This three dimensional model counts with some advantages in relation with the previous two-dimensional approach. In this case, the coordinate system does not imply any symmetry assumptions. Therefore, the lightning channel can be located in any position and with any inclination, allowing us for simulating the case of elves triggered by tilted lightning channels.

The inclusion of a tilted background magnetic field is also possible as a consequence of the absence of symmetrical assumptions. The electron gyro frequency ($\omega_b = e\mathbf{B}_0/m_e$) can now depend on a vectorial magnetic field \mathbf{B} generated by the inner core of each planet, if existent. The inclusion in the model of this background magnetic field influences electromagnetic wave propagation, resulting in non-symmetrical elves emissions.

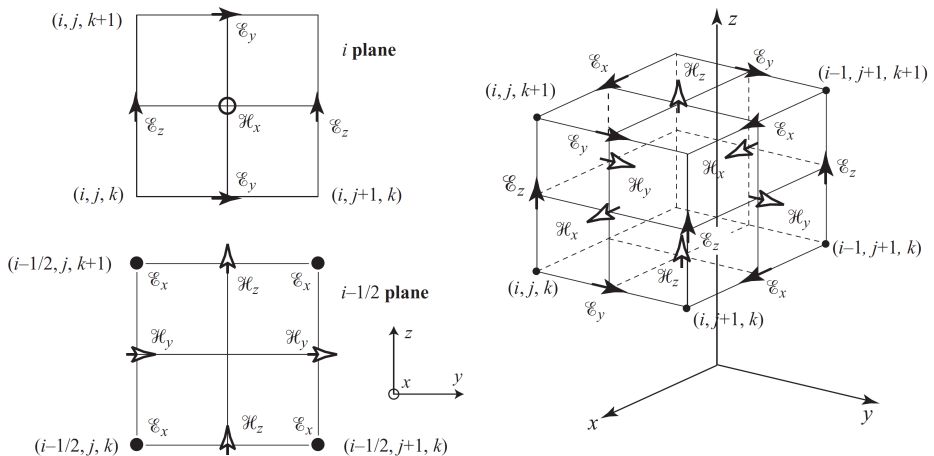


Figure 2.3: Yee cell in the three-dimensional Cartesian coordinate system showing the discretization of the spatial derivatives. The space is discretized in a grid formed by a given number of cells. This sketch is taken from *Inan and Marshall (2011)*. In this spatial discretization, we locate the components of the current density vector \mathbf{J} in entire subindex points (i, j, k) (*Lee and Kalluri, 1999*).

In this case, we write the components of the Maxwell equations (2.10) and (2.11) in a 3-D Cartesian system following *Lee and Kalluri (1999)*; *Inan and Marshall (2011)* as:

$$\frac{\partial H_x}{\partial t} = -\frac{1}{\mu_0} \left[\frac{\partial E_z}{\partial y} - \frac{\partial E_y}{\partial z} \right] \quad (2.33)$$

$$\frac{\partial H_y}{\partial t} = -\frac{1}{\mu_0} \left[\frac{\partial E_x}{\partial z} - \frac{\partial E_z}{\partial x} \right] \quad (2.34)$$

$$\frac{\partial H_z}{\partial t} = -\frac{1}{\mu_0} \left[\frac{\partial E_y}{\partial x} - \frac{\partial E_x}{\partial y} \right] \quad (2.35)$$

$$\frac{\partial E_x}{\partial t} = \frac{1}{\epsilon_0} \left[\frac{\partial H_z}{\partial y} - \frac{\partial H_y}{\partial z} - J_x \right] \quad (2.36)$$

$$\frac{\partial E_y}{\partial t} = \frac{1}{\epsilon_0} \left[\frac{\partial H_x}{\partial z} - \frac{\partial H_z}{\partial x} - J_y \right] \quad (2.37)$$

2. ELECTRODYNAMICAL MODELS

$$\frac{\partial E_z}{\partial t} = \frac{1}{\epsilon_0} \left[\frac{\partial H_y}{\partial x} - \frac{\partial H_x}{\partial y} - J_z \right], \quad (2.38)$$

while the Ohm's modified equation (2.12) in this system is (*Lee and Kalluri, 1999*)

$$\begin{bmatrix} \frac{dJ_x}{dt} \\ \frac{dJ_y}{dt} \\ \frac{dJ_z}{dt} \end{bmatrix} = \mathbf{\Omega} \begin{bmatrix} J_x \\ J_y \\ J_z \end{bmatrix} + \epsilon_0 \omega_p^2 \begin{bmatrix} E_x \\ E_y \\ E_z \end{bmatrix} \quad (2.39)$$

where $\mathbf{\Omega}$ is given by *Lee and Kalluri (1999)* as

$$\mathbf{\Omega} = \begin{bmatrix} -\nu & -\omega_{bz} & \omega_{by} \\ \omega_{bz} & -\nu & \omega_{bx} \\ \omega_{by} & \omega_{bx} & -\nu \end{bmatrix}. \quad (2.40)$$

Following the same scheme than in the previous two-dimensional case, we write the discretized form of Maxwell equations as (*Lee and Kalluri, 1999; Inan and Marshall, 2011*)

$$H_x|_{i,j+1/2,k+1/2}^{n+1} = H_x|_{i,j+1/2,k+1/2}^{n+1} - \frac{\Delta t}{\mu_{i,j+1/2,k+1/2}} \left[\frac{E_z|_{i,j+1,k+1/2}^n - E_z|_{i,j,k+1/2}^n}{\Delta y} - \frac{E_y|_{i,j+1/2,k+1}^n - E_y|_{i,j+1/2,k}^n}{\Delta z} \right] \quad (2.41)$$

$$H_y|_{i+1/2,j,k+1/2}^{n+1} = H_y|_{i+1/2,j,k+1/2}^{n+1} - \frac{\Delta t}{\mu_{i+1/2,j,k+1/2}} \left[\frac{E_x|_{i+1/2,j+1,k}^n - E_x|_{i+1/2,j,k}^n}{\Delta z} - \frac{E_z|_{i+1,j,k+1/2}^n - E_z|_{i,j,k+1/2}^n}{\Delta x} \right] \quad (2.42)$$

$$H_z|_{i+1/2,j+1/2,k}^{n+1} = H_z|_{i+1/2,j+1/2,k}^{n+1} - \frac{\Delta t}{\mu_{i+1/2,j+1/2,k}} \left[\frac{E_y|_{i+1,j+1/2,k}^n - E_y|_{i,j+1/2,k}^n}{\Delta x} - \frac{E_x|_{i+1/2,j+1,k}^n - E_x|_{i+1/2,j,k}^n}{\Delta y} \right] \quad (2.43)$$

$$\begin{aligned}
 E_x|_{i+1/2,j,k}^{n+1} &= E_x|_{i+1/2,j,k}^{n+1} + \frac{\Delta t}{\epsilon_{i+1/2,j,k}} \\
 &\left[\frac{H_z|_{i+1/2,j+1/2,k}^{n+1/2} - H_z|_{i+1/2,j-1/2,k}^{n+1/2}}{\Delta y} - \frac{H_y|_{i+1/2,j,k+1/2}^{n+1/2} - H_y|_{i+1/2,j,k-1/2}^{n+1/2}}{\Delta z} \right] \\
 &\quad - \frac{\Delta t}{2\epsilon_{i+1/2,j,k}} \left[J_x|_{i+1,j,k}^{n+1/2} + J_x|_{i,j,k}^{n+1/2} \right]
 \end{aligned} \tag{2.44}$$

$$\begin{aligned}
 E_y|_{i,j+1/2,k}^{n+1} &= E_y|_{i,j+1/2,k}^{n+1} + \frac{\Delta t}{\epsilon_{i,j+1/2,k}} \\
 &\left[\frac{H_x|_{i,j+1/2,k+1/2}^{n+1/2} - H_x|_{i,j+1/2,k-1/2}^{n+1/2}}{\Delta z} - \frac{H_z|_{i+1/2,j+1/2,k}^{n+1/2} - H_z|_{i-1/2,j+1/2,k}^{n+1/2}}{\Delta x} \right] \\
 &\quad - \frac{\Delta t}{2\epsilon_{i+1/2,j,k}} \left[J_y|_{i,j+1,k}^{n+1/2} + J_y|_{i,j,k}^{n+1/2} \right]
 \end{aligned} \tag{2.45}$$

$$\begin{aligned}
 E_z|_{i,j,k+1/2}^{n+1} &= E_z|_{i,j,k+1/2}^{n+1} + \frac{\Delta t}{\epsilon_{i,j,k+1/2}} \\
 &\left[\frac{H_y|_{i+1/2,j,k+1/2}^{n+1/2} - H_y|_{i-1/2,j,k+1/2}^{n+1/2}}{\Delta x} - \frac{H_x|_{i,j+1/2,k+1/2}^{n+1/2} - H_x|_{i,j-1/2,k+1/2}^{n+1/2}}{\Delta y} \right] \\
 &\quad - \frac{\Delta t}{2\epsilon_{i+1/2,j,k}} \left[J_z|_{i,j+1,k}^{n+1/2} + J_z|_{i,j,k}^{n+1/2} \right],
 \end{aligned} \tag{2.46}$$

and the discretized form of the Ohm's modified equation as (*Lee and Kalluri, 1999*)

$$\begin{aligned}
 &\begin{bmatrix} J_x|_{i,j,k}^{n+1/2} \\ J_y|_{i,j,k}^{n+1/2} \\ J_z|_{i,j,k}^{n+1/2} \end{bmatrix} = \mathbf{A}(\Delta t) \begin{bmatrix} J_x|_{i,j,k}^{n-1/2} \\ J_y|_{i,j,k}^{n-1/2} \\ J_z|_{i,j,k}^{n-1/2} \end{bmatrix} + \\
 &\frac{\epsilon_{i,j,k}}{2} \omega_p^2|_{i,k}^n \mathbf{K}(\Delta t) \begin{bmatrix} E_x|_{i+1/2,j,k}^n + E_x|_{i-1/2,j,k}^n \\ E_y|_{i,j,+1/2k}^n + E_r y|_{i,j-1/2,k}^n \\ E_z|_{i,j,k+1/2}^n + E_r|_{i,j,k-1/2}^n \end{bmatrix}
 \end{aligned} \tag{2.47}$$

2. ELECTRODYNAMICAL MODELS

The rest of the model assumptions remain similar as in the two-dimensional case, i.e., the boundary conditions and the coupling with the chemical scheme.

Chapter 3

Electrical phenomena in the atmosphere of the Earth

3.1 Transient Luminous Events: Halos and elves

3.1.1 Introduction

Transient Luminous Events (TLEs) are fast optical emissions produced by upper atmospheric discharges, as explained in section 1.2. Their optical emissions can provide useful information about the lower ionosphere, while the cascade of chemical reactions that are triggered after their inception can influence the atmospheric chemistry. As seen in section 1.2, there exist several types of TLEs occurring at different altitudes and with different shapes and sizes. This diversity is in part due to the nature of the different components of the electromagnetic field.

In this section we investigate some characteristics of terrestrial halos and elves, two kind of TLEs described in subsections 1.2.1 and 1.2.5. We have developed two self-consistent electro-dynamical models coupled to a set of kinetic reactions to simulate the inception and evolution of halos and elves, predicting their local chemical impact and optical emissions. These electro-dynamical models are detailed in section 2.2 and 2.3, while the detailed chemical scheme is listed in Appendix A.1.

3.1.2 Electric breakdown in the mesosphere

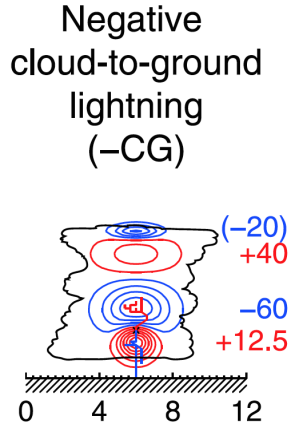


Figure 3.1: Distribution of electrical charges in a cloud during the inception of a -CG lightning discharge. The negative charge -60 C is removed from the cloud. Sketch taken from *Pasko et al.* (2012).

Figure 3.1 shows the charge distribution in a cloud during the development of a -CG lightning discharge. The discharge channel can be seen from the mesosphere as an electric dipole current $I(t)$ flowing between two electrically charged regions. Each of these clouds of charge are enveloped by an electrical charge of opposite sign. In the case of cloud discharges, the regions that define the dipole are the positive and negative charged layers of clouds. On the contrary, the electric current that forms a cloud-to-ground discharge takes place between an electrical charged layer on the clouds (-60 C charged region of figure 3.1) and the ground, which can be approximated as a perfect electric conductor (PEC). In this case, the two regions with opposite net electric charge are the charged cloud at an altitude h and its mirror charge at a distance h below the ground. As the lightning discharge proceeds, the charges that forms the dipole are removed. However, the electric charges that enveloped the main charge remain in the cloud, resulting in an positively charged cloud after the removal of the -60 C charged region of

figure 3.1. The total charge accumulated by lightning after a time t' from the beginning of a lightning discharge can be expressed as

$$Q(t) = \int_0^{t'} I(t) dt. \quad (3.1)$$

Following the example illustrated in figure 3.1, the total charged accumulated in the clouds at the end of the discharge would have a value of +60 C.

The Charge Moment Change (CMC) produced by a lightning discharge is oftenly employed to parameterize the strength of the discharge. The CMC produced by a lightning discharge channel with a longitude h can be then defined as $M(t) = hQ(t)$ in the case of cloud discharges and $M(t) = \frac{hQ(t)}{2}$ in the case of CG discharges.

The electric field produced by a lightning discharge at an altitude z can be written as the field created by a radiating dipole following the analytical expression given by *Jackson* (1962) as

$$E(z, t) = \frac{1}{\pi\epsilon_0} \left(\frac{1}{(z - z_p)^3} M(t) + \frac{1}{c(z - z_p)^2} \frac{d}{dt} M(t) + \frac{\sin(\alpha)}{2c^2(z - z_p)} \frac{d^2}{dt^2} M(t) \right), \quad (3.2)$$

where z_p is the altitude of the dipole that forms the lightning discharge and α is the angle between the direction of the dipole and the direction of wave propagation .

First, second and third terms of equation (3.2) correspond to the quasi-electrostatic, induction and radiation fields produced by the discharge, respectively. Different time and spatial dependence of these fields and their interaction with the mesospheric ionized layer lead to the production of different TLEs. In this section, we focus on the cases of halos and elves.

Halos are disc-shaped emissions with a diameter of more than 100 km taking place at altitudes between 75 and 85 km and lasting less than 10 ms. This type of TLE is often accompanied by a sprite (*Pasko et al.*, 1996, 2012), another type of TLE described in subsection 1.2.5. However, they

3. ELECTRICAL PHENOMENA IN THE ATMOSPHERE OF THE EARTH

can exceptionally appear as a single event (*Kuo et al.*, 2013). Halos are usually associated with cloud-to-ground lightning discharges (*Barrington-Leigh et al.*, 2001; *Bering et al.*, 2002, 2004b,a; *Frey et al.*, 2007), as the CMC of CG lightning is often larger than the CMC of cloud discharges (*Rakov and Uman*, 2003).

The physical mechanism behind the optical emissions of halos is mesospheric glow discharges. When the quasielectrostatic field produced by lightning discharges (first term of equation (3.2)) is applied to the low-density mesospheric air, free electrons can be accelerated. These electrons interact with nitrogen and oxygen molecules by means of two main chemical processes; collisional ionization and attachment. Ionization creates an electron and a positive ion, while attachment produces the removal of one electron and the creation of a negative ion (*Barrington-Leigh et al.*, 2001; *Wescott et al.*, 2001; *Bering et al.*, 2002; *Moudry et al.*, 2003). These ionizations and attachment reactions are written as



In addition, electrons released by associative detachment of O^- by N_2 can contribute to halo and sprite inception (*Luque and Gordillo-Vázquez*, 2011). This mechanism seems to be the main process behind the ignition of delayed sprites (*Luque and Gordillo-Vázquez*, 2011):



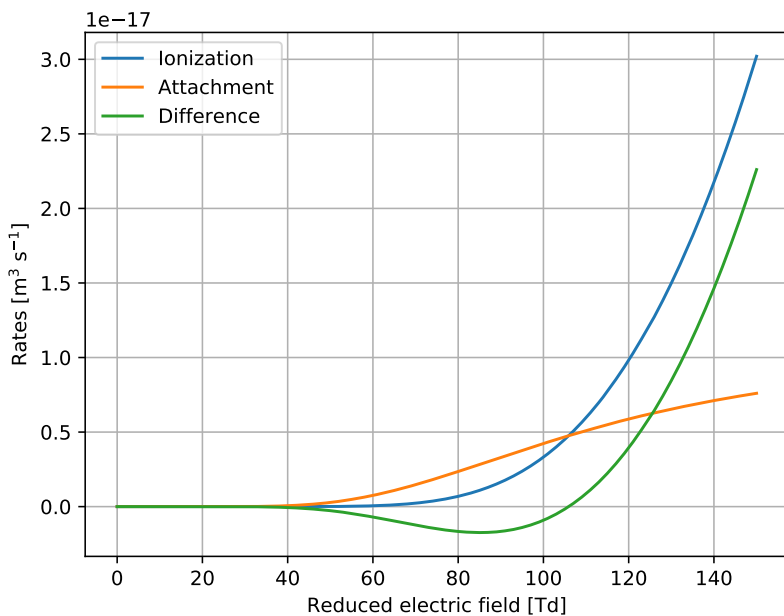


Figure 3.2: Total ionization and attachment rates as a function of the reduced electric field with the chemical scheme detailed in Appendix A.1. These rates have been calculated with BOLSIG+ (*Hagelaar and Pitchford, 2005*) in air.

However, the rates of these four reactions are highly dependent on the reduced electric field E/N , defined as the value of the applied electric field over the air density. Attachment process dominates over collisional ionization for low reduced electric fields, while the situation changes when the field exceeds the “breakdown field”, defined as the reduced electric field at which ionization rate overtakes attachment. On Earth, this breakdown field has a value of about 110 Td. Figure 3.2 shows the electric-field dependence of the total ionization and attachment rates. The total ionization and attachment rates, k_i and k_a , have been obtained as

$$k_i = 0.78k_{i,N_2} + 0.22k_{i,O_2} \quad (3.5)$$

3. ELECTRICAL PHENOMENA IN THE ATMOSPHERE OF THE EARTH

and

$$k_a = 0.22k_{a,O_2}, \quad (3.6)$$

where k_{i,N_2} , k_{i,O_2} and k_{a,O_2} are the rates of reactions 3.3. The coefficients 0.78 and 0.22 correspond to the proportion of N_2 and O_2 in air, respectively. Halos are triggered when ionization overpasses attachment and the excited species produce a cascade of chemical reactions that lead to the emission of photons.

After the halo ignition, the field-induced currents in the lower ionosphere tend to screen the electric field. The air conductivity, defined as $\sigma = e\mu_e N_e$ with μ_e being the electron mobility, depends on altitude according to the electron concentration N_e . This quantity can be used to estimate the halo duration at different altitudes according to the Maxwell relaxation time $\tau_m = e/\sigma$. We plot in figure 3.3 the Maxwell relaxation time dependence with altitude together with the effective ionization time at different reduced electric fields. The effective ionization time $\tau_{i,eff}$ is defined as the inverse of the difference between the ionization and the attachment frequencies, ν_i and ν_a , respectively.

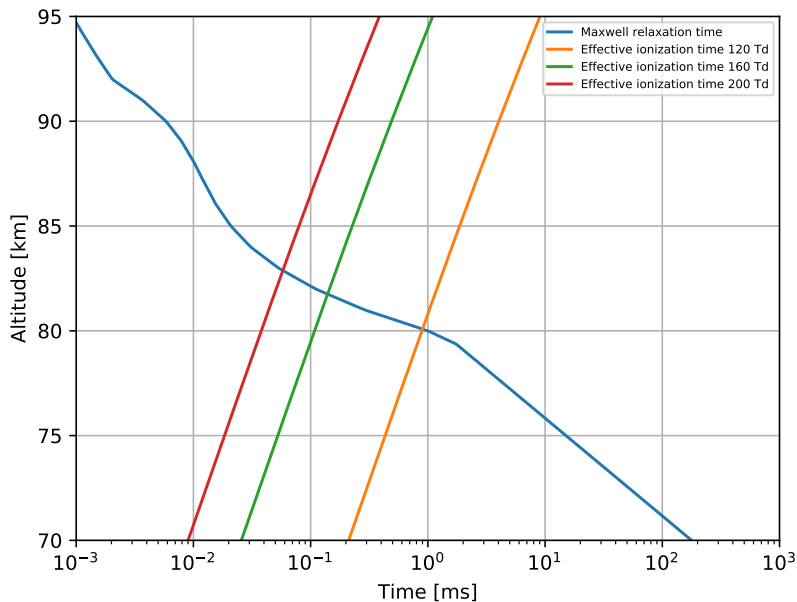


Figure 3.3: Maxwell relaxation and effective ionization times at different reduced electric field under the chemical scheme detailed in Appendix A.1.

As previously mentioned, halos are often followed by a sprite, a more luminous TLE formed by a complex structure of streamers. Sprite inception occurs near the center of the halo, where atmospheric instabilities tend to concentrate the ionization front in the head of a streamer (*Luque and Ebert, 2009*).

Optical emissions from halos are mainly distributed in the first and second positive systems of molecular neutral nitrogen (1PS N_2 and 2PS N_2), the first negative system of the molecular nitrogen ion (N_2^+ -1NS), the Meinel band of the molecular nitrogen ion (Meinel N_2^+) and the Lyman-Birge-Hopfield (LBH) band of the molecular neutral nitrogen. There exist some early reports of noisy halo spectra, as the one reported by *Wescott et al. (2001)* and later on analyzed by *Gordillo-Vázquez et al. (2011)*. On the contrary, the higher brightness of sprites have enabled to measure their optical

3. ELECTRICAL PHENOMENA IN THE ATMOSPHERE OF THE EARTH

spectra. One of the firsts spectra of sprites was recorded by *Hampton et al.* (1996) with a spectral resolution of about 10 nm. Later on *Kanmae et al.* (2007) recorded the spectrum of a sprite in the first positive system of the N_2 with a spectral resolution of 3 nm and a temporal resolution of 3 ms. The spectra of halos are expected to be quite similar to the spectra of halos (*Gordillo-Vázquez et al.*, 2011, 2012).

During the last decade, the local chemical impact and optical signatures from halos have been modeled using different approaches. Some of them have implemented zero-dimensional or one-dimensional models to predict the chemical impact and optical emissions of halos and sprites at different altitudes (*Sentman et al.*, 2008; *Gordillo-Vázquez*, 2008, 2010; *Gordillo-Vázquez et al.*, 2012; *Parra-Rojas et al.*, 2013a; *Winkler and Nothold*, 2014; *Parra-Rojas et al.*, 2015). Some authors have also implemented two-dimensional models in cylindrically symmetrical coordinates to study the electrodynamic features of halos (*Kuo et al.*, 2007; *Luque and Ebert*, 2009).

In addition to the efforts in the study of both the chemical impact and optical signature of halos, possible ways to measure the quasioleostatic field of this type of TLE have also received attention. In this regard, *Bennett and Harrison* (2013) measured the electrostatic field from thunderstorms, reporting a reversal in the electric field polarity and a violation of the cubic decay law. *Bennett* (2014) proposed the influence of the halo-driven quasioleostatic field as a possible reason behind these unexpected observations.

Elves are very fast optical emissions produced by the interaction between lower ionospheric electrons and lightning-emitted electromagnetic pulses (EMP) lasting less than 1 ms, as explained in subsection 1.2.5. The magnitude of these pulses is given by the radiation component of the electromagnetic field (third term of equation 3.2). The pass of these pulses through the lower ionosphere heats free electrons, triggering collisional reactions that lead to optical emissions (*Inan et al.*, 1997; *Moudry et al.*, 2003).

Elves are usually seen as ring-shaped optical emissions at about 88 km of altitude with a radial extension of more than 200 km (*Boeck et al.*, 1992;

Chang et al., 2010; *Adachi et al.*, 2016; *van der Velde and Montanyà*, 2016b). The shape of the elves is a consequence of the radiation emission pattern of the electric dipole that defines the lightning discharge (third term of equation 3.2).

The main optical emissions produced by elves are located in the first and second positive systems of the molecular neutral nitrogen (1PS N_2 and the 2PS N_2), the first negative system of the molecular nitrogen ion (N_2^+-1NS), Meinel band of the molecular nitrogen ion (Meinel N_2^+) and the Lyman-Birge-Hopfield (LBH) band of the molecular neutral nitrogen, as in the case of halos. However, the propagation velocity of the radiated pulse that heats ionospheric electrons leads to a duration of the elves of about 1 ms, shorter than optical emissions produced by halos.

Ground-based observations (*van der Velde et al.*, 2011; *van der Velde and Montanyà*, 2016b) and space missions, such as ISUAL (*Chang et al.*, 2010) and JEM-GLIMS (*Adachi et al.*, 2016), have greatly contributed to the knowledge of elves. The global occurrence of elves can be larger than one per second (*Chern et al.*, 2014), being the most frequent TLE. Apart of revealing some characteristics of their parent lightning, elves can also be used as an “ionospheric sounding” capable of providing valuable information about the lower ionosphere. For instance, visible spatial oscillations in elves can be an indicator of the structure of gravity waves (*van der Velde et al.*, 2011). They are also related with the so-called LOREs, an acronym for LOng Recovery Early VLF events (*Gordillo-Vázquez et al.*, 2016). In addition, very recent investigations on the so-called elves “doublet” points to very impulsive discharge sources that could be related with lightning inception mechanisms or with the production of TGFs (*Cummer et al.*, 2014; *Lyu et al.*, 2015; *Liu et al.*, 2017).

Models of elves are usually based on electromagnetic wave propagation through the atmosphere (*Inan et al.*, 1991; *Taranenko et al.*, 1993; *Kuo et al.*, 2007; *Marshall et al.*, 2010). These kind of approaches are useful to predict the shape of the optical emissions produced by this kind of TLE.

3.1.3 Description of models

3.1.3.1 Simulations of halos and elves

We have developed two different two-dimensional electrodynamic models coupled with an extensive set of chemical reactions. These approaches allow us to simulate the temporal evolution of an entire halo or an elve, quantifying their local chemical impact and predicting their emission spectra. The electrodynamic models employed here are particularizations of the general models described in section 2.2 for the case of halos and in subsection 2.3.1 for the case of elves, while the chemical reaction set coupled with the electrodynamic models is listed in Appendix A.1. This kinetic scheme is formed by 136 species interacting through more than 1000 chemical reactions, some of which are activated in the presence of an applied electric field. In addition, this scheme includes the effect of cosmic rays in the lower ionosphere, as well as the electron and ion mobility dependence on the applied electric field. The proposed set of reactions detailed in Appendix A.1 is an upgraded collection of processes used by other authors to simulate TLEs (*Gordillo-Vázquez, 2008; Sentman et al., 2008; Parra-Rojas et al., 2013a, 2015*). Let us now classify the types of reactions included in this model and highlight the upgrades with respect to previous models:

1. Electron impact excitation of neutral species given by



and ionization given by



where the species A can be N₂, O₂, N, O, NO, N₂O, O₃ or CO₂. The species A* can be electronically and/or vibrationally excited in the case of N₂, while only electron excitation is considered for the rest of

species. A^+ stands for the positive ion of the molecule or atom A. The cross sections used to calculate these reaction rates are referenced in the Appendix A.1.

2. Electron attachment processes, among which the most important is the electron driven dissociative attachment of O_2 molecules,



This attachment reaction dominates electron-ionization processes of N_2 and O_2 for reduced electric fields below the breakdown value. When the breakdown field is reached, ionization becomes larger than attachment, triggering a cascade of reactions that, ultimately, lead to the observation of TLEs. The cross sections and reaction rates used to compute the effect of these reactions are referenced in the Appendix A.1.

3. Electron detachment processes. As previously studied by *Luque and Gordillo-Vázquez (2011)*, some detachment processes like associative detachment of O^- by N_2 can dominate the production of electrons even for electric fields below the breakdown value. We consider the electric-field dependent rates of electron detachment from negative ions by N_2 and O_2 reported by *Pancheshnyi (2013)*. Furthermore, we also include electron detachment from O^- interacting with other important species, such as CO and NO (*Biondi et al., 1971; Kossyi et al., 1992*). However, according to *Moruzzi et al. (1968)*, the electric field dependence of $O^- + CO$ and $O^- + NO$ detachment rates is negligible.
4. Electron-ion and ion-ion recombination processes, contributing to remove charge carriers (*Gordillo-Vázquez, 2008; Sentman et al., 2008; Parra-Rojas et al., 2013a, 2015*).

3. ELECTRICAL PHENOMENA IN THE ATMOSPHERE OF THE EARTH

5. Vibrational redistribution, energy pooling, Vibrational-Translational (VT) and Vibrational-Vibrational (VV) processes involving electronically and vibrationally excited molecules of N_2 (*Gordillo-Vázquez, 2010*).
6. Active state chemistry (*Gordillo-Vázquez, 2008; Sentman et al., 2008; Parra-Rojas et al., 2013a, 2015*).
7. Positive and negative ion chemistry, in addition to ground state chemistry. These reactions contribute to the enhancement of some neutral species (*Gordillo-Vázquez, 2008; Sentman et al., 2008; Parra-Rojas et al., 2013a, 2015*).
8. Odd hydrogen and odd nitrogen reactions (*Sentman et al., 2008*).
9. Radiative decay, electronic quenching and vibrational quenching. These three processes compete to de-excite molecules and atoms. Most important quenching reactions include N_2 and O_2 . The most of the radiative decay constants and electronic and vibrational quenching rates used in this work are taken from *Gordillo-Vázquez (2010); Parra-Rojas et al. (2015)*. However, to the best of our knowledge, the electronic quenching rate of $N_2(E^3\Sigma_g^+)$ by N_2 or O_2 is not described in the literature. This process can be important to describe the Vibrational Distribution Function (VDF) of the electro-vibrationally excited molecule $N_2(C^3\Pi_u, v)$. As an approximation of the electronic quenching rate of $N_2(E^3\Sigma_g^+)$ we set its value equal to the quenching rate of the molecule $N_2(C^3\Pi_u, v = 0)$.

Some of the proposed chemical reaction rates depend on the reduced electric field. This dependence, as well as the mobility dependence on the electric field, is obtained by solving off-line the steady-state Boltzmann equation for air using the software package BOLSIG+ (*Hagelaar and Pitchford, 2005*).

The initial conditions of the atmosphere before the onset of the discharge must be in chemical and electrical equilibrium in order to obtain reliable results. To ensure that, we perform a chemical relaxation method that couples the set of chemical reactions with the cosmic rays. Firstly, we use the air density profile from the US Standard Atmosphere (*United States Committee on Extension to the Standard Atmosphere, 1976*) and the electron density proposed by *Hu et al. (2007)*. Then we calculate the evolution of the chemical species simulating 6.5 seconds under the presence of cosmic ray ionization (*Thomas, 1974*) by solving the continuity equation of each species. The concentrations of the most abundant species (N_2 , O_2 , CO , CO_2 and H_2O) are assumed to take their ambient values for each altitude. We plot in figure 3.4 the obtained equilibrium profile.

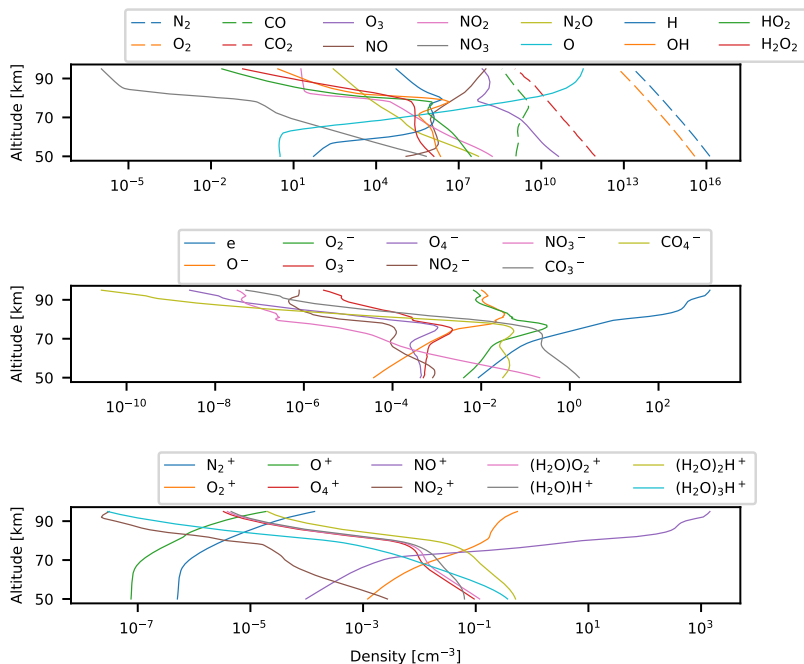


Figure 3.4: Most important species at equilibrium conditions. Dashed lines correspond to most abundant species. The H_2O concentration is set constant to $1.6 \times 10^9 \text{ cm}^{-3}$.

3. ELECTRICAL PHENOMENA IN THE ATMOSPHERE OF THE EARTH

The developed electrodynamical model for halos takes as input a lightning discharge and calculates the quasielectrostatic field between the ground and the lower ionosphere. Apart from the lightning-created electric field, the model also computes the induced current in the mesosphere and the electric field produced by the separation of electrons and ions. For these purposes, the model includes a Poisson equation solver (FISHPACK (*Sweet, 1977*)) together with the diffusion-advection equation for electrons and ions (*Montijn et al., 2006*).

Let us describe now the particularization of the general model described in section 2.2 for the case of terrestrial halos. We set as input of the electric field a CG lightning discharge with a channel extension of 7 km. We assume that the accumulated charge by the stroke in the cloud is confined within a sphere of radius 0.5 km at 7 km of altitude (*Maggio et al., 2009*). The variation in time of the charge follows the bi-exponential function (*Rakov and Uman, 2003*)

$$\frac{dQ(t)}{dt} = I(t) = \frac{Q_{\max}}{\tau_1 - \tau_2} (\exp(-t/\tau_1) - \exp(-t/\tau_2)), \quad (3.10)$$

where Q_{\max} is the opposite sign total charge lowered to the ground and where $\tau_1 = 1$ ms and $\tau_2 = 0.1$ ms are, respectively, the total discharge time and the rise time of the discharge current.

The Poisson solver domain consists in a cylindrical box with an altitude of 97 km and a radius of 300 km, while the chemistry is solved exclusively for altitudes above 50 km and for radial distances below 250 km. This domain is discretized in a cylindrical grid with a spatial resolution given by the spatial steps $\Delta z = 100$ m in the horizontal direction and $\Delta r = 500$ m in the radial direction. We set an adaptive time step Δt that remains always less than 3×10^{-6} seconds. The electrodynamical model is solved step-by-step and coupled with the kinetic scheme detailed in Appendix A.1. Continuity equations of chemical species are solved for all the species listed in the kinetic scheme (Appendix A.1), while the transport equations are solved for

all the charged particles. We set as output of the model the value of the electric field, the charged particles fluxes and the density of each species in the entire simulation domain every $30 \mu\text{s}$.

In the case of the elve model, the Poisson equation is not adequate to compute the electromagnetic pulses (EMP) that trigger the elves. The developed electrodynamical model, detailed in subsection 2.3.1, solves the Maxwell equations of the electromagnetic field using a self-consistent Finite-Difference Time Domain (FDTD) scheme of electromagnetic wave propagation. The cylindrically symmetrical simulation domain is discretized according to the Yee algorithm (Yee, 1966) with different space steps for each type of discharge, while the time step is set to 10 ns. Both the space and the time discretization must satisfy the conditions listed in subsection 2.3.1 in order to preserve the stability. The induced currents in the lower ionosphere are calculated using a modified Ohm's equation for altitudes above 50 km, where the conductivity of the atmosphere is not negligible. At elves altitude near 88 km, the electron conductivity is orders of magnitude higher than the ion conductivity, hence we neglect the induced ion current.

We set different lightning-discharges as source of the EMPs in order to compare the elves triggered by each discharge. On the one hand, we study elves produced by vertical CG lightning discharges with different CMCs. On the other hand, we investigate elves produced by some types of vertical cloud discharges, such as CIDs and EIPs, described in section 1.1. Let us enumerate the characteristic of each type of discharge and the domain discretization:

1. Four different vertical cloud-to-ground lightning discharges are considered whose electric current follows the bi-exponential function given by equation 3.10 with a risetime of $40 \mu\text{s}$ and a total duration of the stroke of $400 \mu\text{s}$ (Rakov and Uman, 2003). As an extremely weak discharge, we set another CG lightning with a rise time and a total discharge time of $100 \mu\text{s}$ and $1000 \mu\text{s}$, respectively. The channel longitudes are

3. ELECTRICAL PHENOMENA IN THE ATMOSPHERE OF THE EARTH

set to 7 km, while the maximum transferred charges are in each case 50.0 C, 115.0 C, 142 C and 230 C as an extreme case. These discharges produce CMCs of 560 C km, 800 C km, 1000 C km and 1600 C km in each case. The current peaks of each of these lightning discharges are 154 kA, 220 kA, 276 kA and 440 kA, respectively. The extremely low case has a peak current of 90 kA and a CMC of 560 C km. According to *Barrington-Leigh and Inan (1999)*, the lightning peak current threshold for the production of elves is about 60 kA, while the detection threshold of the ISUAL instrument is 80 kA (*Kuo et al., 2007; Chern et al., 2014*). For all the cases of CG lightning discharges, our model domain is a cylindrical mesh with 97 km of altitude and a radius of 550 km. The space is discretized in horizontal steps of $\Delta r = 0.5$ km and vertical steps of $\Delta z = 0.1$ km. We include 20-cell-wide absorbing boundaries in the upper and horizontal extremes of the domain.

2. Two different cloud discharges. We simulate elves produced by a CID and an EIP with a similar channel of 1 km length. The CID, located at 18 km of altitude, consists in an impulsive electrical discharge with a characteristic time of several microseconds, shorter than the typical time of CG lightning discharges. We use the Modified Transmission Line Exponential Increasing (MTLEI) model proposed by *Watson and Marshall (2007)* for downward positive discharges, with a peak current of about 400 kA (*Cummer et al., 2014; Lyu et al., 2015; Liu et al., 2017*). The other discharge, the EIP, consists in a negative current source located at 13 km of altitude with a channel longitude of 1 km. The function that defines the temporal dependence of the current is taken from *Liu et al. (2017)*, who simulated EIP-driven elves produced by a current with a peak of about 500 kA. As *Liu et al. (2017)* claims, this current could produce TGFs detectable by Fermi (*Briggs et al., 2010; Cummer et al., 2014; Lyu et al., 2015*). Both the CID and the EIP are simulated in a cylindrical domain with a radius of 250 km

and an altitude of 97 km. Both the vertical and the horizontal spatial steps are set to 0.1 km.

After setting up the lightning discharge, the model starts to calculate the electromagnetic field in the computational domain and the mesospheric induced currents step by step, coupling the electrodynamical scheme with the set of kinetic reactions collected in Appendix A.1. As in the case of halos, the evolution of the concentration of each species is computed step-by-step by solving their continuity equations. In this case, we set as output of the model the value of the electromagnetic field, the mesospheric induced charges and the density of each species in the entire simulation domain every 5 μs .

The output of both the halo and the elves models allow us to follow the electrodynamical and chemical temporal evolution of halos and elves, computing their local chemical impact and predicting their optical emissions as follows:

1. The calculation of the species production of halos and elves is performed by comparing the total molecules of each species before the TLE onset and at a given time later. To obtain these quantities, we integrate the species density over the domain.
2. Knowledge of the charged particles fluxes and/or induced mesospheric currents together with the TLE duration allows us to estimate the energy deposited in the mesosphere by halos and elves. We compute this energy as the product of these induced current, the electric field and the total time of the event. We compute this quantity in all the cells of the computation domain and then calculate the total energy deposited in the cylindrically symmetrical TLE.
3. Optical emissions from halos and elves are obtained from the spatial density distribution of each emitting species $n_i(\vec{r})$. Emitting species are those that suffer radiative decay emitting photons according to

3. ELECTRICAL PHENOMENA IN THE ATMOSPHERE OF THE EARTH

the radiative decay constant of de-excitation A_i . The value of these constants are given in the set of reactions collected in Appendix A.1 for each emitting species (mainly $N_2(B^3\Pi_g, v = 0, \dots, 6)$, $N_2(C^3\Pi_u, v = 0, \dots, 4)$, $N_2(a^1\Pi_g, v = 0, \dots, 15)$, $NO(A^2\Sigma^+)$, $O_2(A^3\Pi_u^+)$, $O_2(b^1\Pi_g^+)$, $O_2(a^1\Delta_g)$, $O(^1S)$, $O(^1D)$, $O(^3P)$, $O(^5P)$ and some vibrationally excited states of CO_2). The total number of photons emitted by each of these species can be calculated integrating in volume as

$$I = \int A_i N_i(\vec{r}) dV. \quad (3.11)$$

The synthetic emission spectra of halos and elves can be calculated from the emitted photons within each spectral line. In addition, the effect of optical transmittance of the atmosphere must be applied to this emission spectra in order to predict the observed spectra at a given distance from the event. We compute the air transmittance of the atmosphere using the software MODTRAN 5 (*Berk et al.*, 2005). As can be seen in figure 2 of *Gordillo-Vázquez et al.* (2012), the air transmittance dependence on the light frequency is irregular. We use a tool written in Python programming language previously described in *Parra-Rojas et al.* (2013b) to obtain the rovibronic bands of the 1PG N_2 system. This program is based in the calculation of the decay constant of each rovibrational level following the method described in *Kovacs* (1969) for triplet transitions. Afterwards, the obtained transmittance for different altitudes can be applied to the emitted spectra to derive the predicted observed optical signature of halos and elves as would be seen from ground-based spectrographs like GRASSP (*Passas et al.*, 2016).

3.1.4 Results and discussion

In this section we detail and discuss the results of the simulation of terrestrial halos and elves. As we explained in the previous subsection 3.1.3, we

simulate halos and elves using the two-dimensional electrodynamical models detailed in sections 2.2 and 2.3.1, respectively. Both models are coupled with the chemical scheme listed in Appendix A.1.

We analyze the obtained electric fields and their influence on the mesospheric conductivity in subsection 3.1.4.1, emphasizing the analysis of the quasielectrostatic field created by halos at ground level. The calculated local chemical impact of halos and elves in the upper atmosphere is discussed in subsection 3.1.4.2, while their optical signature is analyzed in subsection 3.1.4.3.

3.1.4.1 Electromagnetic fields and conductivity in the lower ionosphere

The electromagnetic fields created by lightning discharges and the changes that they produce in the mesosphere are the main driver of the evolution of halos and elves. The computed electric fields and their interactions with the upper atmosphere are presented in this section.

The electromagnetic fields created by lightning discharges and the changes that they produce in the mesosphere are the main driver of the evolution of halos and elves. The computed electric fields and their interactions with the upper atmosphere are presented in this section.

We start the analysis with the case of halos triggered by vertical CG lightning discharges. Upper six panels of figure 3.5 show some snapshots of the reduced electric field produced by CG lightning discharges with different total CMCs, while the lower six panels show the enhancement of electrons related to these electric fields. As can be seen in the figure, reduced electric fields higher than the breakdown value of 110 Td trigger the production of free electrons as a consequence of ionization. This breakdown field value is reached in the case of the two most energetic discharges. It can also be seen in figure 3.5 how the enhancement of electrons contributes to screen the reduced electric field after several milliseconds.

3. ELECTRICAL PHENOMENA IN THE ATMOSPHERE OF THE EARTH

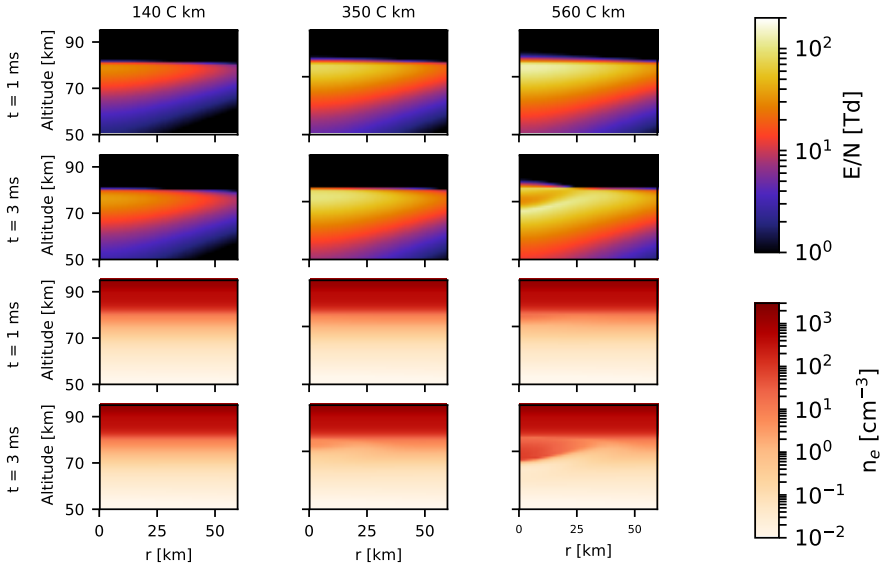


Figure 3.5: Snapshots showing the reduced electric field and the electron concentration in the upper atmosphere 1 ms and 3 ms after the onset of three vertical CG lightning discharges. The lightning channel is always located at $r = 0$ and between the ground and an altitude of 7 km. Each column show results for lightning discharges with different CMCs.

We follow the analysis of the reduced electric field created by lightning discharges plotting in figure 3.6 the case of elves. In this figure, we show the reduced electric field as well as the density of the emitting species $N_2(C^3\Pi_u, v = 0)$ several milliseconds after the onset of two different vertically oriented CG lightning discharges. Both the pulse emitted by the temporal derivative of the lightning discharge current and the quasielectrostatic field produced by the charge accumulation in the cloud can be distinguished. The high value of the EMP heats electrons, producing electronic excitation from the ground electronic state of N_2 molecules to $N_2(C^3\Pi_u, v = 0)$. The elves can be appreciated in the last two rows of figure 3.6 at around 88 km of altitude, where the density of $N_2(C^3\Pi_u, v = 0)$ will produce toroid-shaped optical emissions in the 337 nm spectral line by radiative decay.

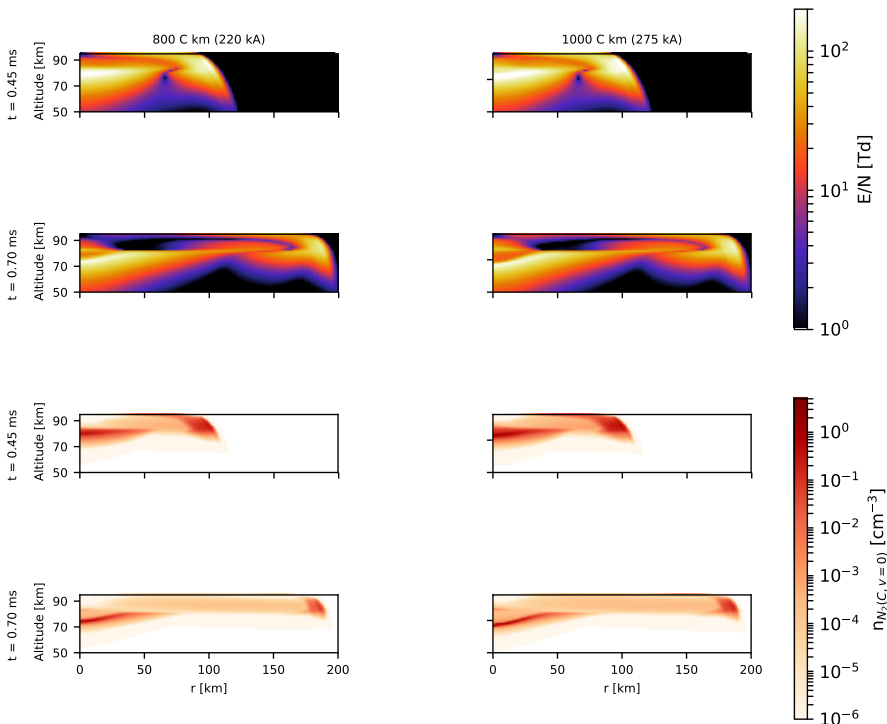


Figure 3.6: Snapshots of the reduced electric fields and densities of $N_2(C^3\Pi_u, v = 0)$ in the upper atmosphere produced by two different vertically oriented CG lightning discharges. The CMC value of each discharge is 560 C km and 800 C km. The lightning discharge that triggers these electric fields start at 0 ms.

Finally, we simulate elves produced by other types of discharges. In this case, we set as lightning discharges a CID and an EIP, very impulsive discharges with characteristic times of microseconds and with a channel length of 1 km. Figure 3.7 shows the same quantities that in the previous case together with the E_r and E_z components of the electric field triggered by both a CID and an EIP. As previously studied by other authors, such as *Marshall et al. (2015)* and *Liu et al. (2017)*, the EMP produced by CIDs and EIPs can trigger a succession of two elves or elve “doublet” as a consequence of the primary wave ground-reflexion. This fact can be appreciated in figure 3.7, where the consecutive pulses are seen both in the E_r and in

3. ELECTRICAL PHENOMENA IN THE ATMOSPHERE OF THE EARTH

the E_z components of the electric field. In addition, this figure also shows how each pulse is formed by two sub-pulses with different polarization, due to the fast sign reversal of the derivative of the electric current at the source (Watson and Marshall, 2007; Liu et al., 2017). The delay between the consecutive elves at a given distance from the center is different in the case of CIDs and EIPs as a consequence of the different altitudes of the current sources.

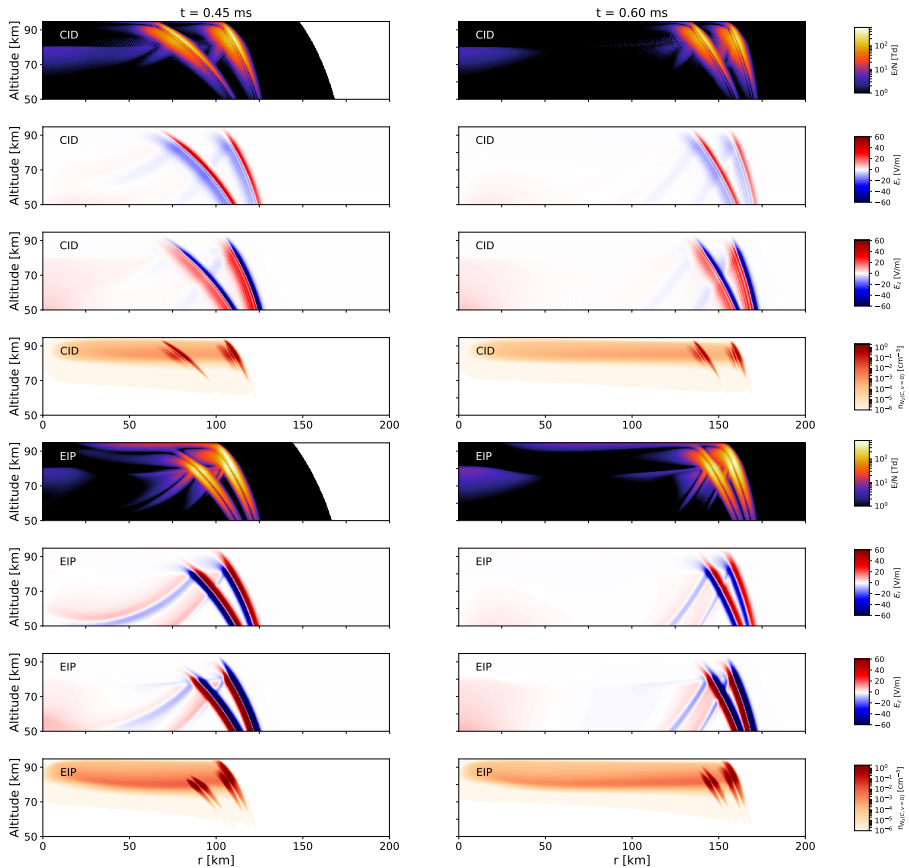


Figure 3.7: Snapshots of the reduced electric field, E_r and E_z electric field components and the density of $N_2(C^3\Pi_u, v = 0)$ in the upper atmosphere produced by CIDs and EIPs. The lightning discharge that triggers these electric fields start at 0 ms.

3.1.4.2 Chemical impact of halos and elves

In this section, we discuss the local chemical impact of single halos and elves and estimate their possible global influence in the atmosphere of the Earth.

In this section, we discuss the local chemical impact of single halos and elves and estimate their global impact in the atmosphere of the Earth. It can be seen that the main chemical effect of halos is focused at altitudes around 75 km. Furthermore, this effect has an horizontal influence up to 20 km from the center of the halo.

Figures 3.8 and 3.9 summarize the density variation of some of the main neutrals and ions in the atmosphere of the Earth 3 ms after the onset of a halo. The density of some initial ground state neutrals suffers an enhancement in the center of the halo. The atomic nitrogen N increases by about 300 %, followed by other species like O, N₂O, NO₂, and NO, with increases with respect to their ambient values of ~ 0.7 %, ~ 0.2 %, ~ 0.1 % and ~ 0.01 %, respectively.

The main processes that contribute to enhance the densities of N and O are the collisions of electrons with N₂ and O₂, respectively. The enhancement of the N₂O density is due to associative detachment of O⁻ by N₂, while the increase of the NO density is influenced by the processes that involve N(²D) and O₂. Finally, NO interacts with molecules containing O atoms to create NO₂.

3. ELECTRICAL PHENOMENA IN THE ATMOSPHERE OF THE EARTH

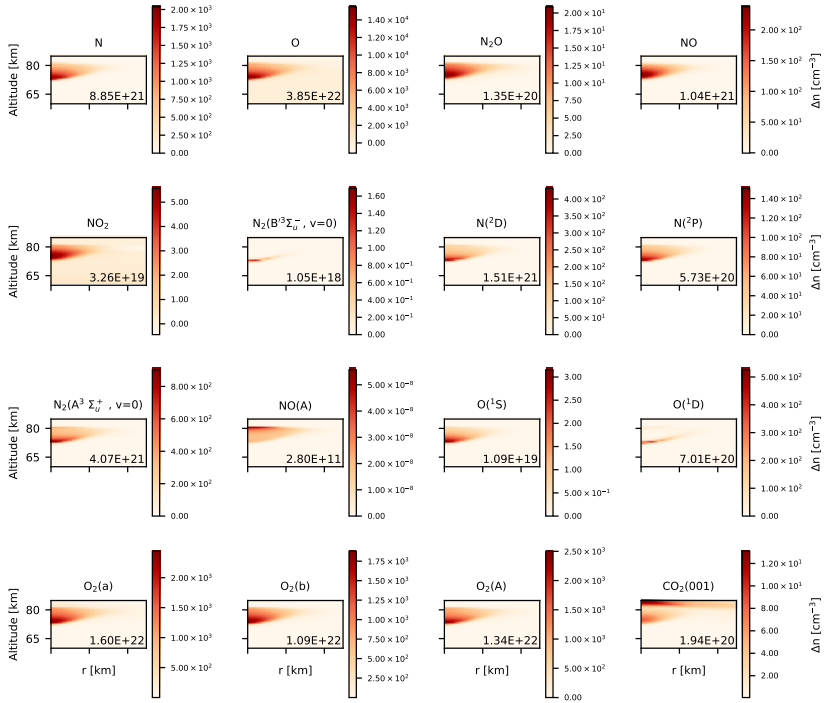


Figure 3.8: Variation (with respect to ambient values) of the density of some neutrals in the atmosphere of the Earth 3 ms after the beginning of a CG lightning discharge with a CMC of 560 C km. We show the total number of molecules created by the halo in the lower right corner of each subplot.

Let us analyze now the evolution of the halo 3 ms after its onset. Some of the chemical reactions listed in Appendix A.1 have characteristic times of the order of seconds. Therefore, a simulation of at least one second is necessary to estimate in certain detail the local chemical impact of halos. However, sprites often appear several milliseconds after the onset of the halo. Hence, it is necessary to analyze the capability of our model to deal with the possible inception of a sprite.

3.1 Transient Luminous Events: Halos and elves

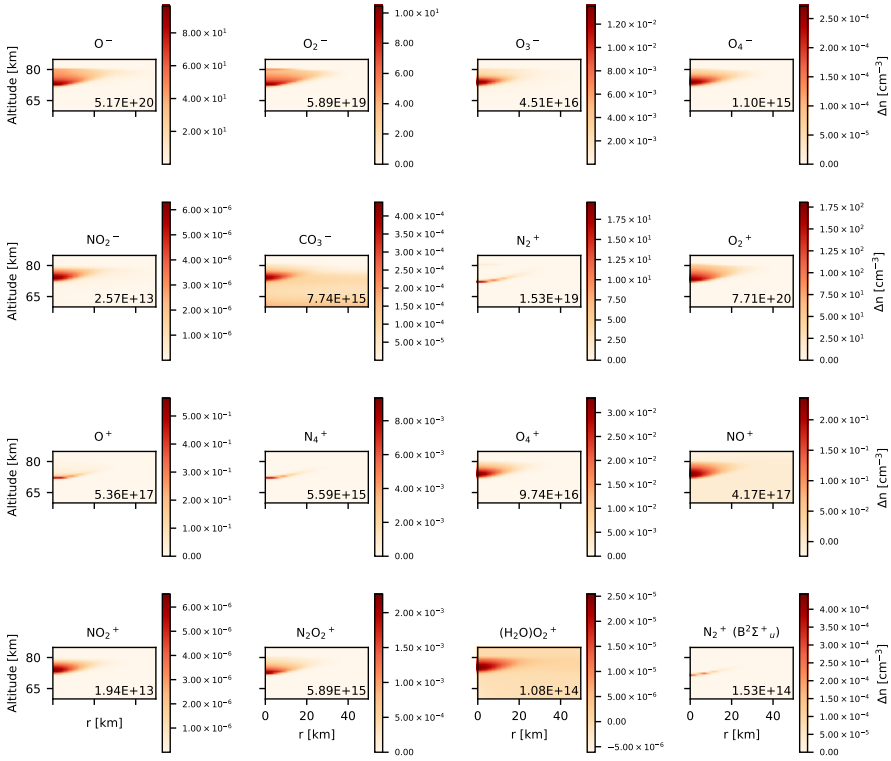


Figure 3.9: Density (with respect to ambient values) variation of some ions in the atmosphere of the Earth 3 ms after the onset of a CG lightning discharge with a CMC of 560 C km. We show the total number of molecules created by the halo in the lower right corner of each subplot.

Figure 3.10 shows the temporal evolution of the $N_2(C^3\Pi_u(v=0))$ density and the reduced electric field in a vertical column above two different discharges. For the weakest discharge, with a CMC of 140 C km, optical emissions due to $N_2(C^3\Pi_u(v=0))$ disappear around 4 ms after the beginning of the discharge, while the reduced electric field is too low to produce emissions or ionization below 75 km of altitude. However, for higher CMCs the reduced electric field is above the breakdown value at altitudes below 75 km. In that region, the lack of electrons entails a Maxwell relaxation time of tens of milliseconds, resulting in a long lasting halo that disagrees with observations. Probably, a sprite would appear in this situation, screening

3. ELECTRICAL PHENOMENA IN THE ATMOSPHERE OF THE EARTH

the electric field below 75 km of altitude. However, our model is not capable of describing the evolution of sprite streamers.

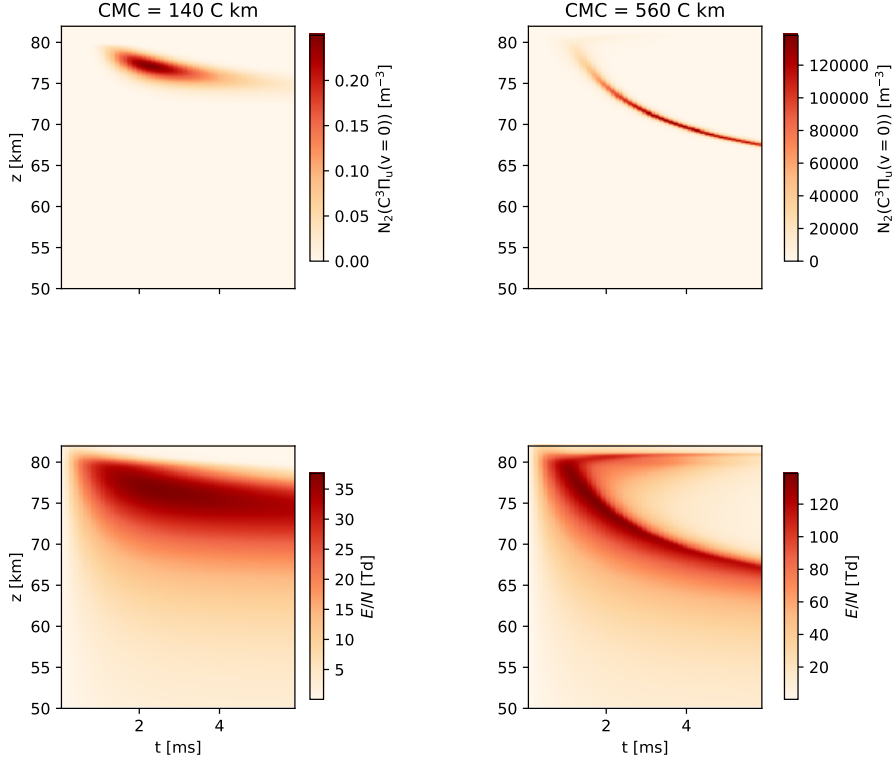


Figure 3.10: Temporal evolution of the density of the emitting species $N_2(C^3\Pi_u(v=0))$ (top panels) and the reduced electric field (bottom panels) in a vertical column above the lightning discharge. Panels in the first and second column correspond to two different lightning discharges with CMCs of 140 C km and 560 C km, respectively.

Although we cannot extend the previous simulation from 3 ms to one second, we propose a different and realistic approach to obtain the chemical impact of a halo one second after its onset. This approach is based on observations reported by *Kuo et al. (2013)* where some very luminous halos were triggered by lightning discharges with large CMCs, greater than 800 C km, without sprite inception. In this section we model halos produced by a lightning discharge that accumulates 80 C of charge during one millisecond,

followed by another discharge that removes the accumulated charge in the next five milliseconds. This approach allows us to avoid sprite inception. In addition, the hypothesis whereby the charge on clouds is removed would explain the exceptional single halos reported by *Kuo et al.* (2013).

After the cloud charge removal, the only net charge in the atmosphere would be the halo-induced charge in the mesosphere. According to our simulation, these charges would produce a maximum reduced electric field of 13 Td, quite lower than the breakdown field. We neglect the effect of this field and deactivate the Poisson solver and the transport of charged particles in order to accelerate the numerical calculations. In addition, we decrease the spatial resolution. This allows us to extend the simulation in time to predict the chemical influence of lightning discharges in the lower ionosphere up to the scale of seconds.

After the cloud charge removal, the only net charge present in the atmosphere would be the halo-induced charge in the mesosphere. According to our simulation, these charges would produce a maximum reduced electric field of 13 Td, quite lower than the breakdown field. We neglect the effect of this field and deactivate both the Poisson solver and the transport of charged particle in order to accelerate computation. In addition, we decrease the spatial resolution. This allows us to extend the simulation to predict the chemical influence of lightning discharges in the lower ionosphere up to the scale of seconds.

The most important variations in the density of neutrals during 1 second are plotted in figure 3.11. Although the relative increase of ground neutrals with respect to background densities shown in figure 3.4 is always below 0.1 %, it is interesting to note and quantify the enhancements of some important species, such as N, N₂O and NO. The increase of these species in the center of the halo is of the order of ~ 600 %, ~ 0.2 % and ~ 0.1 %, respectively.

3. ELECTRICAL PHENOMENA IN THE ATMOSPHERE OF THE EARTH

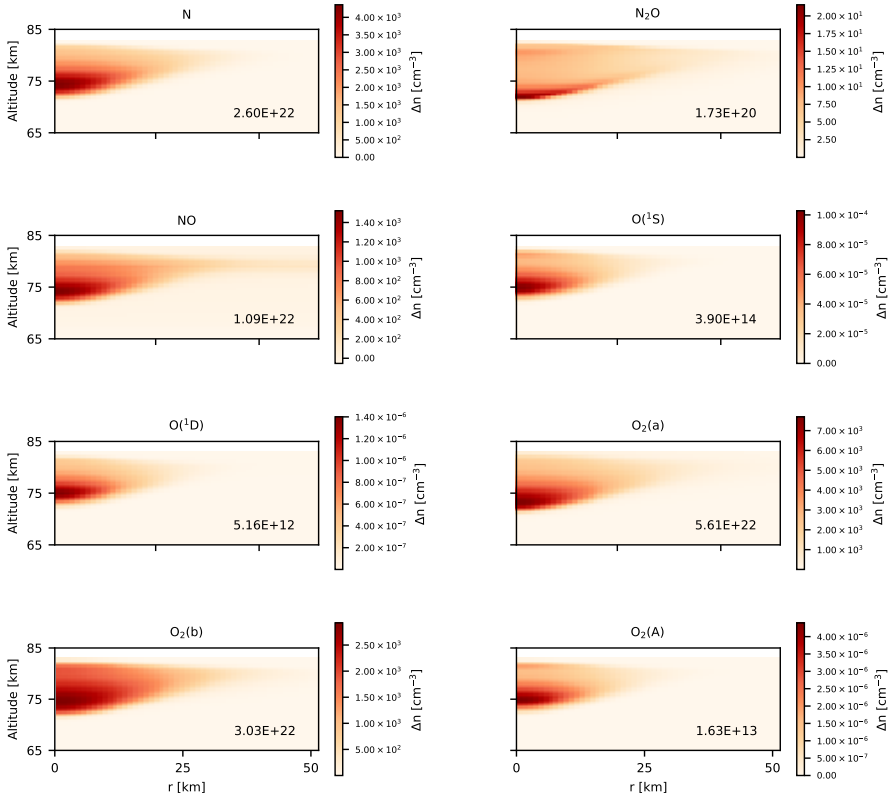


Figure 3.11: Variation of the density of some neutrals in the atmosphere of the Earth 1 second after the beginning of a CG lightning discharge producing a CMC of 560 C km producing a bright halo. We show the total number of molecules created by the halo in the lower right corner of each subplot.

Let us now estimate the energy deposited in the mesosphere by a halo using these results. Given both the computed temporal evolution of the flux of electrons in the mesosphere and the electric field produced by the lightning discharge, the power deposited in the mesosphere can be calculated as the product of these two quantities and the total volume of the halo. Therefore, the total deposited energy can be estimated knowing the duration of the event. This calculation leads us to estimate that the total amount of energy deposited in the mesosphere by a halo is about 10^6 J. Therefore, the production rate of NO by a halo can be approximated in

terms of energy as 10^{16} molecules of NO/J, one order of magnitude lower than the production rate of NO by lightning, estimated in 10^{17} molecules of NO/J (*Price et al.*, 1997). The ISUAL instrument observations estimated that the annual occurrence of TLEs is of the order of 1.2×10^7 (*Chern et al.*, 2014). The 6% of the observed TLEs by ISUAL were halos. The computed production of NO molecules by a halo together with the observation of halo occurrence by ISUAL allow us to estimate the total amount of NO created by halos in 2×10^{-7} teragrams of nitrogen per year (Tg N/y). This value is quite below the estimated global production of NO by lightning discharges, estimated between 5 and 9 Tg N/y (*Schumann and Huntrieser*, 2007; *Nault et al.*, 2017).

The global chemical impact of elves can also be estimated following this same approach. We analyze the elves triggered by CG lightning discharges with current peaks are 90 kA, 110 kA and 220 kA. A lightning with a current peak of 90 kA lightning can produce an elve slightly above the ISUAL detection threshold, estimated in parent lightning discharges with peak currents about 80 kA (*Kuo et al.*, 2007; *Chern et al.*, 2014). The simulated elves triggered by CG lightning discharges with a current peaks of 90 kA, 110 kA and 220 kA create about 4×10^{16} , 5×10^{16} NO and 2×10^{21} molecules, respectively. We also compute (following the method described in section ??) the total amount of energy deposited in the mesosphere by these two elves, obtaining 7×10^5 J, 10^6 J and 10^7 J, respectively. According to these quantities, the production rate of NO by elves can be given in terms of energy as 5×10^{10} molecules of NO/J and 2×10^{14} molecules of NO/J, between 6 and 2 orders of magnitude below the production rate of halos. According to ISUAL observations, 74% of annually observed TLEs are elves (*Chern et al.*, 2014). The results of our elve simulations together with the observation of elves by ISUAL allow us to estimate that the total global amount of NO created by elves is between 8×10^{-12} Tg N / y and 5×10^{-7} Tg N / y. This quantity is between 12 and 7 orders of magnitude lower than the esti-

3. ELECTRICAL PHENOMENA IN THE ATMOSPHERE OF THE EARTH

mated global annual production of NO by lightning discharges, between 5 and 9 Tg N / y (*Schumann and Huntrieser, 2007; Nault et al., 2017*).

It is worth analyzing the temporal evolution of electrons up to 1 second after the onset of a halo. Figure 3.12 shows the evolution of the density of electrons and O^- in the atmosphere of the Earth. It can be seen how the ion O^- is transformed into electrons between 15 ms and 1 s after the onset of the halo. The main chemical process that contributes to this transformation is the associative detachment reaction



that exceeds other associative detachment processes when the applied electric field is zero. However, at the very initial moment when the halo develops and the electric field is high, the rate of this reaction does not change, since it does not depend on the electric field (*Moruzzi et al., 1968*).

3.1 Transient Luminous Events: Halos and elves

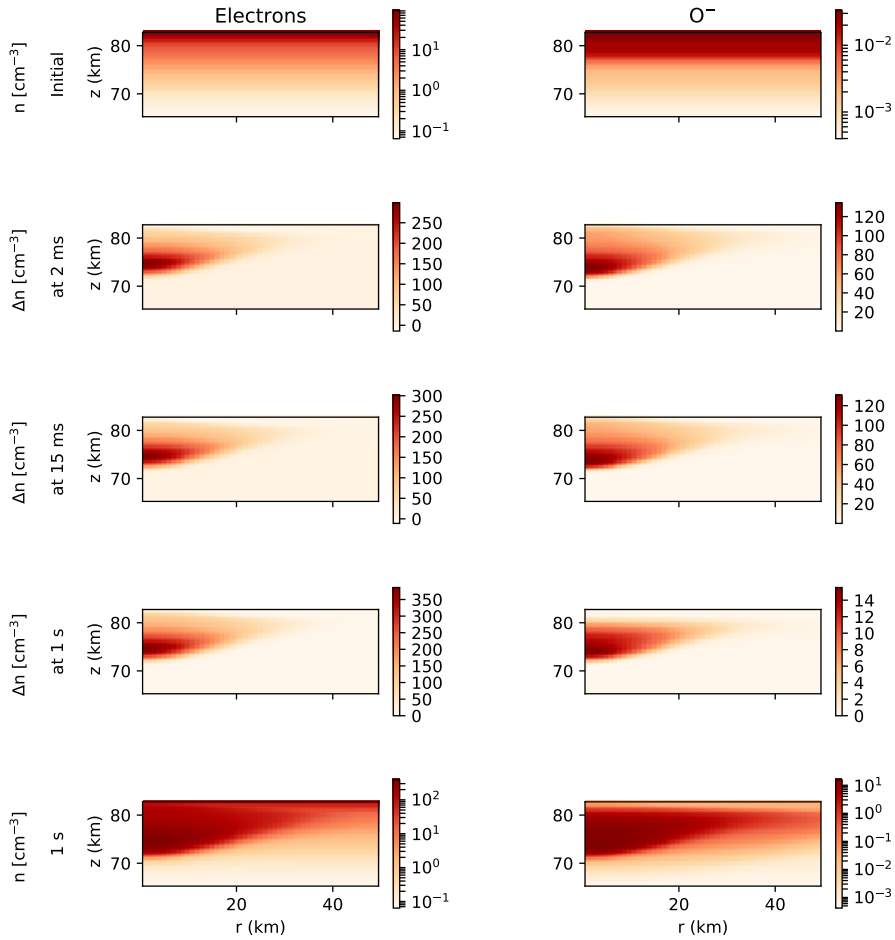


Figure 3.12: Evolution of the density of electrons and O^- in the atmosphere of the Earth during 1 second after the onset of a CG lightning discharge with a CMC of 560 C km producing a bright halo. The first and the last rows show the initial and final profiles, respectively. The second, third and fourth rows show the increase in the density at different times since the beginning of the lightning discharge.

3. ELECTRICAL PHENOMENA IN THE ATMOSPHERE OF THE EARTH

3.1.4.3 Optical signature of halos and elves

We continue the analysis of the evolution of simulated halos and elves by computing their optical emissions. The electric field that triggers these types of TLEs lead to the production of several electronically and ro-vibrationally excited species. An important part of these excited species can lose the gained energy by emitting photons according to the radiative decay processes shown in Appendix A.1. In this section, we apply the scheme proposed in subsection 3.1.3 to estimate the optical emissions of halos and elves computing the amount of emitted photons from the calculated concentration of emitting species. We also predict what would be the observed spectra of these TLEs at several distances from the source.

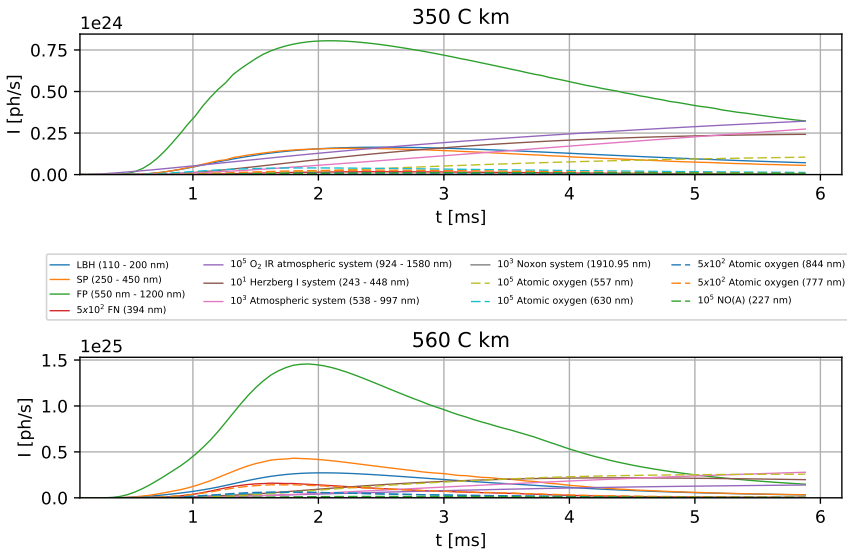


Figure 3.13: Temporal evolution of the total emitted photons per second (for the main spectral bands) from halos. This figure shows results for two halos triggered by two CG lightning discharges with total CMCs of, respectively, 350 C km and 560 C km. As can be seen in the legend box, some lines have been multiplied by different factors in an effort to plot all of them together. LBH, SP, FP and FN correspond to the Lyman-Birge-Hopfield band, second positive, first positive and first negative systems of molecular nitrogen, respectively.

3.1 Transient Luminous Events: Halos and elves

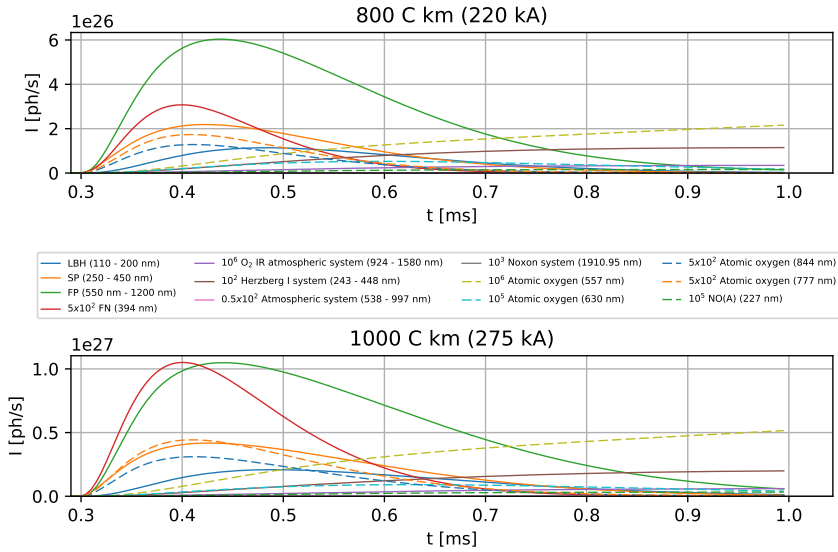


Figure 3.14: Temporal evolution of the total emitted photons per second (for the main spectral bands) from elves. This figure shows results for two elves triggered by two CG lightning discharges producing total CMCs of 560 C km (154 kA) and 800 C km (220 kA). As in figure 3.13, some lines have been multiplied by different factors in an effort to plot all of them together. LBH, SP, FP and FN correspond to the Lyman-Birge-Hopfield band, second positive, first positive and first negative systems of the molecular nitrogen, respectively.

3. ELECTRICAL PHENOMENA IN THE ATMOSPHERE OF THE EARTH

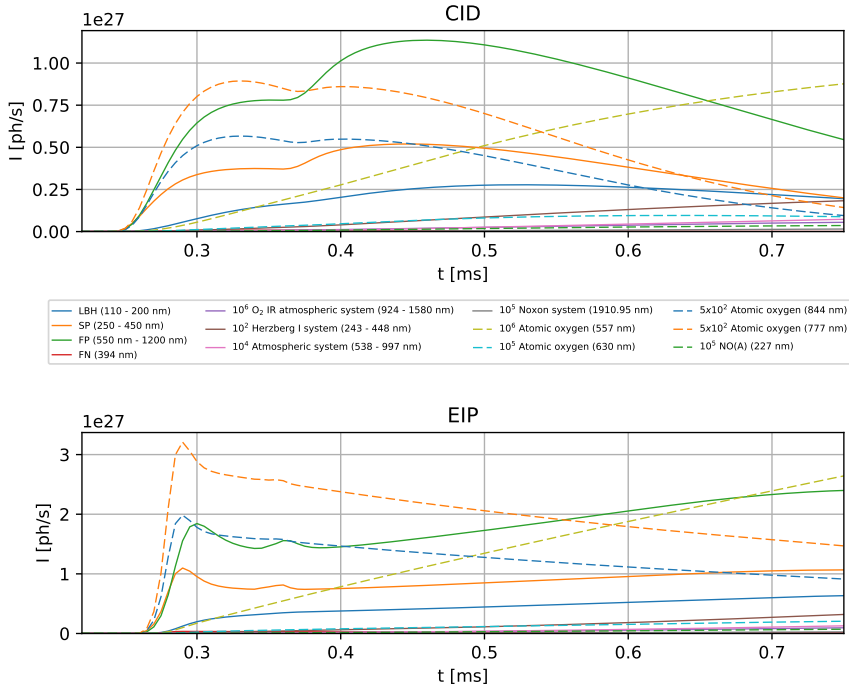


Figure 3.15: Temporal evolution of the total emitted photons per second (for the main spectral bands) from elves produced by CIDs and EIPs. As in figure 3.13, some lines have been multiplied by different factors in an effort to plot all of them together. LBH, SP, FP and FN correspond to Lyman-Birge-Hopfield band, second positive, first positive and first negative systems of molecular nitrogen, respectively.

Let us start the analysis of the optical emissions of halos and elves by calculating the total amount of emitted photons in different spectral bands. Figure 3.13 shows the temporal evolution of the emitted photons (within the main spectral bands) by two halos, while figures 3.14 and 3.15 correspond to the emissions in the same spectral bands due to elves triggered by CG and cloud lightning discharges, respectively. Let us analyze the common features of the optical emissions from each species for these simulated halos and elves:

1. Optical emissions from excited states of molecular nitrogen: The first positive system of the molecular nitrogen dominates over other spectral bands, followed by the second positive system of the same molecule. The intensity of the LBH band is comparable to the intensity of the second positive system. The number of emitted photons per second in the first negative system are around 3 orders of magnitude lower than optical emissions of the first positive system. It is interesting to note that the temporal position of each intensity peak is different as a consequence of the different lifetimes of each of the emitting species.
2. Optical emissions from excited states of molecular oxygen: We obtain emitted photons from molecular oxygen in several spectral bands. These optical emissions are distributed between the infrared atmospheric system (924 - 1580 nm), the Herzberg I system (243 - 448 nm), the atmospheric system (538 - 997 nm) and the Noxon system (~ 1911 nm). As can be seen in the plots, emissions from molecular oxygen are always between 1 and 6 orders of magnitude lower than emissions from the first positive system of molecular nitrogen.
3. Optical emissions from excited states of atomic oxygen and nitric oxide: The figures also show the temporal emissions produced by radiative decay of electronically excited states of atomic oxygen (O) and nitric oxide (NO). In particular, our calculations indicate that some weak emissions corresponding to 227 nm, 557 nm, 630 nm, 777 nm and 844 nm would be produced by halos. However, these emissions would possibly be too weak to be detected by current instruments.

Despite these common features, there are some obvious differences between the transient optical emissions due to halos, CG lightning-driven elves and CIDs and EIPs driven elves. The relative importance of the first negative system of N_2 is higher in the case of elves. In addition, the double peak

3. ELECTRICAL PHENOMENA IN THE ATMOSPHERE OF THE EARTH

in the calculated optical emissions of elves produced by CIDs and EIPs indicates the existence of an elve “doublet”, as also recently reported by several authors (*Marshall et al.*, 2015; *Liu et al.*, 2017). These two double emission peaks are produced by the EMP shown in figure 3.7.

The computation of the concentration of each vibrational level in $N_2(B^3\Pi_g, v = 0, \dots, 6)$, $N_2(C^3\Pi_u, v = 0, \dots, 4)$ and $N_2(a^1\Pi_g, v = 0, \dots, 15)$ allows us to build the Vibrational Distribution Function (VDF) of these electronically excited species. Therefore, we can also derive synthetic emission spectra of halos and elves with vibrational resolution in the mentioned bands. We plot in figure 3.16, 3.17, 3.18 and 3.19 the calculated spectra of halos and elves corresponding to different spectral bands triggered by different types of lightning discharges. Furthermore, we plot in these figures the predicted observed spectra at different observer altitudes (3 km and 275 m) and at an horizontal distance of 350 km from the halo. The software MODTRAN 5 (*Berk et al.*, 2005) has been used to calculate the optical transmittance of the atmosphere needed to derive the predicted observed spectra. In the case of a spacecraft observing from its orbit, the recorded spectra would be similar to the emitted spectra at the source, given the low attenuation of light in the atmosphere at altitudes above 80 km of altitude.

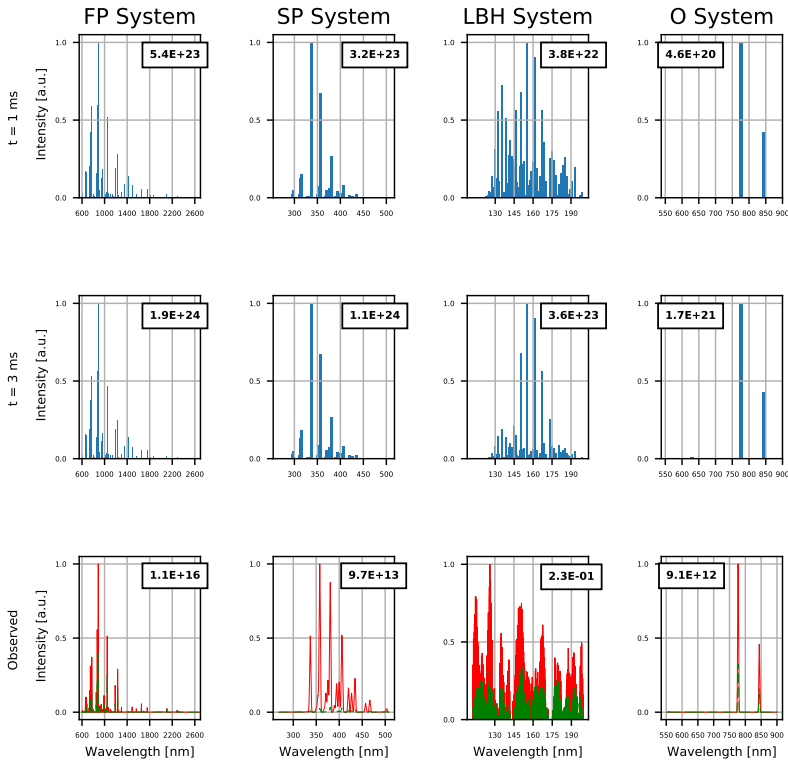


Figure 3.16: Calculated spectra of halos for different spectral bands. The first and the second rows show different moments of the emission spectra at the source, while the third row shows the predicted observed spectra at 3 km (red solid line) and 275 m (green dashed line) over the sea and at an horizontal distance of 350 km (between the halo and the observer). We plot the intensity of the bands in arbitrary units, normalizing each subplot to the stronger transition in each band. The numbers in the boxes correspond to photons per second in the case of emission spectra, and photons per second and squared meters in the case of the predicted observed spectra.

3. ELECTRICAL PHENOMENA IN THE ATMOSPHERE OF THE EARTH

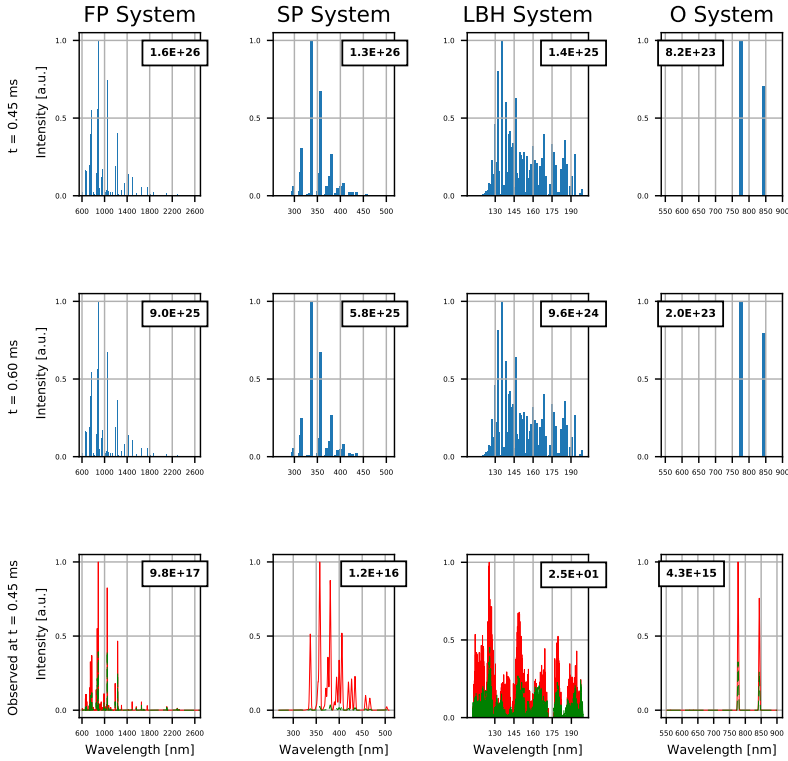


Figure 3.17: Calculated spectra of elves produced by a CG lightning discharge of 1000 C km (276 kA) for different bands. The first and the second rows show the emission spectra at the source, while the third row shows the predicted observed spectra at 3 km (red solid line) and 275 m (green dashed line) over the sea and at an horizontal distance of 350 km. We plot the intensity of the bands in arbitrary units, normalizing each subplot to the stronger transition in each band. The numbers in the boxes correspond to photons per second in the case of emission spectra, and photons per second and squared meters in the case of the predicted observed spectra.

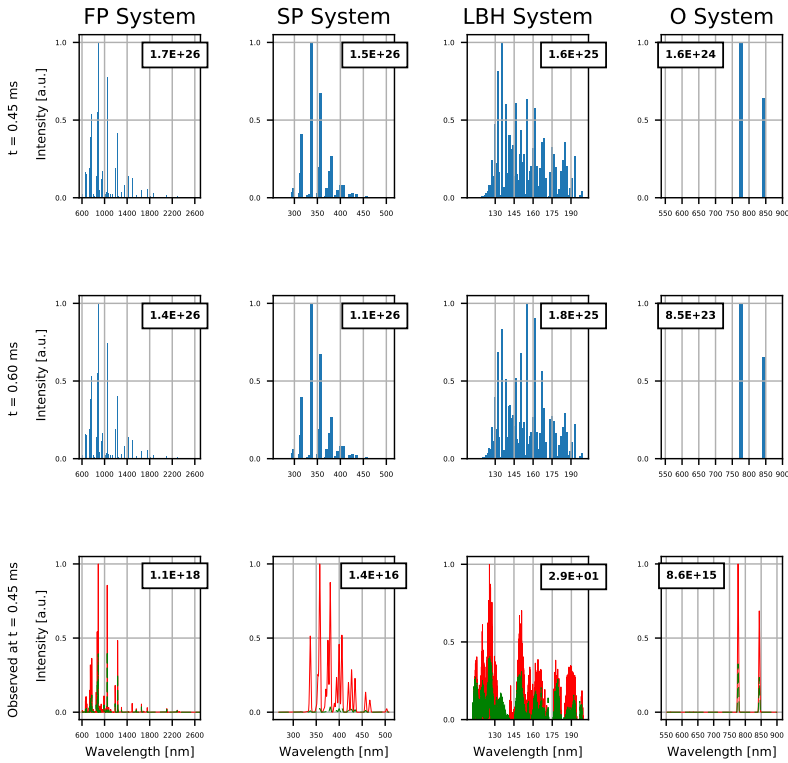


Figure 3.18: Calculated spectra of elves produced by a CID for different bands. The first and the second rows show the emission spectra at the source, while the third row shows the observed spectra at 275 m (red solid line) and 3 km (green dashed line) over the sea and at an horizontal distance of 350 km. We plot the intensity of the bands in arbitrary units, normalizing each subplot to the stronger transition in each band. The numbers in the boxes correspond to photons per second in the case of emission spectra, and photons per second and squared meters in the case of the predicted observed spectra.

3. ELECTRICAL PHENOMENA IN THE ATMOSPHERE OF THE EARTH

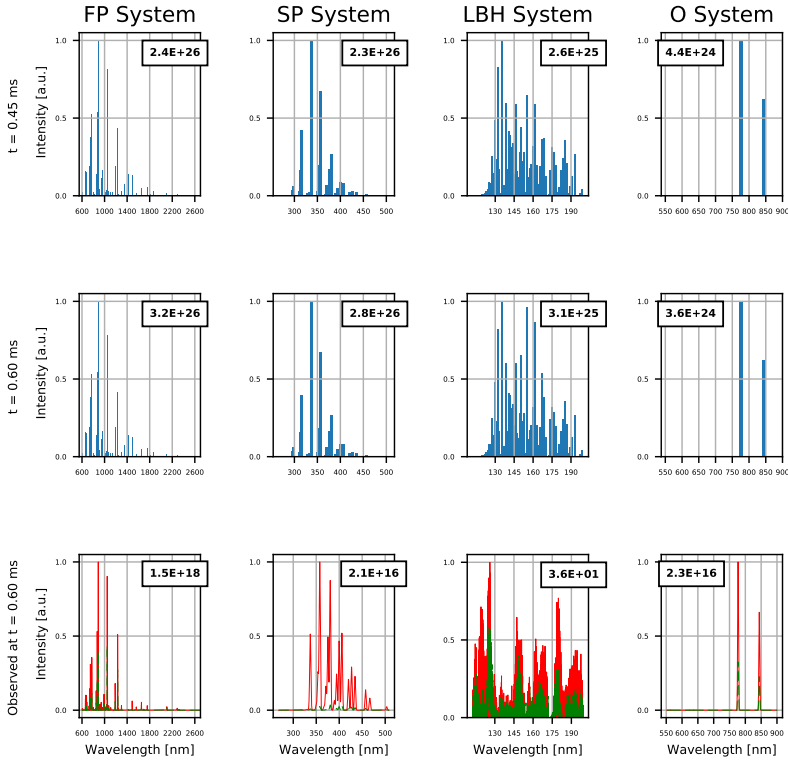


Figure 3.19: Calculated spectra of elves produced by an EIP for different bands. The first and the second rows show the emission spectra at the source, while the third row shows the observed spectra at 275 m (red solid line) and 3 km (green dashed line) over the sea and at an horizontal distance of 350 km. We plot the intensity of the bands in arbitrary units, normalizing each subplot to the stronger transition in each band. The numbers in the boxes correspond to photons per second in the case of emission spectra, and photons per second and squared meters in the case of the predicted observed spectra.

The predicted observed halo spectra plotted in figure 3.16 can be compared with the ones previously calculated by *Gordillo-Vázquez et al.* (2011, 2012). It can be seen how the first and second positive systems, as well as the LBH systems of the molecular nitrogen are in good agreement with halo

spectra shown in *Gordillo-Vázquez et al. (2011, 2012)*.

Finally, it is worth comparing the predicted observed spectra of the different simulated halos and elves. Finding some characteristic differences in these spectra could provide empirical methods to determine the type of discharge producing the observed TLEs. Some slight differences can be appreciated between the spectra of halos and each different type of lightning-driven elve (figures 3.16, 3.17, 3.18 and 3.19). However, these differences can be attributed to the influence of the reduced electric field in the ionosphere rather than to the type of discharge. This is shown in figure 3.20, where we plot in detail the observed spectral bands corresponding to the FP and the SP systems of N_2 of each TLE, i.e., the spectra of a halo, several CG lightning-driven elves, a CID-driven elve and an EIP-driven elve.

Observed halos are very noisy as a consequence of their low luminosity, as the one recorded shown in *Wescott et al. (2001)* and later on analyzed by *Gordillo-Vázquez et al. (2011)*. However, we can compare our results with the optical sprite spectrum observed by *Kanmae et al. (2007)*, also plotted in figure 3.20. The sprite region observed by *Kanmae et al. (2007)* was located at an altitude between 84 and 86 km, while the observation point was located in a mountain at an altitude of about 3 km and at an horizontal distance of 350 km from the TLE. It can be seen that the predicted spectra of the FP system of N_2 agrees with reported observations.

3. ELECTRICAL PHENOMENA IN THE ATMOSPHERE OF THE EARTH

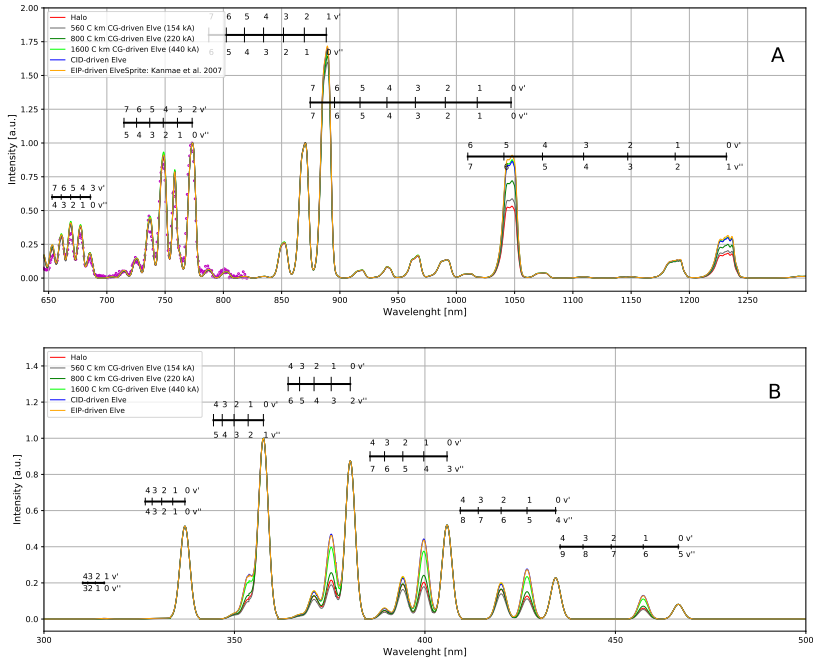


Figure 3.20: Calculated spectra of the (A) first positive system of N₂ and (B) second positive system N₂ for halos and elves produced by different atmospheric discharges as seen by an observer located at an altitude of 3 km and a horizontal distance of 350 km. The magenta circles correspond to the sprite spectrum observed by *Kanmae et al.* (2007). The observation of this sprite was performed from an altitude of 3.25 km and at horizontal distance of 350 km, and the observed region of the sprite was between 84 and 86 km of altitude. The normalization of the spectra of the FP and the SP systems of the N₂ spectra were done with respect to the (2,0) and the (0,1) transitions, respectively. We have selected the spectra at the moment of maximum emission of each TLE.

3.1.4.4 Quasielectrostatic field created by a halo

In this section, we present the influence of the simulated halos in the net quasielectrostatic field created by thunderstorms. These results were pre-

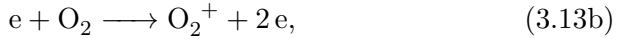
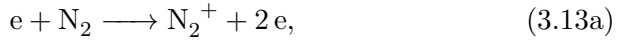
sented in *Pérez-Invernón et al.* (2016a).

The quasioleostatic field created by the charge accumulated in a thunderstorm decays with the third power of the distance to the source. However, *Bennett and Harrison* (2013) reported the detection of lightning-produced electrostatic fields at distances of up to about 300 km from a thunderstorm, suggesting a possible violation of the expected cubic decay law and causing a change in the field polarity. *Bennett* (2014) proposed the influence of the halo-triggered quasioleostatic field as the reason behind the observed violation of the cubic decay law he reported the year before. As we discussed in the previous section, halos can trigger the formation of a disk of charge in the lower boundary of the ionosphere. *Bennett* (2014) modeled this disk-shaped charge accumulation to explain the violation of the cubic decay law and the reverse in the polarity of the measured electrostatic field. We use our self-consistent electrodynamic model of halos (section 2.2) coupled with a simplify set of chemical reactions to investigate how the electric charge accumulates in the lower ionosphere. Our model also computes the influence of the halo in the total electrostatic field produced by the thunderstorm. We conclude that the charge accumulated by the halo is not responsible for the violation of neither the cubic decay law nor the polarity reversal reported by *Bennett and Harrison* (2013).

As in the previous section, we model a halo triggered by a CG lightning discharge with different CMCs and a channel longitude of 7 km. However, in this chemically simplified version of our model we only consider the following basic kinetic scheme:

As in the previous section, we model a halo triggered by a CG lightning discharge with different CMCs and a channel longitude of 7 km. However, in this chemically simplified model we only use the following chemical:

3. ELECTRICAL PHENOMENA IN THE ATMOSPHERE OF THE EARTH



whose rates depends on the reduced electric field, as pointed out in Appendix A.1. These reactions are the most important mechanisms underlying the creation of net charge by a halo.

We analyze the influence of halos in the total quasioleostatic field produced in thunderstorms in two different scenarios. On the one hand, we consider a weak CG lightning discharge with $Q_{\max} = 25 \text{ C}$ (and a CMC of 175 C km) where the ionosphere is mostly undisturbed. On the other hand, we set a stronger CG lightning discharge with $Q_{\max} = 80 \text{ C}$ (and a CMC of 560 C km).

Let us now analyze the quasioleostatic field computed by the model and its comparison with the analytical field produced by the accumulation of charge in the clouds. We calculate this analytical field approximating the charge as a point and both the ground and the ionosphere as two perfect electrical conductors. We assume that both of them are at the same potential, although the voltage difference between ground and ionosphere is about 250 kV (*Rycroft et al.*, 2000). This approximation is mainly justified by the roughly exponential increase of the conductivity in the atmosphere for increasing altitude. This exponential profile causes the potential drop to be almost completely concentrated at low altitude so changes around the ionosphere have a negligible effect on the electric field caused by this potential bias. In addition, in the observations by *Bennett* (2014) the DC bias was filtered out by a 1 Hz high-pass filter. Under these assumptions, the electric field can be calculated by summing an infinite series of image charges. We illustrate the configuration of charges in figure 3.21.

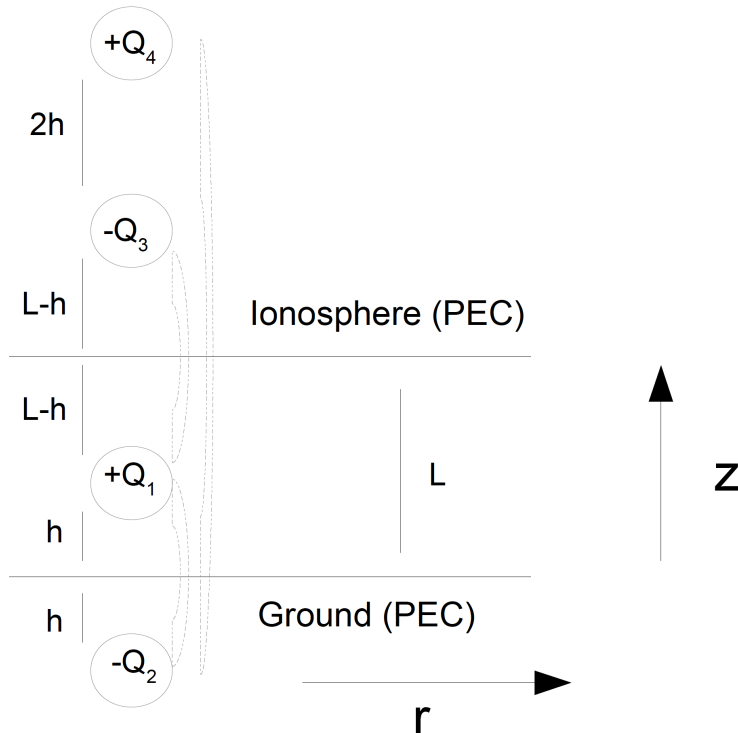


Figure 3.21: Sequence of mirror charges as a consequence of a charge located between two perfect conductors of electricity. Charge $+Q_1$ corresponds to the electrical charge accumulated by a lightning stroke on clouds at altitude h . Both $-Q_2$ and $-Q_3$ are the mirror charges of $+Q_1$ with respect to the ground and the ionosphere, respectively. The charge $+Q_4$ corresponds to the mirror charge of $-Q_3$ with respect to the ionosphere. This sequence of mirror charges respect to ground and ionosphere layers can be extended to an infinite number of charges.

For the vertical component of the electric field at ground level ($z=0$) at an horizontal distance r from the thundercloud we find

$$E_z(r) = -\frac{Q}{2\pi\epsilon_0} \sum_{n=-\infty}^{\infty} \frac{h + 2nL}{[(h + 2nL)^2 + r^2]^{3/2}}, \quad (3.14)$$

where ϵ_0 is the vacuum permittivity, Q is the total charge in the thundercloud, located at an altitude h above ground, and L is the ground-ionosphere

3. ELECTRICAL PHENOMENA IN THE ATMOSPHERE OF THE EARTH

separation. This separation can be set to 90 km in the absence of a halo. However, when a halo lowers down the ionosphere accumulating charge below it, the L parameter is reduced down to 70 km.

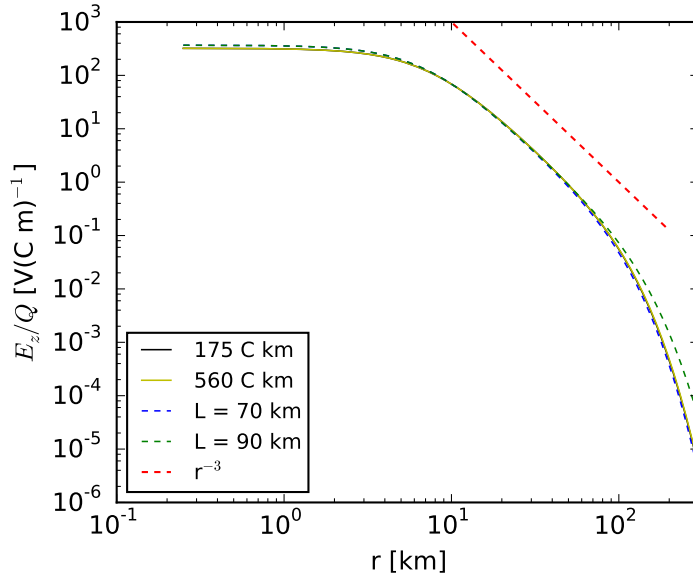


Figure 3.22: Vertical component of the electric field at ground level divided by its causative charge Q . We show two evaluations of equation (3.14) (dashed lines) where the ionosphere is represented by a planar, perfect conductor placed at $L = 90$ km and $L = 70$ km as well as the outcome of two simulations (coincident solid lines). For the simulations, we plot the electric field 10 ms after the start of the discharge. We also provide an arbitrarily placed reference line to illustrate the slope of a r^{-3} decay (*Pérez-Invernón et al.*, 2016a).

In figure 3.22 we compare the numerically simulated electric field at ground level divided by the total charge lowered to the ground together with two analytical approximations given by equation (3.14). We see that the curve is close to that predicted by the analytical expression for $L = 70$ km. The collapse of the two simulation profiles in figure 3.22 indicates that to a good approximation, our results are linear with the driving charge Q_{\max} . However, there are some factors that break this linearity:

1. The dependence of the electron mobility with the electric field. Since electrons are more mobile for low fields ($\mu \propto \frac{1}{E/N}$), the dielectric relaxation of the ionosphere is somewhat faster if the perturbing field is weaker. As we argued above, the relaxation of the ionosphere reduces the ground electric field, so we expect this factor to reduce the E/Q_{\max} ratio for weak discharges (175 C km).

2. Changes in the electron density due to the chemical scheme (3.13). A higher electron density accelerates screening and lowers the ionosphere's edge, whereas a lower electron density slows down the screening. Referring again to our previous statements, this implies that a stronger ionization decreases E/Q_{\max} whereas attachment increases it.

In the upper panels of figure 3.23 we represent the space charge density induced in the lower ionosphere by each of the two discharges. The weak discharge (175 C km) produces a layer of negative charge around 75 km of altitude, which marks the effective altitude of the ionosphere for this case. However, the strong discharge 560 C km creates a bulge in the ionosphere that descends to about 70 km within 30 km from the axis containing the parent discharge. We calculate the accumulated charge in the lower ionosphere by integrating the space charge. We obtain $Q_i = -2.56 C$ and $Q_i = -8.15 C$ for the weak and the strong discharges, respectively.

In the lower panel of figure 3.23 we compare the ratios E/Q_{\max} from our modeled discharges for a range of distances and times. Initially ($t \leq 6$ ms), the effect of the field-dependent mobility dominates and the field is relatively smaller for the weak discharge. However as ionization lowers down the edge of the ionosphere ($t \geq 8$ ms) we see that for relatively short distances ($r \leq 40$ km) the field becomes relatively weaker for the strong discharge. Far from the discharge the electric fields in the ionosphere are not strong enough for promoting ionization so the effects of attachment and field-dependent mobility dominate, so E/Q_{\max} is higher for the strong discharge.

3. ELECTRICAL PHENOMENA IN THE ATMOSPHERE OF THE EARTH

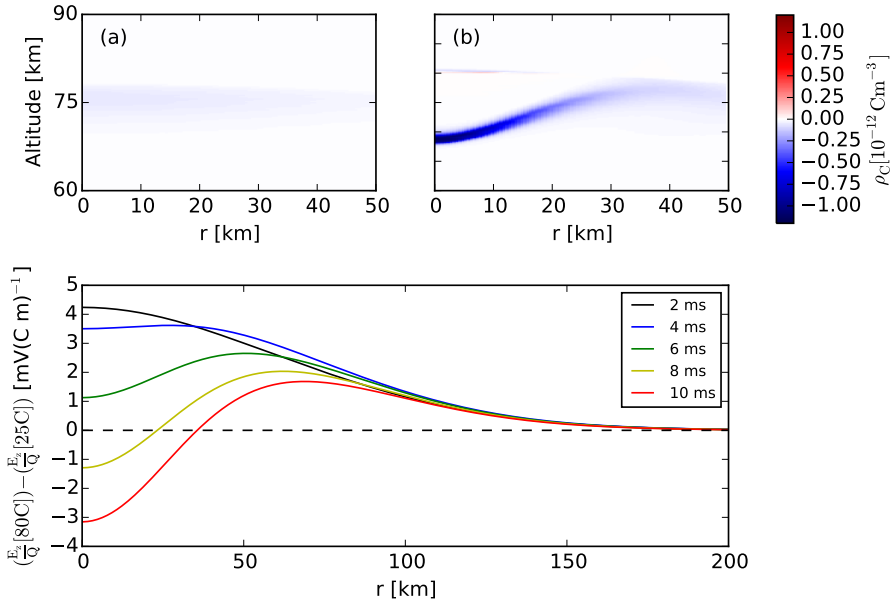


Figure 3.23: In the upper panels we can see the space charge density induced in the lower ionosphere by the thundercloud charge Q_{\max} produced by (a) a weak discharge of $hQ_{\max} = 175 \text{ C km}$ and (b) a strong discharge of $hQ_{\max} = 560 \text{ C km}$ causing a halo. The corresponding total accumulated charge in the lower ionosphere calculated by spatial integration after 10 ms is (a) $Q_i = -2.56 \text{ C}$ and (b) $Q_i = -8.15 \text{ C}$. In the lower panel we plot the difference between E/Q_{\max} at ground level for two different discharges for different times. We can see the influence of the halo in the first kilometers causing a sign change in the difference (*Pérez-Invernón et al.*, 2016a).

Note however that these nonlinear effects are extremely small, amounting to less than 3% of the total field. This effect is therefore probably undetectable. We therefore believe that some other explanation is needed for the observations reported by *Bennett and Harrison* (2013).

3.2 Very Low Frequency wave propagation through the Earth-ionosphere waveguide

3.2.1 Introduction

Lightning discharges radiate electromagnetic pulses in almost the complete spectrum of frequencies. As introduced in section 1.1, part of the lower frequency lightning-emitted radiation waves travel through the spherical cavity formed by the Earth ground and the ionosphere (*Helliwell, 1965*). This interaction between the radiated pulses and the propagation media enables the detection of Extremely Low Frequency (ELF), Very Low Frequency (VLF) and Low Frequency (LF) pulses at large distances from the source, providing useful information about the electrical phenomena that trigger the pulses. Most of the Lightning Location Systems (LLS) take measurements of global lightning-emitted pulses in the range of the lower frequencies (*Nag et al., 2015*).

The ionosphere is not a perfect conductor, since the electron and ion density gradient existing in the lower border of the ionosphere increases the atmospheric conductivity progressively. This conductivity gradient causes wave distortions in the pulses across their way from the source to the detection system. In addition, the superposition of the reflected waves causes both transverse and longitudinal resonances, altering the original signal (*Nickolaenko and Hayakawa, 2002*). The frequency dependence of the wave amplitude and phase distortion is known as the transfer function of the curved Earth-ionosphere waveguide. The knowledge of this distortion pattern is essential to recover the original form of the emitted signal.

In this section, we calculate the transfer function of the curved Earth-ionosphere waveguide (EIWG) using the Stanford Full Wave Method (FWM) for stratified media of *Lehtinen and Inan (2008)*. This model does not simulate wave propagation through the entire planet. Therefore, the effect of the longitudinal Schumann resonances in the propagating wave is not described. We restrict our calculations to frequencies higher than 500 Hz. At

3. ELECTRICAL PHENOMENA IN THE ATMOSPHERE OF THE EARTH

such high frequencies, we avoid dealing with longitudinal resonances caused by the spherical cavity.

The Matlab implemented FWM model, described in *Lehtinen and Inan* (2008), *Lehtinen and Inan* (2009) and *Lehtinen et al.* (2010), solves the Maxwell equations and calculates all the electromagnetic field components in the frequency domain for a wave generated in and propagating through a stratified medium in the presence of a background magnetic field. The method departs from the knowledge of the electromagnetic field value in a plane. The electromagnetic field components are then separated into perpendicular and parallel parts with respect to that plane in order to apply the Clemmow and Heading (CH) equation (*Clemmow and Heading*, 1954). This equation is used to derive the evolution of the electromagnetic field in the vertical direction. As the propagation media is stratified, the FWM uses the Booker equation for the vertical component of the refractive index in each layer (*Budden*, 1985). We refer to *Lehtinen and Inan* (2008, 2009); *Lehtinen et al.* (2010) for more details about the method, such as the boundary conditions, the implementation of the source current or the description of the method in different systems of coordinates. The simulations using the FWM are carried out in a CSIC computer cluster in Madrid called “Trueno”.

3.2.2 Transfer function of the Earth-ionosphere waveguide

The aim of this section is to calculate the EIWG transfer function for waves with frequencies between 500 Hz and 20 kHz using the previously described FWM (*Lehtinen and Inan*, 2008). This transfer function can be used to analyze electrical events radiating VLF pulses located up to 4000 km away from the detection point in any given direction. In the following calculations, the source is assumed to be a vertical dipole with a current moment of 1 A·m located at 13 km of altitude. We calculate the EIWG transfer function for an observer located at ground level.

As previously mentioned, the propagation of VLF waves through the EIWG is highly influenced by the lower ionosphere. The electron and ion density profiles in the ionosphere are one of the main factors that influence this propagation. The ionospheric profile depends on the location of the electrical event under analysis, as well as on the time and season when it occurred. We will calculate the transfer function for pulses traveling under extreme ionospheric conditions, i.e., summer night, summer day, winter day and winter night. The EIWG transfer function under other conditions can be interpolated using these four extreme cases. The ionospheric electron and ion density profiles have been obtained from the International Reference Ionosphere (*Bilitza and Reinisch, 2008*).

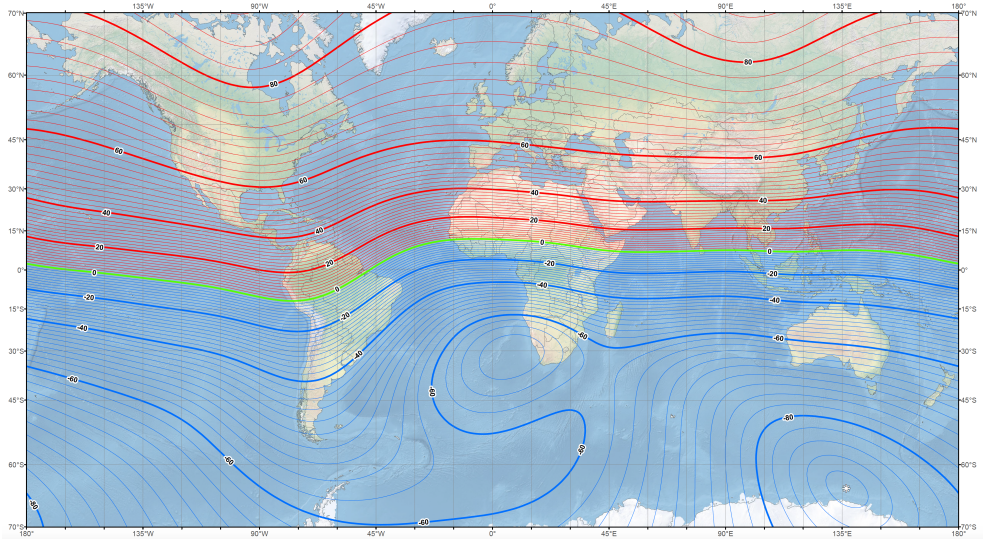


Figure 3.24: Inclination of the geomagnetic field in degrees in 2015. This map has been developed by NOAA/NGDC and CIRES.

Other important factor that influences the propagation of electromagnetic pulses is the geomagnetic field inclination. The current version of the FWM does not allow us to calculate electromagnetic wave propagation with a tilted geomagnetic field and at the same time considering the curvature of the Earth. However, it is capable to include the Earth's curvature ef-

3. ELECTRICAL PHENOMENA IN THE ATMOSPHERE OF THE EARTH

fect together with a vertically oriented geomagnetic field. We propose the following method to calculate the EIWG transfer function from a given location taking into account the effect of the Earth's curvature and a tilted geomagnetic field without the need of upgrading the FWM:

The procedure, schematized in figure 3.25, is formed by the following steps:

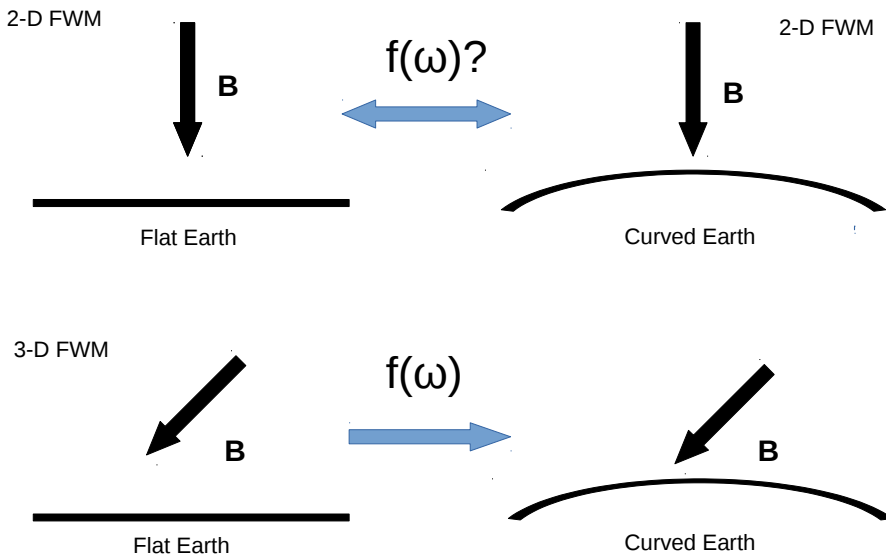


Figure 3.25: Schematic procedure to obtain the EIWG transfer function of a curved Earth with a tilted geomagnetic field using the FWM.

1. Calculation of the EIWG transfer function with a vertically oriented geomagnetic field taking into account the curvature of the Earth. For this, we use the 2-D FWM version.
2. Calculation of the EIWG transfer function with a vertically oriented geomagnetic field for a flat Earth. Again, we use for this the 2-D

FWM version.

3. Derivation of an approximated frequency dependent transform $f(\omega)$ to turn the EIWG transfer function of the flat case into the case with curvature. We describe this procedure below.
4. Calculation of the EIWG transfer function for the flat case with a tilted geomagnetic field using the 3-D FWM version. The inclination of the geomagnetic field is determined by the mean value between the event and the detection point. Most of the electrical phenomena in the atmosphere of the Earth take place in latitudes between 60°N and 60°S . In these calculations, we assume that the magnetic field has an inclination of 45° . This value is chosen as a representative inclination of the geomagnetic field in the mid latitude regions (See figure 3.24). The International Geomagnetic Reference Field (*Thébault et al., 2015*) can be used to obtain the geomagnetic field through the propagation path.
5. Application of the approximated transform deduced in step 3 to the EIWG transfer function obtained in step 4 for a flat Earth with tilted geomagnetic field to derive the final EIWG transfer function under the effect of a realistic geomagnetic field.

3. ELECTRICAL PHENOMENA IN THE ATMOSPHERE OF THE EARTH

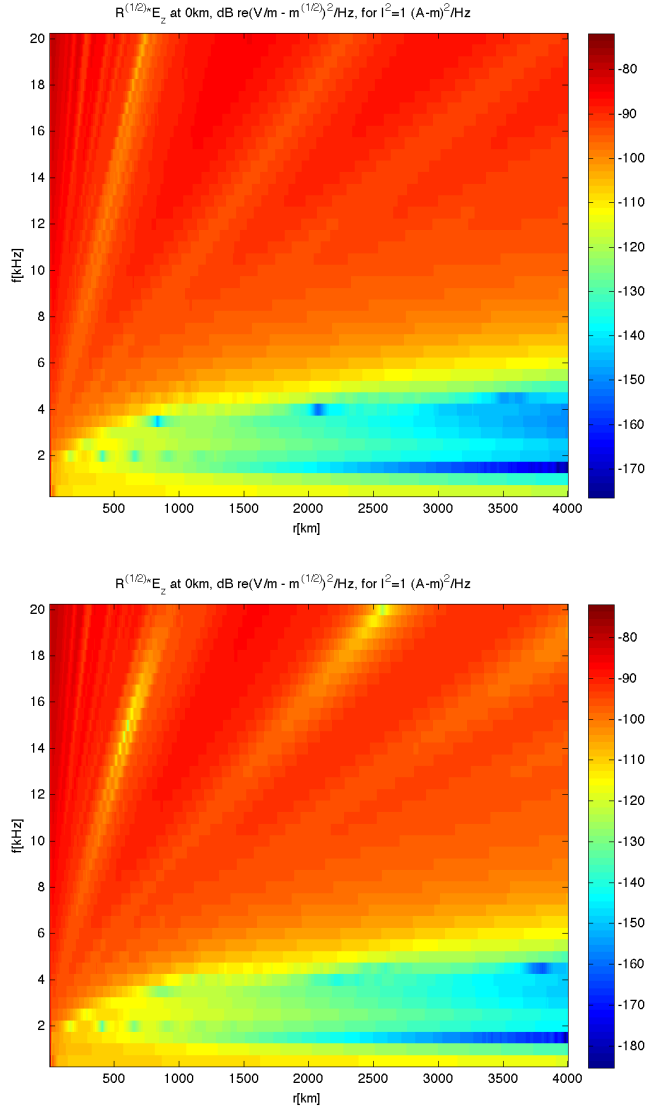


Figure 3.26: EIWG transfer functions at ground level in decibels for a flat Earth (upper panel) and a curved Earth (lower panel). The horizontal axis corresponds to the distance between the radiating source and the point of detection. The values of the EIWG transfer functions are calculated for frequencies between 500 Hz and 20 kHz with a frequency step of 500 Hz. Both calculations have been performed using the 2-D FWM version under summer day conditions and in the presence of a vertically oriented geomagnetic field.

Let us now describe the deduction of the approximated equation that transform the EIWG transfer function for a flat Earth into one for a curved Earth. We show in figures 3.26 the EIWG transfer functions giving the signal decay in decibels of curved and flat cases under the same ionospheric conditions (summer day). Decibels are calculated as 20 multiplied by the logarithm of the product between the square of the distance and the signal.

The main effects of considering the Earth's curvature in the propagated wave are a phase shift in the r direction and a change in the amplitude of the peaks. We compare the two cases and propose an equation to transform the flat case into the case with curvature based on the shift and on the change in the peaks amplitudes. This function will depend on the distance and will be different for each frequency. We plot in the upper row figure 3.27 the decay of a signal of 16 kHz for both the flat and the curved Earth. In addition, we plot in the lower row figure 3.27 the position of the signal peaks for the flat and the curved case together with their differences in the amplitude.

3. ELECTRICAL PHENOMENA IN THE ATMOSPHERE OF THE EARTH

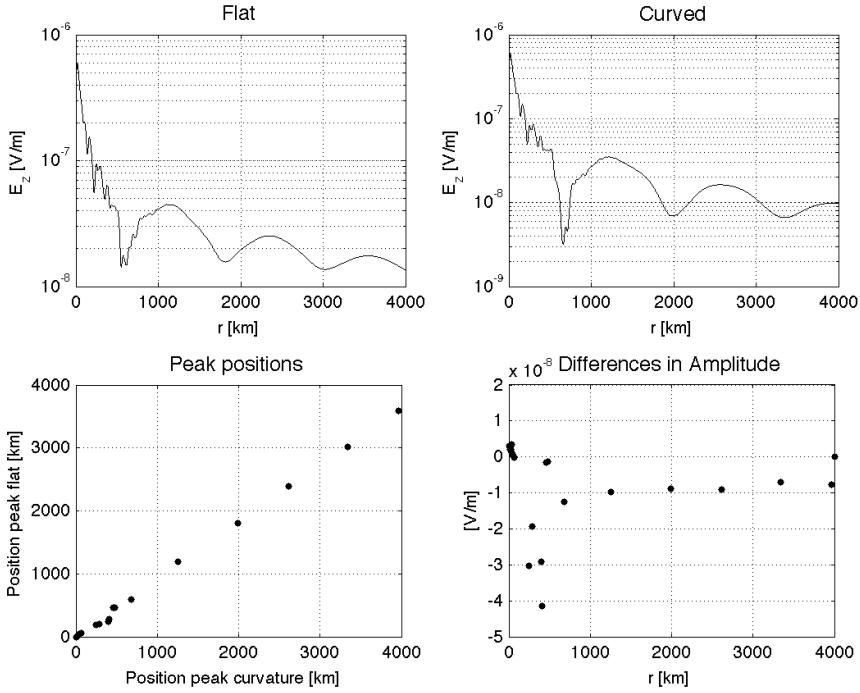


Figure 3.27: Panels in the upper row show the decay of a signal with 16 kHz over the distance for a flat and a curved Earth, respectively. The background magnetic field vertical to the ground in both cases. The left panel in the lower row shows the positions of each signal peak for the flat and the curved case after establishing a one-to-one correlation. The differences in amplitude of each peak pair over the peak position is plotted in the right panel of the lower row.

Given the spatial decay of a signal $S_{flat}(r)$ calculated with the FWM at a given frequency in a flat Earth, the corresponding decay of the signal in the case with curvature $S_{curved}(r)$ will have a shift in the direction r and a change in amplitude, as seen in figure 3.27. We write the signal decay in the curved case in terms of the decay of the signal in the flat case as

$$S_{curved}(r) = C(r) \cdot S_{flat}(r + \Delta(r)), \quad (3.15)$$

where $\Delta(r)$ corresponds to a shift of the signal in the curved case with respect to the signal in the flat case. This shift depends on the distance,

i.e., the differences between the wave phase at a given distance from the source of the signals corresponding to the flat and the curved cases is not the same for all the distances. The term $C(r)$ takes into account the change in amplitudes, that also depends on the distance from the source. As we describe in the next paragraphs, we obtain an approximation to $\Delta(r)$ and $C(r)$ by analyzing the position and the amplitude of the peaks, respectively.

The shift $\Delta(r)$ is applied to the signal of the flat case in order to change its phase, finally coinciding with the phase of the signal of the curved case. As we mentioned, we focus on the position of the peaks of both signals (flat and curved) in order to obtain the phase shift. We denote the position of the peaks in the curved and flat signals as r_c and r_f , respectively. We obtain the form of the shift $\Delta(r)$ comparing the position of the peaks of two signals calculated for a flat and a curved Earth with a vertically oriented geomagnetic field and under the same ionospheric conditions. We collect the data of the peak positions and fit them to a polynomial of grade two:

$$r_c = a \cdot r_f. \quad (3.16)$$

The adjust coefficient a is different for each frequency, as the position of the peaks is frequency-dependent. The function that describes the change in wave phase between the signals of the curved and flat cases is then given by

$$\Delta(r) = r - a \cdot r. \quad (3.17)$$

The function that describes the change in peak amplitudes $C(r)$ is calculated from the ratio between the amplitudes A_f^i and A_c^i of the flat and the curved cases, defined as

$$C^i = \frac{A_{curved}^i}{A_{flat}^i}. \quad (3.18)$$

3. ELECTRICAL PHENOMENA IN THE ATMOSPHERE OF THE EARTH

We obtain the value of the ratio C^i for each pair of peaks and fit them to obtain the r dependence of the factor C :

$$C(r) = \alpha \cdot \exp\left(-\frac{r}{r_0}\right) + \beta \quad (3.19)$$

where α , β and r_0 are different for each frequency. The factor r_0 corresponds to the approximate distance where the signal decay dependence with the distance changes from the form r^{-1} to $r^{-1/2}$. We can then write the final form of the signal of the curved case in terms of the signal of the flat case as

$$S_{curved}(r) = \left(\alpha \cdot \exp\left(-\frac{r}{r_0}\right) + \beta\right) \cdot S_{flat}(r + (r - a \cdot r)). \quad (3.20)$$

The values of the obtained fitting coefficients for different frequencies of the signals are shown in table 3.1.

3.2 Very Low Frequency wave propagation through the Earth-ionosphere waveguide

Frequency [kHz]	\mathbf{a}	α	β	r_0
0.5	1	-0.0055	1.0108	18500
1	1.0046	-0.0127	1.0177	37000
1.5	0.9641	0.2511	0.7986	55500
2	0.9564	-0.1210	1.1021	74000
2.5	1.0150	-0.0938	1.0885	92500
3	0.9496	0.0072	0.9999	111000
3.5	0.9316	0.0438	0.9670	129500
4	0.9738	-0.1717	1.1732	148000
4.5	0.8845	-0.3923	1.3055	166500
5	1.0485	-0.1014	1.0797	185000
5.5	0.9942	0.1015	0.9149	203500
6	0.9923	0.0647	0.9422	222000
6.5	0.9841	0.0724	0.9332	240500
7	0.9843	0.0815	0.9232	259000
7.5	0.9797	0.0963	0.9078	277500
8	1.0002	0.0965	0.9079	296000
8.5	0.9792	0.1207	0.8911	314500
9	0.9498	0.1514	0.8546	333000
9.5	0.9790	0.1797	0.8284	351500
10	0.6307	0.0495	0.9366	370000
10.5	0.9627	0.2427	0.7656	388500
11	0.9581	0.2679	0.7413	407000
11.5	0.9440	0.2951	0.7244	425500
12	0.9451	0.3269	0.6963	444000
12.5	0.9388	0.3303	0.6785	462500
13	0.9488	0.3530	0.6650	481000
13.5	0.9420	0.3783	0.6362	499500
14	0.9395	0.4057	0.6123	518000
14.5	0.9310	0.4278	0.5866	536500
15	0.9367	0.4786	0.5458	555000
15.5	0.8833	0.4499	0.5066	573500
16	0.8989	0.4590	0.5172	592000
16.5	0.9480	0.5578	0.4773	610500
17	0.9369	0.5676	0.4967	629000
17.5	0.9529	0.5955	0.5184	647500
18	0.9349	0.6306	0.4465	666000
18.5	0.9270	0.6473	0.4239	684500
19	0.9426	0.6370	0.4702	703000
19.5	0.9345	0.6187	0.4820	721500
20	0.9555	0.5977	0.4549	740000

Table 3.1: Coefficients of the transform equation (3.20). This equation transforms the EIWG transfer function for a flat Earth to the case with curvature.

3. ELECTRICAL PHENOMENA IN THE ATMOSPHERE OF THE EARTH

The method can be checked comparing the FWM-calculated signal in a case with curvature and vertically oriented geomagnetic field with the transformed signal of a previously calculated flat case. Figure 3.28 shows an example of the application of this procedure to a signal calculated in a flat Earth with a frequency of 16 kHz and a vertically oriented geomagnetic field to obtain the corrected signal ,that includes the effect of the curvature. We also plot in this figure the FWM-calculated signal in a Earth with curvature and a vertical geomagnetic field. It can be seen that the tendency of the corrected field agrees with the field calculated in the case with curvature.

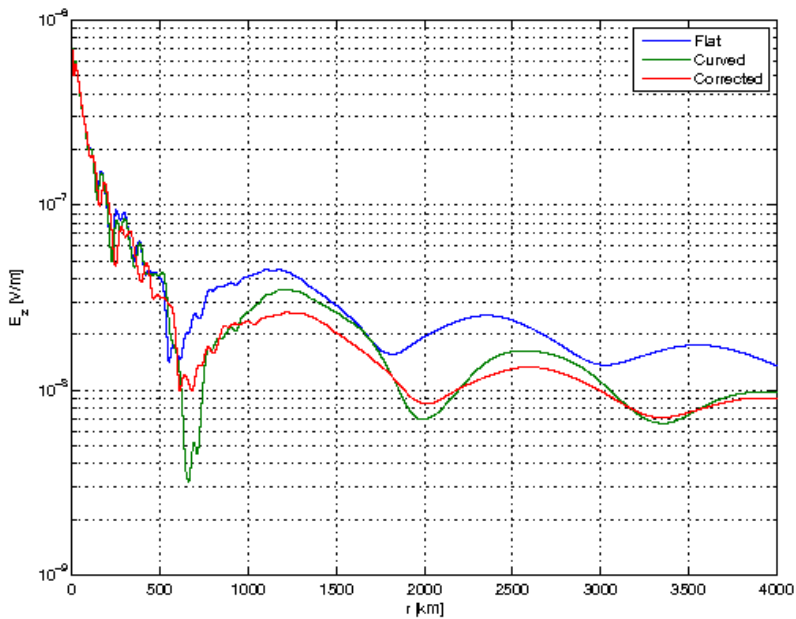


Figure 3.28: Electric field at ground level for the flat case (blue), curved case (green) and corrected case (red), for a frequency of 16 kHz and with a vertical geomagnetic field. Both the blue and the green signals are calculated with the 2-D FWM version, while the red signal is obtained after applying the described transform method to the blue signal. The electric field is expressed in Vm^{-1} units and is produced by a dipole current of 1 A·m

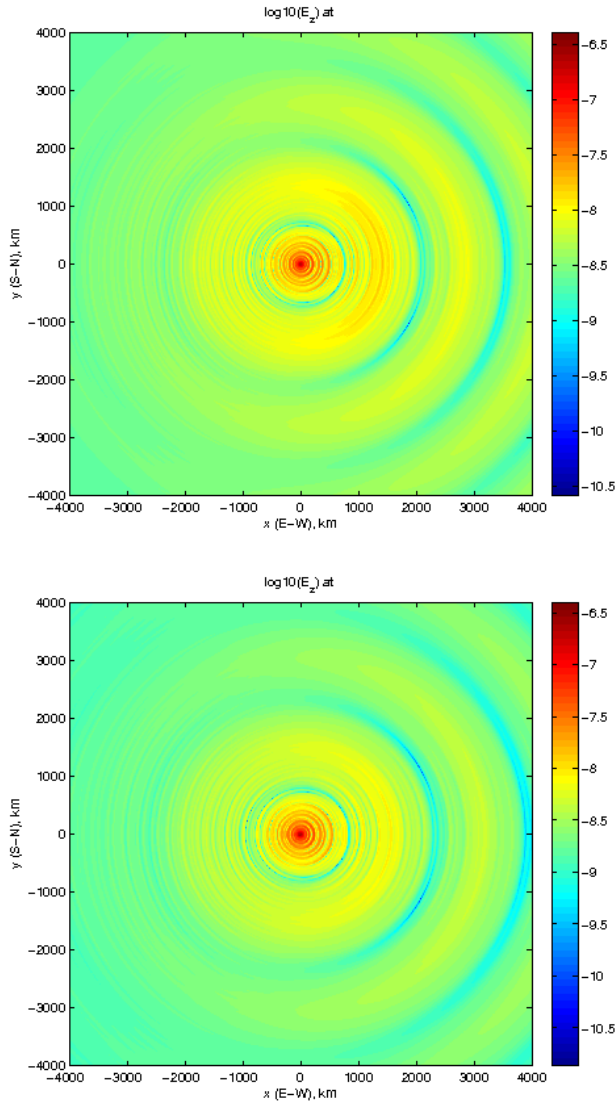


Figure 3.29: Electric field at ground level for a propagating wave with a frequency of 16 kHz in the flat case calculated with the 3-D FWM (upper panel) and in the case with curvature after applying the transform method (lower panel). The electric field is expressed in Vm^{-1} units and is produced by a dipole current of 1 A·m located at 13 km of altitude and in the center of the x-y coordinate system shown.

3. ELECTRICAL PHENOMENA IN THE ATMOSPHERE OF THE EARTH

Finally, we plot in figure 3.29 the electric field at ground level for a flat Earth with a tilted magnetic field with a frequency of 16 kHz and its transform to the case with curvature. The obtained transfer function have been used in by *Mezentsev et al.* (2018) to investigate the pulses radiated from regions where Terrestrial Gamma-ray Flashes (TGFs) are produced.

Chapter 4

Analysis of optical signals emitted by TLEs

4.1 Introduction

Transient Luminous Events (TLEs) emit optical signals in a wide range of frequencies. These signals contain valuable information about the physical processes behind the inception and evolution of the emitting TLEs. The development of methods to analyze the optical signals is necessary to extract physical information.

Halos, elves and sprites can be detected from ground, planes, balloons, or from space-based instruments. The observation from ground is useful to determine some of their features, such as the complexity of the sprites. However, the atmosphere can alter or absorb the emitted optical signals, especially the part of the spectrum corresponding to the Lyman-Birge-Hopfield (LBH) band of the N_2 .

As these TLEs are produced in the upper atmosphere where the air density is low, the emitted light can travel from the source to space-based detectors without suffering significant absorption. This is one of the main reasons that motivated the launch of some missions to investigate the optical emissions produced by TLEs from space.

Since the first observation of an elve from spacecraft was accomplished by the Space Shuttle (*Boeck et al.*, 1992), other missions such as ISUAL

(NSPO) (*Chern et al.*, 2003) and GLIMS (JAXA) (*Sato et al.*, 2015; *Adachi et al.*, 2016) have reported TLE observations from space. The results provided by these missions have contributed substantially to the characterization and estimation of the global occurrence rates of different types of TLEs.

However, there are still several open questions about the inception and evolution of these events. For instance, their relation with the parent lightning or with other lightning induced events such as the Terrestrial Gamma-ray Flashes (TGFs). Future space missions as the “Atmosphere-Space Interactions Monitor” (ASIM) (ESA) (*Neubert et al.*, 2006) and the “Tool for the Analysis of RAdiations from lightNings and Sprites” (TARANIS) (CNES) (*Blanc et al.*, 2007) will probably shed light on these questions. These missions will record optical signals emitted by thunderstorms during the next years (2018-2022). As we will detail in this chapter, ASIM and TARANIS will be equipped with several photometers and cameras that will be able to collect photons emitted by TLEs. The analysis of the signals detected by these instruments will require specific algorithms.

In this chapter, we present some methods developed to derive the reduced electric field inside a TLE from the knowledge of its emitted optical signals. As a first validation of these methods, we apply them to the predicted (synthetic) optical signatures of halos and elves obtained in chapter 3 from models. This procedure allows us to compare the inferred value of the reduced electric field with the value computed by the halo and elve models. Afterward, we test the developed methods with several optical signatures of elves reported by the ISUAL and GLIMS spacecraft.

4.2 Methods for the analysis of light emissions from TLEs

4.2.1 Deduction of the reduced electric field

Some authors have used the recorded intensity ratios of some spectral bands to estimate the electric field that produces molecular excitation in air discharges (*Paris et al.*, 2005; *Celestin and Pasko*, 2010; *Bonaventura et al.*,

2011; Holder *et al.*, 2016). These works were based on the analysis of the optical emissions from the first negative system and second positive system of molecular nitrogen.

The aim of this section is to develop an optical diagnostic method to extract the reduced electric field from the observation of light emitted by TLEs in the lower ionosphere. We explore the possibility of using this procedure to analyze the recorded optical emissions from TLEs to be recorded by future spacecraft such as ASIM or TARANIS.

Let us define $I(t)$ as the temporal evolution of an observed intensity at a particular wavelength or interval of wavelengths. The density of the emitting species, $N_s(t)$, can be estimated from the decay constant A' of the transitions that produce photons in the considered wavelength as

$$N_s(t) = \frac{I(t)}{A'}. \quad (4.1)$$

Using the continuity equation of the emitting species, the temporal production rate $S(t)$ of the considered species can be obtained as

$$S(t) = \frac{dN_s(t)}{dt} + A \times N_s(t) + Q \times N_s(t) \times N - C \times N'(t) + O(t), \quad (4.2)$$

where A is the total radiative decay constant in s^{-1} , Q represent to all the quenching rate constants by air molecules of the considered species in $cm^{-3}s^{-1}$ and N is the density of air in cm^{-3} . $N'(t)$, in cm^{-3} , accounts for the density of all the species that populates the species $N_s(t)$ by radiative cascade with rate constants C , in s^{-1} . Finally, the term $O(t)$ in $cm^{-3}s^{-1}$ includes the rest of loss processes, such as intersystem processes or vibrational redistribution, that is usually negligible compared to quenching.

We use equations (4.1) and (4.2) to obtain the ratios of production of two different species 1 and 2 at a fixed time t_i as $\frac{S_1(t_i)}{S_2(t_i)}$ in a first approach. We use this quantity and the theoretical electric field dependent ratio of productions of species 1 and 2 by electron impact, given by $\frac{\nu_1(E/N)}{\nu_2(E/N)}$, to estimate the reduced electric field that satisfies the equation

$$\frac{S_1(t_i)}{S_2(t_i)} \simeq \frac{\nu_1(E/N)}{\nu_2(E/N)}. \quad (4.3)$$

4. ANALYSIS OF OPTICAL SIGNALS EMITTED BY TLES

The values of $\nu_i(E/N)$ for all the considered species are calculated using BOLSIG+ for air (*Hagelaar and Pitchford, 2005*).

This approximation assumes an electric field homogeneously distributed in space. However, halo and elve emissions are produced by an inhomogeneous electric field that varies in the scale of kilometers. We propose a method to improve this first approach and account for the spatial distribution of the electric field.

We define the function $H\left(\frac{E'}{N}\right)$ as the number of electrons under the influence of a reduced electric field larger than E/N and weighted by the air density N

$$H\left(\frac{E'}{N}\right) = \int d\vec{r} N(\vec{r}) n_e(\vec{r}) \Theta\left(\frac{E}{N}(\vec{r}) - \frac{E'}{N}\right), \quad (4.4)$$

where $n_e(\vec{r})$ and $\frac{E}{N}(\vec{r})$ are, respectively, the electron density and the reduced electric field spatial distributions. The symbol Θ corresponds to the step function, being 1 if $E/N > E'/N$ or 0 in any other case. The function defined by equation 4.4 is monotonic and decreasing. In addition, we know that $N\left(\frac{E_{max}}{N}\right) = 0$ by definition. Therefore, we can assume that this function can be approximated by a linear equation as

$$H\left(\frac{E'}{N}\right) \simeq \alpha \left(\frac{E_{max}}{N}(\vec{r}) - \frac{E'}{N}\right). \quad (4.5)$$

The total excitation of species i by electron impact can be written as

$$\nu_i = \int_0^{\frac{E_{max}}{N}} d\left(\frac{E'}{N}\right) \left| \frac{dH}{d\left(\frac{E'}{N}\right)} \right| k_i\left(\frac{E'}{N}\right), \quad (4.6)$$

where $k_i\left(\frac{E'}{N}\right)$ is the coefficient of excitation by electron impact of species i , again calculated using BOLSIG+ (*Hagelaar and Pitchford, 2005*).

From the derivative of equation (4.5), equation (4.6) can be expressed as

$$\nu_i = \alpha \int_0^{\frac{E_{max}}{N}} d\left(\frac{E'}{N}\right) k_i\left(\frac{E'}{N}\right), \quad (4.7)$$

and the ratio of production of two species by electron impact $\frac{S_1(E/N)}{S_2(E/N)}$ can be finally written as

$$\frac{S_1(E/N)}{S_2(E/N)} \simeq \frac{\int_0^{\frac{E_{max}}{N}} d\left(\frac{E'}{N}\right) k_1\left(\frac{E'}{N}\right)}{\int_0^{\frac{E_{max}}{N}} d\left(\frac{E'}{N}\right) k_2\left(\frac{E'}{N}\right)}. \quad (4.8)$$

Equation (4.2) allows us to calculate species production by electron impact from observed intensities, while equation (4.8) gives the theoretical reduced electric field dependence of these productions. We can then use these two equations to estimate the maximum reduced electric field underlying halo and elve optical emissions.

4.2.2 Treatment of the signal emitted by an elve

As we discussed in chapter 3, elves are fast ring-shaped optical emissions with an extension of hundreds of kilometers triggered by lightning-radiated electromagnetic pulses.

The characteristic time of elves is shorter than 1 ms, while their lateral extension is of the order of 300 km. The relation between the short time and the large spatial extension entails that an observer would receive simultaneously photons from the elve that were not emitted at the same time. Therefore, the method developed in the previous section to infer the reduced electric field cannot be directly applied to the case of an optical signal observed from an elve.

In this section, we develop an inversion method to deduce the temporal evolution of the source optical emissions of an elve knowing the signal observed by a spacecraft (direct method). Firstly, we use the emissions of a modelled elve to calculate the observed signal as seen from a spacecraft. Then, we describe an inversion method to recover the emission source.

4.2.2.1 Observed signal

The aim of this section is to develop an approximate procedure to calculate the observed signal of an elve from spacecraft given the temporal profile of emitted photons. Using a cylindrically symmetrical two-dimensional coordinate system, the elve center is located right above the lightning discharge, at

4. ANALYSIS OF OPTICAL SIGNALS EMITTED BY TLES

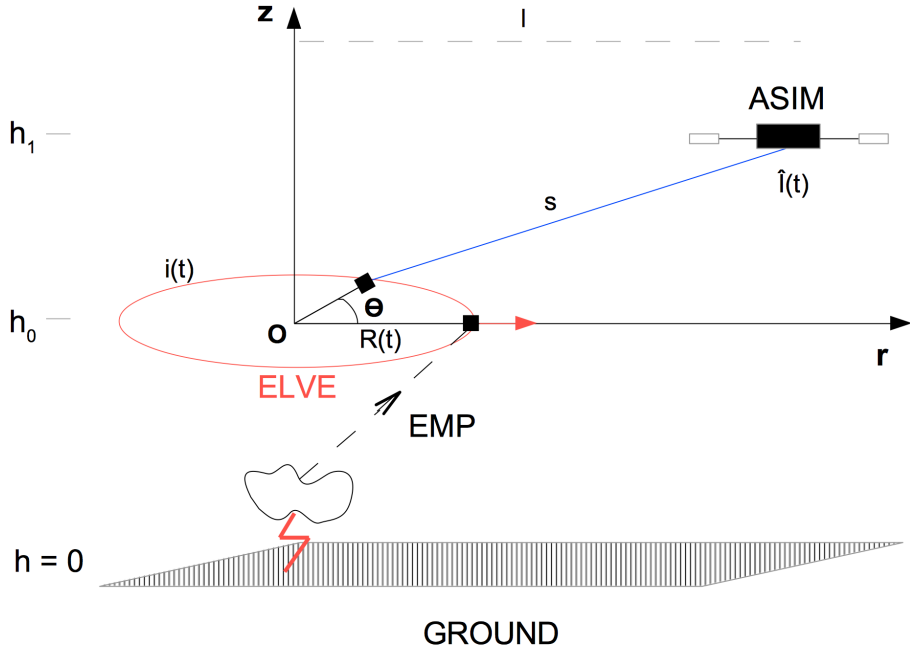


Figure 4.1: Geometry for calculating the observed signal from ASIM. The elve and the spacecraft are located at altitudes h_0 and h_1 from the ground, respectively. $I(t)$ and $i(t)$ are the temporal evolution of the observed and emitted intensities, respectively. The center of the elve, denoted as O , is located at an horizontal distance l from ASIM. $R(t)$ corresponds to the temporal dependence of the elve radius, that is radially symmetrical. The blue line (s) represents the path of an observed photon emitted from the elve at a point given by (R, θ) .

an altitude h_0 . Let's suppose that the spacecraft is located at an altitude h_1 and horizontally separated from the elve center by a distance l , as illustrated in figure 4.1. We can calculate the emitted photons per second $i(t)$ using the elve model described in subsection 3.1.4.2 for a given lightning discharge. It is important to note that the maximum emissions are ring-shaped with a radius that increases in time according to $R(t) = \sqrt{(c^2t^2 + 2th_0c)}$, where c is the velocity of light. Then, the distance $s(t)$ between an elve emitting point and the spacecraft is given by

$$s(t) = \sqrt{(h_1 - h_0)^2 + (l + R(t) \cos(\theta))^2 + R^2(t) \sin^2(\theta)}, \quad (4.9)$$

where θ is the angle between the r -axis and the emitting point. We can now calculate the observed signal at a time τ

$$\hat{I}(\tau) = \frac{A_{ph}}{4\pi} \int_{-\infty}^{\tau} i(t)R(t)dt \int_{-\pi}^{\pi} s^{-2}(t)\delta\left[\tau - \left(t + \frac{s(t)}{c}\right)\right] d\theta, \quad (4.10)$$

where A_{ph} is the area of the detector photometer.

Firstly, we calculate the angular integration, given by

$$K(\tau, t) = \int_{-\pi}^{\pi} s^{-2}(t)\delta\left[\tau - \left(t + \frac{s(t)}{c}\right)\right] d\theta, \quad (4.11)$$

For this purpose, we can use the Dirac delta function property

$$\int f(x)\delta(G(x))dx = \sum_i \frac{f(x_i)}{|G'(x_i)|} \quad (4.12)$$

where x_i are the zeros of $G(x)$. In our case we have the function of θ

$$G(\theta) = \tau - \left(t + \frac{s(t)}{c}\right). \quad (4.13)$$

Solving $G(\theta) = 0$ we obtain

$$\theta = \pm \arccos\left(-\frac{(h_1 - h_0)^2 + l^2 + R^2(t) - c^2(\tau - t)^2}{2R(t)l}\right), \quad (4.14)$$

while the derivative of equation 4.13 is

$$G'(\theta) = -\frac{R(t)l}{c^2(\tau - t)} \sin(\theta). \quad (4.15)$$

4. ANALYSIS OF OPTICAL SIGNALS EMITTED BY TLES

We can combine the four last equations and replace $s \rightarrow c(\tau - t)$ to solve the angular integration

$$K(\tau, t) = \frac{2}{R(t)l(\tau - t)\sin(\theta)}. \quad (4.16)$$

Finally, we can replace (4.16) in equation (4.10) and integrate in time to obtain the observed signal. We distinguish between two possible cases:

1. If the center of the elve is located just below the spacecraft, the horizontal distance l is equal to zero. In this particular case the integrand of equation (4.11) does not depend on the angle θ , and can be analytically expressed as

$$K(\tau, t) = 2\pi s^{-2}(t)\delta\left[\tau - \left(t + \frac{s(t)}{c}\right)\right]. \quad (4.17)$$

As a consequence, the integration given by equation (4.10) can be solved analytically using the Dirac's delta function properties to obtain the observed signal $I(\tau)$.

2. In a more general case, there exists a non-zero horizontal distance l between the elve center and the spacecraft, therefore the integration (4.10) must be numerically solved. It is important to integrate carefully over the angle θ near the singularities contained in equation (4.14), which will be referred to as t_{inf} and t_{sup} . The value of t_{inf} and t_{sup} can be obtained by setting $\cos\theta = \pm 1$ in equation (4.14) and solving for t , that is,

$$\pm 1 = \frac{(h_1 - h_0)^2 + l^2 + R^2(t) - c^2(\tau - t)^2}{2R(t)l}. \quad (4.18)$$

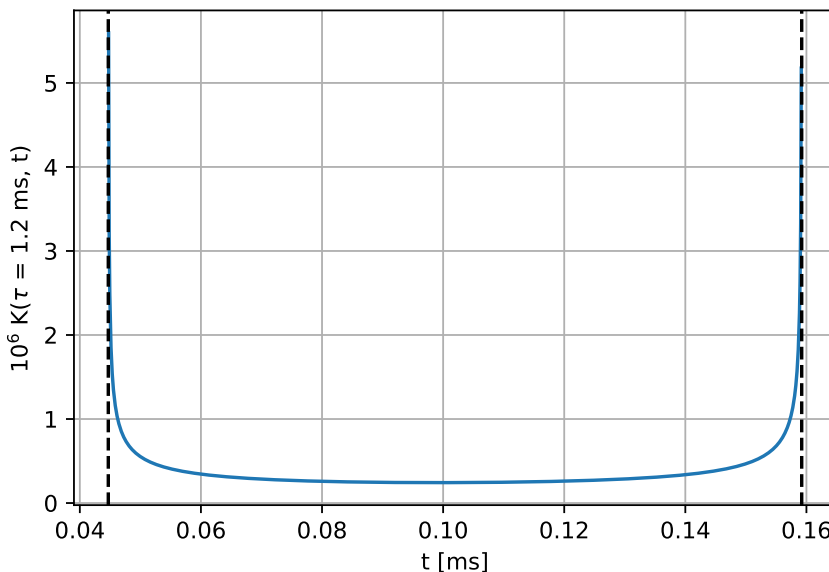


Figure 4.2: Value of the kernel (equation (4.16)) for an arbitrary value of τ . There are two vertical asymptotes in t_{inf} and t_{sup} as a consequence of the singularities of equation (4.14).

The kernel, represented by equation (4.16), contains integrable singularities at t_{inf} and t_{sup} as a consequence of the singularities of equation (4.14). We can visualize the temporal dependence of the kernel for an arbitrary value of τ in figure 4.2.

The integration will be then performed assuming a piecewise-constant emitted intensity as (see figure 4.3)

$$\hat{I}(\tau) = \frac{A_{ph}}{4\pi} \int_{-\infty}^{\tau} K(\tau, t) i(t) dt \simeq \frac{A_{ph}}{4\pi} \sum_j i_j \int_{\max(t_{inf}, t_{j-\frac{1}{2}})}^{\min(t_{sup}, t_{j+\frac{1}{2}})} K(\tau, t) dt \quad (4.19)$$

Elves are extensive structures of light with radius of more than 200 km, therefore it is possible that some emitted photons are out of the photometer

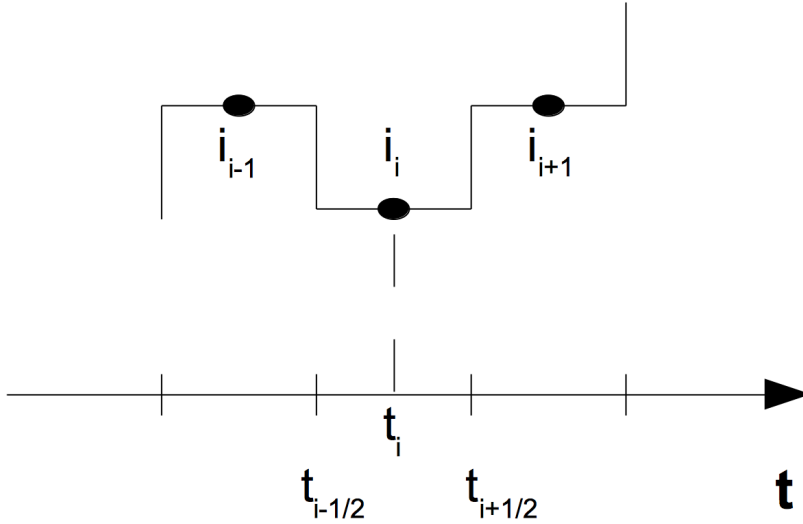


Figure 4.3: Piecewise-constant $i(t)$.

field of view (FOV). Assuming a circular photometer aperture with a given FOV angle and knowing the horizontal and vertical separation between the elve and the photometer, we can calculate the maximum distance s_0 between an elve emitting point and the photometer as

$$s_0 = (h_1 - h_0) \cos^{-1} \left(\frac{FOV}{2} \right), \quad (4.20)$$

We can then calculate the observed intensity excluding the photons that come from distances greater than s_0 using the Heaviside function Θ . Equation (4.10) becomes

$$\hat{I}(\tau) = \frac{A_{ph}}{4\pi} \int_{-\infty}^{\tau} i(t) R(t) dt \int_{-\pi}^{\pi} s^{-2}(t) \delta \left[\tau - \left(t + \frac{s(t)}{c} \right) \right] \Theta(s(t) - s_0) d\theta. \quad (4.21)$$

This method is valid if the emissions are concentrated on a thin ring. However, the molecules excited by the lightning-radiated pulse do not decay instantaneously. These emitting species decay according to a radiative decay constant ν . Therefore, the elve would be seen as a ring with a thickness and

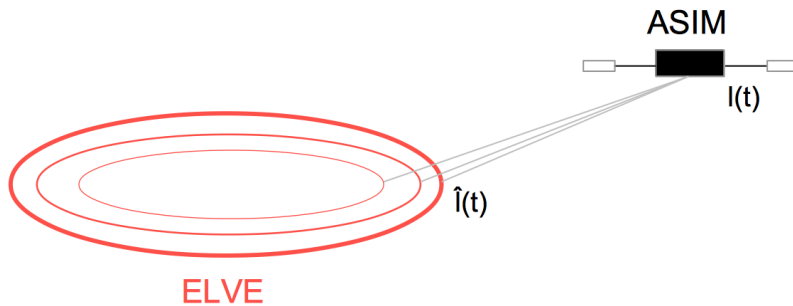


Figure 4.4: Approximation of an elve as a succession of thin rings. $I(t)$ corresponds to the signal observed from ASIM, while $\hat{I}(t)$ would be the observed signal observed if all the emissions were focused in an instantenous and, consequently, thin ring.

a radial brightness dependency determined by the radiative decay constant of each species. We can then approximate the elve as a sequence of thin rings that emit with different intensities (see figure 4.4), resulting in an observed intensity $I(\tau)$ that can be calculated as the convolution of each ring intensity with its corresponding decay function as

$$I(\tau) = \int_0^{\tau} \exp(-\nu t) \hat{I}(\tau - t) dt, \quad (4.22)$$

Finally, the atmospheric absorption at each wavelength can be applied to the observed signal $I(\tau)$ in case it is necessary.

4.2.2.2 Inversion of the signal

Following our notation, the observed optical signal from a spacecraft would be denoted by $I(\tau)$. In this section we describe a procedure to invert this signal and obtain the emitting source $i(t)$ that defines the elve. Firstly, we deconvolve the total signal $I(\tau)$ to obtain an individual ring-shaped source $\hat{I}(\tau)$ using the Wiener deconvolution in the frequency domain. We assume

4. ANALYSIS OF OPTICAL SIGNALS EMITTED BY TLES

a signal-to-noise ratio

$$SNR(t) = \frac{\sqrt{I(\tau)\Delta t}}{\Delta t}, \quad (4.23)$$

where Δt is the integration time of the observed signal. Now define the Fourier transform of the signal-to-noise ratio as

$$SNR_f(f) = \mathcal{F}[SNR]. \quad (4.24)$$

As we explained before, the thickness of the ring-shaped emissions is a consequence of the radiative decay constant (ν) of the emitting species. We calculate the Fourier transform of this decay as

$$D_f(f) = \mathcal{F}[\exp(-\nu t)], \quad (4.25)$$

finally, we define the Fourier transform of the observed signal as

$$I_f(f) = \mathcal{F}[I(\tau)], \quad (4.26)$$

We can obtain the observed signal of each individual ring-shaped source in the frequency domain ($\hat{I}_f(f)$) using the Wiener deconvolution as

$$\hat{I}_f(f) = \frac{I_f(f)}{D_f(f)} \left[\frac{|D_f(f)|^2}{|D_f(f)|^2 + SNR_f(f)^{-1}} \right], \quad (4.27)$$

Finally, we can obtain $\hat{I}(\tau)$ as the inverse Fourier transform of $\hat{I}_f(f)$

$$\hat{I}(\tau) = \mathcal{F}^{-1}[\hat{I}_f(f)], \quad (4.28)$$

The following step of this inversion process is more complex and has to be accomplished numerically, since the goal is to obtain the function $i(t)$ from the integral equation (4.21). The resolution of this kind of equation, known as Fredholm integral equation of the first kind, is a common problem in mathematics. We use the numerical method proposed by *Hanson* (1971) to solve the equation using singular values.

Following the notation used in *Hanson* (1971), the kernel $k(s_i, t_j)$ of our integral equation is given by equation (4.16), where the quantities s_j and t_j correspond to times of observation and emissions, respectively. In our

case, the experimentally sampled function $g(s_i)$ is determined by the emitted photons per second from one ring, obtained after applying the Wiener deconvolution to the observed data $I(\tau)$ according to equation (4.27).

Let us describe the method proposed by *Hanson* (1971) to solve a Fredholm integral equation of the first kind and its application to our particular case. We write the integral equation (4.21) as a linear system given by

$$KF = G, \tag{4.29}$$

where G is a vector of size m containing the observed signal, F is an unknown vector of size n corresponding to the emitted signal at the source, and K is a $m \times n$ matrix representing the kernel $k(s_i, t_j)$. We assume that the measurements g_i have some random error ϵ_i as

$$g_i = \hat{g}_i + \epsilon_i, \tag{4.30}$$

where $\text{Var}(\epsilon_i) = \sigma_i^2$ and \hat{g}_i represents the hypothetical measurements without error. In our case, we assume that the error follows a Poisson distribution and set

$$\sigma_i = \frac{\sqrt{g_i \Delta t}}{\Delta t}, \tag{4.31}$$

where Δt is the integration time of the signal.

Assuming a Gaussian noise we want to find the F that maximizes the likelihood

$$L = \alpha \prod_{i=1}^m \exp\left(-\frac{((KF)_i - G_i)^2}{\sigma_i^2}\right), \tag{4.32}$$

where α is a normalization factor. This is the same as minimizing

$$-\log(L) = \sum_{i=1}^m \frac{((KF)_i - G_i)^2}{\sigma_i^2} = |\Sigma KF - \Sigma G|^2, \tag{4.33}$$

where

$$\Sigma = \begin{pmatrix} \sigma_1^{-1} & 0 & 0 \\ 0 & \sigma_2^{-1} & 0 \\ 0 & 0 & \dots \end{pmatrix}. \tag{4.34}$$

4. ANALYSIS OF OPTICAL SIGNALS EMITTED BY TLES

In principle we can just minimize (4.33) using least squares but in some cases we would be overfitting the noise in G . We want an estimate of the “extra” error that we allow in (4.33) to avoid strong oscillations in F . For this we use the Singular-Value Decomposition (SVD):

$$\Sigma K = U \begin{bmatrix} S \\ 0 \end{bmatrix} V^T, \quad (4.35)$$

where U and V are orthogonal ($U^T U = \mathbb{I}$ and $V^T V = \mathbb{I}$) and

$$\begin{bmatrix} S \\ 0 \end{bmatrix} = \begin{bmatrix} S_1 & 0 & 0 & 0 & \dots \\ 0 & S_2 & 0 & 0 & \dots \\ \dots & \dots & \dots & \dots & \dots \\ 0 & 0 & 0 & \dots & S_n \\ 0 & 0 & 0 & \dots & 0 \end{bmatrix} V^T, \quad (4.36)$$

results in a matrix $n \times m$.

To see how the SVD is useful we note that

1. $|\Sigma K F - \Sigma G| = \left| \begin{bmatrix} S \\ 0 \end{bmatrix} V^T F - U^T \Sigma G \right|$

2. The column vectors of U and V form basis in \mathbb{R}^m and \mathbb{R}^n , respectively. That is, calling these vectors u_i and v_i we have

$$u_i u_j = \delta_{ij} \quad (4.37)$$

$$v_i v_j = \delta_{ij} \quad (4.38)$$

so we can decompose

$$F = x_1 v_1 + x_2 v_2 + \dots \quad (4.39)$$

$$\Sigma G = e_1 u_1 + e_2 u_2 + \dots \quad (4.40)$$

this is,

$$U^T \Sigma G = \begin{bmatrix} e_1 \\ e_2 \\ \dots \\ e_m \end{bmatrix}, \quad (4.41)$$

$$V^T F = \begin{bmatrix} x_1 \\ x_2 \\ \dots \\ x_n \end{bmatrix}. \quad (4.42)$$

But then we have the following vector with m components

$$\begin{bmatrix} S \\ 0 \end{bmatrix} V^T F = \begin{bmatrix} s_1 x_1 \\ s_2 x_2 \\ \dots \\ s_n x_n \\ 0 \\ \dots \end{bmatrix}. \quad (4.43)$$

Combining equations (4.41), (4.42) and (4.43),

$$\begin{bmatrix} S \\ 0 \end{bmatrix} V^T F - U^T \Sigma G = \begin{bmatrix} (s_1 x_1 - e_1) \\ (s_2 x_2 - e_2) \\ \dots \\ (s_n x_n - e_n) \\ e_{n+1} \\ \dots \\ e_m \end{bmatrix}, \quad (4.44)$$

and the norm that we want to “minimize” is

$$|\Sigma K F - \Sigma G|^2 = \sum_{i=1}^m (s_i x_i - e_i)^2 + \sum_{i=n+1}^m e_i^2. \quad (4.45)$$

We minimize this by setting $x_i = e_i/s_i$. But, as said above, we do not want to minimize this “too much”, we accept an error

$$|\Sigma KF - \Sigma G|^2 \simeq \text{Var}(|\Sigma G|) = \frac{\text{Var}(g_1)}{\sigma_1^2} + \frac{\text{Var}(g_2)}{\sigma_2^2} + \dots = m. \quad (4.46)$$

So we set as many $x_i = 0$ as we can by dropping first those with the smallest s_i because they are responsible of the largest oscillations in F . Once we have all the x_i we use equation (4.39) to get F .

4.3 Results

The methods described above can be applied to the modelled optical emissions of elves and halos as well as to the optical signals recorded by spacecraft. This section is divided into two parts. In subsection 4.3.1 we apply the analysis methods to the modelled optical emissions of halos and elves. This approach allows us to compare the inferred reduced electric field with the self-consistently calculated field given by the models.

Then, we discuss in subsection 4.3.2 the possibility of applying the developed procedures to signals reported by ISUAL and GLIMS as well as to the future observations taken by ASIM and TARANIS.

4.3.1 Analysis of the signals obtained with the halo and elve models

4.3.1.1 Reduced electric field in halos

Spacecraft devoted to the observation of TLEs are often equipped with photometers collecting photons in the lines 760 nm, 337 nm and 394 nm as well as in the spectral (LBH) band between about 150 nm and about 280 nm. In this section, we discuss the possibility of using the observed optical emissions comprised in these wavelengths to deduce the reduced electric field inside a halo with a CMC of 560 C km simulated in chapter 3.

The halo model allows us to obtain, among others, the temporal evolution of the optical emissions in the 760 nm, 337 nm and 394 nm lines from

the First Positive, the Second Positive Systems of N_2 and from the First Negative Systems of N_2^+ . The model also computes the optical emissions in the LBH band between 130 nm and 280 nm. We denote the intensities of these optical emissions as $I_{FPS}(t)$, $I_{SPS}(t)$, $I_{FNS}(t)$ and $I_{LBH}(t)$, respectively. We can then use equations 4.1 and 4.2 to deduce the temporal production rate of these emitting species using the kinetic rates collected in Appendix A.1. However, in the case of halos, the use of the observed LBH band to deduce the production rate of all the molecules emitting in these wavelengths is not possible as a consequence of their quenching rates. As halos are descending events, we cannot use a fixed altitude to estimate the quenching rates of the molecules emitting in the LBH band. In addition, we cannot neglect these quenching rates, as the quenching altitudes of some of them are located above the halo, that is, at altitudes above 80 km (see figure 4.5). Therefore, we cannot use the observed intensity of the LBH band in order to deduce the reduced electric field inside halos.

After obtaining the production rate ratios of the emitting species from their corresponding observed optical emissions, we particularize equation (4.8) to the case of the considered emitting species to obtain the theoretical reduced electric field dependence of these ratios. To obtain these theoretical production rates, we have to include in equation (4.8) the production rates (denoted as k) of each species. Let us discuss the particularities of the theoretical production rate of each emitting species depending on the spectral line or band where the emission is produced:

1. Emissions in the 394 nm line are produced by the radiative decay process $N_2^+(B^2 \Sigma_u^+, v=0) \rightarrow N_2^+(X^1 \Sigma_g^+, v=0) + h\nu$. Therefore, the theoretical production rate of the molecule $N_2^+(B^2 \Sigma_u^+)$ has to be used in equation (4.8) before comparing with the production deduced from the observed 394 nm line. Following the kinetical scheme proposed in Appendix A.1, the only process that contributes to populate this state is the electron impact ionization of N_2 molecules. Therefore, we use the rate of the reaction $e + N_2(X^1 \Sigma_g^+, v=0) \rightarrow e + e + N_2^+(B^2 \Sigma_u^+, v=0)$ in $cm^{-3}s^{-1}$ to calculate the theoretical production of $N_2^+(B^2 \Sigma_u^+, v=0)$ in equation (4.8).

4. ANALYSIS OF OPTICAL SIGNALS EMITTED BY TLES

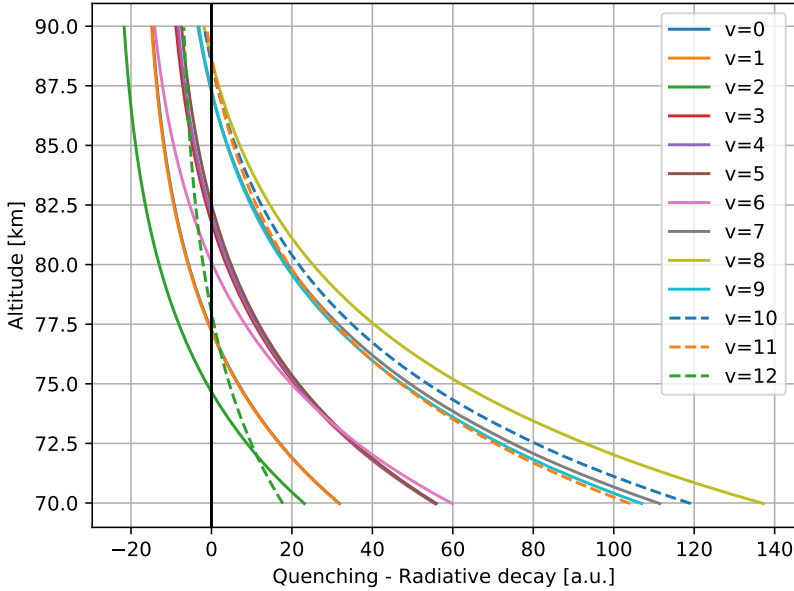


Figure 4.5: Difference between the quenching and the radiative decay rates of each vibrational state $N_2(a^1 \Pi_g, v = 0, \dots, 12)$ for different altitudes in $cm^{-3}s^{-1}$ multiplied by a scale factor. The altitude at which the quenching rate is similar to the radiative decay rate is called the quenching altitude. The quenching of each state can be neglected for altitudes significantly above the quenching altitude. These rates have been calculated using the Appendix??.

2. Emissions in the 337 nm line are produced by the radiative decay process $N_2(C^3 \Pi_u, v = 0) \rightarrow N_2(B^3 \Pi_g, v = 0) + h\nu$. Following the previous case, the theoretical production rate of the molecule $N_2(C^3 \Pi_u, v = 0)$ has to be used in equation (4.8) before comparing with the production deduced from the observed 337 nm line. According to Appendix A.1, there are two processes that contribute to populate this states, the excitation impact of electron with N_2 molecules and the radiative decay process $N_2(E^3 \Sigma_g^+) \rightarrow N_2(C^3 \Pi_u, v = 0) + h\nu$. We can consider this radiative decay process as instantaneous, as its characteristic time is much shorter than the halo lifetime. Therefore, we use the rate of the reaction $e + N_2(X^1 \Sigma_g^+, v = 0) \rightarrow e + e + N_2(C^3$

$\Pi_u, v = 0$) together with the rate of the reaction $e + N_2(X^1 \Sigma_g^+, v = 0) \rightarrow e + N_2(E^3 \Sigma_g^+)$ to calculate the theoretical production of $N_2(X^1 \Sigma_g^+, v = 0)$ in equation (4.8). However, as the $N_2(E^3 \Sigma_g^+)$ molecules can also radiatively decay to other states ($N_2(A^3 \Sigma_u^+, v = 0)$ and $N_2(B^3 \Pi_g, v = 0)$), we multiply the rate of the process $e + N_2(X^1 \Sigma_g^+, v = 0) \rightarrow e + N_2(E^3 \Sigma_g^+)$ by the portion of $N_2(E^3 \Sigma_g^+)$ molecules that would decay to the state $N_2(B^3 \Pi_g, v = 0)$. This portion can be calculated using the radiative decay constants of the three processes that contribute to de-excite the $N_2(E^3 \Sigma_g^+)$ molecules, as at halo altitudes the quenching of $N_2(E^3 \Sigma_g^+)$ is negligible.

3. Emissions in the 760 nm line are produced by the radiative decay process $N_2(B^3 \Pi_g, v = 3) \rightarrow N_2(A^3 \Sigma_u^+, v = 1) + h\nu$. Therefore, the theoretical production rate of the molecule $N_2(B^3 \Pi_g, v = 3)$ has to be used in equation (4.8) before comparing with the production deduced from the observed 760 nm line. Apart from the excitation impact of electron with N_2 molecules, the radiative decay of $N_2(C^3 \Pi_u, v = 0..4)$ molecules can also contribute to populate the state $N_2(B^3 \Pi_g, v = 3)$. Again, we can consider these radiative decay processes as instantaneous, as their characteristic time is lower than the halo lifetime. Therefore, we use the rate of the reaction $e + N_2(X^1 \Sigma_g^+, v = 0) \rightarrow e + N_2(B^3 \Pi_g, v = 3)$ together with the rate of the electron impact processes that populate the $N_2(C^3 \Pi_u, v = 0..4)$ states to calculate the theoretical production of $N_2(B^3 \Pi_g, v = 3)$ in equation (4.8). As in the previous case, we have to multiply these rates by the portion of $N_2(C^3 \Pi_u, v = 0, \dots, 4)$ molecules that decay to the particular state $N_2(B^3 \Pi_g, v = 3)$.

Finally, we can calculate the reduced electric field necessary to match the observed and theoretical ratios of production at each time. The results are plotted in figure 4.6 together with the maximum reduced electric field given by the simulation. The comparison between the derived electric fields from optical line intensity ratios with the electric field given by the model allows us to test the accuracy of the proposed methods for the optical diagnosis of halos using ASIM optical data.

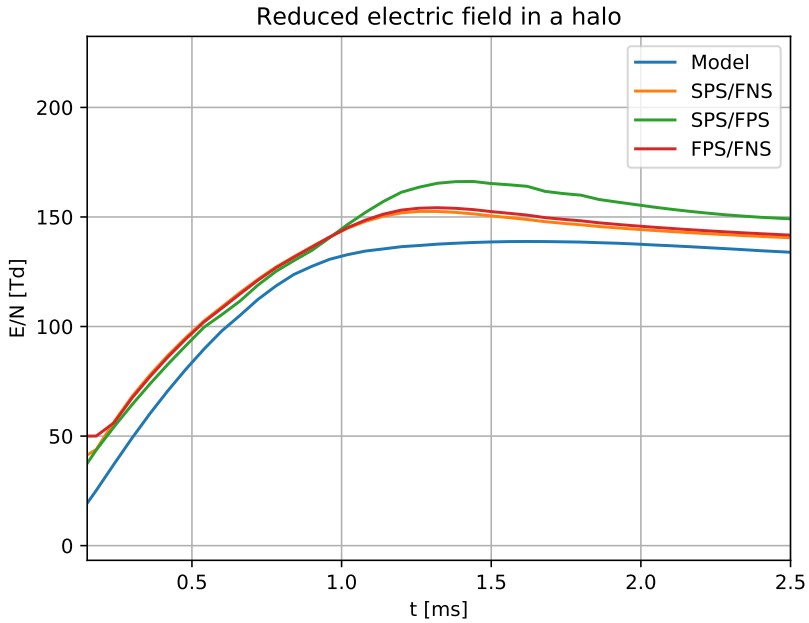


Figure 4.6: Temporal evolution of the maximum reduced electric field inside a halo. The blue line corresponds to the maximum reduced electric field according to the halo model. The rest of the lines correspond to the inferred reduced electric field using the ratios of the observed First and Second Positive Systems of N_2 and the First Negative Systems of N_2^+ following subsection 4.2.1.

4.3.1.2 Reduced electric field in elves

Let us now apply the previous electric field deduction method to the elves simulated in chapter 3 and triggered by a lightning stroke with a current peak current of 220 kA. As in the case of the halo model, the elve model allows us to calculate the intensities of the optical emissions $I_{FPS}(t)$, $I_{SPS}(t)$, $I_{FNS}(t)$ and $I_{LBH}(t)$.

Again, the first step to derive the reduced electric field inside the TLE is to use equations 4.1 and 4.2 to deduce the temporal production rate of these emitting species using the kinetic rates collected in Appendix A.1. Elves are always produced at altitudes of about 88 km, where the quenching of all the states emitting in the LBH band is less important than the radiative decay (see figure 4.5). Therefore, we can now neglect in our calculations the quenching of all these species at a fixed altitude of 88 km and use the intensities observed in the LBH band to deduce the reduced electric field.

The second step is to particularize equation (4.8) to the case of the considered emitting species to obtain the theoretical reduced electric field dependence of their ratios. We use the same steps enumerated in section 4.3.1.1 to deduce the theoretical production rate of each emitting species with the following exceptions:

1. We do not include the radiative decay process $N_2(E^3 \Sigma_g^+) \rightarrow N_2(C^3 \Pi_u, v = 0) + h\nu$ in the calculation of the theoretical production of $N_2(C^3 \Pi_u, v = 0)$ molecules, as we cannot consider now this reaction as instantaneous. The characteristic time of this process is about 0.6 ms, similar to the characteristic time of elve emissions.
2. Emissions in the LBH band are produced by the radiative decay processes $N_2(a^1 \Pi_g, v = 0, \dots, 15) \rightarrow N_2(X^1 \Sigma_g^+, v = 0, \dots, 8) + h\nu$. Therefore, the theoretical production rates of the molecules $N_2(a^1 \Pi_g, v = 0, \dots, 15)$ have to be used in equation (4.8) before comparing with the production deduced from the observed LBH band. Apart from the excitation impact of electron with N_2 molecules, the radiative decay of $N_2(w^1 \Delta_u)$ molecules can also contribute to populate the states $N_2(a^1 \Pi_g, v = 0, \dots, 15)$. However, we cannot now consider this reaction as

4. ANALYSIS OF OPTICAL SIGNALS EMITTED BY TLES

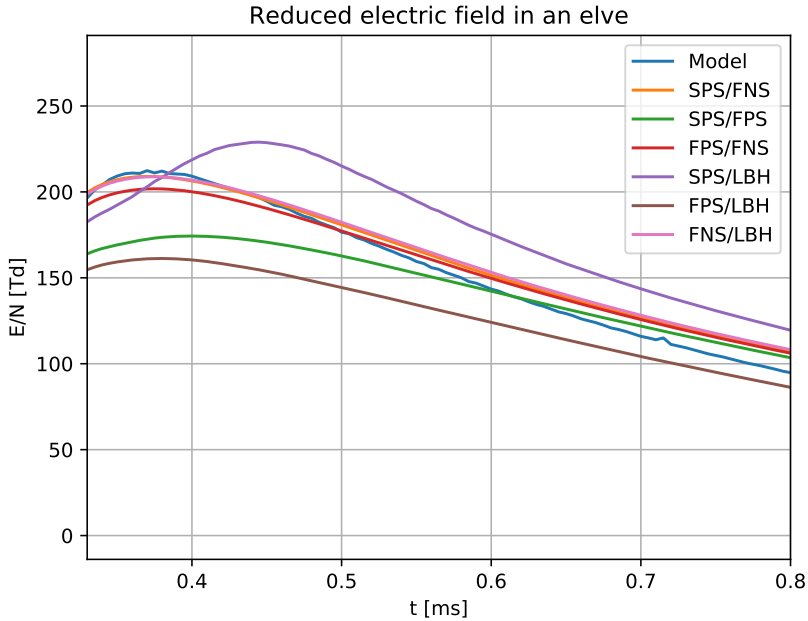


Figure 4.7: Temporal evolution of the maximum reduced electric field producing an elve. The blue line corresponds to the maximum reduced electric field according to the elve model. The rest of the lines correspond to the inferred reduced electric field using the ratios of the observed First Positive System, Second Positive System, First Negative System and LBH band of the N_2 following subsection 4.2.1.

instantaneous, as its characteristic time is about 6.5 ms, quite similar to the elve lifetime. Therefore, we use the rate of the reactions $e + N_2(X^1 \Sigma_g^+, v = 0) \rightarrow e + N_2(a^1 \Pi_g, v = 0, \dots, 15)$ to calculate the theoretical production of $N_2(a^1 \Pi_g, v = 0, \dots, 15)$ in equation (4.8).

As in the case of halos, the next step would be to calculate the reduced electric field necessary to match the observed and theoretical ratio of production at each time. The results are plotted in figure 4.7 together with the maximum reduced electric field given by the simulation. The comparison between the deduced electric fields with the electric field given by the model allows us to test the accuracy of these methods for elves

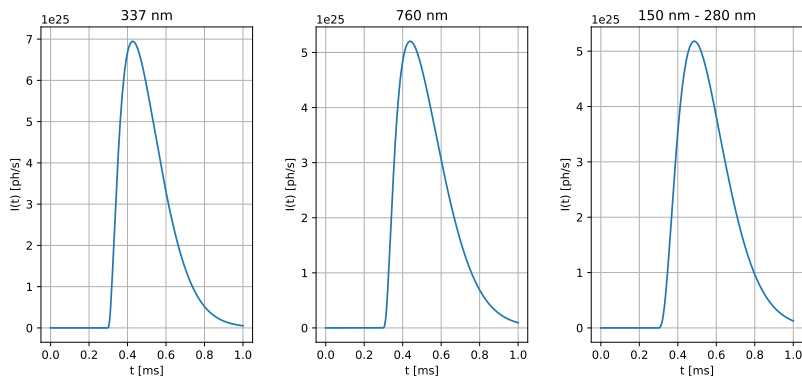


Figure 4.8: Optical emissions in different wavelengths of an elve simulated in chapter 3 and triggered by a lightning with a current peak current of 220 kA.

4.3.1.3 Emitting source of elves

In the previous section we have deduced the reduced electric field of halos and elves considering that the observed emissions and the emitting source follow the same temporal evolution. However, as we discussed before, this assumption is not true for the case of elves. Therefore, it is necessary to invert the observed signal in order to obtain the emitting source before deducing the reduced electric field in the elve. In this section, we apply the methods described in subsection 4.2.2.1 to calculate how a spacecraft would observe a simulated elve optical emission. Afterward, we invert this signal following the process detailed in subsection 4.2.2.2 to recover the emitting source.

We use as source of the optical emissions the elve simulated in chapter 3 and triggered by a lightning stroke with a current peak current of 220 kA. We plot in figure 4.8 the emitting source that we will treat in this section.

The method developed in subsection 4.2.2.1 to calculate the signal observed by a spacecraft receives as input the optical emissions of a thin ring-shaped elve. We convolve the emissions shown in figure 4.8 with their corresponding decay function (see subsection 4.2.2.1) to obtain the observed emissions due to an instantaneous and thin ring.

Let us now follow the method of subsection 4.2.2.1 to calculate the signal

4. ANALYSIS OF OPTICAL SIGNALS EMITTED BY TLES

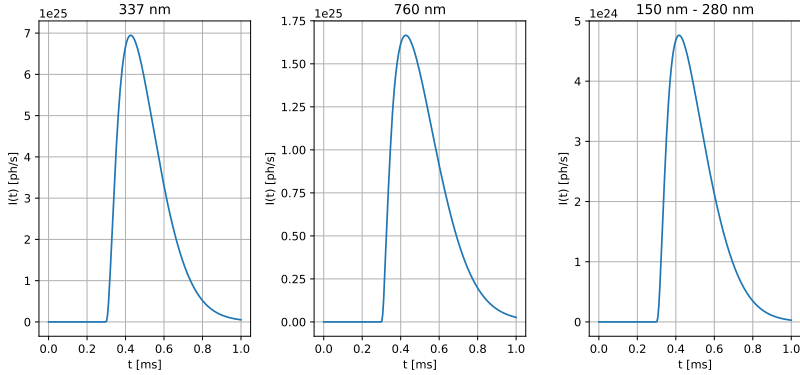


Figure 4.9: Optical emissions in different wavelengths of an elve simulated in chapter 3 and triggered by a lightning with a current peak current of 220 kA convolved with their corresponding decay function.

observed from a spacecraft. We assume that the observation instrument is located at an altitude of 410 km and at a horizontal distance from the center of the elve of 80 km. In addition, we assume that the photometer has a Field Of View (FOV) of 55° , a sampling rate of 20 kHz and a circular aperture with a total area of 0.04 m^{-2} . We plot in figure 4.10 the calculated received signals.

The inversion method described in subsection 4.2.2.2 can be directly applied to the received signals in order to recover the emitting sources. However, before applying the inversion method, we turn to a more realistic case adding some artificial noise to the received signals as follows. We denote as S_i the i - nth point of a received signal and as S_{max} the maximum value of the signal. Then, we define a parameter g that will control the noise:

$$g = \frac{a}{S_{max}}, \quad (4.47)$$

where a is an arbitrary number that controls the noise. Afterward, we use this parameter (g) to generate the random number b with a Poisson distribution with mean value gS_i . Finally, the S_i value of the signal is

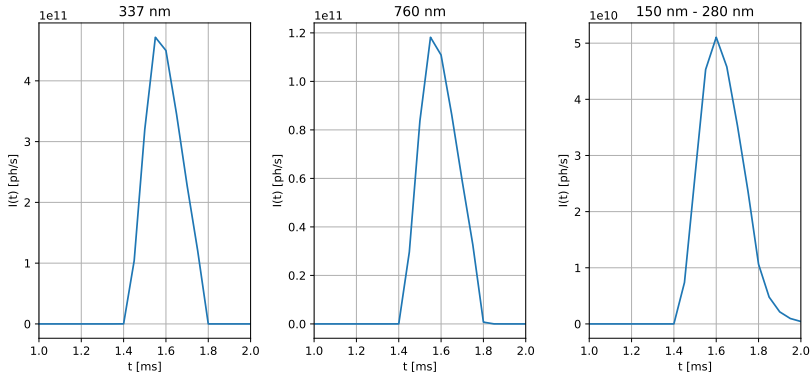


Figure 4.10: Received signals from an elve at a spacecraft located at an altitude of 410 km and at a horizontal distance from the center of the elve of 80 km. We have assumed that the photometer has a FOV of 55° , an observation frequency of 20 kHz and a circular aperture with a total area of 0.04 m^{-2} .

modified to be

$$S'_i = \frac{b}{g}. \quad (4.48)$$

Setting the a parameter to 50, we obtain the signal with noise shown in figure 4.11.

We can now apply the inversion method developed in subsection 4.2.2.2 to the received signals with noise in order to compare with the signals given by the models. We plot the results in figure 4.12.

Let us now determine the influence of the FOV in the inversion of the signal. We consider the same observation configuration with larger FOV of 90° . We plot the results in figure 4.13.

Comparison of figures 4.12 and 4.13 shows that the use of a larger FOV allows us to obtain the temporal evolution of the source up to larger times. The underlying reason is that a photometer with larger FOV would collect photons emitted by the elves for larger times than a photometer with a smaller FOV, reporting more information about the evolution of the elve.

4. ANALYSIS OF OPTICAL SIGNALS EMITTED BY TLES

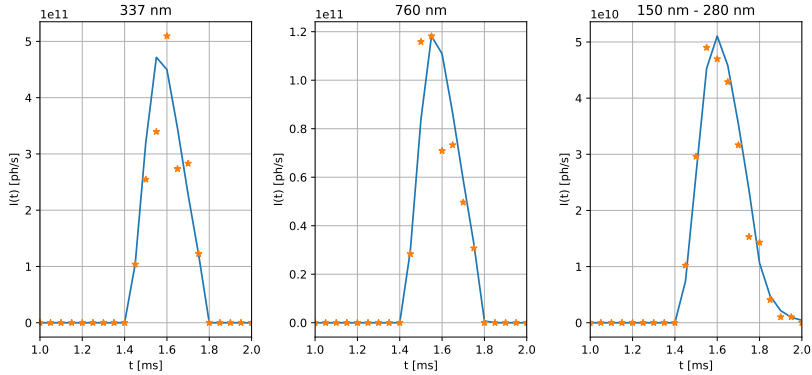


Figure 4.11: Signals of figure4.10 (solid line) and signals after adding an artificial noise (dots).

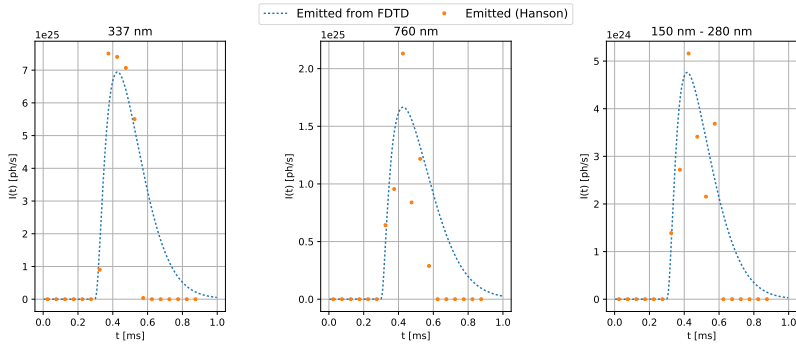


Figure 4.12: Result of inverting the signals plotted in figure 4.10 (Orange points). We also plot the emitted signal given by the FDTD elve model (blue line).

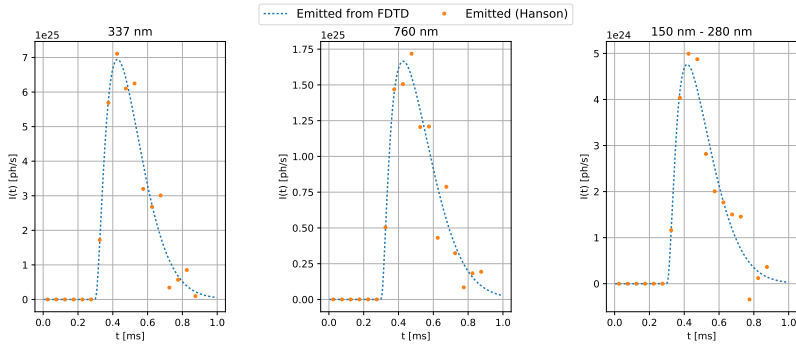


Figure 4.13: Same as figure 4.12, but considering a larger FOV of 90° .

4.3.2 Analysis of signals recorded from space

In this section we analyze the particularities listed in table 4.1 of the photometers integrated in ISUAL, GLIMS, ASIM and TARANIS for the investigation of TLEs. In addition, we apply the inversion method described in subsection 4.2.2.2 to one LBH signal emitted by an elve and detected by GLIMS.

Mission	Photometer	FOV	Frequency	Inclination
ISUAL	SP1: 150 - 290 nm	22 deg (H) \times 3.6 deg (V)	10 kHz	Limb
	SP2: 337 nm	22 deg (H) \times 3.6 deg (V)	10 kHz	Limb
	SP3: 391 nm	22 deg (H) \times 3.6 deg (V)	10 kHz	Limb
	SP4: 624 - 750 nm	22 deg (H) \times 3.6 deg (V)	10 kHz	Limb
	SP5: 777.4 nm	22 deg (H) \times 3.6 deg (V)	10 kHz	Limb
	SP6: 250 - 390 nm	22 deg (H) \times 3.6 deg (V)	10 kHz	Limb
	AP1 (16 CH): 370 - 450 nm	22 deg (H) \times 3.6 deg (V)	0.2, 2 or 20 kHz	Limb
	AP2 (16 CH): 530 - 650 nm	22 deg (H) \times 3.6 deg (V)	0.2, 2 or 20 kHz	Limb
GLIMS	PH1: 150 - 280 nm	42.7°	20 kHz	Nadir
	PH2: 332 - 342 nm	42.7°	20 kHz	Nadir
	PH3: 755 - 766 nm	42.7°	20 kHz	Nadir
	PH4: 599 - 900 nm	80.8°	20 kHz	Nadir
	PH5: 310 - 321 nm	42.7°	20 kHz	Nadir
	PH6: 386 - 397 nm	42.7°	20 kHz	Nadir
ASIM	PH1: 145 - 230 nm	61.4°	100 kHz	Nadir
	PH2: 337 nm	61.4°	100 kHz	Nadir
	PH3: 777.4 nm	61.4°	100 kHz	Nadir
TARANIS	PH1: 145 - 280 nm	55°	20 kHz	Nadir
	PH2: 337 nm	55°	20 kHz	Nadir
	PH3: 762 nm	55°	20 kHz	Nadir
	PH4: 600 - 800 nm	100°	20 kHz	Nadir

Table 4.1: Optical characteristic of the photometers onboard ISUAL (*Chern et al., 2003*), GLIMS (*Sato et al., 2015; Adachi et al., 2016*), ASIM (*Neubert et al., 2006*) and TARANIS (*Blanc et al., 2007*) It is also indicated the observation mode of each photometer.

The photons emitted by TLEs can travel from the source to the photometer without suffering an important atmospheric absorption. However, the signal of TLEs observed in the nadir can be contaminated by the photons emitted by the parent-lightning discharge. An exception to this are the emissions of the LBH, as the photons emitted by lightning in these short wavelengths are totally absorbed by the atmosphere (*Mende et al., 2005*). For this reason, the signals detected in the FPS, SPS or FN cannot be analyzed following our inversion methods unless the parent lightning is out of the FOV.

The reported signals from TLEs taking place behind the limb would not be contaminated by the photons emitted by the lightning stroke. If the

4. ANALYSIS OF OPTICAL SIGNALS EMITTED BY TLES

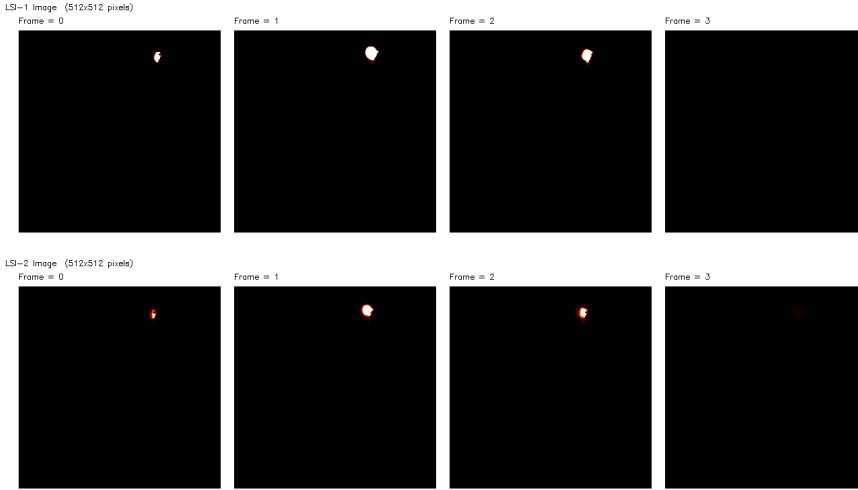


Figure 4.14: Image data obtained by the broadband 768 nm - 830 nm filter (LSI-1) (first row) and by the narrowband 760 nm - 775 nm filter (LSI-2) (second row) for an event reported by GLIMS at a time of 16.28.04 (UT) on December 13, 2012. The temporal separation between each frame is about 33 ms.

absorption of the atmosphere is used to correct the observed signals, it is then possible to apply of our inversion methods to the analysis of data.

4.3.2.1 Deduction of the source of an elve reported by GLIMS

We apply the inversion method described in subsection 4.2.2.2 to the LBH signal of an elve reported by GLIMS and provided by the JEM-GLIMS science team. The signal of this elve was recorded by GLIMS at 16.28.04 (UT) on December 13, 2012. At the moment of the detection, the instrument was located at 422 km of altitude.

Figure 4.14 shows the event recorded by the optical camera Lightning and Sprite Imager (LSI) onboard GLIMS. This camera has a FOV of 28.3° and is equipped with two frequency filters, a broadband (768 nm - 830 nm) filter (LSI-1) and a narrowband (760 nm - 775 nm) filter (LSI-2).

The second frame of figure 4.14 corresponds to the moment in which a photon in the LBH band reached the photometer. Therefore, the flash

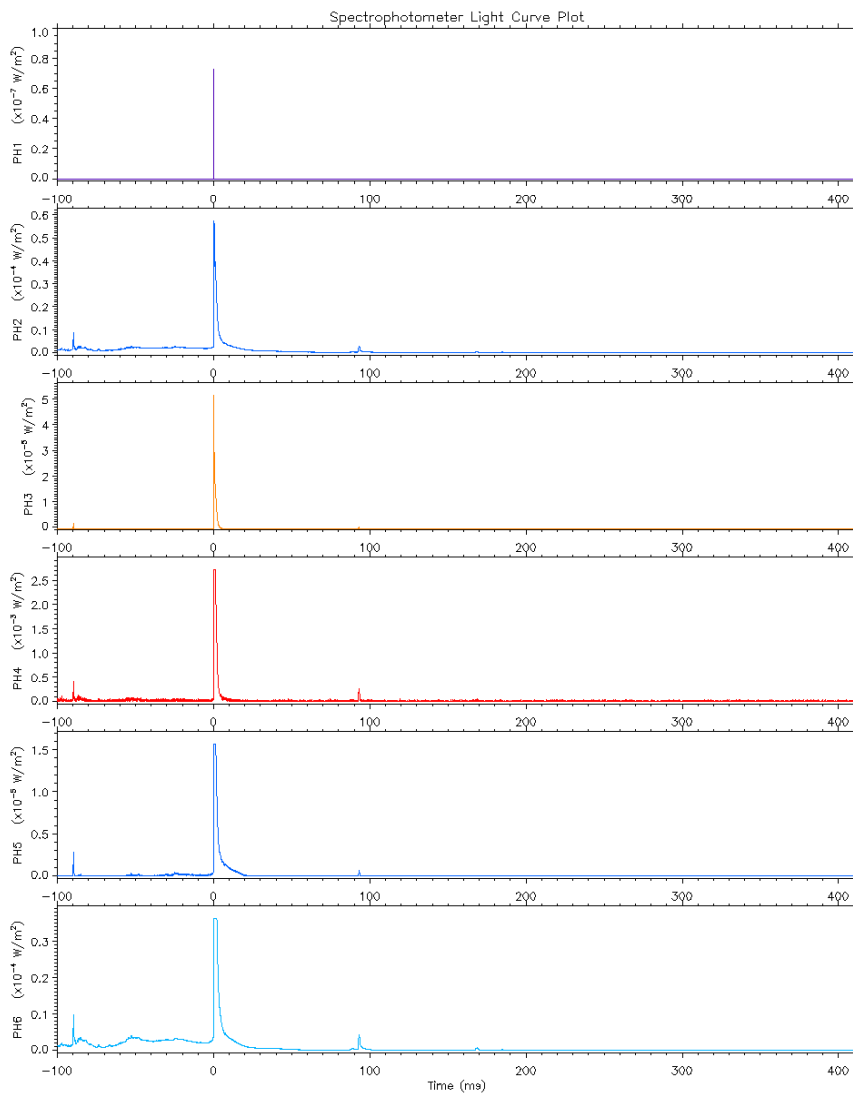


Figure 4.15: Photometer data for an event reported by GLIMS at a time of 16.28.04 (UT) on December 13, 2012. The characteristics of each photometer are shown in table 4.1.

4. ANALYSIS OF OPTICAL SIGNALS EMITTED BY TLES

observed in the second frame would probably be the parent lightning of the elve. The reported photometer data associated with this event is shown in figure 4.15. In this figure, the detection of LBH photons (PH1) is clearly located at $t = 0$ ms, together with a burst of photons with other wavelengths (PH2 - PH6).

Before applying the inversion method (subsection 4.2.2.2) to this LBH signal, we have to deduce the horizontal separation between the photometers and the center of the elve (l). For this purpose, we use the camera data shown in figure 4.14. The altitude of GLIMS at the moment of the elve detection is known to be 422 km, while we can assume that the elve took place at an altitude of 88 km. In addition, we know that the FOV of the camera is 28.3° . Therefore, the camera can observe a square with a lateral dimension of 168 km in the plane of the elve (at 88 km of altitude). If we assume that the parent-lightning is located just below the center of the elve, we can use this information together with the number of pixels between the center of the camera FOV and the parent-lightning of figure 4.14 to calculate the horizontal separation between the elve center and the photometer. In this case, this separation is 55 km.

We also need to estimate the moment at which the source started its emissions in relation with the moment of detection of the first photon (t_E). That is, the difference between the time of the elve detection and the time of the elve onset. The deduction of this time is not direct, as the radius of the elve expands faster than light as can be demonstrated using the scheme plotted figure 4.16.

We can calculate the expansion of the elve radius during a time $\tau = \tau_2 - \tau_1$ knowing that the pulse radiated by the lightning discharge travels at the speed of light and that the difference of altitudes between the elve and the lightning is $h_0 - h_{lightning}$. At the moment τ_1 , the distance r_1 between the intersection of the wavefront and the lightning is given by

$$r_1 = c\tau_1, \tag{4.49}$$

then we can write the distance A , corresponding to the radius of the

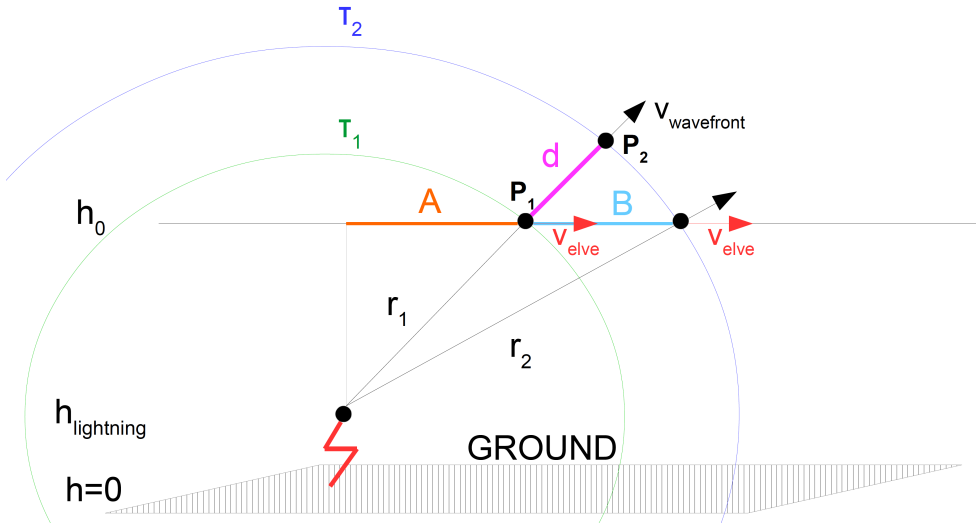


Figure 4.16: Expansion of the elve wavefront and the elve radius during a time of $\tau = \tau_2 - \tau_1$. Lightning and elve are located at altitudes of $h_{lightning}$ and h_0 , respectively. The elve wavefront propagates at the velocity of light.

elve at a time of τ_1 , as

$$A = \sqrt{c^2\tau_1^2 - (h_0 - h_{lightning})^2}. \quad (4.50)$$

If now we call B the radius of the elve at a time $\tau_2 > \tau_1$, we can calculate the expansion of the elve radius during the time $\tau_2 - \tau_1$ as

$$B - A = \sqrt{c^2\tau_2^2 - (h_0 - h_{lightning})^2} - \sqrt{c^2\tau_1^2 - (h_0 - h_{lightning})^2} > d, \quad (4.51)$$

while the elve wavefront would have advanced a distance of only $d = c(\tau_2 - \tau_1)$. We plot in figure 4.17 the advance of the wavefront and the radius of the elve during 0.1 ms for different times after the onset of the parent lightning. It can be clearly seen that the radius of the elve expands faster than the wavefront, which travels at the speed of light.

Therefore, the first observed photon would be the one that travels the minimum path from the source to the photometer. We can calculate the time of flight of that photon by minimizing equation (4.9), obtaining the minimum optical path (s_{min}). The time at which $s(t) = s_{min}$ is the time

4. ANALYSIS OF OPTICAL SIGNALS EMITTED BY TLES

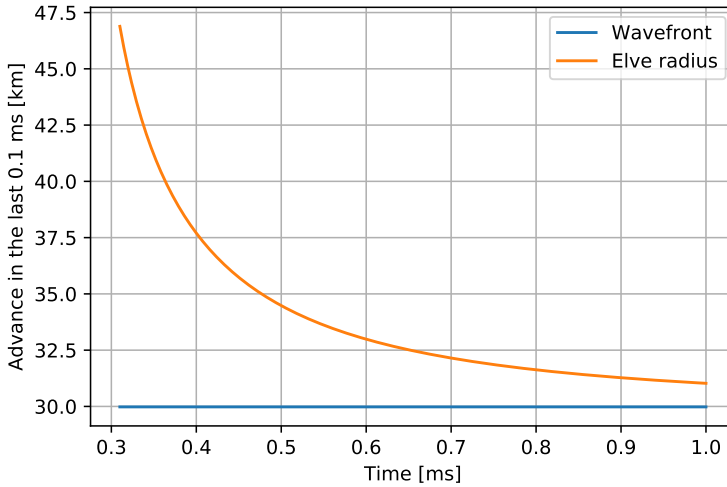


Figure 4.17: The horizontal axis corresponds to the time since the beginning of the parent lightning. In the vertical axis we plot the advance of the wavefront and the radius of the elve during 0.1 ms before the corresponding time plotted in the horizontal axis.

after the elve onset at which the photon was emitted (t_{min}). The time of flight of that photon is then given by $\frac{s_{min}}{c}$. We can finally estimate the moment at which the source started its emissions in relation with the moment of detection of the first photon as the sum of the time of flight of the first detected photon and the time at which it was emitted as

$$t_E = \frac{s_{min}}{c} + t_{min}. \quad (4.52)$$

The last step before applying the inversion method is to convert the detected signal (figure 4.15) from W/m^2 to ph/s . To do that, we use multiply the signal by the area of the detector of radius 12 mm. We also divide by the signal by the energy of the received photons. The photons received by the photometer PH1 have wavelengths between 150 nm and 280 nm. As most of the photons emitted by the elve have wavelengths closer to 150 nm rather than to 280 nm (chapter 3), we calculate this energy as the corresponding energy of a photon with a wavelength of 180 nm. The observed signal in

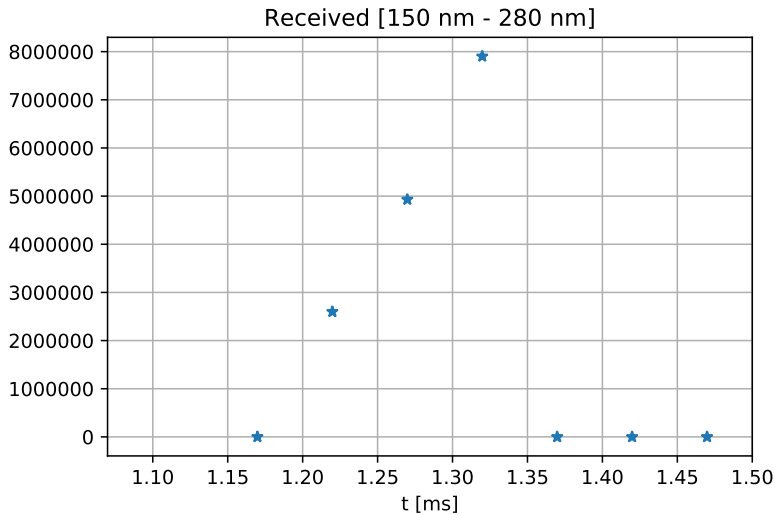


Figure 4.18: Photons received by GLIMS in the 150 nm - 280 nm band from an elve.

ph/s is shown in figure 4.18.

As we explained in subsection 4.2.2.2, the first step of the inversion procedure is to apply a Wiener deconvolution to the observed signal to obtain the signal of a thin ring. We show in figure 4.19 the signal after applying the Wiener deconvolution.

Then, we can apply the Hanson method to the signal of figure 4.19 in order to obtain the temporal evolution of the emitted signal by a thin ring. We plot the source in figure 4.20.

However, the obtained emitting source corresponds to the source of a thin ring. Therefore, we can obtain the real emitting source by convoluting the obtained emitting source of an instantaneous thin ring with its corresponding decay function. The final emitting source is shown in figure 4.21.

4. ANALYSIS OF OPTICAL SIGNALS EMITTED BY TLES

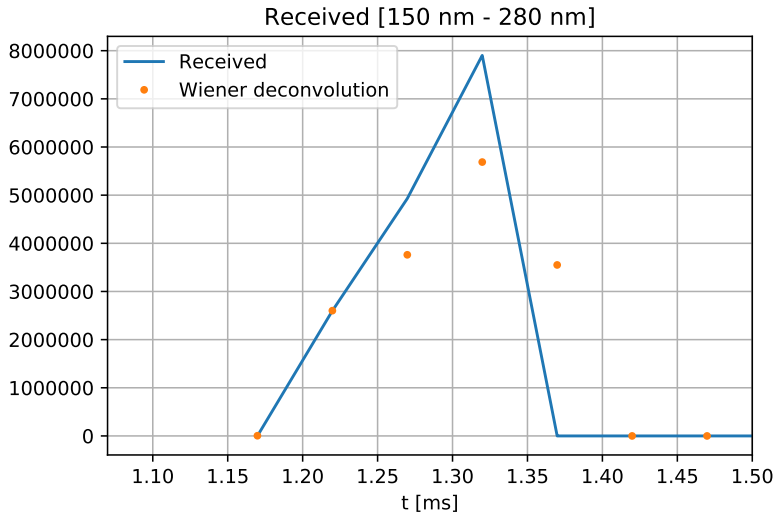


Figure 4.19: Signal plotted in figure 4.18 after the application of the Wiener deconvolution in order to approximate the elve as a thin ring.

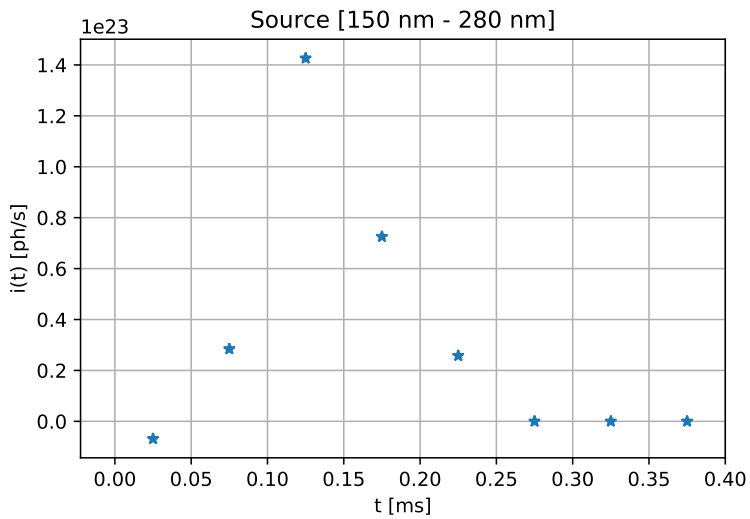


Figure 4.20: Emitting source for an instantaneous thin ring.

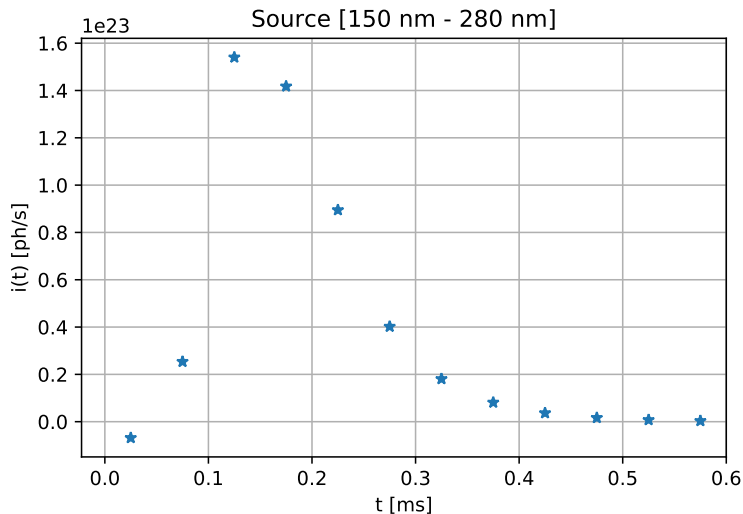


Figure 4.21: Source plotted in figure 4.20 after the convolution with the corresponding decay function in order to obtain the emitting source. This source emits photons with wavelengths between 150 nm and 280 nm.

We can now use the FDTD elve model developed in chapter 3 to explore the current peak of the parent lightning that would produce an elve with an emitting source similar to the one shown in figure 4.21. We plot a comparison between the obtained result and a simulated emitting source in figure 4.22 for a CG lightning discharge with current peak of 83 kA. After comparing both curves, we can conclude that the analyzed elve detected by GLIMS was triggered by a CG lightning discharges with a current peak slightly below 83 kA.

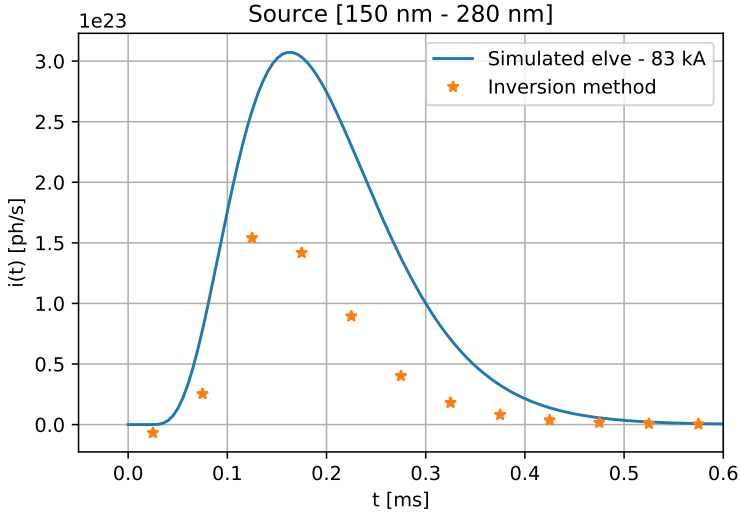


Figure 4.22: Comparison between the source intensity derived using the inversion method and the simulated intensity emitted by an elve triggered by a CG lightning discharge with current peak of 83 kA. The simulated emitted intensity has been calculated using the FDTD elve model developed in chapter 3.

4.3.2.2 Remarks about the possibility of applying the inversion method to signals reported by other space missions

In the last section we have applied the inversion method described in subsection 4.2.2.2 to an elve signal reported by GLIMS in a range of wavelengths between 150 nm and 280 nm. We mentioned that, in general, it is not possible to apply this method to the optical signals detected in other frequencies, as the lightning would contaminate them. However, the detection of an elve whose parent lightning is out of the photometer FOV could be analyzed with our method providing that the position of the lightning stroke is known. A lightning detection network (local or global) could provide this information.

In the case of ASIM and TARANIS, the FOV of the photometers and the optical cameras are the same. Therefore, if an elve is detected without its parent-lightning, the picture of the elve taken by the optical cameras could be useful to estimate the position of the elve center and the lightning. In the

case of ASIM, the photometers and the optical cameras will be part of the Modular Multispectral Imagin Array (MMIA). The cameras record at 12 fps. However, the weak intensity of elves observed at the nadir difficults their detection by the cameras. If the optical cameras of ASIM and TARANIS are not sensible enough to distinguish the shape of the elves, some detection network, as in the case of GLIMS, must give the position of the lightning stroke.

The case of ISUAL is different, as it is capable of reporting elves taking place behind the limb without the contamination of the parent lightning. However, our inversion method is highly dependent of the elve position. *Kuo et al.* (2007) developed a procedure to obtain the distance between ISUAL and the elve center using the optical cameras. However, we think that this procedure is not accurate enough to be used together with our inversion method. Therefore, a lightning detection network must probably give the position of the elve center, determined by the location of the parent lightning.

4. ANALYSIS OF OPTICAL SIGNALS EMITTED BY TLES

Chapter 5

Signature of possible lightning from the Venusian atmosphere

5.1 Introduction

Venus is a terrestrial-like planet with a dense atmosphere mainly composed by carbon dioxide, nitrogen and traces of other gases, as atomic oxygen or carbon monoxide. Despite its proximity to the Earth, some features of the Venusian atmosphere remain unknown. It is for example the case of the long standing controversy regarding the existence of lightning in Venus. As explained in subsection 1.3.2, some electromagnetic signals reported by orbiters suggest that lightning discharges can take place on Venus. However, the lack of unambiguous optical detection keep the existence of Venusian lightning unclear.

The Pioneer Venus Orbiter (PVO) and the Venus Express (VEX) spacecraft reported some of the most solid electromagnetic signatures supporting the possible existence of lightning in Venus. The nature of the pulses reported by these spacecraft has been discussed by some authors (*Scarf et al.*, 1980; *Huba*, 1992; *Huba and Rowland*, 1993; *Strangeway et al.*, 1993; *Strangeway*, 1995; *Cole and Hoegy*, 1997; *Strangeway*, 2003; *Russell et al.*, 2013), but the controversy remains. However, as we explained in subsection 1.3.2,

5. SIGNATURE OF POSSIBLE LIGHTNING FROM THE VENUSIAN ATMOSPHERE

other spacecraft did not succeed in the search of electromagnetical or optical Venusian lightning signatures.

Possible Venusian lightning are expected to take place in the cloud layer between 40 km and 65 km of altitude. Pressure at such altitudes is between 1 bar and 50 mbar, similar to the pressure where terrestrial lightning take place. The high altitude of the Venusian clouds together with the high pressure at ground level would favor the inception of cloud lightning discharges rather than CG lightning discharges (see figure 1.18). According to some laboratory experiments with discharges in CO₂, the oxygen atomic line O 777.6 nm would dominate the spectra of Venusian lightnings (*Borucki et al.*, 1996).

Another important factor to determine the detectability of Venusian lightning is the optical energy that would be emitted by each stroke. Based on optical bursts reported by the Soviet Veneras 9 and 10, *Krasnopolsky* (1980) estimated that the total energy released by Venusian lightning ranges between 8×10^8 J and 10^{10} J. These values are similar to the energy released by terrestrial lightning discharges. In addition to the estimation of the total energy released by Venusian strokes, laboratory experiments demonstrated that the optical efficiency of hypothetical Venusian lightning would be very similar to the efficiency of terrestrial lightning (*Borucki and McKay*, 1987). However, the dense and opaque cloud layer of Venus could prevent lightning-produced optical emissions to be seen from space (*Yair et al.*, 2008).

Difficulties in the detection of Venusian lightning from space led *Yair et al.* (2009) to propose the search of Venusian TLEs as an indirect evidence of electrical discharges in the planet. *Yair et al.* (2009) investigated the possibility of TLE inception in the lower ionosphere of Venus. According to their estimation, cloud discharges with CMCs about 500 C km could trigger halos or sprites between 80 km and 90 km of altitude. One year later, *Dubrovin et al.* (2010) conducted a laboratory experiment simulating possible Venusian TLE glows at 65 km of altitude (about 50 mbar) of pressure. *Dubrovin et al.* (2010) reported the detection of optical emissions in the 300 - 400 nm and the 400 - 700 nm ranges, associated to the second positive system (SPS) and the first positive system (FPS) of N₂, as well as in several CO transitions.

The Japanese Akatsuki probe, currently orbiting the Venusian atmosphere, is equipped with a high temporal resolution camera called Lightning and Airglow Camera (LAC) capable of recording optical flashes from the Venusian atmosphere in the 777 nm line. Another objective of the LAC instrument is the investigation of the Venusian nightglow in the 557 nm spectral line (*Takahashi et al.*, 2008; *Peralta et al.*, 2016).

The aim of this chapter is twofold. On the one hand, we present results about modeling of possible TLEs in Venus and their detection as an indirect evidence of the existence of Venusian lightning. For this purpose, we simulate possible Venusian halos and elves using the halo and elve models described in sections 2.2 and 2.3.2. According to our results, both hypothetical Venusian halos and elves could emit light in the 557 nm line, one of the spectral lines in which the Akatsuki probe can observe the planet (*Peralta et al.*, 2016). These results are detailed in *Pérez-Invernón et al.* (2016b, 2017b). On the other hand, we model the lightning-produced whistler wave propagation through the atmosphere of Venus using the FWM developed by *Lehtinen and Inan* (2008) in order to compare our results with electromagnetic pulses recorded by POV and VEX. We conclude that either the energy released by Venusian lightning or their global occurrence is some orders of magnitude greater than in the case of terrestrial lightning (*Pérez-Invernón et al.*, 2017a).

5.2 The atmosphere of Venus: Mesosphere and ionospheric plasma conditions

The atmosphere of Venus is mainly composed by a mixture of CO₂ and N₂ with a 96.5/3.5 ratio. In addition, there exist important traces of other species, such as CO or O. In this section, we focus on the description of the Venusian upper atmospheric characteristics that are important for TLE inception and for the propagation of lightning-produced electromagnetic pulses up to orbiters.

Electron and ion density profiles are some of the most important characteristics of the atmosphere regarding TLE inception and electromagnetic wave propagation. The available measurements of the Venusian nighttime

5. SIGNATURE OF POSSIBLE LIGHTNING FROM THE VENUSIAN ATMOSPHERE

and daytime electron density at the lowest altitude were recorded by the PVO mission at around 120 km (*Taylor et al.*, 1979; *Bauer et al.*, 1985), while there exist some modeled profiles below 75 km of altitude *Borucki et al.* (1982); *Michael et al.* (2009). The electron and ion composition of the atmosphere between 75 km and 120 km of altitude remains unknown.

According to POV measurements taken above 120 km at nighttime conditions, O_2^+ is the main positive ion species between 120 km and 150 km, while O^+ is dominant at altitudes above 150 km (*Taylor et al.*, 1979; *Bauer et al.*, 1985). Electrons are the most important negatively charged particle species at these altitudes. The lack of measurements below 120 km forces us to use models to estimate ion and electron atmospheric composition. According to *Borucki et al.* (1982) and *Michael et al.* (2009), negative and positive clusters are dominant charge carriers below 60 km of altitude, while electrons and positive clusters are the main charged particles between 60 km and 75 km.

5.2.1 Electric breakdown in the nightside lower ionosphere of Venus

In this section we extend the investigation about the possibility of TLE inception in Venus started by *Yair et al.* (2009) and discuss the atmospheric conditions in the region where they could take place. Before that, it is necessary a good knowledge of the composition of the lower ionosphere of Venus.

Yair et al. (2009) estimated the ignition of Venusian sprites and halos at altitudes between 80 km and 90 km. In order to investigate the inception and evolution of TLEs at such altitudes we first need to know the ambient nighttime electron density profile from the cloud deck ($\simeq 60$ km) up to the lower ionosphere ($\simeq 120$ km). However, as we mentioned before, the electron and ion composition of the atmosphere between 75 km and 120 km of altitude remains unknown.

We have derived approximate electron and ion density profiles in equilibrium (see below) for altitudes between 75 km and 120 km during daytime conditions. For that purpose, we have developed a basic kinetic model solv-

ing the continuity equation of each considered species for a long time up to the equilibrium of the system. The inputs considered by the model are the concentration of some minority neutrals (CO (*Gilli et al.*, 2011), O₂ and O (*Krasnopolsky*, 2010)) together with the total gas density as a function of the altitude from a Venus reference atmosphere (*Lopez-Valverde et al.*, 2007), considering CO₂/N₂ with a 96.5/3.5 ratio. We consider a constant gas temperature of 210 K in the 75 - 120 km altitude range. As sources of ionization, we have implemented ionization profiles from solar extreme ultraviolet (EUV) and X rays and galactic cosmic rays (*Nordheim et al.*, 2015) controlling the ionization of the atmosphere. The solar and cosmic galactic ray ionizing radiation produce electrons and positive ions such as CO₂⁺ and O⁺ and lighter (much less abundant) ions like H⁺ and He⁺ (*Tsang et al.*, 2015). The considered species and the set of chemical reactions are detailed in Appendix A.2. We assume that the concentration of the most abundant neutrals CO₂, N₂, O₂, O and CO remains the same as their input values.

Solid lines in figure 5.1 shows the obtained daytime equilibrium profiles. It is interesting to note that our daytime model solutions agree with, respectively, available model results (*Borucki et al.*, 1982; *Michael et al.*, 2009) at around 70 km (where solar radiation does not influence atmospheric ionization) and with PVO daytime electron density measurements at around 120 km. It should be noted that the dominant positive ions are CO₂⁺ and O₂⁺ (not O⁺) because, according to our model, once O⁺ is produced by the photoionization processes considered (*Nordheim et al.*, 2015) it is rapidly converted into O₂⁺ through the reaction $O^+ + CO_2 \rightarrow CO + O_2^+$. In the altitude range (70 - 125 km) investigated, where the concentration of CO₂ prevails over that of O, our kinetic model predicts that O₂⁺ dominates over O⁺ in agreement with nighttime PVO observations and the Venus International Reference Atmosphere (VIRA) (*Bauer et al.*, 1985).

As terrestrial TLEs often take place at nighttime conditions when the lower ionosphere is positioned at higher altitudes, we are interested in the Venus nightside electron density profile. However, the solar-antisolar circulation driven by day-night contrast in solar heating occurring above $\simeq 110$ km of altitude produces strong winds with speeds of $\simeq 120$ m s⁻¹ (*Bougher et al.*, 2006; *Lellouch et al.*, 1997)) that can influence the nightside

5. SIGNATURE OF POSSIBLE LIGHTNING FROM THE VENUSIAN ATMOSPHERE

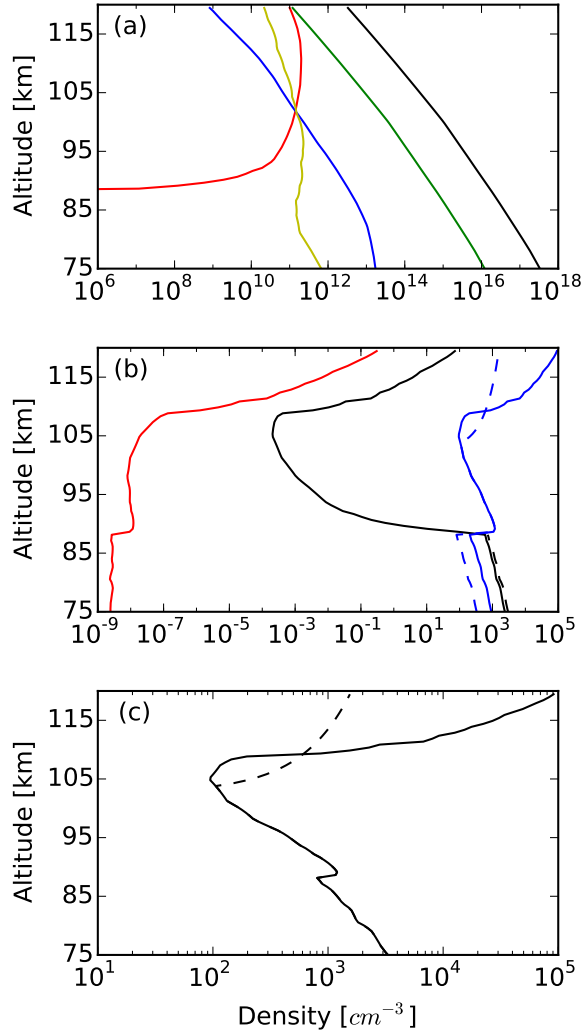


Figure 5.1: Ambient equilibrium daytime (solid lines) and nighttime (dashed lines) concentrations of (a) neutrals CO_2 (black line), N_2 (green line), O_2 (blue line), O (red line) and CO (yellow line), (b) positive ions CO_2^+ (black line), O_2^+ (blue line) and O^+ (red line), and (c) electrons in the mesosphere of Venus as a function of the altitude (Pérez-Invernón *et al.*, 2016b).

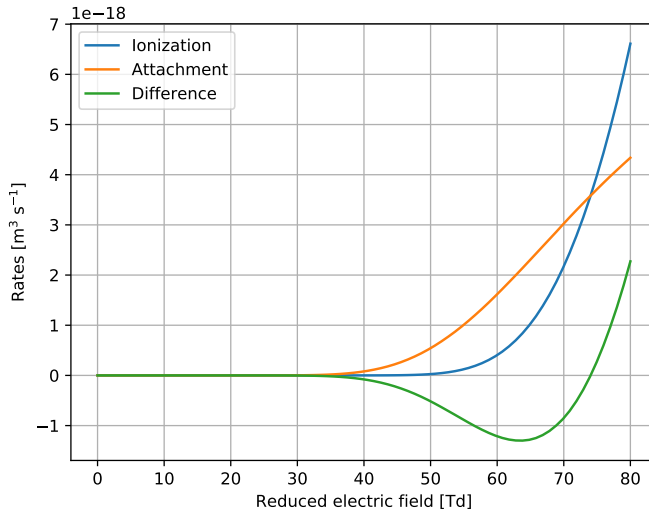


Figure 5.2: Total ionization and attachment rates for a Venusian atmosphere as a function of the reduced electric field. These rates have been calculated with BOLSIG+ (*Hagelaar and Pitchford, 2005*).

electron density profiles carrying electrons and ions from the dayside and our model can not account for the wind effects. Thus, we stop our electron density simulations at $\simeq 105$ km where solar ionization is negligible (*Nordheim et al., 2015*). At this altitude we perform linear interpolation up to the PVO nightside electron density recordings at $\simeq 120$ km.

The obtained nighttime equilibrium profiles are shown in dashed lines in figure 5.1. The maximum electron density in the nighttime profile between 75 km and 120 km is located at around 75 km influenced by the proximity to the maximum of the galactic cosmic ray ionization taking place at 63 km (*Nordheim et al., 2015*).

Now we are able to analyze the electrical breakdown in the Venusian lower ionosphere following the same assumptions made for the terrestrial case (in subsection 3.1.2). In the atmosphere of Venus, the most efficient processes that could trigger TLE inception would be electron-impact ionization of CO_2 and N_2 ($e + \text{CO}_2 / \text{N}_2 \rightarrow \text{CO}_2^+ / \text{N}_2^+ + 2e$). These reactions would compete with electron-driven dissociative attachment of CO_2 ($e +$

5. SIGNATURE OF POSSIBLE LIGHTNING FROM THE VENUSIAN ATMOSPHERE

$\text{CO}_2 \rightarrow \text{CO}^- + \text{O}$) and of CO ($e + \text{CO} \rightarrow \text{O}^- + \text{C}$) in the total budget of electron production under the effect of an electric field. The breakdown electric field is reached when the ionization rate is equal to the attachment rate. We plot in figure 5.2 these quantities, noticing that the value of the breakdown reduced electric field is about 74 Td.

Finally, we can also estimate both the electron mobility and the conductivity in the Venusian lower ionosphere for nighttime conditions. The electron mobility is obtained by calculating the electron energy distribution function (*Hagelaar and Pitchford, 2005*) in a gas mixture with the proportions of the Venus atmosphere and assuming a negligible ($\simeq 0$ Td) ambient reduced electric field. We plot these quantities in figure 5.3, where the mobility is scaled up for the different pressures (altitudes) considered. These calculated values of the mobility and conductivity of ambient nighttime electrons show a growing trend with increasing altitudes and their lower bound (70 - 80 km) values agree well with previous calculations by *Michael et al.* (2009) in the absence of cloud particles and available only up to altitudes of 70 km.

Let us now estimate the altitudes where Venusian TLEs could be triggered. We plot in Figure 5.4 the Maxwell relaxation time and the effective ionization time (inverse of the difference between total ionization and attachment frequencies) for the nighttime electron density profile in the mesosphere of Venus calculated for three values of the reduced electric field close to breakdown ($E/N = 80$ Td $\simeq 1.1 E_k/N$), for $E/N = 148$ Td = $2 E_k/N$ and for $E_k/N = 0$ Td. We note that electric breakdown would occur less than a millisecond after the application of the field and at altitudes between $\simeq 95$ km and $\simeq 100$ km.

5.2.2 Model of a cloud discharge in the atmosphere of Venus

The exploration of Venus performed by the Venus Express spacecraft provided detailed information about the characteristics of the Venusian clouds (*Markiewicz et al., 2007*). The thick cloud layer that covers Venus is composed by sulfuric acid, aerosols and SO_2 . The dynamic of these clouds is determined by the influence of the strong horizontal winds that are charac-

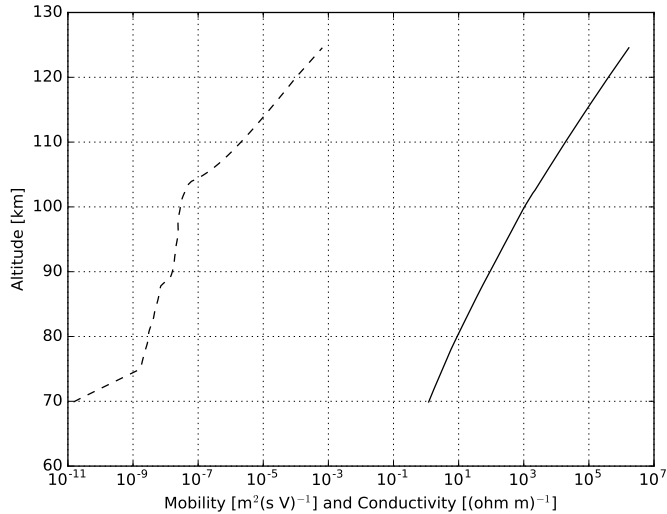


Figure 5.3: Electron mobility (solid line) and conductivity (dashed line) ($\sigma = e\mu_e N_e$) of nighttime electrons in the mesosphere of Venus assuming $E/N = 0$ Td(ambient conditions) (Pérez-Invernón *et al.*, 2016b).

teristics in Venus together with vertical transport produced by convection. Despite the lack of information about the accumulation of charge inside Venusian clouds, we assume in our study that enough charge is accumulated in order to trigger Venusian lightnings.

Let us now model the characteristics of a possible Venusian cloud discharge as seen from the lower ionosphere. As we explained above, Venusian lightning discharges would probably take place between or within clouds in the 40 km - 65 km altitude range, inside a layer of sulfuric acid clouds. These hypothetical cloud discharges would produce an electromagnetic field that could have some effect in the lower ionosphere, as proposed by *Yair et al.* (2009).

As in the case of the Earth, Venusian halos would be produced by the effect of lightning-driven quasielectrostatic fields in the lower ionosphere. Terrestrial halos are usually associated to CG lightning discharges, while Venusian halos would be triggered by cloud discharges. This type of discharge can be considered as an electric dipole (p) that induces negative electric

5. SIGNATURE OF POSSIBLE LIGHTNING FROM THE VENUSIAN ATMOSPHERE

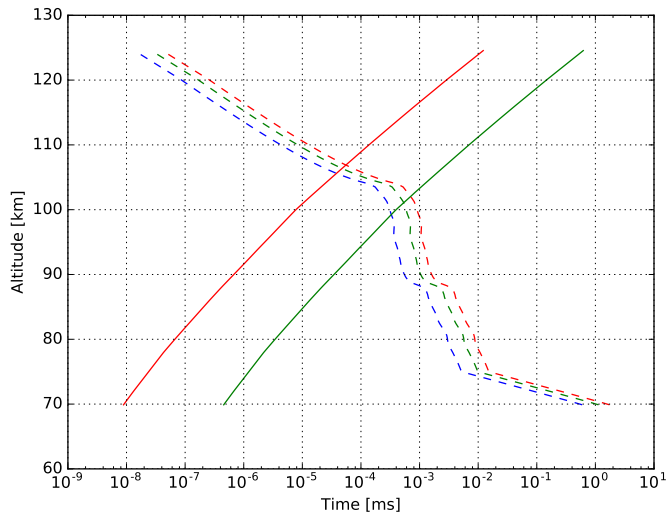


Figure 5.4: Maxwell relaxation times for $E/N = 0$ (ambient conditions) (dashed blue line), $E/N = 80$ Td (dashed green line) and $E/N = 2 E_k/N$ (dashed red line). Effective ionization times for $E/N = 80$ Td (solid green line) and $E/N = 2 E_k/N$ (solid red line). (*Pérez-Invernón et al.*, 2016b).

charge in the upper atmospheric layers immediately below the ionosphere. The total quasielectrostatic field in the ionosphere is $E = 0 = E_p + E_S$ where E_p and E_S are the electric fields produced by, respectively, the dipole p and a negative screening charge induced by the dipole below the ionosphere. As the cloud discharge proceeds, the induced subionospheric negatively charged layer moves down towards lower mesospheric altitudes so that when the original cloud discharge is gone, that is, when its equivalent electric dipole is discharged, negative charge and its complementary positive charge remain at mesospheric altitudes (between 40 km and 65 km) due to the longer Maxwell relaxation times at lower Venusian altitudes where electrical conductivity is smaller than at ionospheric altitudes (see figure 5.4). The induced negative and positive charge layers at mesospheric altitudes can be imagined as a new emerging electric dipole $p'(t) = p(t) - p(0)$ (with $p'(t = 0) = 0$ and $p(t = 0) = p(0) \neq 0$) that charges up as time progresses and generates a quasielectrostatic field $E_{p(t)'} = E_{p(t)} - E_{p(0)}$. Our cloud discharge lightning model here corresponds to the charging electric dipole. The quasielectrostatic field produced by this dipole could trigger a halo.

Let us now describe the lightning discharge current that we use as input of our halo and elve models. We consider that the center of the cloud lightning discharge channel is located around 45 km above ground where the ambient pressure is 1 bar, at cloud level altitudes. We also assume that the charge centers are vertically separated by a distance $a = 10$ km, that is, the cloud discharge takes place between aligned clouds at 40 km and 50 km above the surface of Venus. Following *Dubrovin et al.* (2014a) we assume that the charge is being accumulated in uniformly charged, non-overlapping identical spheres. We set the radius of these spheres to $R = 2.5$ km, as in the case of the Earth (*Maggio et al.*, 2009). By considering that the total energy released in a Venus cloud lightning discharge ranges between 8×10^8 J and 10^{10} J (*Krasnopolsky*, 1980) and 10^{11} J as an extreme case, the calculation of the electrostatic energy stored by this configuration,

$$U_p = \frac{2Q_T^2}{4\pi\epsilon_0} \left(\frac{3}{5R} - \frac{1}{2a} \right), \quad (5.1)$$

allows to estimate that the total dissipated or accumulated charge Q_T ranges between 15 C and 170 C. The total charge moment change (CMC) associated

5. SIGNATURE OF POSSIBLE LIGHTNING FROM THE VENUSIAN ATMOSPHERE

to these cloud discharges, defined as the product of the transmitted charge and the cloud to ground distance or half the cloud to cloud distance ($M = Q_T a/2$), ranges between 75 C km and 850 C km. We further assume that the current flowing through the lightning channel follows a bi-exponential function of the form

$$I(t) = I_0 (\exp(-t/\tau_1) - \exp(-t/\tau_2)), \quad (5.2)$$

where τ_2 is the rise time of the current wave, typically 10 times faster than the overall duration of the stroke, represented by τ_1 . Considering recent results on the average duration of $\simeq 1$ ms for cloud flashes on the Earth (*Gaopeng et al.*, 2010), we have considered that, for a hypothetical 10 km length lightning channel on Venus, the total cloud lightning discharge duration will be of the order of $\tau_1 = 1$ ms with a rising time $\tau_2 \simeq 0.1 \times \tau_1 = 0.1$ ms in agreement with recordings of IC lightning times on Earth (*Rakov and Uman*, 2003). Finally, the accumulated electric charge in our Venus cloud lightning discharge model grows as

$$Q(t) = \int_0^t I(t') dt', \quad (5.3)$$

so that $Q(t=0) = 0$ and $Q(t \rightarrow \infty) = Q_T$.

We can estimate the capability of this kind of cloud discharge for triggering halos and elves. As in the case of electromagnetic fields produced by terrestrial lightning discharges (subsection 3.1.2), we can use equation 3.2 to calculate the quasielectrostatic, induction and radiation fields produced by a Venusian discharge in the lower ionosphere. We plot the temporal evolution of those field components in figure 5.5. According to the right panel, the proposed cloud discharge would be able to produce reduced electric field higher than the breakdown field, triggering Venusian TLEs. In addition, the left panel shows that the radiation field component can be higher than the quasielectrostatic field for times shorter than 0.1 ms. The importance of the radiation field at short times near 100 km of altitude implies that Venusian elves could be triggered by possible lightning.

The detection of these hypothetical TLEs would provide an indirect evidence of the existence of Venusian lightning discharges. About this possibility, it is worth mentioning that the existence of lightning induced transient

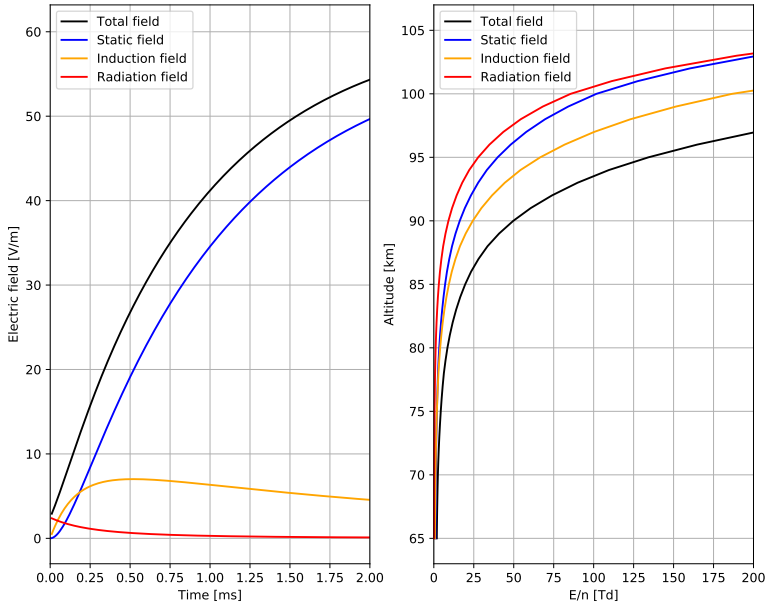


Figure 5.5: Time evolution of the applied electric field components due to an in-cloud discharge with a released energy of 10^{10} J calculated according to equation (3.2). The left panel shows the value of the field components at 100 km vs time, while the right panel shows the maximum value of each reduced electric field component at different altitudes for a discharge with a characteristic time of 0.1 ms. We do not take into account the effect of the ionosphere in this plots.

5. SIGNATURE OF POSSIBLE LIGHTNING FROM THE VENUSIAN ATMOSPHERE

airglow enhancements in the Earth was detected for the first time from the space shuttle. On October 1990, the shuttle Discovery (on mission STS-41) in orbit at 296 km to 327 km altitude recorded (in the 360 nm - 720 nm range) a sequence of sudden brightening at the altitude of the airglow layer in coincidence with lightning flashes (*Boeck et al.*, 1992). The region of enhanced luminosity was 10 km to 20 km thick and around 500 km in diameter with a brightness of about twice that of the background airglow *Boeck et al.* (1992). We now know that what space Shuttles recorded were the fast ($\ll 1$ ms) transient optical emissions of the first and second positive systems of N_2 excited by elves (*Fukunishi et al.*, 1996), (*Israelevich et al.*, 2004). Halos, due to the lightning-induced quasielectrostatic electric fields, have characteristic scales of $\simeq 100$ km (shorter than elves) but last longer, about ten times more or $\simeq 1$ ms.

5.2.3 Plasma conditions in the ionosphere of Venus

In this section we discuss the characteristics of the ionospheric plasma that can interact with electromagnetic waves propagating from hypothetical Venusian lightning up to spacecraft. The electromagnetic measurements taken by PVO and VEX spacecraft that could be possibly related to lightning events in Venus are within the ELF (defined as 300–3000 Hz) and VLF (3 kHz–30 kHz) range of frequencies. On Earth, waves in this range of frequencies can travel through the ionosphere and magnetosphere as right-hand circularly polarized whistler-mode waves, following the geomagnetic field lines or irregularities in the electron and ion density profiles. During propagation, they may also undergo amplification by interacting with energetic charged particles in the plasma. In the Earth ionosphere, attenuation in this frequency range is usually low enough so that the waves are detectable from spacecraft. A wave is called ducted when its propagation is restricted to irregularities in the ionosphere with a layer or tube structure where the refractive index gradient allows this region to behave as a cavity that guides the radio signals. On the contrary, a wave is non-ducted when there is no such guiding irregularity, so that the wave suffers attenuation due to geometric divergence as the wave front expands. Figure 5.6 illustrates

the different propagation of ducted and unducted whistler waves through the atmosphere of the Earth.

Ducted waves are not subject to such geometric attenuation because the wave front does not expand, being restricted to the transverse size of the irregularity. We should note here, however, that the geometric attenuation may also be small in the case of whistler waves in the Earth's ionosphere and magnetosphere, due to their propagation being restricted to the cone within the Storey angle (*Storey, 1953*). Some studies suggest that the ducted wave propagation mode is also possible on the Earth magnetosphere (*Cerisier, 1974; Loi et al., 2015*). For an introduction to whistler-mode propagation through the ionosphere and its peculiarities in relation with other propagation modes we refer to the textbooks by *Helliwell (1965)* and *Budden (1985)*.

In the case of Venus, the lack of an intrinsic magnetic field would prevent whistler propagation through its ionosphere. However, the solar wind interaction with its ionosphere induces a magnetic field of complex structure with values of the order of tens of nT (*Marubashi et al., 1985*). This complex structure is illustrated in figure 5.7.

Whistler wave propagation through the ionosphere of Venus is determined by the background magnetic field and particle collision frequency profiles. The attenuation mostly depends on electron-neutral, ion-neutral and electron-ion collisions. Although electron-ion collision frequency is greater than electron-neutral collisions above 140 km under typical Venus ionospheric conditions, we have the opposite situation in ionospheric holes (*Huba, 1992; Huba and Rowland, 1993*). For this reason, we have only included electron-neutral and ion-neutral collisions in our scheme. Electron-neutral and ion-neutral collision frequencies, denoted respectively as ν_e and ν_i , depend on electron mobility K_e and ion mobility K_i as

$$\nu_{e,i} = \frac{e}{K_{e,i} m_{e,i}}, \quad (5.4)$$

where e and m_e are the electron charge and mass, respectively. We obtain the mobility of electrons in the ionospheric plasma from BOLSIG+ (*Hagelaar and Pitchford, 2005*). In the case of ions, we calculate the mobility

5. SIGNATURE OF POSSIBLE LIGHTNING FROM THE VENUSIAN ATMOSPHERE

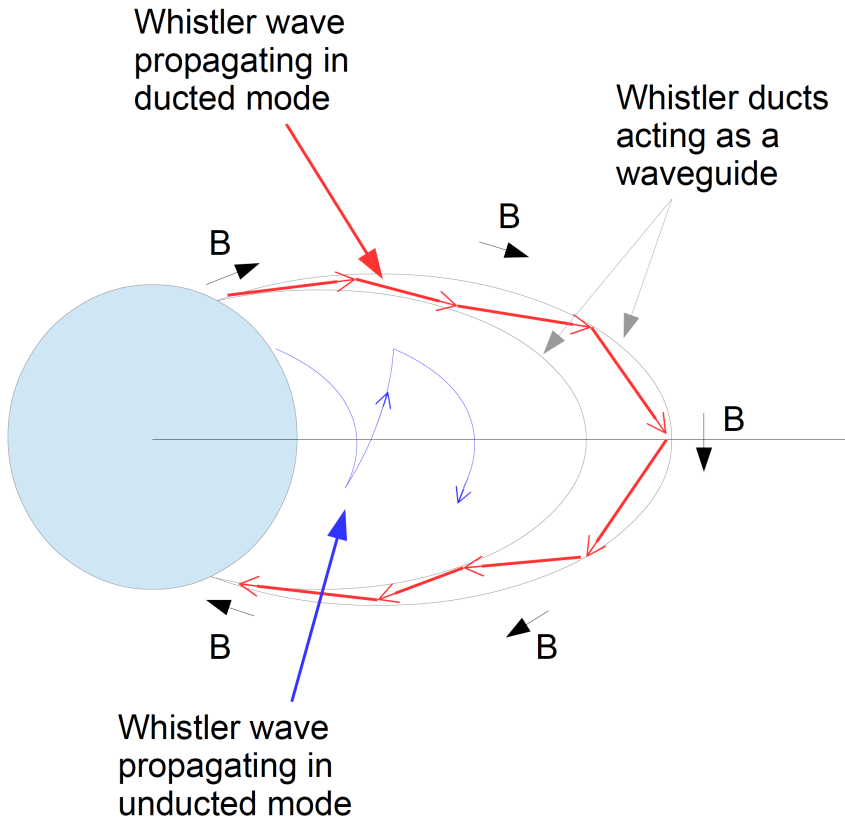


Figure 5.6: Representation of the propagation of ducted and unducted whistler waves through the magnetosphere of the Earth. The direction of the background magnetic field is also represented. The unducted whistler wave can be reflected when its frequency is equal to the local lower hybrid resonance frequency.

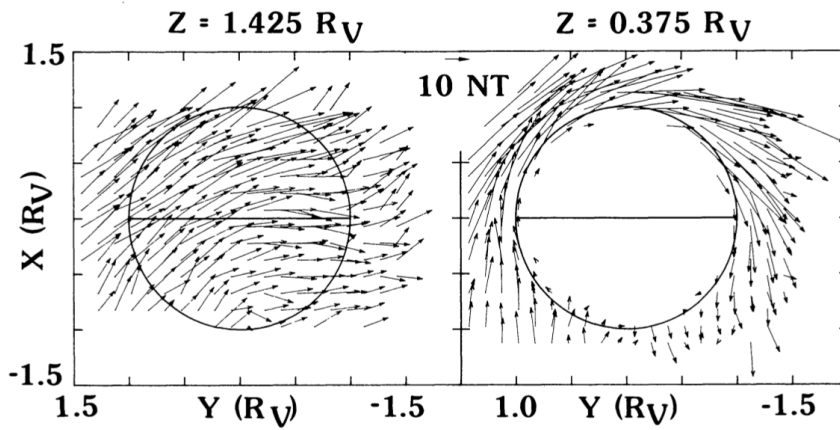


Figure 5.7: Structure of the magnetic field vector induced in the atmosphere of Venus by solar winds in the \mathbf{X} and \mathbf{Y} directions. R_V denotes distances in terms of the planetary radius. Data are folded into a single $+\mathbf{Z}$ hemisphere. Each panel represents a Z position range of $\pm 0.075 R_V$. These magnetic fields have been obtained by PVO measurements near the solar maximum. The vector labelled as 10 nT represents a magnetic field vector with a module of 10 nT. Adapted from *Phillips et al.* (1986).

5. SIGNATURE OF POSSIBLE LIGHTNING FROM THE VENUSIAN ATMOSPHERE

of each considered ion following *Mcdaniel and Mason (1973)* and *Borucki et al. (1982)* as

$$K_i = 3.74 \times 10^{20} (M_i \xi)^{-0.5} n^{-1} [cm^2 V^{-1} s^{-1}], \quad (5.5)$$

where n is the number density of the atmosphere at a given altitude, ξ is the polarizability of CO_2 , and M_i is the reduced mass of the ion, related to the mass of each ion (m_i) and the mass of CO_2 molecules (m_{CO_2}), as given by

$$M_i = \frac{m_i m_{CO_2}}{m_i + m_{CO_2}}. \quad (5.6)$$

Strangeway (1996) obtained that the collisional Joule dissipation can be important in the lower ionosphere of Venus for electric field amplitudes between 10 mV/m and 100 mV/m. However, the electric fields obtained in our work are below these values. Therefore, we neglect the effect of the collisional Joule dissipation.

According to the PVO measurements taken above 120 km altitude at nighttime conditions, O_2^+ is the main positive ion species between 120 km and 150 km, while O^+ is dominant at altitudes above 150 km (*Taylor et al., 1979; Bauer et al., 1985*). Electrons are the most important negatively charged particle species at these altitudes. The lack of measurements below 120 km forces us to use models to estimate ion and electron atmospheric composition. According to *Borucki et al. (1982)* and *Michael et al. (2009)*, negative and positive clusters are dominant charge carriers below 60 km of altitude, while electrons and positive clusters are the main charged particles between 60 km and 75 km. We use here the calculated electron and ion density profiles calculated by *Pérez-Invernón et al. (2016b)*, where electrons, O_2^+ and CO_2^+ ions are the dominant charged particles between the altitudes 75 km and 120 km.

Both the orientation and value of the background magnetic field are crucial in the propagation of a wave through a plasma. Whistler mode propagation is more feasible when the background magnetic field is parallel to the wave propagation direction. On the other hand, this propagation is prevented by a horizontal background magnetic field. Following this rea-

soning, figure 5.7 shows that whistler wave propagation would only be possible at some concrete locations and moments depending on the momentary configuration of the background magnetic field. According to PVO and VEX measurements, the observation of whistler waves coincided with vertical background magnetic field orientation and holes in the charged particle density profiles (*Taylor et al., 1979; Strangeway, 2003; Russell et al., 2013*).

Let us now analyze the possibility of whistler wave propagation given the characteristic of the Venusian ionospheric plasma. For that purpose, we use the Clemmow-Mullay-Allis (CMA) diagram for a two-component plasma (see figure 5.8)

This diagram demonstrates different plasma wave modes for a given frequency ω , depending on the relation between that frequency, the electron gyrofrequency Ω_e and electron plasma frequency ω_{pe} determined by the plasma. Namely, the diagram shows different regions in which ω is smaller or greater than Ω_e and ω_{pe} , explaining the propagation mode of the electromagnetic wave for each case.

For parameters relevant to our study the wave propagation is not very affected by ions, as in the case of a background magnetic field of 10 nT the lower hybrid frequency and the ion gyrofrequency are below 5 Hz and 2×10^2 Hz, respectively.

The Budden parameters (*Budden, 1985*) $Y = \Omega_e/\omega$ and $X = \omega_{pe}^2/\omega^2$ serve as the ordinate and the abscissa of the diagram, and the values of the parameters

$$R = 1 - \frac{\omega_{pe}^2}{\omega(\omega - \Omega_e)} - \frac{\omega_{pi}^2}{\omega(\omega + \Omega_i)}, \quad (5.7)$$

$$L = 1 - \frac{\omega_{pe}^2}{\omega(\omega + \Omega_e)} - \frac{\omega_{pi}^2}{\omega(\omega - \Omega_i)}, \quad (5.8)$$

$$P = 1 - \frac{\omega_{pe}^2 + \omega_{pi}^2}{\omega^2}, \quad (5.9)$$

and

$$S = \frac{R + L}{2}, \quad (5.10)$$

described in *Stix (1992)*, form the bounding surfaces that determine regions where the wave changes its propagation mode. An electromagnetic

wave propagates in whistler mode when its frequency is lower than the plasma frequency ($\omega \ll \omega_{pe}$) and has a value between the ion gyrofrequency and the electron gyrofrequency ($\Omega_i \ll \omega \ll \Omega_e$). These constraints are represented in the CMA diagram by regions 7 and 8 (*Stix*, 1992, p. 27), where the conditions

$$\frac{\omega_{pe}^2 + \omega_{pi}^2}{\omega^2} > 1 \quad (5.11)$$

and

$$\Omega_e > \omega \quad (5.12)$$

are satisfied.

To analyze the case of whistler waves propagating through the Venusian ionosphere we can assume an electron density peak of $n_{e0} = 3 \times 10^4 \text{ cm}^{-3}$ at nighttime conditions (*Bauer et al.*, 1985) and O^+ ions as the main positive charged particle. We can calculate the electron plasma frequency ω_{pe} , ion plasma frequency ω_{pi} , electron gyrofrequency Ω_e and ion gyrofrequency Ω_i for a wave of frequency 100 Hz with different background magnetic fields. We estimate that whistler-mode propagation conditions in regions 7 and 8 of the CMA diagram are satisfied by a wave of 100 Hz when the vertical component of the background magnetic field is greater than 3.57 nT if the electron density peaks at $3 \times 10^4 \text{ cm}^{-3}$. We also estimate that $\omega_{pe} > 100 \text{ Hz}$ even in electron density holes with the electron density peak reduced up to ~ 8 orders of magnitude (i.e., a factor of $\sim 10^8$), establishing this density value as the lowest at which non-ducted whistler-mode propagation through the Venusian atmosphere is possible. The upper electron density values for a given background magnetic field, on the other hand, are constrained by the condition that attenuation due to electron collisions is low enough for the signals to be detectable.

5.3 Optical signature of possible Venusian TLEs

5.3.1 Description of the models

Following the investigations by *Yair et al.* (2009), we have discussed in subsection 5.2.1 the possibility of halo and elve inception in the lower ionosphere of Venus. In this section we use the models of halos and elves previously described in sections 2.2 and 2.3.2 in order to simulate these types of TLEs in Venus.

Let us start the description of the developed models of Venusian TLEs by introducing the proposed kinetic scheme. We use a chemical scheme formed by the species listed in table A.17 of Appendix A.2. These species interact through the chemical reactions described in table ?? of Appendix A.2. According to the proposed scheme, the main source of ionization that drives the inception and evolution of Venusian TLEs is the reaction $e + \text{CO}_2 \rightarrow \text{CO}_2^+ + 2e$. We include in this proposed chemical model electronic and vibrational excitation of some molecules in the presence of an applied reduced electric field. Optical emissions of terrestrial TLEs are dominated by some spectral features of the N_2 molecule. Optical emissions from some N_2 vibro-rotational band transitions could be possible in the case of the Venusian atmosphere and have been included in our proposed kinetic scheme. In particular, our model computes optical emissions from the LBH, SPS and FPS of N_2 radiating in the ultraviolet (150 - 250 nm), near ultraviolet-blue (250 nm - 450 nm) and in the visible-near infrared (500 nm - 1.5 μm). We have also included infrared emissions corresponding to the transition $\text{N}_2(W^3\Delta_u) \rightarrow \text{N}_2(B^3\Pi_g)$.

Despite the possibility of Venusian TLEs emitting light in the mentioned optical transition, the lower concentration of N_2 in this planetary atmosphere suggest that optical emissions from other spectral molecular bands or atomic lines could also be important. For this reason, we have included electronic excitation of atomic oxygen to the states $\text{O}(^1\text{S})$ and $\text{O}(^1\text{D})$. The $\text{O}(^1\text{S})$ could be produced by electron impact of energetic electrons with CO_2 through the process $e + \text{CO}_2 \rightarrow \text{O}(^1\text{S}) + \text{CO} + e$, while the $\text{O}(^1\text{D})$ would be the product of the radiative deexcitation of $\text{O}(^1\text{S})$. These two excited species can emit photons by radiative decay in the green line at 557.7 nm

and in the red line at 630 nm, respectively. It is interesting to note that emissions in the 557.7 nm line occur in the Venusian nightside continuously as a consequence of the atomic oxygen nightglow. Brightness of these natural emissions changes temporal and spatially between less than 10 R and 167 R (*Slanger et al.*, 2006; *Gray et al.*, 2014).

Finally, we include as a possible source of optical emissions the radiative decay from some vibrational levels of CO₂. These species can be excited by electron impact. However, their densities at ambient conditions ($E/N \simeq 0$ Td) are also important. We include as initial conditions altitude-dependent profiles of eight vibrational levels of CO₂ ((00⁰1), (10⁰0), (01¹0), (02⁰2), (02²2), (03¹0), (03³0) and (11¹0)) previously calculated under steady-state nonlocal thermodynamic equilibrium (N-LTE) (*Lopez-Valverde et al.*, 2007). The reduced kinetic scheme of our discharge model includes electron-impact excitation of CO₂, vibrational-vibrational (VV), vibrational-translational (VT) processes and radiative deexcitation producing IR optical emissions. However, because of the differences between our reduced kinetic scheme and the Non-LTE kinetics used to calculate ambient CO₂(v) concentrations, our discharge model produces $dN_{CO_2(v)}(E/N = 0)/dt = A(v) \neq 0$. In order to have $dN_{CO_2(v)}(E/N = 0)/dt = 0$ we reformulate the continuity equations for the considered CO₂(v) by subtracting $A(v)$ to each of them.

The rest of the details concerning this set of chemical reactions are described in Appendix A.2. This kinetic scheme is coupled with two electro-dynamical models taking as inputs the atmosphere of Venus and a hypothetical lightning discharge. As in the case of the Earth, we simulate halos and elves using the models described in sections 2.2 and 2.3.2, respectively. Let us now describe the peculiarities of the application of these two models to the case of Venus.

For the case of halos, we use the two-dimensional model in cylindrically symmetrical coordinates described in subsection 2.2. We define vertically oriented cloud discharges described in section 5.2.2. In particular, we simulate halos triggered by three cloud discharges with total energy released of 8×10^8 J and 10^{10} J (*Krasnopolsky*, 1980) and 10^{11} J as an extreme case. The channel length is set to 10 km. The spatial domain is composed by a fixed

5. SIGNATURE OF POSSIBLE LIGHTNING FROM THE VENUSIAN ATMOSPHERE

cylindrical grid with a radius of 250 km and a range of altitudes between the ground and 125 km. As in the case of the Earth, both the ground and the ionospheric layer are approximated as a PEC. We use Neumann type boundary conditions at $r = 250$ km for the resolution of the Poisson equation. The advection-diffusion equations of the chemical species are solved in a reduced computational domain between the horizontal distance range from $r = 0$ km $r = 200$ km and for altitudes greater than $z = 70$ km, where the concentration of charged particles becomes important. We impose Neumann type boundary conditions at these domain limits. The time step is set to 10 ns. Each parallelized simulation is run during a time of about 7 days using 10 CPUs.

In the case of elve simulations, we use the three-dimensional model in Cartesian coordinates described in subsection 2.3.2. The inclusion of a third dimension allows us to simulate elves produced by tilted cloud lightning discharges. As in the case of halos, we investigate elves produced by cloud discharges described in subsection 5.2.2. However, in this case we define two cloud discharges whose total energy released are 10^6 J and 10^7 J (similar to terrestrial lightning) (*Maggio et al.*, 2009), other two with energies of 10^{10} J and 2×10^{10} J (*Krasnopolsky*, 1980), and 10^{11} J as an extreme case. We assume again that the channel lightning has a length of 10 km. However, we now change the inclination of the lightning channel simulating elves produced by vertical, horizontal and oblique (45°) lightning discharges. The spatial domain is formed by a three-dimensional mesh where the x and y directions correspond to S-N and W-E directions, and z corresponds to altitude. The lightning discharge is located in the center of the mesh, at an altitude of 45 km. Horizontal distances are between -250 km and 250 km, with a step of 1 km for the vertical and horizontal channel cases and 0.5 km for the oblique channel case, while the altitude domain is between 0 km and 135 km, with a vertical step of 0.5 km. We include 15-cell-wide absorbing boundaries. The continuity equation of the considered species as well as the Ohm's modified equation are exclusively solved where the electron density is important, that is, at altitudes above 70 km (*Borucki et al.*, 1982). The lightning current density will be confined in a tube with a width of one cell. Regarding the time step, we set it to 10 ns, ensuring that the constrains

detailed in section 2.3.2 are satisfied, choosing a time step smaller than the Maxwell relaxation time in the upper domain region, whose value is about 50 ns. We run each parallelized simulation during a time of about 5 days using 10 CPUs.

5.3.2 Results

The previously developed models allow us to investigate the possible inception of halos and elves in the atmosphere of Venus. In this section we present the results of these two models. We discuss the characteristics of the optical emission produced by hypothetical Venusian TLEs, focusing on the predicted brightness in each spectral emission bands.

5.3.2.1 Venusian Halos

We explore the inception of halos in the Venusian atmosphere using the halo model described in subsection 5.3.1. We show in figure 5.9 the reduced electric field in the atmosphere of Venus produced by different lightning discharges. The reduced electric field in the mesosphere reaches higher values than the reduced electric (74 Td) for lightning energies above 10^{10} J. In such situations, halos could be triggered.

If a halo is triggered, ionization would produce an enhancement in the amount of free electrons in the mesosphere. This increase in the number of electrons can be seen in figure 5.10, where we plot the electron density in the atmosphere of Venus under the influence of different lightning discharges. Both figures 5.9 and 5.10 indicates that Venusian halos could be triggered at an altitude of about 100 km if a cloud discharge with 2×10^{10} J of energy takes place in the troposphere.

The calculation of the density of emitting species allow us to compute the total number of emitted photons in several spectral bands and lines. Table 5.1 collects the total emitted photons 1 ms after the onset of the halo in the most important spectral bands considered and for different parent lightning energies.

5. SIGNATURE OF POSSIBLE LIGHTNING FROM THE VENUSIAN ATMOSPHERE

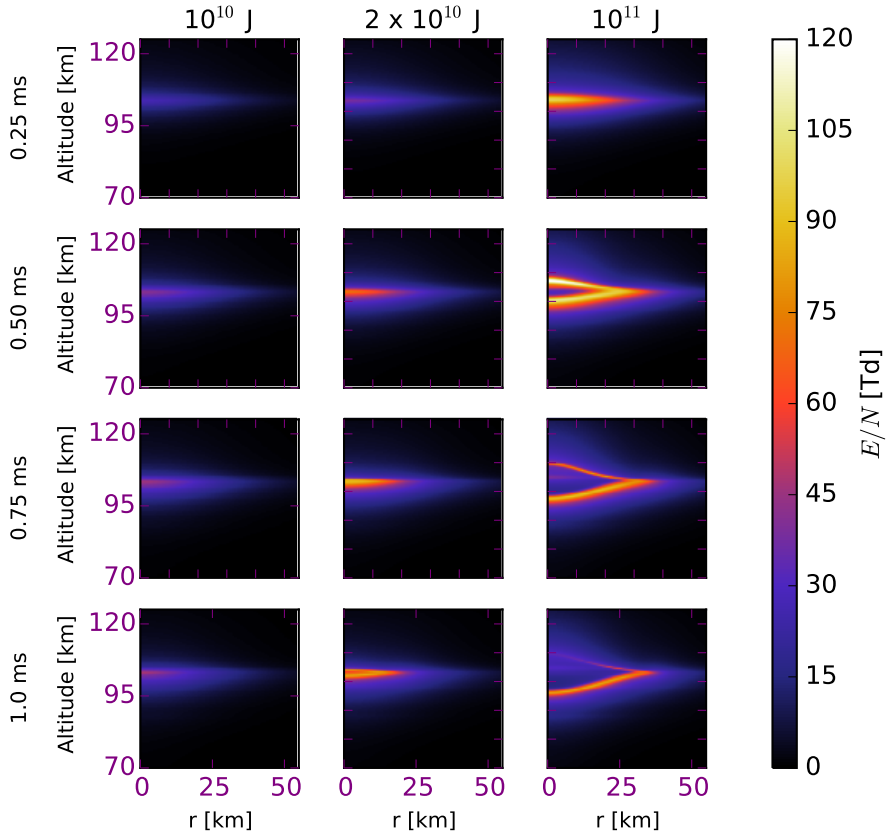


Figure 5.9: Time evolution of the reduced electric field E/N in the atmosphere of Venus under different cloud lightning discharges with total released energy of 10^{10} J, 2×10^{10} J and 10^{11} J. Four snapshots are shown for each energy. The discharge length of the cloud discharge channel in this case is 10 km, and the radius of the spheres (acting as clouds) that contain the charges is set to 2.5 km (*Pérez-Invernón et al.*, 2016b). Note that the reduced breakdown field in the Venusian atmosphere is ~ 75 Td.

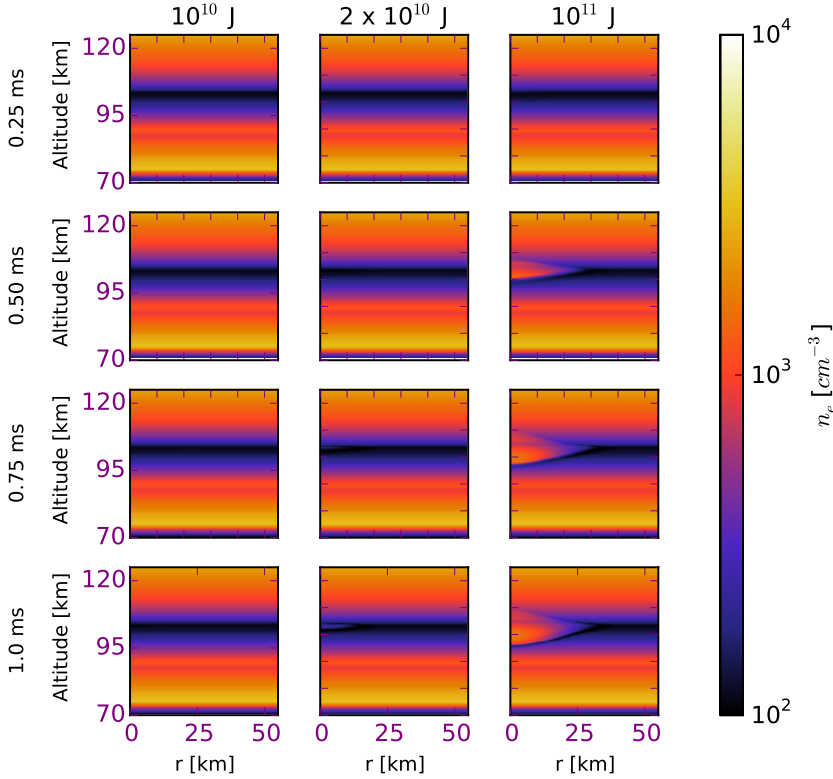


Figure 5.10: Time evolution of the electron density in the atmosphere of Venus under different cloud lightning discharges with total released energy of 10^{10} J, 2×10^{10} J and 10^{11} J. Four snapshots are shown for each energy (Pérez-Invernón *et al.*, 2016b).

5. SIGNATURE OF POSSIBLE LIGHTNING FROM THE VENUSIAN ATMOSPHERE

Transition	Wavelength	Emitted photons (10^{10} J, 2×10^{10} J, 10^{11} J)
$O(^1S) \rightarrow O(^1D)$	557 nm	9.26×10^{16} , 2.45×10^{20} , 1.57×10^{22}
$N_2(B^3\Pi_g \text{ (all } v')) \rightarrow N_2(A^3\Sigma_g^+ \text{ (all } v'))$	550 nm - 1.2 μm	5.26×10^{17} , 3.84×10^{20} , 2.05×10^{22}
$N_2(C^3\Pi_u \text{ (all } v')) \rightarrow N_2(B^3\Pi_g \text{ (all } v'))$	250 - 450 nm	4.24×10^{16} , 9.74×10^{19} , 5.57×10^{21}
$N_2(W^3\Delta_u \text{ (} v' = 0)) \rightarrow N_2(X^1\Sigma_g^+ \text{ (} v'' = 5))$	208 nm	1.27×10^{13} , 7.10×10^{18} , 1.13×10^{20}
$N_2(W^3\Delta_u \text{ (} v' = 0)) \rightarrow N_2(B^3\Pi_g \text{ (} v'' = 0))$	136.10 μm	6.30×10^{13} , 1.43×10^{18} , 2.32×10^{19}
$N_2(a^1\Pi_g \text{ (} v' = 0)) \rightarrow N_2(a'^1\Sigma_u^- \text{ (} v'' = 0))$	8.25 μm	1.77×10^{16} , 1.06×10^{19} , 4.01×10^{20}
$N_2(a^1\Pi_g \text{ (all } v')) \rightarrow N_2(X^1\Sigma_g^+ \text{ (all } v'))$	120 - 280 nm	1.81×10^{17} , 3.00×10^{19} , 2.85×10^{21}

Table 5.1: Total number of emitted photons for cloud lightnings with total released energy of 10^{10} J, 2×10^{10} J and 10^{11} J one millisecond after the onset of the halo (*Pérez-Invernón et al.*, 2016b).

In addition, we plot in figures 5.11-5.14 the time-dependent total number of photons emitted per second from the entire transient glowing halo. The shown optical emissions per second exhibit a sudden increase (up to around 0.4 ms) when the reduced electric field reaches breakdown producing a strong rise in the densities of excited species.

As can be seen in table 5.1, nighttime Venusian halos could emit an important amount of photons in the atomic oxygen green line 557 nm. The spectral line of these emissions coincide with the natural nightglow of Venus, whose brightness varies temporally and spatially between 10 R and 167 R (*Slanger et al.*, 2006; *Gray et al.*, 2014). We calculate the brightness of the halo in the 557 nm line in order to compare it with the nightglow brightness. The optical emission brightness (EB) at a given time in Rayleigh (R) is calculated from the species densities through the classical expression (*Hunten et al.*, 1956):

$$EB(t) = 10^{-6} \int_L V(l, t) dl \quad (5.13)$$

where $V(l, t)$ is the volume emission rate of each species (in photons $\text{cm}^{-3}\text{s}^{-1}$) at a given time, and the integral is taken along the line of sight through the emission volume over an effective column length L . The total number of photons per second emitted at a given time ($E_{h\nu}(t)$) are calculated integrating $V(l, t)$ over the whole volume domain taking into account the cylindrical symmetry:

$$E_{h\nu}(t) = \int_V V(l, t) dV \quad (5.14)$$

The resultant 557 nm brightness of the halo from its center to its outer region is plotted in figure 5.15.

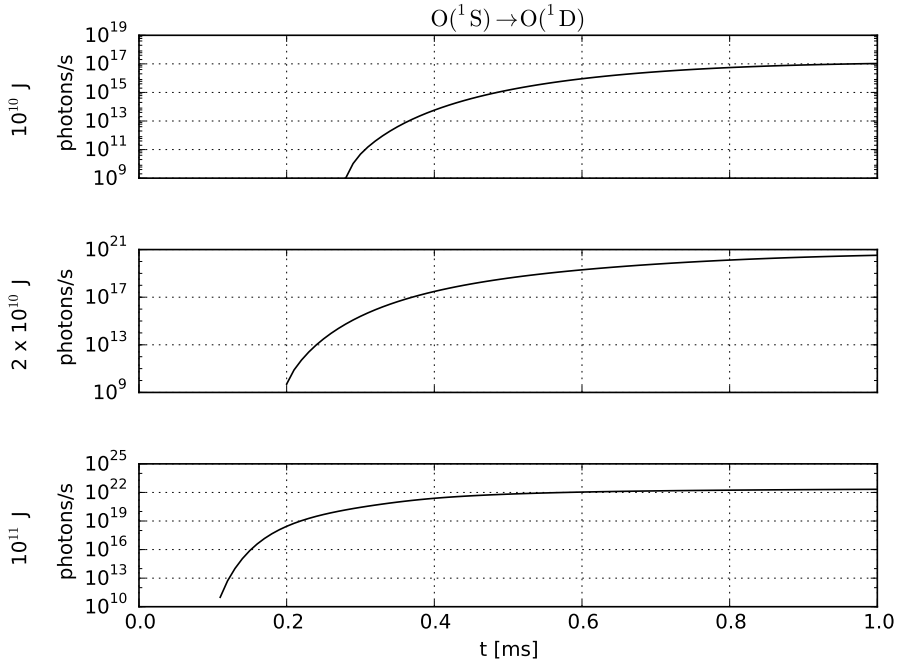


Figure 5.11: Total number of photons per second emitted by the entire halo up to 1 ms due to the radiative decay $O(^1S) \rightarrow O + h\nu$ (557 nm). The considered cloud discharges release a total energy of 10^{10} J (top panel), 2×10^{10} J (middle panel) and 10^{11} J (bottom panel) (*Pérez-Invernón et al., 2016b*).

5. SIGNATURE OF POSSIBLE LIGHTNING FROM THE VENUSIAN ATMOSPHERE

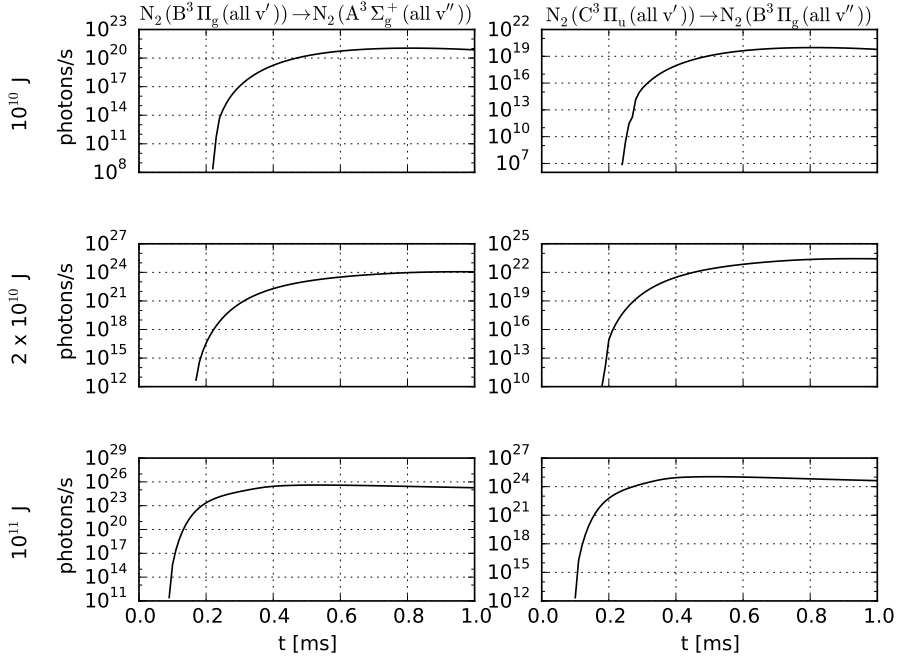


Figure 5.12: Total number of photons per second emitted by the entire halo up to 1 ms due to the radiative decays $\text{N}_2(B^3\Pi_g \text{ (all } v')) \rightarrow \text{N}_2(A^3\Sigma_g^+ \text{ (all } v'')) + h\nu$ (550 nm - 1.2 μm) and $\text{N}_2(C^3\Pi_u \text{ (all } v')) \rightarrow \text{N}_2(B^3\Pi_g \text{ (all } v'')) + h\nu$ (250 - 450 nm). The considered cloud discharges release a total energy of 10^{10} J (top panel), 2×10^{10} J (middle panel) and 10^{11} J (bottom panel) (Pérez-Invernón et al., 2016b).

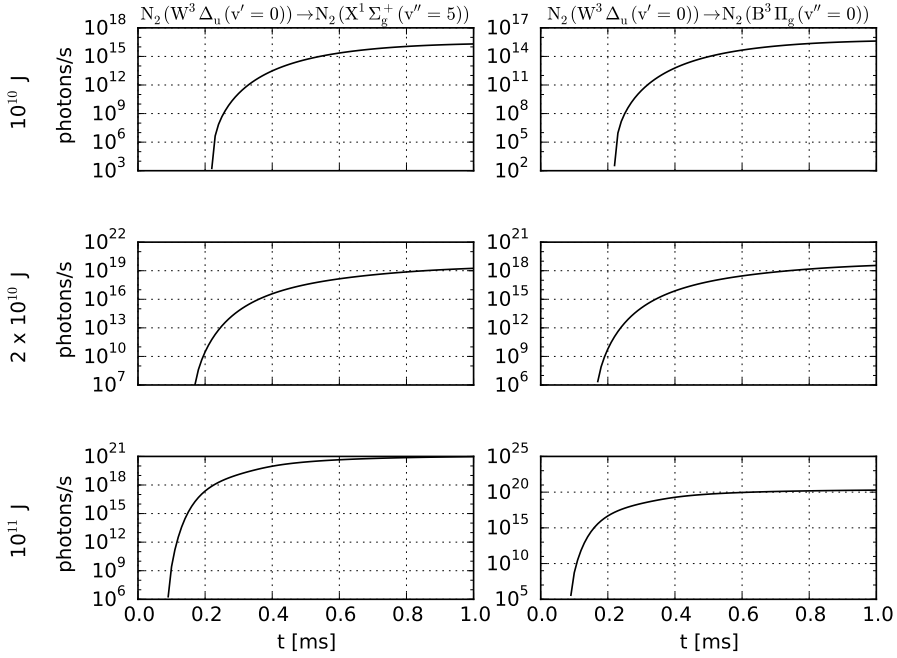


Figure 5.13: Total number of photons per second emitted by the entire halo up to 1 ms due to the radiative decays $N_2(W^3\Delta_u(v'=0)) \rightarrow N_2(X^1\Sigma_g^+(v''=5)) + h\nu$ (208 nm) and $N_2(W^3\Delta_u(v'=0)) \rightarrow N_2(B^3\Pi_g(v''=0)) + h\nu$ (136.10 μm). The considered cloud discharges release a total energy of 10^{10} J (top panel), 2×10^{10} J (middle panel) and 10^{11} J (bottom panel) (Pérez-Invernón *et al.*, 2016b).

5. SIGNATURE OF POSSIBLE LIGHTNING FROM THE VENUSIAN ATMOSPHERE

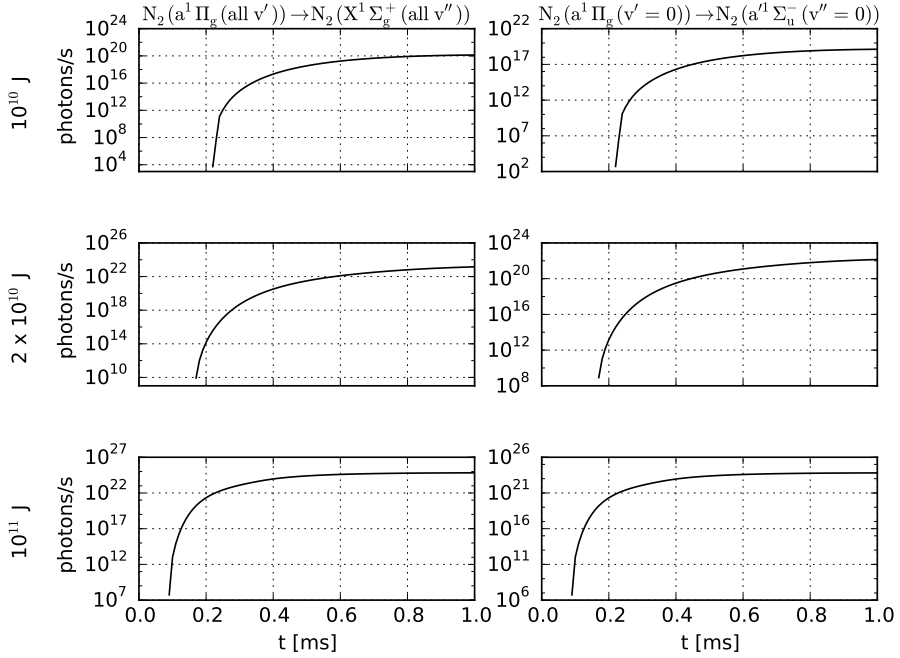


Figure 5.14: Total number of photons per second emitted by the entire halo up to 1 ms due to the radiative decays $N_2(a^1\Pi_g(\text{all } v')) \rightarrow N_2(X^1\Sigma_g^+(\text{all } v'')) + h\nu$ (120 - 280 nm) and $N_2(a^1\Pi_g(v' = 0)) \rightarrow N_2(a^1\Pi_g(v'' = 0)) + h\nu$ (8.25 μm). The considered cloud discharges release a total energy of 10^{10} J (top panel), 2×10^{10} J (middle panel) and 10^{11} J (bottom panel) (Pérez-Invernón *et al.*, 2016b).

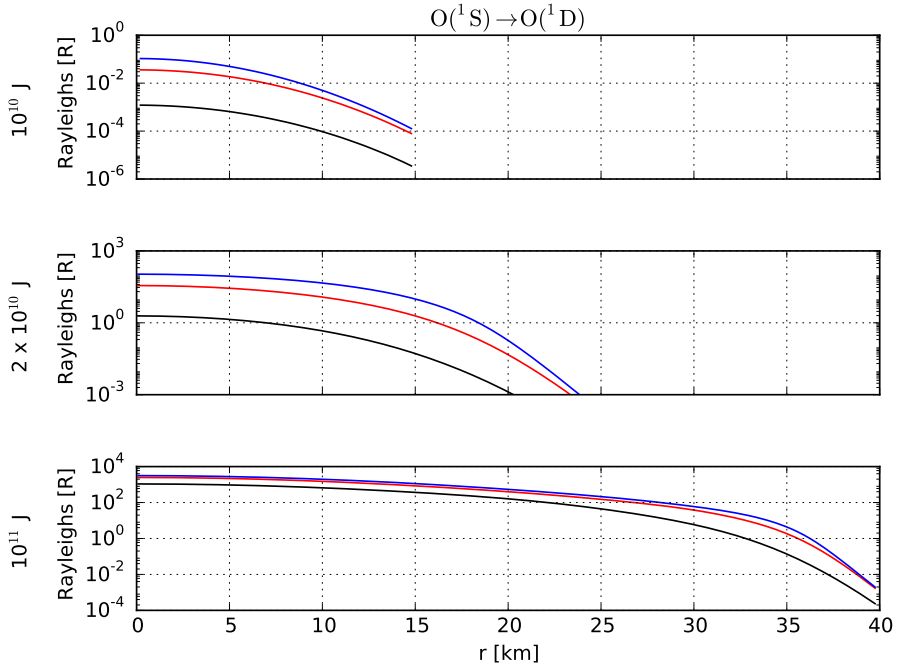


Figure 5.15: Emission brightness in Rayleigh from the radiative decay $O(^1S) \rightarrow O(^1D)$ (557 nm) along different positions of the glowing disc and for different times after the beginning of the IC discharge: 0.5 ms (black line), 0.75 ms (red line) and 1 ms (blue line). The considered cloud discharges release a total energy of 10^{10} J (top panel), 2×10^{10} J (middle panel) and 10^{11} J (bottom panel) (Pérez-Invernón *et al.*, 2016b).

5. SIGNATURE OF POSSIBLE LIGHTNING FROM THE VENUSIAN ATMOSPHERE

We can see in figure 5.15 that the maximum brightness occurs in the center ($r = 0$ km) of the halo with the strongest optical emissions being due to cloud discharges with total energies above 2×10^{10} J (middle panel). In particular, the brightness of halos triggered by cloud discharges with 2×10^{10} J of energy are of the same order than the Venusian natural nightglow. Therefore, emissions in the 557 nm line could be detectable by spacecraft orbiting the planet as an increase in the natural nightglow.

The produced $O(^1D)$ can also be a source of optical emissions. At halo altitudes, where the total density is low, the radiative decay of $O(^1S)$ (see Appendix A.2) dominates over collisional deactivation, causing an increase in the concentration of $O(^1D)$ in a timescale of several hundreds of milliseconds. After formation, $O(^1D)$ will decay radiatively emitting photons in the red line 630 nm in a longer timescale ($\simeq 200$ s) than that of the glowing halo. Although we do not extend our simulation up to the scale of a second, we expect that emissions in the 630 nm line would occur.

Halo optical emissions from electronically excited states of N_2 presented in table 5.1 are also important. The strongest emissions are produced in the optical range associated to the FPS and SPS of N_2 , while near infrared and ultraviolet emissions are also possible due to $N_2(W^3\Delta_u)$ and $N_2(a^1\Pi_g)$ states.

Finally, we estimate optical emissions from the vibrational levels of CO_2 . Figure 5.16 shows the time evolution of the $CO_2(001)$ density after the onset of the cloud discharge. $CO_2(001)$ is the only vibrational level that increases according to our results. As we clearly see in figure 5.16(c) the $CO_2(001)$ density growth is weak and confined to a region where the total electric field reaches values close to breakdown. The radiative de-excitation of $CO_2(001)$ takes place $\simeq 2$ ms after being excited and emits light in the near infrared (NIR) range at $4.26 \mu\text{m}$.

5.3.2.2 Venusian Elves

In this section, we present the results of the Venusian elve model described in subsection 5.3.1. This model does not compute the fluxes of ionospheric electrons, but the induced current. These induced currents are adequate to predict Venusian elves due to electron heating. However, this scheme is

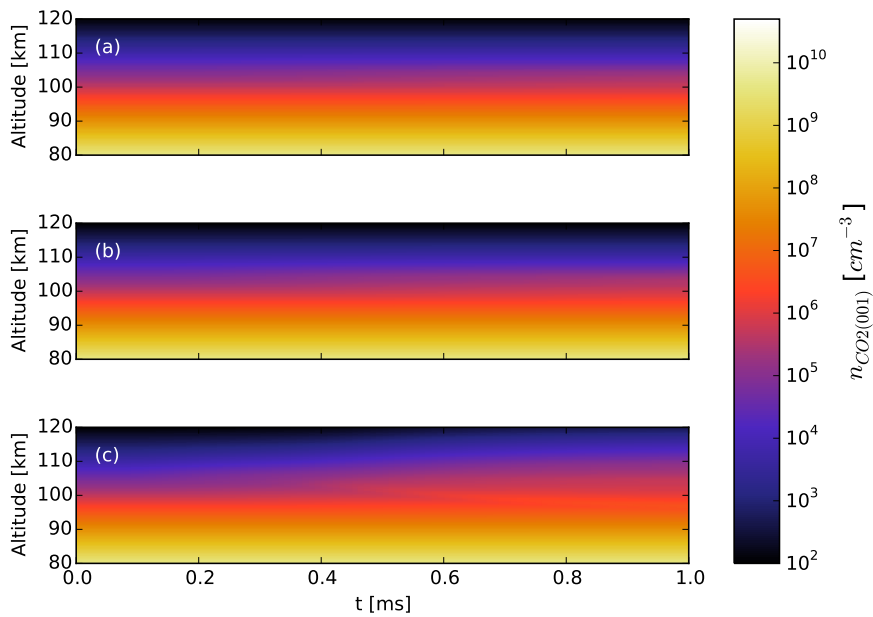


Figure 5.16: Time evolution of the $\text{CO}_2(001)$ density in the center of the halo created by cloud lightning discharges with total released energy of (a) 10^{10} J, (b) 2×10^{10} J and (c) 10^{11} J (Pérez-Invernón *et al.*, 2016b).

5. SIGNATURE OF POSSIBLE LIGHTNING FROM THE VENUSIAN ATMOSPHERE

less accurate in the simulation of halos, where fluxes of ionospheric electrons are highly non-linear. Despite this limitation, this elve model is also useful to predict the shape of halos triggered by different lightning channel inclinations.

We investigate the effect of vertical, horizontal and oblique lightning on the upper atmosphere of Venus taking advantage of the three dimensional scheme. We choose lightning discharges with total released energies of 10^6 J, 10^7 J, 10^{10} J, 2×10^{10} J and 10^{11} J.

We plot in figure 5.17 the reduced electric field E/N produced in the Venusian mesosphere by lightning with different channel inclinations and total released energies. The lightning-radiated pulse can be seen in the snapshots at 0.3 ms, while snapshots at 1 ms show the quasi-electrostatic field component. Differences in the discharge emission pattern can be appreciated comparing the three inclinations considered at different times. We analyze this pattern for each inclination, as it will determine some optical emission characteristics. We do not show the lower energetic cases of 10^6 J and 10^7 J, as they produce negligible reduced electric fields below 3 Td.

It is worth to analyze the shape of the radiated pulses in each case, as the shape of the elve would depend on them. The vertical channel emits radiation in two lobes that expand from the channel center in the horizontal direction, producing the pulses shown in figure 5.17, 0.3 ms after the vertical lightning discharge initiation. Snapshots corresponding to the vertical case at 1 ms show the reduced electric field due to the quasi-electrostatic field component, with a maximum right in the vertical line above the discharge.

The situation is rather different when the lightning channel is horizontal. The snapshots of figure 5.17 corresponding to the horizontal case at 0.3 ms show that the discharge emits radiation in a lobe that expands in a vertical plane, producing a reduced electric field higher than in the case of the vertical channel. Snapshots corresponding to the horizontal case at 1 ms show the quasi-electrostatic field produced by this channel with two lobes. Each lobe is located in the vertical right above each charged region or dipole extreme. Quasi-electrostatic fields produced by the horizontal discharge are lower than those produced by the vertical discharge because dipolar fields are higher on the dipole's axis.

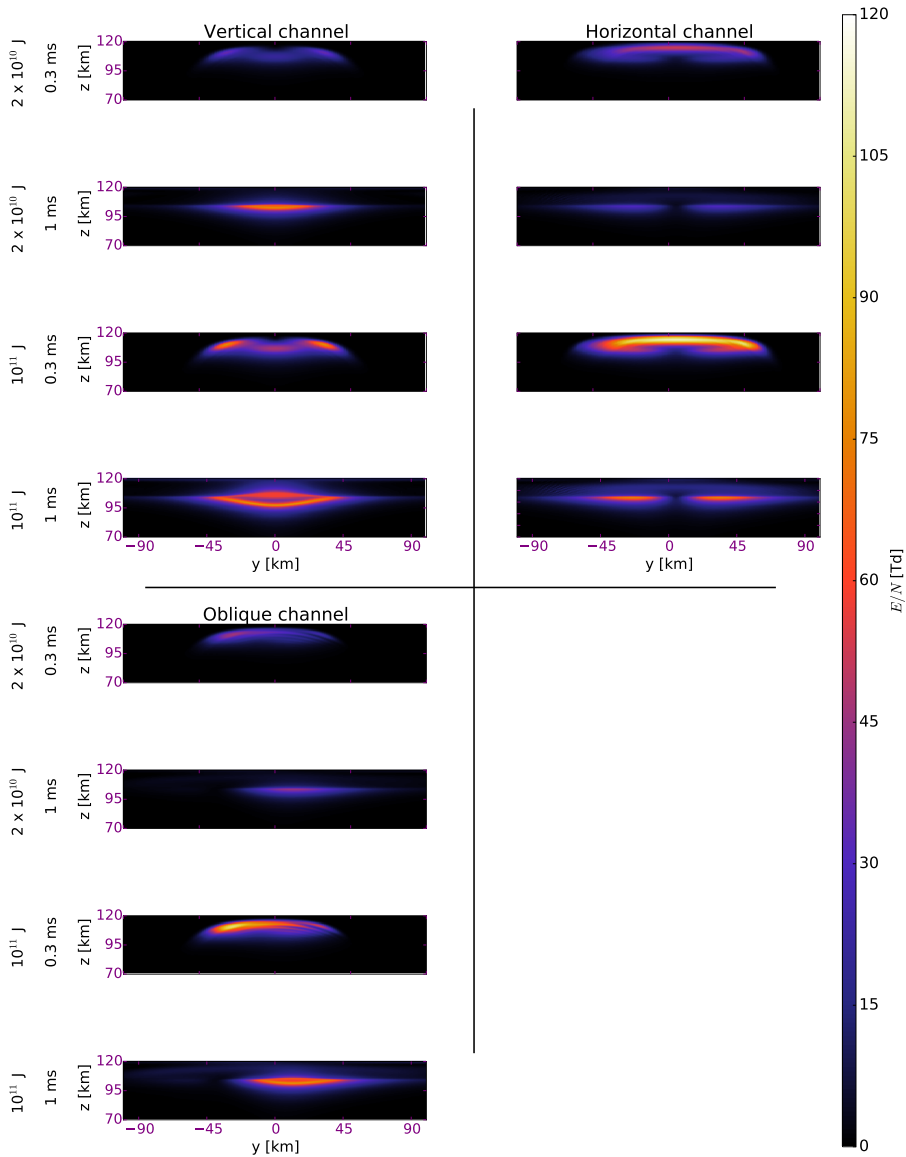


Figure 5.17: Reduced electric field E/N in the atmosphere of Venus created by lightnings with several inclinations. We show snapshots at two different times after the beginning of the discharge with two total released energies: 2×10^{10} J and 10^{11} J. We plot results for three different channel inclinations (Pérez-Invernón *et al.*, 2017b).

5. SIGNATURE OF POSSIBLE LIGHTNING FROM THE VENUSIAN ATMOSPHERE

Finally, the last column of figure 5.17 shows the oblique discharge case, where the lightning channel inclination is 45° . We can see the radiated pulse at 0.3 ms and the lobe due to the quasi-electrostatic field at 1 ms.

As in the previous section, we can calculate optical emissions from the density of the main emitting species. Tables 5.2, 5.3 and 5.4 collect the total number of photons emitted by the combination of a halo and an elve together with their corresponding wavelengths and the total emitted optical energy. We obtain the maximum number of emitted photons in the case of the vertical discharge. This is due to the larger quasi-electrostatic field in vertical discharges, as can be seen in figure 5.17. The total emitted photons in the less energetic cases of 10^6 J and 10^7 J (typical of Earth-like lightning) are zero or have values below our numerical precision.

Wavelength	Vertical channel (Photons / Energy)	Horizontal channel (Photons / Energy)	Oblique channel (Photons / Energy)
557 nm	$7 \times 10^{18} / 3$ J	$2 \times 10^{16} / 7 \times 10^{-3}$ J	$6 \times 10^{13} / 2 \times 10^{-5}$ J
550 nm - $1.2 \mu\text{m}$	$2 \times 10^{19} / 5$ J	$5 \times 10^{16} / 1 \times 10^{-2}$ J	$7 \times 10^{14} / 2 \times 10^{-4}$ J
250 - 450 nm	$3 \times 10^{18} / 2$ J	$3 \times 10^{14} / 2 \times 10^{-4}$ J	$5 \times 10^{12} / 4 \times 10^{-6}$ J
208 nm	$5 \times 10^{18} / 5$ J	$2 \times 10^{16} / 2 \times 10^{-2}$ J	$2 \times 10^{14} / 2 \times 10^{-4}$ J
$136.10 \mu\text{m}$	$1 \times 10^{18} / 1 \times 10^{-3}$ J	$5 \times 10^{15} / 7 \times 10^{-6}$ J	$5 \times 10^{13} / 7 \times 10^{-8}$ J
$8.25 \mu\text{m}$	$6 \times 10^{18} / 1 \times 10^{-1}$ J	$2 \times 10^{16} / 5 \times 10^{-4}$ J	$2 \times 10^{14} / 5 \times 10^{-6}$ J
120 - 280 nm	$2 \times 10^{18} / 2$ J	$2 \times 10^{16} / 2 \times 10^{-2}$ J	$2 \times 10^{14} / 2 \times 10^{-4}$ J

Table 5.2: Total number of emitted photons and approximate optical energy released from the lower ionosphere for cloud lightning discharges on Venus with total released energy of 10^{10} J (*Pérez-Invernón et al., 2017b*). Transitions are as in table 5.10.

Wavelength	Vertical channel (Photons / Energy)	Horizontal channel (Photons / Energy)	Oblique channel (Photons / Energy)
557 nm	$3 \times 10^{20} / 1 \times 10^2$ J	$4 \times 10^{18} / 1$ J	$2 \times 10^{17} / 7 \times 10^{-2}$ J
550 nm - $1.2 \mu\text{m}$	$6 \times 10^{20} / 1 \times 10^2$ J	$1 \times 10^{19} / 2$ J	$1 \times 10^{18} / 2 \times 10^{-1}$ J
250 - 450 nm	$1 \times 10^{20} / 6 \times 10^2$ J	$6 \times 10^{17} / 3 \times 10^{-1}$ J	$6 \times 10^{16} / 3 \times 10^{-2}$ J
208 nm	$1 \times 10^{20} / 1 \times 10^2$ J	$3 \times 10^{18} / 3$ J	$2 \times 10^{17} / 2 \times 10^{-1}$ J
$136.10 \mu\text{m}$	$3 \times 10^{19} / 4 \times 10^{-2}$ J	$6 \times 10^{17} / 9 \times 10^{-4}$ J	$5 \times 10^{16} / 7 \times 10^{-5}$ J
$8.25 \mu\text{m}$	$2 \times 10^{20} / 5$ J	$2 \times 10^{18} / 5 \times 10^{-2}$ J	$2 \times 10^{17} / 5 \times 10^{-3}$ J
120 - 280 nm	$7 \times 10^{19} / 7 \times 10^1$ J	$3 \times 10^{18} / 3$ J	$2 \times 10^{17} / 2 \times 10^{-1}$ J

Table 5.3: Total number of emitted photons and approximate optical energy released from the lower ionosphere for cloud lightning discharges on Venus with total released energy of 2×10^{10} J (*Pérez-Invernón et al., 2017b*). Transitions are as in table 5.10.

Wavelength	Vertical channel (Photons / Energy)	Horizontal channel (Photons / Energy)	Oblique channel (Photons / Energy)
557 nm	$1 \times 10^{22} / 4 \times 10^3$ J	$2 \times 10^{21} / 7 \times 10^2$ J	$2 \times 10^{21} / 7 \times 10^2$ J
550 nm - 1.2 μ m	$2 \times 10^{22} / 5 \times 10^3$ J	$4 \times 10^{21} / 9 \times 10^2$ J	$3 \times 10^{21} / 7 \times 10^2$ J
250 - 450 nm	$5 \times 10^{21} / 3 \times 10^3$ J	$8 \times 10^{20} / 5 \times 10^2$ J	$6 \times 10^{20} / 3 \times 10^2$ J
208 nm	$5 \times 10^{21} / 5 \times 10^3$ J	$8 \times 10^{20} / 8 \times 10^2$ J	$6 \times 10^{20} / 7 \times 10^2$ J
136.10 μ m	$1 \times 10^{21} / 1$ J	$2 \times 10^{20} / 3 \times 10^{-1}$ J	$1 \times 10^{20} / 2 \times 10^{-1}$ J
8.25 μ m	$6 \times 10^{21} / 1 \times 10^2$ J	$7 \times 10^{20} / 2 \times 10^1$ J	$8 \times 10^{20} / 2 \times 10^1$ J
120 - 280 nm	$3 \times 10^{21} / 3 \times 10^3$ J	$8 \times 10^{20} / 8 \times 10^2$ J	$4 \times 10^{20} / 4 \times 10^2$ J

Table 5.4: Total number of emitted photons and approximate optical energy released from the lower ionosphere for cloud lightning discharges on Venus with total released energy of 10^{11} J (*Pérez-Invernón et al.*, 2017b). Transitions are as in table 5.10.

We can also estimate the brightness of elves following the same approach as in the previous section. We plot the column brightness in Rayleigh of some of the simulated elves in figure 5.18 as would be seen at the nadir from a spacecraft orbiting Venus. We show the column brightness of the five most intense lines 0.3 ms after the onset of a lightning discharge with a total released energy of 10^{11} J. These optical emissions are produced by the radiation field component and their shape follows the reduced electric field maxima plotted at 0.3 ms in figure 5.17. As they are produced by electromagnetic pulses, the physical mechanism underlying their generation is the same as in terrestrial elves. As investigated by *Marshall et al.* (2010) for the case of elves on Earth, we also find that the lightning channel inclination influences the shapes of the elve-like mesospheric optical emission in Venus.

As we mentioned above, this model can also be useful to predict the shape of Venusian halos produced by tilted lightning discharges. Figure 5.19 shows optical emission brightness from $O(^1S)$ and $N_2(B^3\Pi_g \text{ (all } v'))$ 1 ms after the discharge initiation. These optical emissions are due to the quasi-electrostatic component of the field, their shape matching the reduced electric field maxima plotted at 1 ms in figure 5.17. In the case of a vertical channel, the brightness is similar to that previously obtained using the halo model. The influence of the channel inclination can be clearly seen by comparing the three columns of figure 5.19, where the vertical and oblique cases originate disc-form emissions, and the horizontal case produces two lobules of light. In the particular case of the line (at 557 nm) emitted by the radiative decay of $O(^1S)$, different shape emissions can be seen at 1 ms, as its long relaxation time of 0.74 s mixes emissions caused by radiation and

5. SIGNATURE OF POSSIBLE LIGHTNING FROM THE VENUSIAN ATMOSPHERE

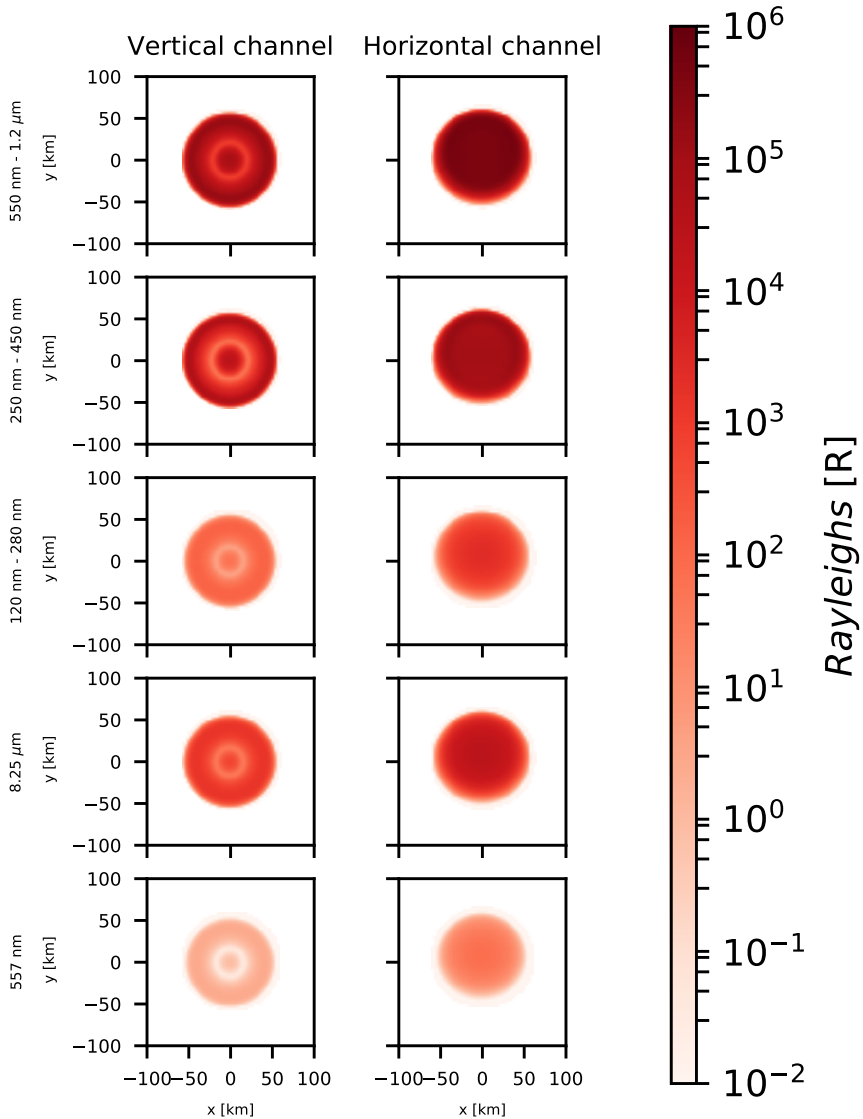


Figure 5.18: Main optical emission brightness, in Rayleigh, in the atmosphere of Venus 0.3 ms after the initiation of a lightning discharge with a total released energy of 10^{11} J. The plots show optical emissions produced by radiative decay of $O(^1S)$ (557 nm), $N_2(B^3\Pi_g)$ (all v') (550 nm - 1.2 μm), $N_2(C^3\Pi_u)$ (all v') (250 - 450 nm), $N_2(a^1\Pi_g)$ (all v') (120 - 280 nm) and $N_2(a^1\Pi_g)$ ($v' = 0$) (8.25 μm). The shown optical emissions correspond to the nadir direction from an orbiting probe without considering atmospheric and geometric attenuation (Pérez-Invernón *et al.*, 2017b).

quasi-electrostatic fields.

5.3.2.3 Comparison with previous measurements

As we mentioned in the introduction, some space missions have attempted to detect transient optical signals from the Venusian atmosphere without success. However, according to our results, if halos and elves exist in Venus, they would emit light. We cross our results with the non-detection of light by some spacecraft in an effort to estimate a upper limit of TLEs occurrence in Venus:

1. Vega balloons (*Sagdeev et al.*, 1986; *Kremnev and the Vega Balloon Science Team*, 1987) were equipped with light sensors capable of detecting light in a range of wavelengths between 400 nm and 1.1 μm . Each balloon floated at cloud altitudes collecting data for approximately 22.5 hours without discovering any source of illumination. However, we cannot use these non-detections to establish an upper limit in the TLEs rate, as measurements were short and local. Furthermore, optical emissions from TLEs could suffer attenuation before reaching the balloons.
2. Cassini optical measurements: The Imaging Science Subsystem (ISS) onboard Cassini spacecraft can detect light between 200 nm and 1.1 μm (*Porco et al.*, 2004). During its second Venus flyby, this instrument collected data for 12 minutes obtaining "flat-field" calibration (*Burton et al.*, 2001). However, no detection of a source of light was reported. The lack of information about these optical measurements together with the short time of observation do not allow us to estimate any TLE upper limit.
3. Venus Express (VEX) optical measurements: The VIRTIS instrument onboard VEX was also equipped with a light detector for wavelengths between 200 nm and 1.1 μm (*Piccioni et al.*, 2007). As TLEs would emit light from the upper atmosphere, their optical emissions would not suffer a significant attenuation in its way up to the spacecraft. *Cardesín Moineo et al.* (2016) performed a dedicated analysis of

5. SIGNATURE OF POSSIBLE LIGHTNING FROM THE VENUSIAN ATMOSPHERE

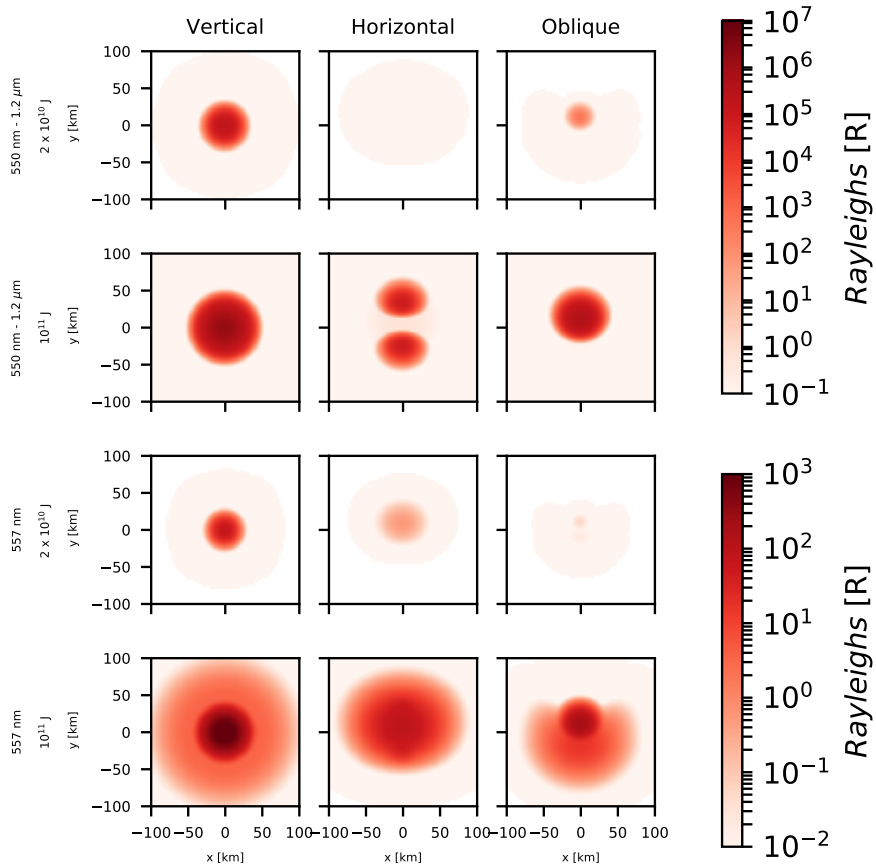


Figure 5.19: Some optical emission brightness, in Rayleigh, in the atmosphere of Venus 1 ms after the initiation of lightning discharges with total released energies of 2×10^{10} J and 10^{11} J and three inclinations. The direction of the horizontal and oblique channels in the xy plane is of 45° . The shown optical emissions correspond to the radiative decay of $O(^1S)$ (557 nm) and $N_2(B^3\Pi_g)$ (all v') (550 nm - $1.2 \mu\text{m}$). The optical emissions shown correspond to the nadir direction from an orbiting probe without considering atmospheric and geometric attenuation (*Pérez-Invernón et al., 2017b*).

the optical data acquired by this detector in an effort to find luminous transient events on the Venus nightside. The data used in this study were collected with different exposure times, from 0.2 s to 20 s. *Cardesín Moinelo et al.* (2016) did not probe the inexistence of transient optical emissions. However, their results indicate that either TLEs are not frequent on Venus or the emitted light is too low to be detected from the spacecraft altitude.

Several studies based on the analysis of electromagnetic signals (see for example *Russell et al.* (1989)) estimated a rate of lightning on Venus of about 100 flashes per second. According to the halo and elve model that we have developed, lightning with a total energy released above 10^{10} J would produce an observable TLE in the upper atmosphere of Venus. The analysis performed by *Cardesín Moinelo et al.* (2016) suggests that the rate of TLEs is lower than 5 per second, which leads us to estimate that at least 95 % of lightning would release a total energy below 10^{10} J.

5.3.2.4 Feasibility of detecting Venusian TLEs from present and future orbiters

The predicted Venusian halos and elves would take place above the cloud deck. Therefore, light emitted by these TLEs would travel to the outer space without suffering atmospheric absorption and providing evidence of Venusian lightning existence. In this section we discuss the feasibility of detecting the simulated Venusian halos and elves from orbiters.

We focus on the possibility of detection of these TLEs by the Japanese Akatsuki probe, currently orbiting Venus at distances from periapsis at 1000 km to apoapsis at 370000 km (*Gibney*, 2016). This spacecraft is equipped with the Lightning and Airglow Camera (LAC) that could be able to detect the transient green (557.7 nm) line produced by the radiative decay of $O(^1S)$ (*Takahashi et al.*, 2008). According to our models, both Venusian halos and elves would emit light in the 557 nm spectral line. Figures 5.15 and 5.19 show that, for highly energetic cloud discharges, the halo brightness in the green line (557.7 nm) is larger than the maximum natural atomic oxygen nightglow emission of 167 R (*Slanger et al.*, 2006;

5. SIGNATURE OF POSSIBLE LIGHTNING FROM THE VENUSIAN ATMOSPHERE

Gray et al., 2014). This means that a camera with sufficiently high temporal resolution and sufficiently close to the planet could detect the predicted 557.7 nm transient increase above its ambient nightglow value.

Let us now estimate the total number of photons in the 557 nm line that the LAC camera would receive at its periapsis. If we numerically integrate in time (up to 1 ms) the total number of photons emitted per second we obtain the total number of emitted photons up to the instant when the number of photons emitted per second do not grow any further. From this time on, we use the calculated number density of each emitting species at 1 ms to analytically integrate it in time and derive the total number of emitted photons from 1 ms to infinity. The sum of both (numerical and analytical) integrals provides the total number of emitted photons. Afterwards, we can calculate the fraction of emitted photons able to reach an hypothetical detector with a diameter of 25 mm at a distance L from the halo, located at around 1000 km of altitude:

$$\frac{R_{h\nu}}{E_{h\nu}} = \frac{\pi r^2}{4\pi L^2}, \quad (5.15)$$

where $R_{h\nu}$ is the total number of photons that reach the camera, $E_{h\nu}$ is the number of photons emitted by the entire halo, and r is the radius of the camera aperture. The total number of received photons in the 557 nm spectral line for halos triggered by lightning discharges with released energies of 10^{10} J, 2×10^{10} J and 10^{11} J would be 4, 10^3 and 6.13×10^5 , respectively. However, the LAC airglow observation mode only uses a section of 1 x 8 pixels of the full (8 x 8 pixels) avalanche photodiode detector (APD) (*Takahashi et al.*, 2008). Therefore, we can conclude that the total amount of photons that reaches the airglow detector section from the transient glowing discharge is 1/8 of the total number of photons received by the full detector.

In addition to LAC, the Akatsuki spacecraft also carries cameras that cover the UV range (258 and 360 nm) and the near-IR (1.0, 1.7, 2.0 and 2.3 μm) (*Takahashi et al.*, 2008) covering the spectral range of optical emissions associated to the electronic states $\text{N}_2(\text{B}^3\Pi_g)$, $\text{N}_2(\text{C}^3\Pi_u)$, $\text{N}_2(\text{W}^3\Delta_u)$ and $\text{N}_2(\text{a}^1\Pi_g)$. In this regard, it is important to note that the transient

lightning-induced NIR optical emissions in the upper atmosphere of Venus corresponding to the strong (high radiative decay constants) transitions $N_2(W^3\Delta_u(v' = 3, 4)) \rightarrow N_2(B^3\Pi_g(v'' = 0))$ centered around, respectively, 2.250 μm and 1.709 μm and $N_2(a^1\Pi_g(v' = 2, 3)) \rightarrow N_2(a^1\Sigma_u^-(v'' = 0))$ centered around, respectively, 2.214 μm and 1.632 μm are within the spectral range of the NIR-IR2 camera of Akatsuki. However, vibrational kinetics is not included in the present version of our model and, consequently, we cannot precisely compute the concentrations of the vibrational levels underlying the above-mentioned NIR transitions.

Optical emissions due to the increase in the density of $\text{CO}_2(001)$ might not be detectable from space due to the strong ambient emission in the 4.26 μm spectral region (*Lopez-Valverde et al., 2007*). However, we speculate that a probe located on the Venus surface (or close to it) could observe this weak and local transient emission increase corresponding to the 4.26 μm vibrational transition of CO_2 .

5.4 Electromagnetical signatures of possible Venusian lightning: Whistler waves

5.4.1 Particularization of the model for the atmosphere of Venus

We calculate the propagation of whistler waves through the ionosphere of Venus using the Stanford Full Wave Method (StanfordFWM) described in *Lehtinen and Inan (2008)*, *Lehtinen and Inan (2009)* and *Lehtinen et al. (2010)* and used in section 3.2. The standard FWM takes an electromagnetic current as input and calculates the propagation of the radiated pulses through the atmosphere of the Earth. In this case, we modify the standard FWM changing the propagation media. We set the plasma characteristics of the Venusian atmosphere described in subsection 5.2.3 and use as electromagnetic pulses a Venusian cloud discharge (see subsection 5.2.2). Finally, we compare the electromagnetic wave that escapes from the planet with measurements reported by PVO and VEX spacecraft. This comparison will allow us to estimate some characteristics of the source from the detected sig-

5. SIGNATURE OF POSSIBLE LIGHTNING FROM THE VENUSIAN ATMOSPHERE

nals. The simulations using the FWM are carried out in a CSIC computer cluster in Madrid called “Trueno”.

The FWM solves the Maxwell equations and calculates all the electromagnetic field components in the frequency domain for a wave generated in and propagating through a stratified medium. Apart from the effect of the plasma characteristic of the medium in the propagation of waves, the method can also include the effect of a background magnetic field. Therefore, we are capable of setting the characteristics of the Venusian ionosphere in this method. As we explained in subsection 5.2.3, the characteristics of the ionosphere of Venus can change in the presence of “ionospheric holes”. These holes exhibit characteristics that favor the propagation of electromagnetic waves. In particular, the density of the charged particles can be more than 3 orders of magnitude lower than the ambient density (*Bauer et al.*, 1985), while a vertically oriented magnetic field with values up to 40 nT can appear. The characteristics of the holes are a direct consequence of the interaction between the ionosphere and the solar wind (*Marubashi et al.*, 1985).

As the characteristics of the ionospheric holes seem to be variable, we investigate whistler propagation at different ionospheric conditions. We perform different simulations using the FWM in order to determine the relation between the holes characteristics and the wave propagation. For this purpose, we calculate wave propagation from a cloud discharge through the Venusian ionosphere for vertical background magnetic fields with magnitudes between 0 nT and 40 nT. We also reduce the charged particle density between 0 and 8 orders with respect to the ambient value. This strategy will allow us to determine the ideal hole characteristics that favor the propagation of whistler waves through the atmosphere of Venus.

As we explained in section 3.2, the FWM can be applied to calculate wave propagation in different coordinate systems. Since we are interested in the whistler wave propagation in the presence of a vertical magnetic field, we use a cylindrically symmetrical scheme. Finally, results are transformed to a Cartesian coordinate system as we will explain below.

As we are exclusively interested in the propagation of waves in the upward direction, we neglect the planetary curvature in our calculations. This

approach is justified for frequencies above the Schumann resonances, that would be produced at frequencies between 9 Hz and 24 Hz in the Venusian atmosphere (*Simões et al.*, 2008).

In the case of a horizontal discharge, the source has two spatial components, denoted as I_x and I_y . Electromagnetic wave propagation from an horizontal discharge channel can be modeled with FWM taking advantage of the source expansion in axial harmonics, provided that the dielectric permittivity is axisymmetric. We use the fact that the Fourier transform of any function $A(x, y)$ defined in the space coordinates x and y that depends on the radial distance r as

$$A(x, y) = A(r) \exp(i n \phi), \quad (5.16)$$

where i is the imaginary unit and n is an integer, is

$$A(k_x, k_y) = \frac{2\pi}{i^n} A_n(k) \exp(i n \chi), \quad (5.17)$$

where the 2D Fourier transform is defined as

$$A(k_x, k_y) = \int \exp(-i(k_x x + k_y y)) A(x, y) dx dy, \quad (5.18)$$

and

$$A(x, y) = \int \exp(i(k_x x + k_y y)) A(k_x, k_y) \frac{dk_x dk_y}{(2\pi)^2}, \quad (5.19)$$

with the integrals having infinite limits. The polar coordinates used above are

$$x = r \cos(\phi), y = r \sin(\phi) \quad (5.20)$$

$$k_x = k \cos(\chi), k_y = k \sin(\chi), \quad (5.21)$$

while $A_n(k)$ is the Hankel transform of $A(r)$, defined as

$$A_n(k) = \int_0^\infty A(r) J_n(kr) r dr \quad (5.22)$$

$$A(r) = \int_0^\infty A_n(k) J_n(kr) k dk, \quad (5.23)$$

5. SIGNATURE OF POSSIBLE LIGHTNING FROM THE VENUSIAN ATMOSPHERE

where $J_n(kr)$ is the n th order Bessel function of the first kind.

The function A is a scalar, which can be any of the components of a vector, e.g., I_x , I_y or I_z . However, the FWM takes as an input of the source the values of $I_x(k)$, $I_y(k)$ and $I_z(k)$ at $\chi = 0$ (Lehtinen and Inan, 2008, 2009; Lehtinen et al., 2010). To calculate the fields we need to know the angular dependence $I_x(\chi)$, $I_y(\chi)$ and $I_z(\chi)$. The input to the FWM requires that the polar components of the current in (k_x, k_y, z) -space satisfy $(I_k, I_\chi, I_z) \sim \exp(im\chi)$. Then the polar components of the electromagnetic fields in the (k_x, k_y, z) -space, will also have the same χ -dependence (due to linearity and axial symmetry of the dielectric permittivity). These can be then converted to fields in (x, y, z) -space at $\phi=0$.

The geometrical scheme used in this model is shown in figure 5.20. It can be summarized as follows:

1. Cylindrical coordinate system, where the r axis is parallel to the ground and the axis of symmetry, denoted as z , points towards nadir. We do not take into account the planetary curvature, as our purpose is to calculate upward propagation from a stroke locally. Results are transformed to Cartesian coordinates before plotting.
2. Background magnetic field vertical to the ground everywhere.
3. Two different lightning-channel inclinations, parallel and vertical to the ground. The source is located in the z axis. The direction and propagation of the emitted electromagnetic wave will be obtained for each case.

Let us now describe the method to compare our results with reported signals by PVO and VEX. The FWM allows us to obtain the electromagnetic wave components at different altitudes and horizontal distances from the source. However, we cannot directly compare our calculated fields with the observations by PVO and VEX, as these spacecraft did not measure electromagnetic field components, but the power spectral density within a frequency band during a certain time interval (Scarf et al., 1980; Strangeway, 2003; Russell et al., 2013). In this section, we will explain an approx-

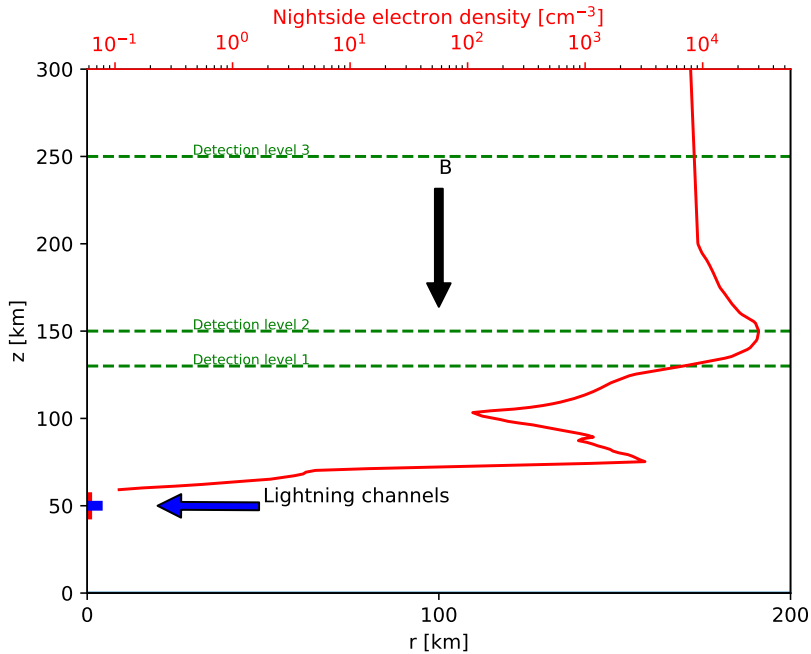


Figure 5.20: Geometrical scheme in cylindrical coordinates and ambient concentration of electrons in the nightside of Venus (red line) (*Borucki et al.*, 1982; *Bauer et al.*, 1985; *Pérez-Invernón et al.*, 2016b). Lightning channels can be vertical (red) or horizontal (blue). We calculate lightning-produced electromagnetic fields at detection levels (green dashed lines) to compare with observations. The background magnetic field is vertical to ground everywhere (*Pérez-Invernón et al.*, 2017a).

5. SIGNATURE OF POSSIBLE LIGHTNING FROM THE VENUSIAN ATMOSPHERE

imate method to compare our results with the available measurements at frequencies between 5 Hz and 100 Hz.

The FWM takes as input the ω -space current moment. We calculate it as the Fourier transform of the equation (5.2) multiply by the length of the dipole (L) as:

$$K(\omega) = LI_0 \left(\frac{1}{\frac{1}{\tau_1} - i\omega} - \frac{1}{\frac{1}{\tau_2} - i\omega} \right). \quad (5.24)$$

We use the FWM to calculate the Cartesian electromagnetic field components $\mathbf{F}(\omega) = (E_x, E_y, E_z, H_x, H_y, H_z)$ at a given altitude for a particular frequency. The transfer functions can be defined as the ratio of absolute values between each field component and the source:

$$T_j(\omega) = \frac{|F_j(\omega)|}{|K(\omega)|}, \quad (5.25)$$

where j denotes the electromagnetic field component.

To relate the experimentally observed power spectrum of electromagnetic radiation to the power spectrum radiated by the source (equation 5.24), we need to make some assumptions regarding the lightning temporal distribution. The simplest approximation is to assume a constant rate ν of planetary lightning strokes per second with similar characteristics, neglecting stationality and lightning occurrence correlation. Then the power spectral density for each electromagnetic field component is

$$S_j(\omega) = \nu |T_j(\omega)|^2 |K(\omega)|^2. \quad (5.26)$$

Russell et al. (1989) obtained an approximate value for the rate ν of 80 flashes per second with a total released energy of 2×10^{10} J per flash. We will normalize our computations to a value of $\nu=1$ flash per second. By scaling our results we can then obtain the rate that best agrees with the measured power spectral density.

This way to calculate the power spectral density assumes an approximate lightning flash rate value that is constant in time. However, both PVO and VEX spacecraft recorded time variations of the power spectral density that

can be due to several factors, as for example, a temporal dependence of the lightning distribution or due to some instrumental aspects.

The Pioneer Venus Orbiter was equipped with the Orbiter Electric Field Detector (OEFD), a plasma wave instrument with four band-pass channels centered at 100 Hz, 730 Hz, 5.4 kHz, and 30 kHz (*Scarf et al.*, 1980; *Colin*, 1980). This instrument had an antenna (*Russell and Scarf*, 1990) that recorded electric field components on a plane, hence the changes of the angle between the direction of the wave propagation and the plane of measurement during the time of observation could entail a temporal variation in the measured power spectral density. In this work, we will compare our calculated power spectral density with PVO peak measurements at altitudes of 130 km, 150 km (*Strangeway*, 2003) and 250 km (*Scarf et al.*, 1980) in the band-pass channel centered at 100 Hz, where whistler waves were observed.

The Venus Express instrumentation was different to that onboard PVO, as it recorded magnetic field components instead of electric field components. The VEX spacecraft was equipped with a magnetometer system (MAG) consisting of two sensors for measuring the magnetic field magnitude and direction (*Titov et al.*, 2006). We will also compare our power spectral density calculations with the measurements taken by VEX during nightside observations at 250 km altitude (*Russell et al.*, 2013). Interestingly, VEX recorded transverse right-handed guided waves were consistent with whistler mode propagation.

5.4.2 Results: Characteristic of whistler waves traveling through the Venusian ionosphere

We calculate the characteristics of a whistler wave propagating through the ionosphere of Venus following the previous scheme based on the FWM. We present the obtained results in this section. We divide the results in two subsections, as the aim of these calculations is the comparison with measurements of PVO and VEX. The first section is devoted to the power spectral densities based on the electric field components of the wave, while the second section presents the power spectral density based on the magnetic field components. Finally, we calculate the Poynting flux of the signal and

5. SIGNATURE OF POSSIBLE LIGHTNING FROM THE VENUSIAN ATMOSPHERE

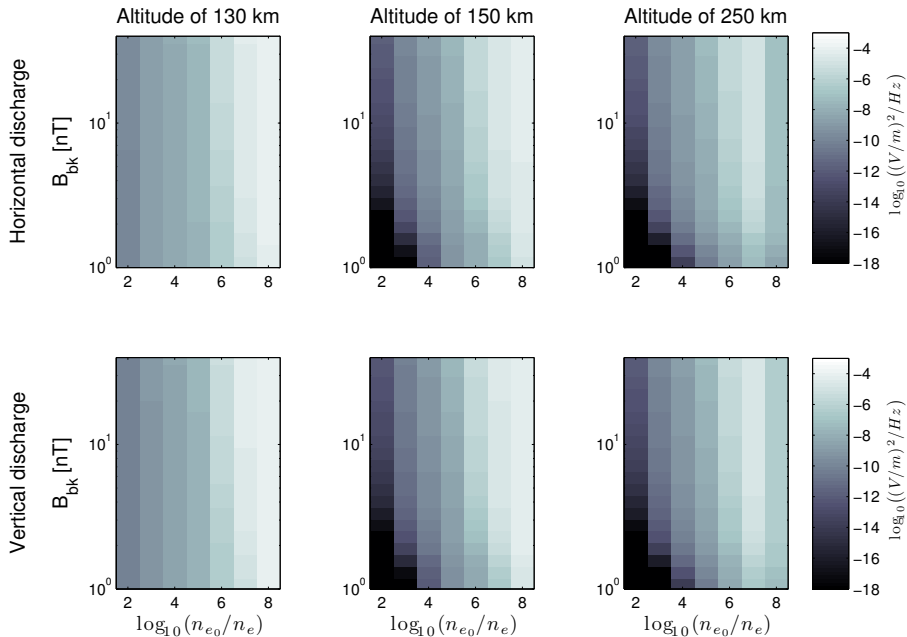


Figure 5.21: Maximum power spectral density (PSD) in $(\text{V/m})^2\text{Hz}^{-1}$ calculated from the E_x and E_y components at different altitudes and resulting from a lightning rate of 1 stroke per second for horizontal discharges (first row) and vertical discharges (second row). The x-axis represent the background magnetic field and the y-axis corresponds to the ionospheric hole magnitude, defined as the reduction of the electron density compared to the background value (n_{e0}) which peaks at around $3 \times 10^4 \text{ cm}^{-3}$. This definition of the x-axis alludes explicitly to the holes detected by PVO. We plot results for background magnetic fields greater than 1 nT (*Pérez-Invernón et al., 2017a*).

estimate the transfer function of the Venusian ionosphere.

5.4.2.1 Power spectral density based on the electric field

We will first analyze the power spectral density of the electric field components at a frequency 100 Hz. We focus on this frequency in order to compare with the power spectral density of the electric field reported by PVO at 100 Hz.

Figure 5.21 shows the calculated power spectral density of the electric field at different altitudes for horizontal and vertical lightning discharges

with a rate of 1 stroke per second and a total released energy per stroke of 2×10^{10} J. These calculations are performed for different background magnetic field (vertical axis) and different reductions in the peak electron and ion density (horizontal axis) in the charged particle density profiles (see the figure caption for the definition).

The maximum power spectral densities measured by PVO at 100 Hz between 130 km and 250 km of altitudes were of the order of 10^{-4} (V/m)²Hz⁻¹ (Scarfe *et al.*, 1980; Strangeway, 2003). The second row of figure 5.21 shows the power spectral density for a flash per second. According to this figure, a lightning rate of 100 flashes per second would produce a power spectral density similar to the one reported by PVO if the background magnetic field ranges between 5 nT and 40 nT and the electron and ion profile suffer a reduction between 10^5 and 10^6 . The expected power spectral density decreases steeply when the hole is less pronounced. It is interesting to note that the calculated power spectral density at 250 km of altitude also decreases in the case of a depletion of 10^8 in electron density. This effect can be due to the lack of electrons creating unfavorable conditions to whistler mode propagation.

Figures 5.22 and 5.23 shows the electromagnetic field and Poynting vector components produced by a vertically and a horizontally oriented lightning discharge in the ionosphere of Venus, respectively. According to the spatial distribution of the horizontal components of the electromagnetic field (E_x and E_y), whistler mode propagation is possible at horizontal distances between 10 km and 100 km from the source. The Poynting vector components indicate the direction of the energy flux and the region of maximum absorption. It can be seen that the maximum wave attenuation is produced at altitudes around 125 km. This altitude coincides with the largest enhancement in the electron density, where the induced current in the ionosphere shields the electromagnetic field and influences the flux direction. In the case of the horizontally oriented lightning discharge, the whistler wave traverses the ionosphere traveling along a vertical column right above the source. The vertical component of the Poynting vector exhibits negative values at an horizontal distance of ~ 50 km from the lightning discharge, indicating a downwards flux of energy produced by the reflection of the wave

5. SIGNATURE OF POSSIBLE LIGHTNING FROM THE VENUSIAN ATMOSPHERE

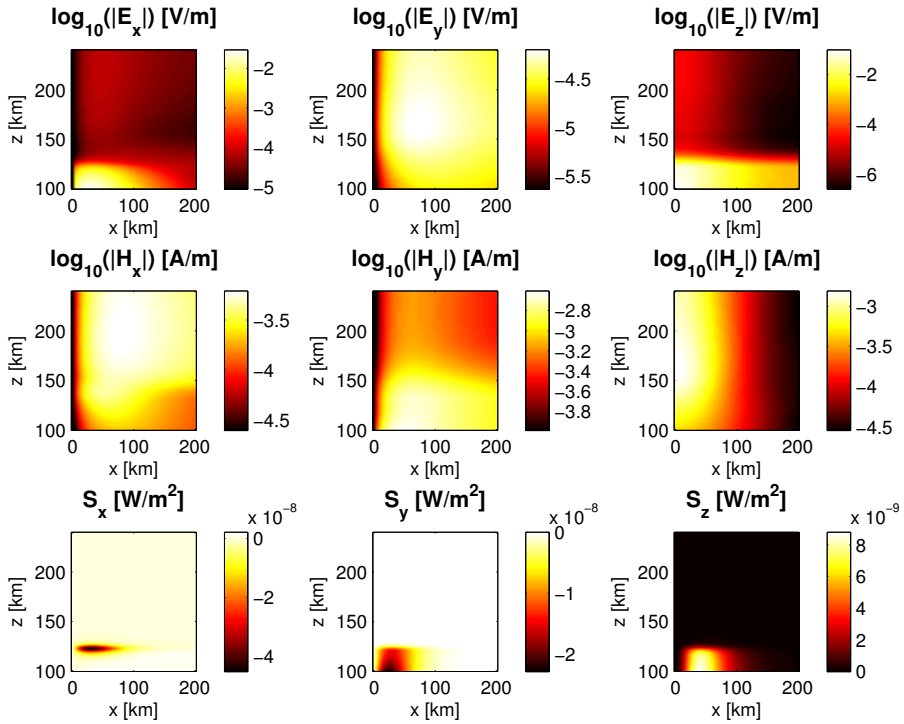


Figure 5.22: Time averaged electromagnetic field and Poynting vector components produced by a vertical discharge in the ionosphere of Venus under a background magnetic field of 20 nT and a reduction of 5 orders of magnitude in the electron and ion densities. The vertical lightning discharge is located at 45 km of altitude and produces a wave with a frequency of 100 Hz. This plot shows atmospheric regions above an altitude of 100 km (*Pérez-Invernón et al., 2017a*).

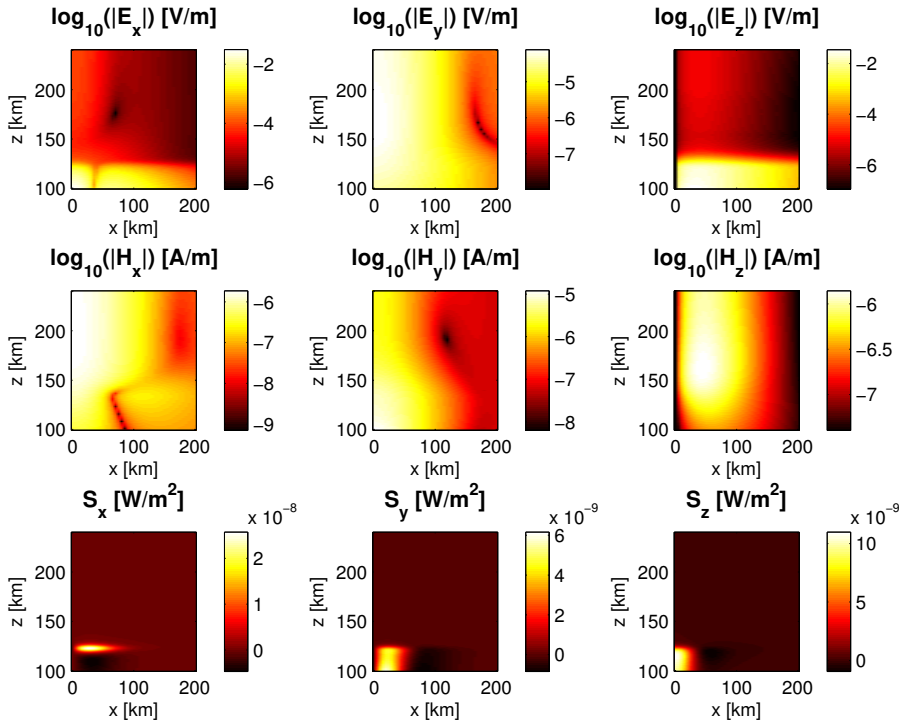


Figure 5.23: Time averaged electromagnetic field and Poynting vector components produced by a horizontal discharge in the ionosphere of Venus under a background magnetic field of 20 nT and a reduction of 5 orders of magnitude in the electron and ion densities. In this case, The horizontal lightning discharge is a dipole located at 45 km of altitude and contained in the plane x-z. The source produces a wave with a frequency of 100 Hz. As in figure 5.22, this plot shows atmospheric regions above an altitude of 100 km (Pérez-Invernón *et al.*, 2017a).

in the lower ionosphere.

5.4.2.2 Power spectral density of the magnetic field

Let us now analyze the power spectral density from the calculated magnetic field components in the range of frequencies between 5 Hz and 64 Hz, always above the lower hybrid frequency. In this case, we choose these frequencies (5 Hz - 64 Hz) in order to compare with the power spectral density reported by VEX.

Figure 5.24a shows the maximum calculated power spectral density at 40 Hz and 250 km altitude for vertical lightning discharges assuming a rate of 1 stroke per second and a total released energy per stroke of 2×10^{10} J. Again, the result is calculated for different background magnetic field values (vertical axis) and different reductions of the electron and ion densities (horizontal axis) in the ionosphere of the planet.

In the case of the VEX spacecraft, power spectral measurements were recorded using a magnetometer in the range of frequencies between 0 Hz and 64 Hz. We compare our calculations with measurements of transverse right-handed guided waves recorded by VEX during its nightside observation on June 9, 2006 (*Russell et al.*, 2013). According to the data analysis performed by *Russell et al.* (2013), the maximum power spectral densities at 40 Hz was around 10^{-2} (nT)²Hz⁻¹. However, the calculated power spectral density in figure 5.24a suggests that a rate of around 100 flashes per second and a reduction of 5 orders of magnitude in the electron and ion density would be necessary to produce the VEX observed power spectral density. As in the previous case, an increase in the charged particles density would produce more wave attenuation.

Figure 5.24b shows the frequency dependence of the calculated spectral density for different hole magnitudes and a background magnetic field of 15 nT, together with the VEX recorded spectrum in the nightside by VEX (*Russell et al.*, 2013). We see that different electron and ion densities cause different frequency-dependent attenuation in the propagating wave. Venus Express recorded radio signals for different atmospheric conditions (*Russell et al.*, 2013), obtaining different spectra of the transverse right-handed guided wave during daytime and nighttime conditions. The downward slope

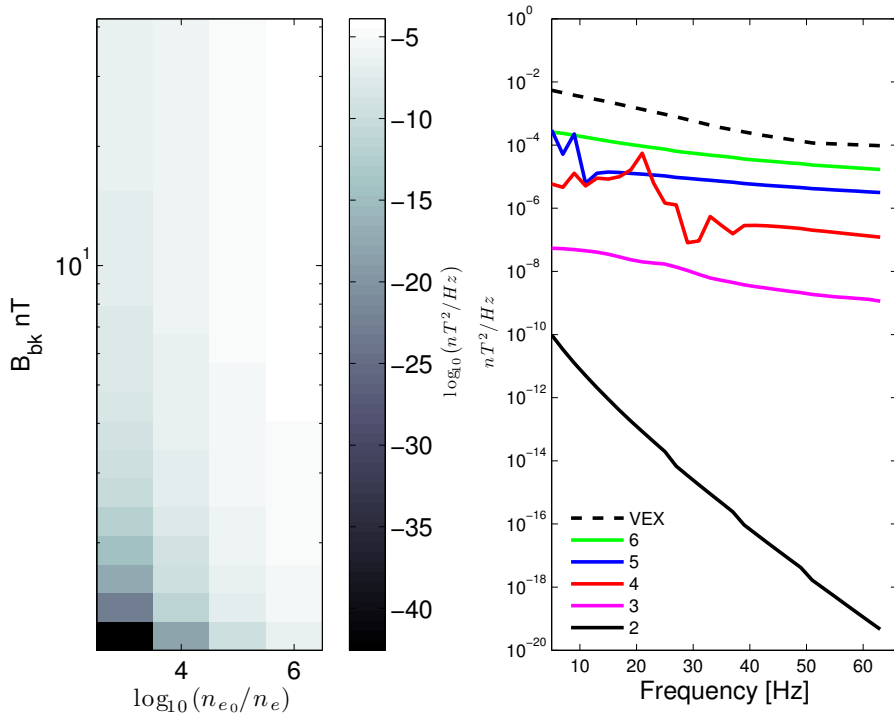


Figure 5.24: (left) Power spectral density at 250 km of altitude in $(\text{nT})^2\text{Hz}^{-1}$ calculated at 40 Hz from the B_x and B_y components at different altitudes and resulting from a lightning rate of 1 stroke per second for vertical discharges. The axes are the same as in figure 5.21. We also plot results for background magnetic fields greater than 1 nT. (right) Calculated power spectral density for different frequencies and a fixed intermediate background magnetic field of 15 nT, where the numbers in the inset indicate the order of magnitude of the reduction in the electron and ion density peak, n_{e0} . The spectrum recorded in the nightside of Venus by VEX is also shown (dashed line) (*Russell et al., 2013*). Results below 24 Hz could change with the inclusion of the planetary curvature as a consequence of the Schumann resonances (*Pérez-Invernón et al., 2017a*).

5. SIGNATURE OF POSSIBLE LIGHTNING FROM THE VENUSIAN ATMOSPHERE

exhibited by the spectra for hole magnitudes of 3, 4 and 5 are approximately similar to the measurements taken by VEX in the Venusian nightside (*Russell et al.*, 2013). If we compare the curves in figure 5.24b for different electron densities (hole magnitude) and curves obtained by VEX for different conditions, we see that the spectrum changes depending on the profile or the presence of a hole. Venus Express was not equipped with an instrument to measure plasma densities. However, our results and available VEX measurements suggest that there exists a direct relation between the spectrum of the wave and the profile of charged particles, with a flatter spectrum for higher electron densities.

5.4.2.3 Transfer function of the Venusian ionosphere

The transfer function indicates the attenuation suffered by a wave travelling through a planetary atmosphere at a given frequency. We can calculate the attenuation in decibels for different Venusian atmospheric conditions (background magnetic field and electron density) using the time-averaged Poynting vector $\mathbf{S} = \frac{1}{2}\Re(\mathbf{E} \times \mathbf{H}^*)$, where $\Re(x)$ stands for the real part of x . The attenuation is $A = 10 \log_{10} \left(\frac{S}{S_0} \right)$, where S is the module of the Poynting vector at 250 km of altitude, and S_0 is the module of the Poynting vector at a reference level (calculated at 75 km of altitude).

Figure 5.25 shows the calculated A for a 100 Hz electromagnetic wave traversing the Venusian atmosphere altitudes from 75 km to 250 km for holes magnitudes between 3 and 7. In the vertical axis, we plot background magnetic fields greater than 3 nT. In the case of a background magnetic field lower than this value or hole magnitudes smaller than 3 the transfer function becomes almost zero.

It can be seen that an ionosphere without holes and background magnetic field produces the strongest attenuation. However, the existence of holes together with background magnetic field enhances wave propagation.

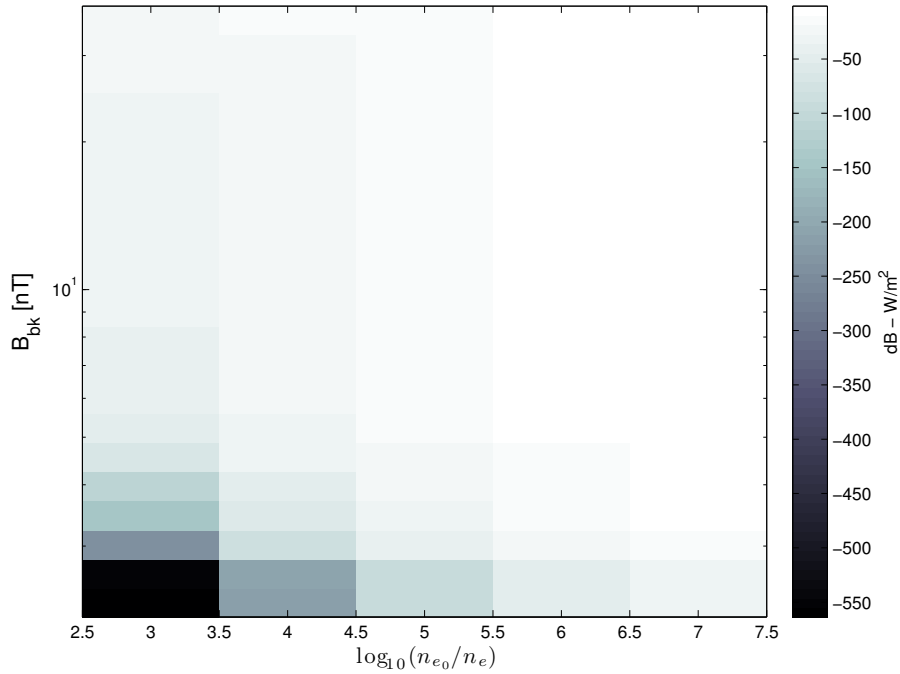


Figure 5.25: Attenuation of the electromagnetic signal (in dB) at 100 Hz after traversing the Venusian ionosphere from 75 km to 250 km altitude under a background magnetic field greater than 3 nT. The axes are the same as in Figure 5.21. Here we plot values of the transfer function for different orders of magnitude in the reduction of the electron and ion density peak (*Pérez-Invernón et al., 2017a*).

5.4.2.4 Remarks about the comparison between calculated and reported signals

Although Very Low Frequency (VLF) waves recorded by Pioneer Venus Orbiter (PVO) and Venus Express (VEX) suggest the existence of lightning in Venus (*Taylor et al.*, 1979; *Scarf et al.*, 1980; *Strangeway*, 2003; *Russell et al.*, 2013), the source of these VLF signals is not completely clear since the altitude where they are produced is not known.

We have calculated the whistler wave propagation of a lightning-produced wave through the Venusian ionosphere in order to compare with observations. We have made realistic assumptions about the lightning characteristics (*Krasnopolsky*, 1980; *Pérez-Invernón et al.*, 2016b) and the atmospheric conditions (*Borucki et al.*, 1982; *Bauer et al.*, 1985; *Marubashi et al.*, 1985; *Ho et al.*, 1991; *Michael et al.*, 2009; *Pérez-Invernón et al.*, 2016b), on the basis of which we obtained both the attenuation of whistler waves and the expected time-averaged power spectral density as a function of a global lightning rate. According to our results, unducted whistler-wave propagation is possible under the existence of local and temporal reductions in the electron and ion density and an induced background magnetic field greater than 4 nT and perpendicular to the wave propagation. These results are consistent with previous studies (*Huba and Rowland*, 1993).

Comparison between the obtained results and the reported signals allow us to estimate the global flash rate (lightning flashes per second) needed to reproduce the observations in the presence of ionospheric holes. For lightning with a total energy released of 2×10^{10} J (*Krasnopolsky*, 1980), the required number of lightning per second is of the order of 100, as in (*Russell et al.*, 1989).

However, for other (more realistic) energies of the order of average terrestrial lightning with total energy released of 10^7 J, the needed number of lightning per second must be as high as around 10^6 . This unrealistic value leads us to suggest that, if the observed signals are generated by lightning, the average energy released by Venusian lightning is considerably greater than the terrestrial lightning energies.

We can also estimate the needed rate of lightning assuming that the

reported whistler wave was propagating in the ducted mode. Although our investigations are based on the propagation of unducted whistler waves, we can estimate the effects of the geometric attenuation in the unducted case compared to ducted propagation. The unducted wave energy at the spacecraft altitude goes through an area which is of the order D^2 where $D \sim 200$ km is the vertical distance between the source and the observing spacecraft. This area may be less if we take into account that the whistler wave group velocities are contained within the Storey cone around the background magnetic field (*Helliwell, 1965*). The geometric attenuation factor is therefore at most D^2/a_{duct} , where a_{duct} is the cross-sectional area of the duct. Thus, for realistically sized ducts of >10 km transverse length, the ducted results would be about 10^2 – 10^3 higher than those of the unducted case. However, the propagation of ducted waves through the terrestrial ionosphere seems to be infrequent (*Cerisier, 1974; Loi et al., 2015*). This suggests that the observation of ducted waves from the Venusian ionosphere would be also improbable.

Future missions with dedicated instrumentation to take precise measurements of plasma parameters together with radio wave signals could be useful to determinate the source of the radio signals observed by the PVO and VEX missions. Furthermore, measurements of the wave attenuation dependence with frequency could provide useful information about the Venusian atmosphere composition.

5. SIGNATURE OF POSSIBLE LIGHTNING FROM THE VENUSIAN ATMOSPHERE

Chapter 6

Elves produced in Giant Gaseous Planets

6.1 Introduction

The first light from an extraterrestrial electrical discharge recorded by a spacecraft was produced in the Jovian atmosphere in 1979 (*Cook et al.*, 1979). The report of this flash by the Voyager 1 (NASA) marked a breakthrough in the field of atmospheric electricity, as it was the proof that lightning is not an exclusively terrestrial phenomenon. This spacecraft also reported whistler waves produced from Jovian electrical discharges (*Gurnett et al.*, 1979).

After the discovery of electrical discharges in the atmosphere of Jupiter, the Voyager 1 continued its journey to another giant gaseous planet, Saturn. The spacecraft reported high frequency (HF) radio emissions probably produced by electrical discharges taking place in the atmosphere of the planet (*Warwick et al.*, 1981). These signals are known as Saturn Electrostatic Discharges (SEDs). However, it was only in 2010 when the first optical light from a Saturnian electrical discharge was detected *Dyudina et al.* (2010, 2013). These flashes were reported by the Cassini spacecraft.

After flying over Saturn, the Voyagers 1 and 2 also visited the other two giant gaseous planets in the Solar System, Uranus and Neptune. These spacecraft also reported electromagnetic signals from the atmosphere of

6. ELVES PRODUCED IN GIANT GASEOUS PLANETS

these planets (*Zarka and Pedersen, 1986; Gurnett et al., 1990; Kaiser et al., 1991*), indicating that the existence of lightning discharges could be a common feature of the giant gaseous planets.

There have been other detection of electrical discharges from the atmospheres of Jupiter and Saturn, as explained in subsection 1.3.1. In this chapter, we investigate the possibility of the existence of Jovian and Saturnian TLEs, as proposed by *Yair et al. (2009)* and also explored by *Dubrovina et al. (2010, 2014b); Luque et al. (2014)*. In particular, we focus on the possibility of elve inception triggered by lightning-driven electromagnetic pulses, although our model also computes the electrostatic and induction field components that could produce halos. In addition, we compare the predicted elve light emissions with the optical flashes reported by the Cassini spacecraft (NASA, ESA and ASI) in order to determine if they were emitted by lightning or TLEs. For this purpose, we follow the same approach of *Luque et al. (2014)*, who developed a two-dimensional model of Saturnian and Jovian elves in a cylindrically symmetrical coordinate systems. However, in our case we have upgraded the model using a three-dimensional approach, previously described in subsection 2.3.2, coupled with the same basic scheme of kinetic reactions used by *Luque et al. (2014)*. The choice of a three-dimensional scheme allows us to investigate the shape and brightness of the predicted elves depending on the inclination of the parent-lightning channel, as well as to include the effect of the background magnetic field produced by the core of each giant gaseous.

6.1.1 Model of TLEs in Jupiter and Saturn

The atmospheres of Jupiter and Saturn are mainly formed by neutral H_2 and He with volume mixing ratios of 89/11 and 90/10, respectively. These giant gaseous planets also contain traces of other important species, such as methane, ammonia or water.

The structure of the Saturnian and Jovian atmospheres is illustrated in figure 6.1. The large quantity of mass of the giant gaseous planets compresses the atmosphere, causing a high internal heating. This energy produces convection movements that reach the mixed-phase cloud layer, where

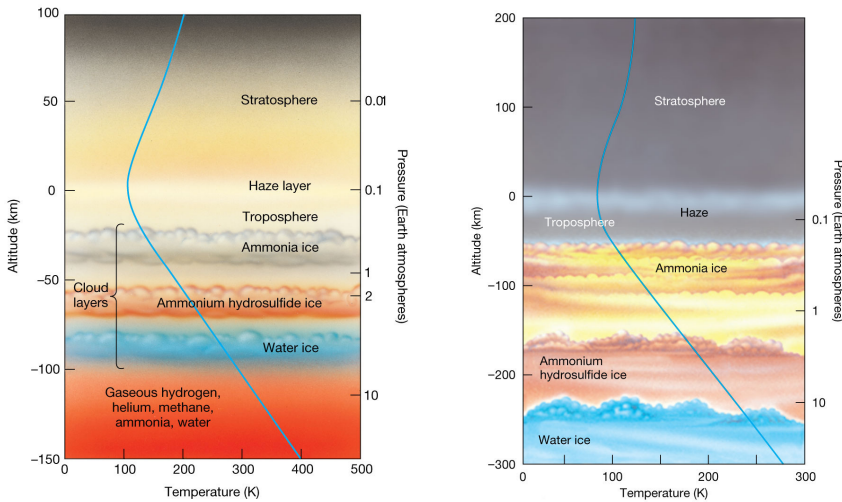


Figure 6.1: Structure of the Jovian (left) and Saturnian (right) atmospheres. Lightning discharges take place in the cloud layers. The altitude of 0 km is conventionally defined at the level where the pressure is 1 bar in each planetary atmosphere. Adapted from Pearson Prentice Hall, Inc. (2011).

water is present. Part of this convective energy is spent in a separation of charge that can trigger lightning discharges (*Williams et al.*, 1983).

Hypothetical elves taking place in the atmosphere of Jupiter and Saturn would be triggered by a parent-lightning discharge. In the case of the giant gaseous planets without a solid layer acting as ground, the only possible type of lightning are the cloud discharges.

Let us characterize the lightning discharges that we will use as inputs of the electrodynamical model of elves (subsection 2.3.2). These lightning discharges take place in the cloud layers of Saturn and Jupiter (see figure 6.1). In our model, we set the altitude of the parent-lightning at an altitude of -160 km in the case of Saturn, and -85 km in the case of Jupiter. We define the cloud discharge current as a bi-exponential function with total and rise times of, respectively, $\tau_1 = 1$ ms and $\tau_2 = 0.1$ ms. According to *Borucki and McKay* (1987); *Yair et al.* (1995); *Fischer et al.* (2007, 2008); *Dyudina et al.* (2010, 2013), the total energy released by lightning in gaseous planets is around 10^{12} J or 10^{13} J, creating a charge moment change (CMC) with a

6. ELVES PRODUCED IN GIANT GASEOUS PLANETS

value between $M=10^4$ C km and $M=10^6$ C km, depending on the lightning channel length h and the charged region radius R (*Dubrovin et al.*, 2014b; *Luque et al.*, 2014).

The electromagnetic field created by these lightning discharges could trigger TLEs in the lower ionosphere of these planets, as in the case of the Earth. *Yair et al.* (2009) hypothesized that Jovian TLEs could take place if the electron-impact ionization of H_2 and He exceed the electron attachment of H_2 as a consequence of a high reduced electric field (*Dubrovin et al.*, 2014b; *Luque et al.*, 2014). This situation would lead to the electronic excitation of H_2 to the states $H_2(d^3\Pi_u)$ and $H_2(a^3\Sigma_g^+)$. These excited molecules could emit photons after suffering radiative decay to $H_2(a^3\Sigma_g^+)$ and $H_2(b^3\Sigma_g)$, respectively (*Dubrovin et al.*, 2014b). These emissions would be distributed in the Fulcher band (390-700 nm) and in the near UV (160-380 nm).

We plot in figure 6.2 the weighted ionization and attachment rates according to the ratio of H_2 and He of the Jovian atmosphere. According to this figure, the value of the breakdown electric field in the atmospheres of Jupiter and Saturn is about 38 Td.

Following this reasoning, we can estimate the reduced electric field that could be reached in the lower ionosphere of these giant gaseous planets as a consequence of a lightning discharge. If this field exceeds the breakdown value, TLEs could be ignited. The approximated value of these fields can be seen in figure 6.3.

It is interesting to note that the radiation electric field component dominates over the quasi-static and induction electric fields. Therefore, the most common TLEs in the Saturnian and Jovian atmosphere would probably be elves.

The value of the reduced lightning-produced electric field in the lower ionosphere would be highly dependent on the shielding caused by the electron density profile. However, Saturnian and Jovian electron density profiles at ionospheric altitudes are uncertain and could vary with the latitude. Following *Luque et al.* (2014), we discuss different scenarios and choose several ionospheric profiles to simulate Saturnian and Jovian TLEs.

In the case of Saturn, the ionospheric profile can be different depending on the existence of a hydrocarbon (CH_x) layer. Therefore we choose two

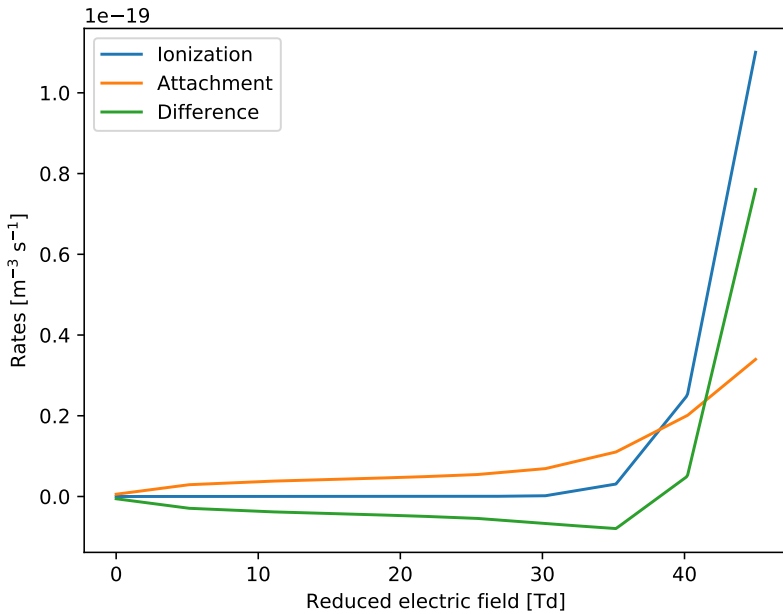


Figure 6.2: Weighted ionization and attachment rates as a function of the reduced electric field in the Jovian atmosphere. These rates have been calculated with BOLSIG+ (*Hagelaar and Pitchford, 2005*).

different profiles, one of them calculated by *Moore et al.* (2004), and other extended by *Galand et al.* (2009) to include an ionized CH_x layer that lowers the ionosphere down to 600 km. In the case of Jupiter, we use ingress and egress radio occultation measurements of the Voyager 2 (V2N and V2X) (*Hinson et al., 1997*).

Another important characteristic of the ionosphere of Saturn and Jupiter is the background magnetic field produced in their inner cores. This magnetic field can influence the propagation of electromagnetic waves, favoring or difficulting the penetration of EMPs in the ionospheric region. In addition, the latitudinal tilt of the magnetic field vector leads to an anisotropic plasma that could influence the shape of the Saturnian and Jovian TLEs. According to *Russell and Dougherty* (2010), the angle between the dipole axis that originates the magnetic field and the rotation axis is less than 1° in the case of Saturn, and about 10° in the case of Jupiter. Therefore we

6. ELVES PRODUCED IN GIANT GASEOUS PLANETS

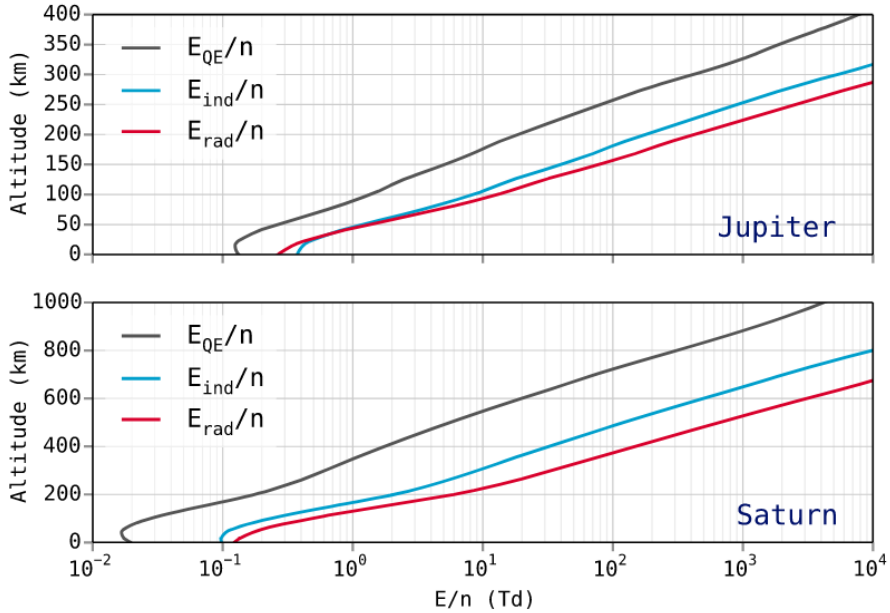


Figure 6.3: Approximated quasi-static, induction, and radiation-reduced electric fields in the atmospheres of Jupiter and Saturn as a consequence of a lightning discharge with a CMC of 10^5 C km and a characteristic discharge time of $100 \mu\text{s}$. In these plots *Luque et al.* (2014) do not take into account the effect of the ionospheric electrons in the electric field. Adapted from (*Luque et al.*, 2014).

can neglect this angle in both cases to calculate the dipolar magnetic field at a given latitude. The equatorial magnetic field is of the order of tens of microteslas in the case of Saturn and hundreds of microteslas in the case of Jupiter. As a reasonable approximation to the values of the magnetic field in the region where lightnings and their effects take place, we consider a value of 20×10^3 nT in the Saturnian atmosphere and 200×10^3 nT in the Jovian atmosphere, although there are no direct measurements of these fields at such altitudes. According to *Dyudina et al.* (2010, 2013), lightning on Saturn during the 2004-2017 Cassini epoch is common at latitudes of about $\pm 35^\circ$. However, Saturnian lightning can also take place at other latitudes, depending on the location of The Great White Spot storms. In the case of Jupiter, there exists evidence of lightning at several different

latitudes, including near the poles (*Baines et al.*, 2007). In our model, the background magnetic field inclination determined by the latitude can influence wave propagation, therefore we study the case of lightning in Saturn at a latitude of 35° (*Dyudina et al.*, 2010, 2013), while on Jupiter we extend the studies to equatorial and polar latitudes.

As we mentioned before, we use the electrodynamic model described in subsection 2.3.2 to investigate the inception of TLEs in the atmospheres of Saturn and Jupiter. In the case of the Saturnian ionosphere model with a layer of ionized CH_x , we set the horizontal distances of our computational domain between -2200 km and 2200 km with altitudes between -1000 km and 1108 km, using 24 cells for the absorbing boundary conditions. We choose a time step of 100 ns ensuring the constraints already discussed in subsection 2.3.2. For the atmosphere without a CH_x layer, the electromagnetic wave will suffer less attenuation than in the case with a CH_x layer, since the amount of electrons between the discharge location and the ionosphere is lower, therefore we run the simulations up to higher layers, with altitudes between -900 km and 1116 km, defining the absorbing boundary conditions in the last 28 cells and setting a smaller time step of 50 ns. In both cases, we restrict the domain where the modified Ohm's equation is solved to altitudes above 400 km.

Horizontal distances in the Jovian atmosphere are set between -1500 km and 1500 km with altitudes between -800 km and 440 km, defining the ideal boundary conditions in the last 20 cells and a time step of 10 ns. We solve the modified Ohm's equation for altitudes above 0 km. The same conditions are used for the two different Jovian electron profiles considered.

In order to obtain the optical signature of Saturnian lightning 5 ms after the discharge initiation in the upper atmosphere, we run each parallelized simulation for about 20 days using 10 CPUs in a cluster. In the case of Jupiter, the atmospheric effects 3 ms after the beginning of a stroke are obtained by running simulations during about 18 days and using the same number of CPUs as in the case of Saturn.

6.2 Results

6.2.1 Reduced electric field and electron density in the lower ionosphere

Lightning discharges in the atmospheres of Saturn and Jupiter would create an electromagnetic field that could affect the ionosphere. We use the electrodynamical model described in subsection 2.3.2 to compute those fields and predict the inception and evolution of TLEs.

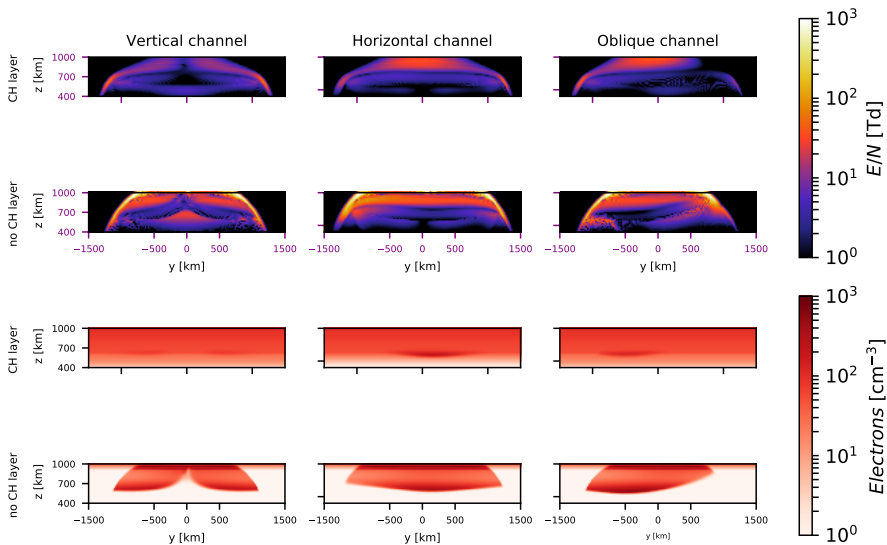


Figure 6.4: Reduced electric field E/N and electron density perturbation in the atmosphere of Saturn created between 4.8 ms and 5 ms after the beginning of a lightning discharge with a CMC of 10^5 C km and different channel inclinations and initial electron density profiles (with and without a CH_x layer). Subplots show results in the y - z plane for a latitude of 35° . The total energy released by the considered lightning is 10^{12} J. In the case of the vertical discharge, the channel is a straight line with coordinates $x = y = 0$, while in the case of the horizontal discharge, its coordinates are $x=z=0$. The oblique channel, contained in the y - z plane, forms an angle of 45° with the y axis. The background magnetic field at this latitude forms an angle of 35° with the vertical axis, and is contained in the plane x - z (Pérez-Invernón *et al.*, 2017b).

Figure 6.4 shows the reduced electric field and the electron density per-

turbation in the Saturnian ionosphere as a consequence of a lightning discharge with a charge moment change of 10^5 C km and considering different initial electron density profiles. If we compare simulations with and without a layer of ionized CH_x , the larger electron density gradient in the case of an atmosphere without a CH_x layer causes a worse description of the reduced electric field due to the continuous reflections in different layers of the atmosphere that ends up producing a complex electric field structure. The details of this structure is not correctly resolved in our mesh.

As explained in figure 6.2 of *Luque et al.* (2014), the electromagnetic pulse influences the ionosphere much more strongly than the quasi-electrostatic field. The reduced electric field produced by the quasi-electrostatic component reaches its maximum at altitudes around 600 km, while the radiation field component creates a larger reduced electric field in the upper region of our domain above 700 km. The quasi-electrostatic field reaches larger values in the vertical case, while radiation field is more important in the horizontal case (see figure 6.4).

It can be seen in the first row of figure 6.4 that the electric field is efficiently attenuated within the simulation domain in the atmosphere with a CH_x layer. However, the second row of figure 6.4 shows how, in the absence of a CH_x layer, the electric field pulse can penetrate the ionosphere of Saturn up to the highest level of the simulation domain. The lightning channel inclination controls the field emission pattern, causing differences in the electron density perturbation and determining the altitudes where the electric field is attenuated.

Let us now analyze the reduced electric field created by Jovian lightnings. Figure 6.5 shows the reduced electric field and the electron density perturbation in the Jovian ionosphere as a consequence of lightning discharges with different orientations and using as input the electron density profile measured at ingress by Voyager 2 (V2N). Large electron density gradients in the upper region of the simulation domain cause a complex electric field structure that is inaccurately described in some regions. The reduced electric fields obtained for the electron profile V2X are lower, as the larger electron density screens the field more efficiently.

The relation between the quasi-electrostatic and the radiation fields is

6. ELVES PRODUCED IN GIANT GASEOUS PLANETS

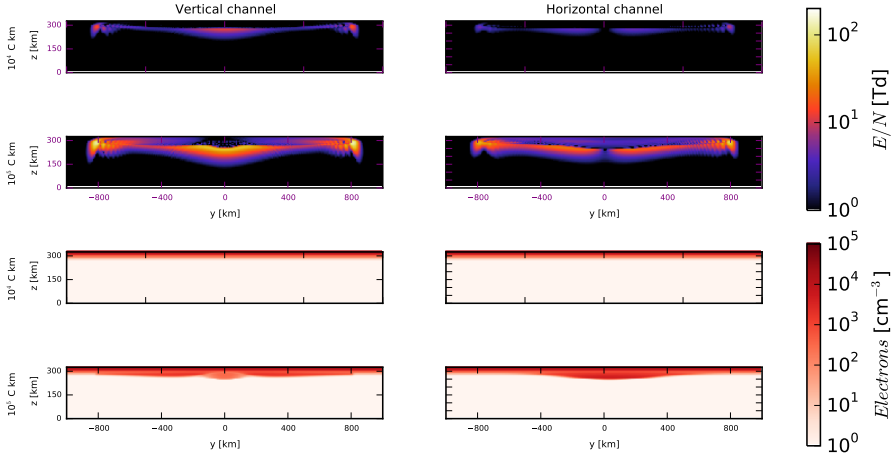


Figure 6.5: Reduced electric field E/N and electron density perturbation in the upper atmosphere of Jupiter as seen 3 ms after the beginning of a Jovian lightning discharge with different inclinations with charge moment changes of 10^4 and 10^5 C km. The subplots show results in the y - z plane for a latitude of 35° with the initial electron density profile measured at ingress of Voyager 2 (V2N). The total energy released by the considered lightning is 10^{12} J. In the case of the vertical discharge, the channel is a straight line with coordinates $x = y = 0$, while in the case of the horizontal discharge, its coordinates are $x = z = 0$. The background magnetic field at this latitude forms an angle of 35° with the vertical axis, and is contained in the plane x - z (Pérez-Invernón *et al.*, 2017b).

different in the case of Jupiter than in the case of Saturn, since shorter distances between the discharge and the Jovian ionosphere entail values of the same order of magnitude for both field components. As can be seen in figure 6.5, the ionosphere of Jupiter lowers in the case of vertical lightning discharges with a CMC of 10^5 C km.

As we mentioned in subsection 6.1.1, Jovian lightning discharges occur in a wide range of latitudes, with magnetic field inclinations relative to the vertical between 0 degrees at the poles and 90 degrees at the equator, which causes different wave attenuations. In figure 6.6 we plot the reduced electric field in the ionosphere of Jupiter produced by lightning at different latitudes. It can be seen that electric field pulses suffer less attenuation at

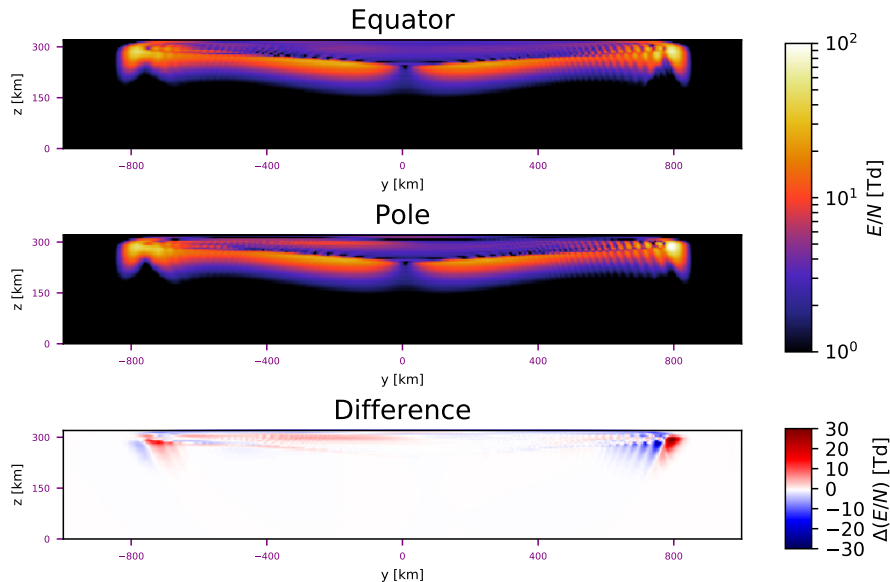


Figure 6.6: Reduced electric field E/N in the upper atmosphere of Jupiter created 3 ms after the onset of a horizontal lightning discharge with a CMC of 10^5 C km as seen at different latitudes (first and second panels). The last panel shows the difference between the second and the first panel. These results correspond to the case of the V2N electron density profile. The total energy released by the considered lightning is 10^{12} J (*Pérez-Invernón et al.*, 2017b).

the poles than at the equator, penetrating deeper into the polar ionosphere.

6.2.2 Optical emissions

The obtained reduced electric field would lead to a production of $\text{H}_2(\text{d}^3\Pi_u)$ and $\text{H}_2(\text{a}^3\Sigma_g^+)$ molecules by electron impact excitation of H_2 . As explained in subsection 6.1.1, these excited molecules would emit photons after suffering radiative decay to $\text{H}_2(\text{a}^3\Sigma_g^+)$ and $\text{H}_2(\text{b}^3\Sigma_g)$, respectively. Such emissions would be distributed in the Fulcher band (390-700 nm) and in the near UV (160-380 nm). In this section we estimate the brightness of the possible optical emissions from the Saturnian and Jovian lower ionospheres and predict their shapes under different conditions.

Figure 6.7 shows the integrated flux of photons as would be seen by a

6. ELVES PRODUCED IN GIANT GASEOUS PLANETS

spacecraft orbiting Saturn above an electrical discharge and looking at the nadir. As on the Earth (*Marshall et al.*, 2010), light emission, shapes, sizes and intensities depend on the lightning channel inclination.

Table 6.1 shows the total number of photons emitted from the upper atmosphere of Saturn as a consequence of electrical discharges with different inclinations and CMCs at 35 degrees of latitude. It can be seen how the lightning characteristics and the electron profile are key aspects in determining the total emitted photons. The existence or absence of a CH_x layer causes a difference of a factor two in the number of emitted photons.

It is also interesting to note the larger number of emitted photons when the lightning is horizontal, which is a direct consequence of the prevalence of the radiation field over the quasi-electrostatic field as can be clearly seen in figure 6.7.

Profile and CMC	Vertical channel (Photons / Optical energy)	Horizontal channel (Photons / Optical energy)	Oblique channel (Photons / Optical energy)
$\text{CH}_x - 10^4$	0	0	-
$\text{CH}_x - 10^5$	$2 \times 10^{25} / 1 \times 10^7 \text{ J}$	$3 \times 10^{25} / 1 \times 10^7 \text{ J}$	$1 \times 10^{25} / 5 \times 10^6 \text{ J}$
$\text{CH}_x - 10^6$	$2 \times 10^{27} / 1 \times 10^9 \text{ J}$	$2.5 \times 10^{27} / 1 \times 10^9 \text{ J}$	-
non $\text{CH}_x - 10^4$	$7.3 \times 10^{24} / 4 \times 10^6 \text{ J}$	$1 \times 10^{25} / 5 \times 10^6 \text{ J}$	-
non $\text{CH}_x - 10^5$	$4 \times 10^{25} / 2 \times 10^7 \text{ J}$	$6 \times 10^{25} / 3 \times 10^7 \text{ J}$	$8 \times 10^{25} / 4 \times 10^7 \text{ J}$
non $\text{CH}_x - 10^6$	-	$3 \times 10^{27} / 1 \times 10^9 \text{ J}$	-

Table 6.1: Total number of emitted photons and approximated optical energy released from the Saturnian ionosphere between 4.8 ms and 5 ms after the onset of a cloud discharge. CH_x corresponds to an electron density profile in the presence of a hydrocarbon layer, while non CH_x corresponds to an electron density profile without a hydrocarbon layer. Charge moment change (CMC) are in C km. Null values are below our numerical precision, while - corresponds to not calculated cases. Emissions are produced by radiative decay of $\text{H}_2(\text{d}^3\Pi_u)$ and $\text{H}_2(\text{a}^3\Sigma_g^+)$ molecules (*Pérez-Invernón et al.*, 2017b).

Figure 6.8 shows the integrated flux of photons from $\text{H}_2(\text{d}^3\Pi_u)$ and $\text{H}_2(\text{a}^3\Sigma_g^+)$ molecules as seen by a spacecraft orbiting Jupiter above an electrical discharge at 35 degrees of latitude. Different shapes and extensions are consistent with the electromagnetic emission pattern of each tilted discharge. The spatial distribution of emitted photons also depends on the channel inclination, causing more localized and intense optical emissions in the case of horizontal discharges. The background magnetic field inclination is also important, as can be seen in the asymmetry of the upper right and

lower left plots of figure 6.8.

Table 6.2 shows the total number of photons emitted from the upper atmosphere of Jupiter 3 ms after electrical discharges with different inclinations and CMCs. We show results for different electron density profiles at 35 degrees of latitude. As on Saturn, the characteristics of the discharge and the electron density profiles determine the number of emitted photons and the detectability of Jovian TLEs.

Profile and CMC	Vertical channel	Horizontal channel
	(n photons / Optical energy)	(n photons / Optical energy)
V2N - 10^4	$5 \times 10^{19} / 3 \times 10^1$ J	$4 \times 10^{21} / 2 \times 10^3$ J
V2N - 10^5	$6 \times 10^{25} / 3 \times 10^7$ J	$5 \times 10^{25} / 2.7 \times 10^7$ J
V2X - 10^4	0	0
V2X - 10^5	0	$7 \times 10^{15} / 3 \times 10^{-3}$ J

Table 6.2: Total number of emitted photons and approximated optical energy released from the Jovian ionosphere 3 ms after a cloud lightning. V2N corresponds to an electron density profile measured at ingress of Voyager 2, while V2X corresponds to measurements at egress. Charge moment change (CMC) are in C km. Null values are below our numerical precision. Emissions are produced by radiative decay of $\text{H}_2(\text{d}^3\Pi_u)$ and $\text{H}_2(\text{a}^3\Sigma_g^+)$ molecules (Pérez-Invernón *et al.*, 2017b).

6.3 Conclusions

The present three-dimensional model requires more computational time than the two-dimensional model previously developed by *Luque et al.* (2014), limiting the total simulated time and the spatial resolution. However, it has allowed us to determine some key features of the optical emissions produced by lightning on gaseous giant planets as well as the effect of a background magnetic field. We have obtained results for vertical discharges that are consistent with previous results reported by *Luque et al.* (2014).

According to our results, vertical lightning causes torodial-shaped optical emissions, while horizontal and tilted discharges produce other disk-shaped emissions with a maximum of light emission near the center of the disk. This information, in addition to emission intensities, can be helpful to deduce intra-cloud lightning characteristics on Saturn and Jupiter from future remote observation. In addition, according to these results, future lightning and TLE observations in these atmospheres could provide valu-

6. ELVES PRODUCED IN GIANT GASEOUS PLANETS

able information about the atmospheric characteristics of each planet, since emissions intensities at each latitude depend on the electron density profile.

High electric fields shown for high altitude values of the vertical channel cases shown in figure 6.4 are not observed in the previous two-dimensional model (*Luque et al.*, 2014), since the tilted background magnetic field included in the three-dimensional model favors wave penetration in the ionosphere. This effect can also be seen in Jupiter (see figure 6.6), where two magnetic field inclinations cause different wave attenuation. These results suggest that the strong background magnetic field in giant gaseous planets can be important for the shape of the optical emissions produced by lightning in the upper atmosphere. Electromagnetic detection of lightning from orbiters is also related to background magnetic field inclination, as pulses can easily escape from the ionosphere if lightning discharges occur at high latitudes.

As previously discussed by *Luque et al.* (2014), optical energy released by TLEs in Saturn and Jupiter may be comparable to the optical energy emitted by lightning (*Dyudina et al.*, 2013). However, the uncertainties about the lightning emitted spectrum (*Borucki and McKay*, 1987; *Little et al.*, 1999; *Dyudina et al.*, 2004, 2013) prevent comparison with emissions predicted in this work. Therefore, we compare the shape of the TLEs emissions and the diameter of observed flashes. *Little et al.* (1999) and *Dyudina et al.* (2010) reported flashes without a central hole. In addition, Saturnian flashes studied by *Dyudina et al.* (2010) had a diameter below 200 km. Figures (6.7) and (6.8) show TLEs without a central hole but with diameters above 1000 km. These resultant sizes suggest that observed flashes are not produced by TLEs, but by lightning themselves. However, the uncertainty in the lower ionosphere composition (including electron density profiles) of the giant gaseous planets maintains the source of observed flashes open. Future data reported by missions like Juno of NASA and the Jupiter Icy Moons Explorer (JUICE) of ESA will probably shed more light on numerous unknown aspects about electrical phenomena in the atmospheres of the giant gaseous planets.

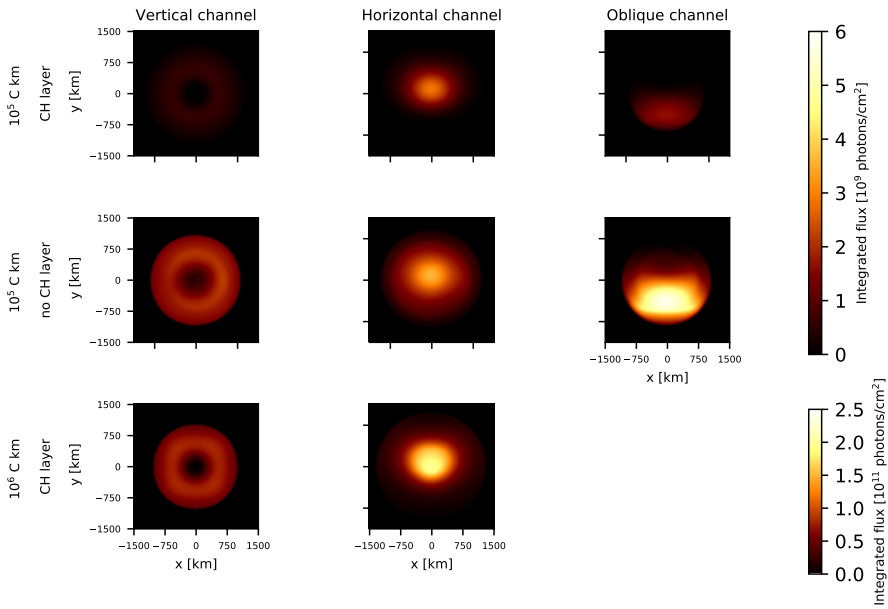


Figure 6.7: Integrated flux of total emitted photons from the radiative decays of $\text{H}_2(d^3\Pi_u)$ and $\text{H}_2(a^3\Sigma_g^+)$ between 4.8 ms and 5 ms after a lightning discharge on Saturn with different CMCs of 10^5 C km and 10^6 C km. Different channel inclinations are shown in each column, while each row corresponds to two different initial electron densities. The total energy released by the considered lightning discharges are 10^{12} J and 10^{13} J. The total number of emitted photons shown corresponds to the nadir direction from an orbiting probe without considering atmospheric and geometric attenuation. Lightning channel and background magnetic field inclinations are as in figure 6.4. (*Pérez-Invernón et al., 2017b*).

6. ELVES PRODUCED IN GIANT GASEOUS PLANETS

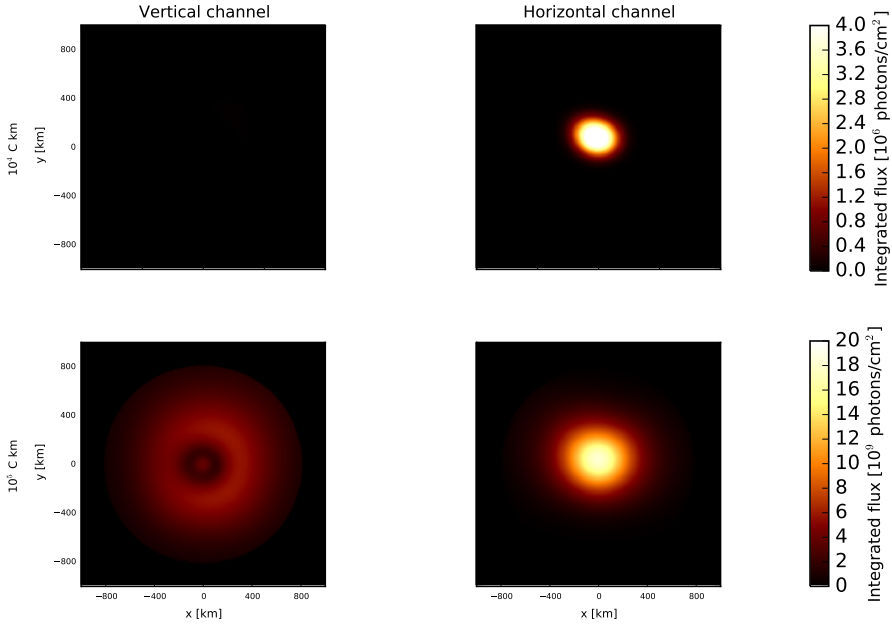


Figure 6.8: Integrated flux of total emitted photons from the radiative decays of $\text{H}_2(\text{d}^3\Pi_u)$ and $\text{H}_2(\text{a}^3\Sigma_g^+)$ 3 ms after Jovian lightning discharges with different charge moment changes. Vertical and horizontal channel inclinations are shown in each column. These results correspond to the case of the V2N electron density profile. The total energy released by lightning is 10^{12} J. The total number of emitted photons shown corresponds to the nadir direction from an orbiting probe without considering atmospheric and geometric attenuation. Lightning channel and background magnetic field inclinations are as in figure 6.5. (*Pérez-Invernón et al., 2017b*).

Chapter 7

Summary

7.1 Summary

We have modeled electrical phenomena in the atmospheres of Venus, the Earth, Saturn and Jupiter. The results of the developed models have been useful to interpret some past measurements as well as to make predictions about possible optical emissions produced by Venusian, Saturnian and Jovian TLEs. In addition, we have developed a method to analyze signals from halos and elves reported by some past and future spacecraft to study atmospheric electricity, such as GLIMS (JAXA), ISUAL (NSPO), ASIM (ESA) and TARANIS (CNES).

We have developed two electrodynamical models to simulate the inception and evolution of halos and elves in the above mentioned planetary atmospheres. These models are coupled with different sets of kinetic reactions that describe the basic chemistry in the mesosphere and upper ionosphere of each planet.

The halo model has allowed us to calculate the quasiolelectrostatic field produced by halos at ground level. *Bennett and Harrison (2013)* reported the detection of lightning-produced electrostatic fields at distances of up to about 300 km from a thunderstorm, suggesting a possible violation of the expected cubic decay law and causing a change in the field polarity. *Bennett (2014)* proposed the influence of the halo-triggered quasiolelectrostatic field as the reason behind the observed violation of the cubic decay law he reported

7. SUMMARY

the year before. However, according to our results, these anomalies in the measurements would not be a consequence of halos. We published these results in (*Pérez-Invernón et al.*, 2016a). We have also used these models to predict ro-vibrational optical spectra of halos and elves as well as to estimate the local and global chemical influence of these TLEs in the atmosphere of the Earth. According to our results, the global NO_x produced by halos and elves would be of the order of 10^{-7} Tg N/y. In addition, we have analyzed the expected differences in the optical emissions of TLEs produced by different types of lightning discharges. We have concluded that although spectra would be similar, the shape of the elves would depend on the type of parent lightning. We have submitted these results to the *Journal of Geophysical Research: Atmospheres*.

There have been two space-based missions devoted to the observation of TLEs, such as GLIMS (2012-2015) and ISUAL (2004-2016). In addition, ASIM and TARANIS will be launched in the next years with the same goal. These past and future optical data from TLEs have motivated us to develop two methods to analyze the signals recorded from space. For this purpose, we have firstly used the synthetic optical emissions from simulated halos and elves in order to use the developed inversion methods to infer the temporal evolution of an emitting source in the mesosphere and the reduced electric field inside halos and elves. Then, we have applied one of these inversion methods to a real elve signal reported by GLIMS. We plan to publish these methods in the near future and to use them as a tool to analyze the data provided by ASIM and TARANIS.

The existence of lightning in Venus is still controversial. *Yair et al.* (2009) proposed the search of Venusian TLEs as an indirect method to probe the existence of lightning discharges in Venus. Hence, we have used the halo and elve models to predict possible TLEs in the atmosphere of Venus. We have obtained that these hypothetical TLEs could emit light flashes in the First and Second Positive Systems of N_2 , as well as in the LBH band. In addition, they could also emit in the 557 nm and 630 nm lines of the atomic oxygen optical spectrum. Emissions in the 557 nm line could possibly be detected by Akatsuki, a Japanese spacecraft currently orbiting Venus and equipped with the Lightning and Airglow Camera (LAC), a high

temporal resolution camera specifically design to detect lightning in Venus. In addition, these emissions could be related with the natural variation of the Venusian nightglow. We have published these results in (*Pérez-Invernón et al.*, 2016b) and *Pérez-Invernón et al.* (2017b).

The versatility of the developed three-dimensional elve model has allowed us to investigate the optical emissions produced by elves in the atmospheres of Jupiter and Saturn. The existence of electrical discharges in these gaseous giant planets was probed by the Voyagers (NASA) and Cassini (NASA, ESA and ASI) spacecraft. However, it was unclear if the reported optical flashes were produced by lightning themselves or by some kind of TLE. *Luque et al.* (2014) developed a two-dimensional elve model to simulate Saturnian and Jovian elves. However, that two-dimensional model was not able to include neither the effect of the background magnetic field nor the inclination of the lightning discharge channel. Our developed three-dimensional model of elves has allowed us to investigate the shape of the optical emissions and their relation with the lightning channel tilt and the latitude. We have concluded that the reported flashes were produced by lightning, as the predicted elves would cover more space than the observed optical emissions. We have published these results in *Pérez-Invernón et al.* (2017b).

Apart from the simulation of halos and elves, we have investigated the propagation of lightning-produced electromagnetic waves through the atmospheres of Venus and the Earth. For these purposes, we have used the Full Wave Method (FWM) developed by *Lehtinen and Inan* (2008). The VLF waves radiated by electrical phenomena in the terrestrial atmosphere travel through the spherical cavity formed by the Earth ground and the ionosphere. The interaction between the radiated pulses and the propagation media enables these pulses to travel large distances from the source, providing useful information about the electrical phenomena that trigger the pulses. The interaction of these pulses with the ionosphere causes wave distortions in the signal across its way from the source to the detection system. In addition, the superposition of the reflected waves causes both transverse and longitudinal resonances, altering the original signal. We have used the FWM to investigate the differences in the wave distortion produced by a flat

7. SUMMARY

and a curved planet surface. We have also calculated the transfer function of the curved Earth-ionosphere waveguide (EIWG). This transfer function has been used in the work published in *Mezentsev et al.* (2018) to investigate the pulses radiated from regions where Terrestrial Gamma-ray Flashes (TGFs) are produced. We have also particularized the FWM to the case of Venus. We have simulated the propagation of lightning-produced whistler waves through the ionosphere of Venus. The obtained results have allowed us to compare the simulated characteristic of whistler waves with the signals reported by PVO (NASA) and VEX (ESA). According to our results, if the observed signals are generated by lightning, the average energy released by Venusian lightning and their occurrence rate are considerably greater than in the terrestrial case. We have published these results in *Pérez-Invernón et al.* (2017a).

The computational simulations to produce the results of this thesis have been carried out in a CSIC computer cluster in Madrid called “Trueno”. The computer cluster located at IAA-CSIC in Granada has also been used in order to test the codes.

Chapter 8

Conclusions

8.1 Conclusions

- Halos and elves can produce an important amount of NO and N₂O in the upper mesosphere.
- The optical spectra of elves does not depend on the type of parent lightning discharge.
- Compact Intracloud Discharges (CID) and Energetic In-cloud Pulses (EIP) can produce elve “doublets”.
- The quasioleostatic field produced by halos at ground level is not detectable by current instruments.
- We have used the FWM to deduce a transformation from the transfer function of the flatted Earth-ionosphere waveguide (EIWG) to the curved EIWG. This transfer function has been used to investigate the pulses radiated from regions where Terrestrial Gamma-ray Flashes (TGFs) are produced.
- We have developed a method to obtain the reduced electric field inside halos and elves from space-based photometers. This method could be used to analyze future optical data reported by ASIM (ESA) and TARANIS (CNES).

8. CONCLUSIONS

- We have developed an inversion method to obtain the temporal evolution of the emitting source of an elve using optical signals reported by spacecraft.
- Hypothetical Venusian halos and elves could be an indirect probe of the existence of lightning discharges in Venus. They would emit light pulses in a wide range of frequencies. Emissions in the 557 nm line could enhance the natural intensity variation of the Venusian night-glow. In addition, they could be detected by the LAC instrument onboard the Akatsuki spacecraft (JAXA).
- We have particularized the FWM to the case of whistler wave propagation through the atmosphere of Venus. According to our results, the signals detected by PVO (NASA) and VEX (ESA) were probably produced by upper atmospheric plasma instabilities rather than by tropospheric lightning discharges.
- We have modeled Saturnian and Jovian elves. According to our results, the optical flashes so far detected by several spacecraft, such as the Voyagers (NASA) and Cassini (NASA, ESA and ASI), were produced by lightning discharges instead of by TLEs. However, according to our models, lightning in Saturn and Jupiter can be accompanied by TLEs.
- The shape and intensity of the elves predicted by our models in the atmospheres of Saturn and Jupiter depend on the latitude, the parent lightning channel inclination and the composition of the upper atmosphere.

Chapter 9

Future work

9.1 Future work

As part of the scientific team of the ASIM and TARANIS missions, we plan to analyze the optical data provided by the photometers and cameras onboard these space platforms. For this purpose, we will use the two analysis methods developed in this thesis and described in chapter 4. Both ASIM and TARANIS will be the first space missions capable of recording TLEs and TGFs at the same time. TGFs are often associated with a high-impulsive intracloud discharges, that could also produce “elve doublets”. Therefore, if ASIM and TARANIS confirm the relation between “elve doublets” and TGFs, the optical analysis of these TLEs could provide useful information about the characteristic of the parent lightning and, consequently, the production mechanism of TGFs.

The Akatsuki spacecraft is currently orbiting Venus. The detection of lightning or TLEs by the cameras onboard Akatsuki would provide new and valuable information about the characteristics of Venusian atmospheric electricity phenomena. We plan to develop new models if the existence of lightning in Venus is confirmed.

The short stay at the National Center for Atmospheric Research (NCAR) of the University Corporation for Atmospheric Research (UCAR) has allowed us to investigate the global parameterization of electricity phenomena in the Whole Atmosphere Community Climate Model (WACCM). This at-

9. FUTURE WORK

atmospheric model can be used as a valuable tool to extend the local models developed in our group on the chemical impact of atmospheric electricity-related phenomena to global models. In this regard, we have tested different lightnings and Blue Jets parameterizations in the mentioned model. We plan to publish these results in the near future. In addition, we plan to use WACCM and other atmospheric models to investigate the relation between some climatic variables, the lightning occurrence rate and the lightning global chemical impact in the atmospheric concentration of NO_x and other important chemical species (SO_2 , H_2SO_4 , HNO_3 , OH , ...) of the atmosphere of the Earth.

Appendix A

Chemical schemes

This appendix collects a set of chemical reactions used in the models of halos and elves for the atmospheres of the Earth and Venus.

A.1 Kinetic model for terrestrial TLEs

This section collects the kinetic scheme of the halo and elve models in the mesosphere of Earth. Some of the rates are given in the literature as a function of the gas temperature (T). In that case, we provide the rate value for a temperature of 200 K. Electric field dependent and electron temperature dependent reaction rates are marked as $f(E/N)$ and $f(T_e)$, respectively. The value of these rates is calculated every time step. Cosmic ray ionization is altitude dependent ($f(h)$). Some reaction rates depend on the vibrational levels involved in the different processes considered, and are given as $f(v)$. Rates corresponding to two-body reactions, three-body reactions and radiative decay processes are given in the units m^3s^{-1} , m^6s^{-1} and s^{-1} , respectively. The symbol M corresponds to molecules of O₂ and N₂. References listed in the table are as follows: [1]: *Thomas* (1974), [2]: Cross sections by *Phelps* (1991), [3]: Cross sections following *Cartwright et al.* (1977), *Borst and Zipf* (1970), *Gordillo-Vázquez* (2010) and *Simek* (2002). [4]: Cross sections by *Lawton and Phelps* (1978), [5]: Cross sections by *Pagnon et al.* (1995), [6]: Cross sections by *Erdman and Zipf* (1987), [7]: Cross sections by *Skalni et al.* (1996), [8]: Cross sections by *Morrill*

(2000), [9]: Cross sections by *Lahey and Gilmore* (1990), [10]: Cross sections by *Pitchford et al.* (2012), [11]: Cross section by *Phelps* (1969), [12]: Cross sections by *Phelps* (2005), [13]: *Pancheshnyi* (2013), [14]: *Kossyi et al.* (1992), [15]: *Peeverall et al.* (2001), [16]: *Whitaker et al.* (1981), [17]: *Starikovskaia et al.* (2001), [18]: *Castillo et al.* (2004), [19]: *Gudmundsson et al.* (2001a), [20]: (*Rodríguez et al.*, 1991), [21]: (*Gordiets et al.*, 1995), [22]: (*Kamaratos*, 2006), [23]: (*Yaron et al.*, 1976), [24]: (*Slanger and Copeland*, 2003), [25]: (*Vallance Jones*, 1974), [26]: (*Viggiano*, 2006), [27]: (*Guerra and Loureiro*, 1999), [28]: (*Zinn et al.*, 1990), [29]: (*Herron and Green*, 2001), [30]: (*Brasseur and Solomon*, 1986), [31]: (*Makhlouf et al.*, 1995), [32]: (*Sentman et al.*, 2008), [33]: (*Turnbull and Lowe*, 1991), [34]: (*Cacciatore et al.*, 2005), [35]: (*Kurnosov et al.*, 2007), [36]: (*Capitelli et al.*, 2000), [37]: (*Linstrom and Mallard*, 2015), [38]: (*Simek*, 2003), [39]: (*Thoman et al.*, 1992), [40]: (*Biondi et al.*, 1971), [41]: (*Kazil et al.*, 2003), [42]: (*Albritton*, 1978), [43]: (*Piper et al.*, 1985), [44]: (*Lepoutre et al.*, 1977), [45]: (*Dagdigian et al.*, 1988), [46]: *Morrill and Benesch* (1996) and (*Gordillo-Vázquez*, 2010), [47]: *Gordillo-Vázquez* (2010) and *Simek* (2002), [48]: (*Calo et al.*, 1971), [49]: *Gordillo-Vázquez* (2010), (*Piper*, 1988) and (*Piper*, 1992), [50]: *Gordillo-Vázquez* (2010) and (*Piper*, 1989), [51]: (*Kam and Pipkin*, 1991), [52]: (*Smirnov and Massey*, 1982), [53]: (*Bates*, 1988), [54]: (*Krupenie*, 1972), [55]: (*Radzig and Smirnov*, 2012), [56]: (*Parra-Rojas et al.*, 2015), [57]: (*Gilmore et al.*, 1992), [58]: (*Gudmundsson et al.*, 2001b).

Reaction	Rate	Reference
$Q + N_2(X^1 \Sigma_g^+, v=0) \rightarrow e + N_2^+ + Q$	$0.585 f(h)$	[1]
$Q + O_2 \rightarrow e + O_2^+ + Q$	$0.154 f(h)$	[1]
$Q + N_2(X^1 \Sigma_g^+, v=0) \rightarrow e + N^+ + N + Q$	$0.185 f(h)$	[1]
$Q + N_2(X^1 \Sigma_g^+, v=0) \rightarrow e + O^+ + O + Q$	$0.076 f(h)$	[1]
$e + N_2(X^1 \Sigma_g^+, v=0) \rightarrow e + e + N_2^+$	$f(E/N)$	[2]
$e + N_2(X^1 \Sigma_g^+, v=0) \rightarrow e + e + N^+ + N$	$f(E/N)$	[2]
$e + O_2 \rightarrow e + e + O_2^+$	$f(E/N)$	[4]
$N_2O + e \rightarrow N_2O^+ + e + e$	$f(E/N)$	[10]
$NO + e \rightarrow NO^+ + e + e$	$f(E/N)$	[11]
$e + O_2 \rightarrow e + e + O^+ + O$	$f(E/N)$	[4]
$NO_2 + e \rightarrow NO_2^+ + e + e$	$f(T_e)$	[18]
$NO + e \rightarrow O^+ + N + e + e$	$f(T_e)$	[18]
$NO_2 + e \rightarrow NO^+ + O + e + e$	$f(T_e)$	[18]

Table A.1: Ionization and dissociative ionization processes.

Reaction	Rate	Reference
$e + N_2(X^1 \Sigma_g^+, v=0) \leftrightarrow e + N_2(X^1 \Sigma_g^+, v=1, \dots, 10)$	$f(E/N)$	[2]
$e + N_2(X^1 \Sigma_g^+, v=0) \rightarrow e + N_2(A^3 \Sigma_u^+, v=0, \dots, 16)$	$f(E/N)$	[3]
$e + N_2(X^1 \Sigma_g^+, v=0) \rightarrow e + N_2(B^3 \Pi_g, v=0, \dots, 6)$	$f(E/N)$	[3]
$e + N_2(X^1 \Sigma_g^+, v=0) \rightarrow e + N_2(C^3 \Pi_u, v=0, \dots, 4)$	$f(E/N)$	[3]
$e + N_2(X^1 \Sigma_g^+, v=0) \rightarrow e + e + N_2^+(B^2 \Sigma_u^+)$	$f(E/N)$	[2]
$e + N_2(X^1 \Sigma_g^+, v=0) \rightarrow e + N_2(a'^1 \Sigma_u^-)$	$f(E/N)$	[2]
$e + N_2(X^1 \Sigma_g^+, v=0) \rightarrow e + N + N$	$f(E/N)$	[2]
$e + N_2(X^1 \Sigma_g^+, v=0) \rightarrow e + N + N(^2D)$	$f(E/N)$	[2]
$e + N_2(X^1 \Sigma_g^+, v=0) \rightarrow e + N_2(a''^1 \Sigma_g^+)$	$f(E/N)$	[2]
$e + N_2(X^1 \Sigma_g^+, v=0) \rightarrow e + N_2(E^3 \Sigma_g^+)$	$f(E/N)$	[2]
$e + N_2(X^1 \Sigma_g^+, v=0) \rightarrow e + N_2(w^1 \Delta_u)$	$f(E/N)$	[2]
$e + N_2(X^1 \Sigma_g^+, v=0) \rightarrow e + N(^2P)$	$f(E/N)$	[2]
$e + N_2(X^1 \Sigma_g^+, v=0) \rightarrow e + N_2(a^1 \Pi_g, v=0, \dots, 15)$	$f(E/N)$	[3]
$e + N_2(X^1 \Sigma_g^+, v=0) \rightarrow e + N_2(W^3 \Delta_u, v=0, \dots, 3)$	$f(E/N)$	[3]
$e + N_2(X^1 \Sigma_g^+, v=0) \rightarrow e + N_2(B'^3 \Sigma_u^-, v=0, 1)$	$f(E/N)$	[3]
$e + O_2 \rightarrow e + O_2(a^1 \Delta_g)$	$f(E/N)$	[4]
$e + O_2 \rightarrow e + O_2(b^1 \Sigma_g^+)$	$f(E/N)$	[4]
$e + O_2 \rightarrow e + O + O(^1D)$	$f(E/N)$	[4]
$e + O_2 \rightarrow e + O + O(^1S)$	$f(E/N)$	[4]
$e + O_2 \rightarrow e + O_2(A^3 \Pi_u^+)$	$f(E/N)$	[4]
$e + O_2 \rightarrow e + O(^3P) + O$	$f(E/N)$	[5]
$e + O_2 \rightarrow e + O(^5P) + O$	$f(E/N)$	[6]
$e + CO_2 \leftrightarrow e + CO_2(001)$	$f(E/N)$	[12]
$e + CO_2 \leftrightarrow e + CO_2(100)$	$f(E/N)$	[12]
$e + CO_2 \leftrightarrow e + CO_2(010)$	$f(E/N)$	[12]
$e + O \rightarrow e + O(^1D)$	$f(E/N)$	[8]
$e + O \rightarrow e + O(^1S)$	$f(E/N)$	[8]
$e + O \rightarrow e + O(^3P)$	$f(E/N)$	[9]
$e + O \rightarrow e + O(^5P)$	$f(E/N)$	[9]

Table A.2: Electronical and vibrational excitation processes by electron impact, including those in which dissociation can occur.

A. CHEMICAL SCHEMES

Reaction	Rate	Reference
$e + O_2 \rightarrow O + O^-$	$f(E/N)$	[4]
$O_3 + e \rightarrow O^- + O_2$	$f(E/N)$	[7]
$O_3 + e \rightarrow O_2^- + O$	$f(E/N)$	[7]
$N_2O + e \rightarrow N_2(X^1 \Sigma_g^+, v=0) + O^-$	$f(E/N)$	[10]
$e + O + N_2(X^1 \Sigma_g^+, v=0) \rightarrow O^- + N_2(X^1 \Sigma_g^+, v=0)$	$f(T_e)$	[14]
$e + NO_2 \rightarrow O^- + NO$	$f(T_e)$	[14]
$e + NO_2 \rightarrow NO_2^-$	$f(T_e)$	[14]
$e + O_3 + O_2 \rightarrow O_3^- + O_2$	$f(T_e)$	[14]
$e + NO + N_2(X^1 \Sigma_g^+, v=0) \rightarrow NO^- + N_2(X^1 \Sigma_g^+, v=0)$	$f(T_e)$	[14]
$e + O_2 + O_2 \rightarrow O_2^- + O_2$	$f(T_e)$	[14]
$e + O_2 + N_2(X^1 \Sigma_g^+, v=0) \rightarrow O_2^- + N_2(X^1 \Sigma_g^+, v=0)$	$f(T_e)$	[14]
$e + O + O_2 \rightarrow O^- + O_2$	$f(T_e)$	[14]
$e + O + O_2 \rightarrow O_2^- + O$	$f(T_e)$	[14]

Table A.3: Attachment processes.

Reaction	Rate	Reference
$O^- + N_2(X^1 \Sigma_g^+, v=0) \rightarrow N_2O + e$	$f(E/N)$	[13]
$O_2^- + M \rightarrow e + O_2 + M$	$f(E/N)$	[13]
$O^- + O_2 \rightarrow e + O_3$	$5 f(E/N)$	[13]
$O_2^- + O_2(a^1 \Delta_g) \rightarrow e + O_2 + O_2$	2.00×10^{-16}	[14]
$O_2^- + O_2(b^1 \Sigma_g^+) \rightarrow e + O_2 + O_2$	3.60×10^{-16}	[14]
$O_2^- + N_2(A^3 \Sigma_u^+, v=0) \rightarrow e + N_2(X^1 \Sigma_g^+, v=0) + O_2$	2.10×10^{-15}	[14]
$O_2^- + N_2(B^3 \Pi_g, v=0) \rightarrow e + O_2 + N_2(X^1 \Sigma_g^+, v=0)$	2.50×10^{-15}	[14]
$O^- + O_2(a^1 \Delta_g) \rightarrow e + O_3$	3.00×10^{-16}	[14]
$O^- + O_2(b^1 \Sigma_g^+) \rightarrow e + O_2 + O$	6.90×10^{-16}	[14]
$O^- + N_2(A^3 \Sigma_u^+, v=0) \rightarrow e + N_2(X^1 \Sigma_g^+, v=0) + O$	2.20×10^{-15}	[14]
$O^- + N_2(B^3 \Pi_g, v=0) \rightarrow e + N_2(X^1 \Sigma_g^+, v=0) + O$	1.90×10^{-15}	[14]
$O_2^- + O \rightarrow e + O_3$	1.50×10^{-16}	[14]
$O_2^- + N \rightarrow e + NO_2$	5.00×10^{-16}	[14]
$O^- + O \rightarrow e + O_2$	5.00×10^{-16}	[14]
$O^- + N \rightarrow e + NO$	2.60×10^{-16}	[14]
$O_3^- + O \rightarrow e + O_2 + O_2$	3.00×10^{-16}	[14]
$NO_2^- + O \rightarrow e + NO_3$	1.00×10^{-18}	[14]
$O^- + NO \rightarrow e + NO_2$	2.60×10^{-16}	[14]
$O^- + O_3 \rightarrow e + O_2 + O_2$	5.00×10^{-16}	[20]
$O^- + CO \rightarrow CO_2 + e$	5.27×10^{-16}	[40]
$O_2^- + O_2(b^1 \Sigma_g^+) \rightarrow O_2 + O_2 + e$	3.60×10^{-16}	[14]
$NO^- + CO_2 \rightarrow NO + CO_2 + e$	8.30×10^{-18}	[42]
$NO^- + CO \rightarrow NO + CO + e$	5.00×10^{-19}	[42]
$NO^- + N_2O \rightarrow NO + N_2O + e$	5.10×10^{-18}	[42]
$NO^- + NO \rightarrow NO + NO + e$	5.00×10^{-18}	[42]

Table A.4: Electron detachment processes.

A.1 Kinetic model for terrestrial TLEs

Reaction	Rate	Reference
$e + N_4^+ \rightarrow N_2(X^1 \Sigma_g^+, v=0) + N_2(X^1 \Sigma_g^+, v=0)$	$f(T_e)$	[14]
$e + O_4^+ \rightarrow O_2 + O_2$	$f(T_e)$	[14]
$e + N_2^+ \rightarrow N + N$	$f(T_e)$	[14]
$e + N_2^+ \rightarrow N + N(^2D)$	$f(T_e)$	[14]
$e + O_2^+ \rightarrow O + O$	$f(T_e)$	[15]
$e + O_2^+ \rightarrow O + O(^1D)$	$f(T_e)$	[15]
$e + O_2^+ \rightarrow O(^1D) + O(^1D)$	$f(T_e)$	[15]
$e + O_2^+ \rightarrow O(^1S) + O(^1D)$	$f(T_e)$	[15]
$e + NO^+ \rightarrow N + O$	$f(T_e)$	[14]
$e + NO^+ \rightarrow O + N(^2D)$	$f(T_e)$	[14]
$e + O_2^+ + M \rightarrow O + O_2 + M$	$f(T_e)$	[14]
$e + N_2^+ + O_2 \rightarrow N_2(X^1 \Sigma_g^+, v=0) + O_2$	$f(T_e)$	[14]
$e + NO^+ + O_2 \rightarrow NO + O_2$	$f(T_e)$	[14]
$e + NO^+ + N_2(X^1 \Sigma_g^+, v=0) \rightarrow NO + N_2(X^1 \Sigma_g^+, v=0)$	$f(T_e)$	[14]
$e + N_4^+ \rightarrow N_2(X^1 \Sigma_g^+, v=0) + N + N$	$f(T_e)$	[16]
$e + O^+ + N_2(X^1 \Sigma_g^+, v=0) \rightarrow O + N_2(X^1 \Sigma_g^+, v=0)$	$f(T_e)$	[14]
$e + O^+ + e \rightarrow O + e$	$f(T_e)$	[14]
$e + O^+ + O_2 \rightarrow O + O_2$	$f(T_e)$	[14]
$e + N_3^+ \rightarrow N_2(A^3 \Sigma_u^+, v=0) + N$	$f(T_e)$	[17]
$e + N_3^+ \rightarrow N_2(B^3 \Pi_g^-, v=0) + N$	$f(T_e)$	[17]
$e + N_3^+ \rightarrow N_2(X^1 \Sigma_g^+, v=0) + N$	$f(T_e)$	[17]
$e + N_2O_2^+ \rightarrow NO + NO$	$f(T_e)$	[17]
$e + e + N^+ \rightarrow e + N$	$f(T_e)$	[14]
$e + N^+ + O_2 \rightarrow N + O_2$	$f(T_e)$	[14]
$e + N^+ + N_2(X^1 \Sigma_g^+, v=0) \rightarrow N + N_2(X^1 \Sigma_g^+, v=0)$	$f(T_e)$	[14]
$O_2NO^+ + e \rightarrow NO + O_2$	$f(T_e)$	[14]
$N_2O_2^+ + e \rightarrow N_2(X^1 \Sigma_g^+, v=0) + O_2$	$f(T_e)$	[14]
$NO_2^+ + e \rightarrow NO + O$	$f(T_e)$	[14]
$N_2O^+ + e \rightarrow N_2(X^1 \Sigma_g^+, v=0) + O$	$f(T_e)$	[14]

Table A.5: Electron-ion recombination processes.

Reaction	Rate	Reference
$O^- + O_2 \rightarrow O + O_2^-$	$f(E/N)$	[13]
$O^- + O_2 + M \rightarrow O_3^- + M$	$f(E/N)$	[13]
$N_2^+ + N_2(X^1 \Sigma_g^+, v=0) + N_2(X^1 \Sigma_g^+, v=0) \rightarrow N_4^+ + N_2(X^1 \Sigma_g^+, v=0)$	5.00×10^{-41}	[14]
$N_2^+ + N + N_2(X^1 \Sigma_g^+, v=0) \rightarrow N_3^+ + N_2(X^1 \Sigma_g^+, v=0)$	6.65×10^{-41}	[14]
$O_2^+ + O_2 + O_2 \rightarrow O_4^+ + O_2$	8.78×10^{-42}	[14]
$O_2^+ + N_2(X^1 \Sigma_g^+, v=0) + N_2(X^1 \Sigma_g^+, v=0) \rightarrow N_2O_2^+ + N_2(X^1 \Sigma_g^+, v=0)$	2.02×10^{-42}	[14]
$NO^+ + N_2(X^1 \Sigma_g^+, v=0) + N_2(X^1 \Sigma_g^+, v=0) \rightarrow N_2NO^+ + N_2(X^1 \Sigma_g^+, v=0)$	1.19×10^{-42}	[14]
$NO^+ + O_2 + N_2(X^1 \Sigma_g^+, v=0) \rightarrow O_2NO^+ + N_2(X^1 \Sigma_g^+, v=0)$	3.00×10^{-43}	[14]
$N_2^+ + O_2 \rightarrow O_2^+ + N_2(X^1 \Sigma_g^+, v=0)$	7.35×10^{-17}	[14]
$O_2^+ + N_2(X^1 \Sigma_g^+, v=0) \rightarrow NO^+ + NO$	2.25×10^{-26}	[26]
$O_2^+ + N \rightarrow NO^+ + O$	1.20×10^{-16}	[14]
$O_4^+ + O_2 \rightarrow O_2^+ + O_2 + O_2$	2.00×10^{-22}	[14]
$O_4^+ + O_2(a^1 \Delta_g) \rightarrow O_2^+ + O_2 + O_2$	1.00×10^{-16}	[14]
$O_4^+ + O_2(b^1 \Sigma_g^+) \rightarrow O_2^+ + O_2 + O_2$	1.00×10^{-16}	[14]
$O_4^+ + O \rightarrow O_2^+ + O_3$	3.00×10^{-16}	[14]
$O_4^+ + NO \rightarrow NO^+ + O_2 + O_2$	1.00×10^{-16}	[14]
$N_4^+ + N_2(X^1 \Sigma_g^+, v=0) \rightarrow N_2^+ + N_2(X^1 \Sigma_g^+, v=0) + N_2(X^1 \Sigma_g^+, v=0)$	2.10×10^{-22}	[27]
$N_4^+ + O_2 \rightarrow O_2^+ + N_2(X^1 \Sigma_g^+, v=0) + N_2(X^1 \Sigma_g^+, v=0)$	2.50×10^{-16}	[14]
$O_2^- + O \rightarrow O^- + O_2$	3.30×10^{-16}	[14]
$O^- + O_2(a^1 \Delta_g) \rightarrow O_2^- + O$	1.00×10^{-16}	[14]
$N^+ + O_2 \rightarrow O_2^+ + N$	2.00×10^{-16}	[28]
$N^+ + O_2 \rightarrow O_2^+ + N(^2D)$	8.40×10^{-17}	[28]
$N^+ + O_2 \rightarrow NO^+ + O$	5.00×10^{-17}	[28]
$N^+ + O_2 \rightarrow NO^+ + O(^1D)$	2.00×10^{-16}	[28]
$N^+ + O_2 \rightarrow O^+ + NO$	2.80×10^{-17}	[28]
$O^+ + O_2 \rightarrow O_2^+ + O$	2.00×10^{-17}	[28]
$O^+ + N_2(X^1 \Sigma_g^+, v=0) \rightarrow NO^+ + N$	1.80×10^{-18}	[28]
$O^+ + N_2(X^1 \Sigma_g^+, v=0) \rightarrow NO^+ + N + O_2$	1.35×10^{-34}	[29]

A. CHEMICAL SCHEMES

Reaction	Rate	Reference
$O^+ + N_2(X^1 \Sigma_g^+, v=0) \rightarrow NO^+ + N + N_2(X^1 \Sigma_g^+, v=0)$	1.35×10^{-34}	[29]
$O_2^- + O_2^+ \rightarrow O_2 + O_2$	2.45×10^{-13}	[14]
$O^- + O_2^+ \rightarrow O_2 + O$	2.45×10^{-13}	[14]
$O_2^- + O_4^+ \rightarrow O_2 + O_2 + O$	1.00×10^{-13}	[14]
$O^- + O_4^+ \rightarrow O_2 + O_2 + O$	1.00×10^{-13}	[14]
$O^- + N_2^+ \rightarrow O + N_2(X^1 \Sigma_g^+, v=0)$	2.45×10^{-13}	[14]
$O^- + N^+ \rightarrow O + N$	2.45×10^{-13}	[14]
$O^- + O^+ \rightarrow O + O$	2.45×10^{-13}	[14]
$O^- + NO^+ \rightarrow O + NO$	2.45×10^{-13}	[14]
$O^- + NO_2^+ \rightarrow O + NO_2$	2.45×10^{-13}	[14]
$O_2^- + N_2^+ \rightarrow O_2 + N_2(X^1 \Sigma_g^+, v=0)$	2.45×10^{-13}	[14]
$O_2^- + N^+ \rightarrow O_2 + N$	2.45×10^{-13}	[14]
$O_2^- + O^+ \rightarrow O_2 + O$	2.45×10^{-13}	[14]
$O_2^- + NO^+ \rightarrow O_2 + NO$	2.45×10^{-13}	[14]
$O_2^- + NO_2^+ \rightarrow O_2 + NO_2$	2.45×10^{-13}	[14]
$O_3^- + N_2^+ \rightarrow O_3 + N_2(X^1 \Sigma_g^+, v=0)$	2.45×10^{-13}	[14]
$O_3^- + N^+ \rightarrow O_3 + N$	2.45×10^{-13}	[14]
$O_3^- + O^+ \rightarrow O_3 + O$	2.45×10^{-13}	[14]
$O_3^- + NO^+ \rightarrow O_3 + NO$	2.45×10^{-13}	[14]
$O_3^- + NO_2^+ \rightarrow O_3 + NO_2$	2.45×10^{-13}	[14]
$NO_2^- + N_2^+ \rightarrow NO_2 + N_2(X^1 \Sigma_g^+, v=0)$	2.45×10^{-13}	[14]
$NO_2^- + N^+ \rightarrow NO_2 + N$	2.45×10^{-13}	[14]
$NO_2^- + O^+ \rightarrow NO_2 + O$	2.45×10^{-13}	[14]
$NO_2^- + NO^+ \rightarrow NO_2 + NO$	2.45×10^{-13}	[14]
$NO_2^- + NO_2^+ \rightarrow NO_2 + NO_2$	2.45×10^{-13}	[14]
$NO_3^- + N_2^+ \rightarrow NO_3 + N_2(X^1 \Sigma_g^+, v=0)$	2.45×10^{-13}	[14]
$NO_3^- + N^+ \rightarrow NO_3 + N$	2.45×10^{-13}	[14]
$NO_3^- + O^+ \rightarrow NO_3 + O$	2.45×10^{-13}	[14]
$NO_3^- + NO^+ \rightarrow NO_3 + NO$	2.45×10^{-13}	[14]
$NO_3^- + NO_2^+ \rightarrow NO_3 + NO_2$	2.45×10^{-13}	[14]
$O_2^+ + O_3^- \rightarrow O_2 + O_3$	7.35×10^{-14}	[14]
$O_2^+ + NO_2^- \rightarrow O_2 + NO_2$	7.35×10^{-14}	[14]
$O_2^+ + NO_3^- \rightarrow O_2 + NO_3$	7.35×10^{-14}	[14]
$O_4^+ + O_3^- \rightarrow O_4 + O_3$	7.35×10^{-14}	[14]
$O_4^+ + NO_2^- \rightarrow O_4 + NO_2$	7.35×10^{-14}	[14]
$O_4^+ + NO_3^- \rightarrow O_4 + NO_3$	7.35×10^{-14}	[14]
$O^- + N_2^+ + M \rightarrow O + N_2^+ M$	5.51×10^{-37}	[14]
$O^- + N^+ + M \rightarrow O + N + M$	5.51×10^{-37}	[14]
$O^- + O^+ + M \rightarrow O + O + M$	5.51×10^{-37}	[14]
$O^- + NO^+ + M \rightarrow O + NO^+ M$	5.51×10^{-37}	[14]
$O^- + NO_2^+ + M \rightarrow O + NO_2^+ M$	5.51×10^{-37}	[14]
$O_2^- + N_2^+ + M \rightarrow O_2 + N_2(X^1 \Sigma_g^+, v=0) + M$	5.51×10^{-37}	[14]
$O_2^- + N^+ + M \rightarrow O_2 + N^+ M$	5.51×10^{-37}	[14]
$O_2^- + O^+ + M \rightarrow O_2 + O^+ M$	5.51×10^{-37}	[14]
$O_2^- + NO^+ + M \rightarrow O_2 + NO + M$	5.51×10^{-37}	[14]
$O_2^- + NO_2^+ + M \rightarrow O_2 + NO_2 + M$	5.51×10^{-37}	[14]
$O_3^- + N_2^+ + M \rightarrow O_3 + N_2(X^1 \Sigma_g^+, v=0) + M$	5.51×10^{-37}	[14]
$O_3^- + N^+ + M \rightarrow O_3 + N^+ M$	5.51×10^{-37}	[14]
$O_3^- + O^+ + M \rightarrow O_3 + O^+ M$	5.51×10^{-37}	[14]
$O_3^- + NO^+ + M \rightarrow O_3 + NO + M$	5.51×10^{-37}	[14]
$O_3^- + NO_2^+ + M \rightarrow O_3 + NO_2 + M$	5.51×10^{-37}	[14]
$NO_2^- + N_2^+ + M \rightarrow NO_2 + N_2(X^1 \Sigma_g^+, v=0) + M$	5.51×10^{-37}	[14]
$NO_2^- + N^+ + M \rightarrow NO_2 + N + M$	5.51×10^{-37}	[14]
$NO_2^- + O^+ + M \rightarrow NO_2 + O + M$	5.51×10^{-37}	[14]
$NO_2^- + NO^+ + M \rightarrow NO_2 + NO + M$	5.51×10^{-37}	[14]
$NO_2^- + NO_2^+ + M \rightarrow NO_2^+ NO_2 + M$	5.51×10^{-37}	[14]
$NO_3^- + N_2^+ + M \rightarrow NO_3 + N_2(X^1 \Sigma_g^+, v=0) + M$	5.51×10^{-37}	[14]
$NO_3^- + N^+ + M \rightarrow NO_3 + N + M$	5.51×10^{-37}	[14]
$NO_3^- + O^+ + M \rightarrow NO_3 + O + M$	5.51×10^{-37}	[14]
$NO_3^- + NO^+ + M \rightarrow NO_3 + NO + M$	5.51×10^{-37}	[14]
$NO_3^- + NO_2^+ + M \rightarrow NO_3 + NO_2 + M$	5.51×10^{-37}	[14]
$N_2O_2^+ + O_2^- \rightarrow NO + NO^+ O_2$	1.00×10^{-13}	[17]
$N_2O_2^+ + O_2^- \rightarrow N_2(X^1 \Sigma_g^+, v=0) + O_2^+ O_2$	1.00×10^{-13}	[17]
$N_2O_2^+ + O^- \rightarrow NO + NO + O$	1.00×10^{-13}	[17]

A.1 Kinetic model for terrestrial TLEs

Reaction	Rate	Reference
$N_2O_2^+ + O^- \rightarrow N_2(X^1 \Sigma_g^+, v=0) + O + O_2$	1.00×10^{-13}	[17]
$N_2O_2^+ + O_3^- \rightarrow NO + NO^+ O_3$	1.00×10^{-13}	[17]
$N_2O_2^+ + O_3^- \rightarrow N_2(X^1 \Sigma_g^+, v=0) + O_2^+ O_3$	1.00×10^{-13}	[17]
$N_2O_2^+ + NO_2^- \rightarrow NO + NO + NO_2$	1.00×10^{-13}	[17]
$N_2O_2^+ + NO_2^- \rightarrow NO_2 + N_2(X^1 \Sigma_g^+, v=0) + O_2$	1.00×10^{-13}	[17]
$N_2O_2^+ + NO_3^- \rightarrow NO + NO + NO_3$	1.00×10^{-13}	[17]
$N_2O_2^+ + NO_3^- \rightarrow NO_3 + N_2^+ O_2$	1.00×10^{-13}	[17]
$N_3^+ + O^- \rightarrow N + N_2(X^1 \Sigma_g^+, v=0) + O$	1.00×10^{-13}	[17]
$N_3^+ + O_3^- \rightarrow N + N_2(X^1 \Sigma_g^+, v=0) + O_3$	1.00×10^{-13}	[17]
$N_3^+ + NO_3^- \rightarrow N + N_2(X^1 \Sigma_g^+, v=0) + NO_3$	1.00×10^{-13}	[17]
$O_2^+ + NO \rightarrow NO^+ + O_2$	3.59×10^{-16}	[30]
$O_4^+ + H_2O \rightarrow (H_2O)O_2^+ + O_2$	1.22×10^{-15}	[30]
$(H_2O)O_2^+ + H_2O \rightarrow (H_2O)H^+ + OH + O_2$	1.63×10^{-16}	[30]
$(H_2O)H^+ + H_2O + M \rightarrow (H_2O)_2H^+ + M$	1.72×10^{-38}	[30]
$(H_2O)O_2^+ + H_2O \rightarrow (H_2O)OHH^+ + O_2$	8.16×10^{-16}	[30]
$(H_2O)OHH^+ + H_2O \rightarrow (H_2O)_2H^+ + OH$	1.14×10^{-15}	[30]
$(H_2O)_2H^+ + H_2O + M \rightarrow (H_2O)_3H^+ + M$	1.16×10^{-38}	[30]
$(H_2O)_3H^+ + H_2O + M \rightarrow (H_2O)_4H^+ + M$	1.21×10^{-38}	[30]
$N_2NO^+ + e \rightarrow NO + N_2(X^1 \Sigma_g^+, v=0)$	1.59×10^{-12}	[14]
$N_3^+ + O_2 \rightarrow O_2^+ + N + N_2(X^1 \Sigma_g^+, v=0)$	2.30×10^{-17}	[14]
$N_3^+ + O_2 \rightarrow NO_2^+ + N_2(X^1 \Sigma_g^+, v=0)$	4.40×10^{-17}	[14]
$N_3^+ + NO \rightarrow N_2O^+ + N_2(X^1 \Sigma_g^+, v=0)$	7.00×10^{-17}	[14]
$O^- + O_3 \rightarrow O_3^- + O$	5.30×10^{-16}	[30]
$O^- + CO_2 + M \rightarrow CO_3^- + M$	2.53×10^{-40}	[30]
$O_2^- + O_2 + M \rightarrow O_4^- + M$	5.25×10^{-43}	[14]
$O_2^- + O_3 \rightarrow O_3^- + O_2$	4.00×10^{-16}	[30]
$O_3^- + O \rightarrow O_2^- + O_2$	3.20×10^{-16}	[14]
$O_3^- + CO_2 \rightarrow CO_3^- + O_2$	4.49×10^{-16}	[30]
$O_4^- + O \rightarrow O_3^- + O_2$	4.00×10^{-16}	[30]
$O_4^- + O \rightarrow O^- + O_2 + O_2$	3.00×10^{-16}	[14]
$O_4^- + O_2(a^1 \Delta_g) \rightarrow O_2^- + O_2^+ O_2$	1.00×10^{-16}	[14]
$O_4^- + CO_2 \rightarrow CO_4^- + O_2$	3.51×10^{-16}	[14]
$CO_3^- + NO \rightarrow NO_2^- + CO_2$	8.98×10^{-18}	[30]
$CO_3^- + NO_2 \rightarrow NO_3^- + CO_2$	1.63×10^{-16}	[30]
$CO_3^- + O \rightarrow O_2^- + CO_2$	8.98×10^{-17}	[30]
$CO_4^- + O \rightarrow CO_3^- + O_2$	1.14×10^{-16}	[30]
$CO_4^- + O_3 \rightarrow O_3^- + CO_2 + O_2$	1.06×10^{-16}	[30]
$N_2O_2^+ + NO^- \rightarrow NO + NO^+ NO$	1.00×10^{-13}	[17]
$N_2O_2^+ + NO^- \rightarrow NO + N_2^+ O_2$	1.00×10^{-13}	[17]
$N_3^+ + NO^- \rightarrow N + N_2(X^1 \Sigma_g^+, v=0) + NO$	1.00×10^{-13}	[17]
$NO^- + N^+ \rightarrow NO + N$	2.45×10^{-13}	[14]
$N^+ + N_2(X^1 \Sigma_g^+, v=0) + N_2(X^1 \Sigma_g^+, v=0) \rightarrow N_3^+ + N_2(X^1 \Sigma_g^+, v=0)$	6.65×10^{-41}	[14]
$N^+ + O + N_2(X^1 \Sigma_g^+, v=0) \rightarrow NO^+ + N_2(X^1 \Sigma_g^+, v=0)$	1.00×10^{-41}	[14]
$N^+ + O + O_2 \rightarrow NO^+ + O_2$	1.00×10^{-41}	[14]
$N^+ + N + N_2(X^1 \Sigma_g^+, v=0) \rightarrow N_2^+ + N_2(X^1 \Sigma_g^+, v=0)$	1.00×10^{-41}	[14]
$N^+ + N + O_2 \rightarrow N_2^+ + O_2$	1.00×10^{-41}	[14]
$N^+ + O \rightarrow O^+ + N$	1.00×10^{-18}	[14]
$N^+ + O_3 \rightarrow NO^+ + O_2$	5.00×10^{-16}	[14]
$N^+ + NO \rightarrow NO^+ + N$	8.00×10^{-16}	[14]
$N^+ + NO \rightarrow N_2^+ + O$	3.00×10^{-18}	[14]
$N^+ + NO \rightarrow O^+ + N_2(X^1 \Sigma_g^+, v=0)$	1.00×10^{-18}	[14]
$N^+ + N_2O \rightarrow NO^+ + N_2(X^1 \Sigma_g^+, v=0)$	5.50×10^{-16}	[14]
$N_2^+ + O \rightarrow N_2(X^1 \Sigma_g^+, v=0) + O^+$	1.08×10^{-17}	[14]
$N_2^+ + O \rightarrow NO^+ + N$	1.59×10^{-16}	[14]
$N_2^+ + O_3 \rightarrow O_2^+ + O + N_2(X^1 \Sigma_g^+, v=0)$	1.00×10^{-16}	[36]
$N_2^+ + N_2O \rightarrow N_2O^+ + N_2(X^1 \Sigma_g^+, v=0)$	5.00×10^{-16}	[36]
$N_2^+ + N_2O \rightarrow NO^+ + N + N_2(X^1 \Sigma_g^+, v=0)$	4.00×10^{-16}	[36]
$N_2^+ + NO \rightarrow NO^+ + N_2(X^1 \Sigma_g^+, v=0)$	3.30×10^{-16}	[14]
$N_3^+ + N_2(A^3 \Sigma_u^+, v=0) \rightarrow N_3^+ + N_2(X^1 \Sigma_g^+, v=0)$	3.00×10^{-16}	[17]
$N_3^+ + N \rightarrow N_2^+ + N_2(X^1 \Sigma_g^+, v=0)$	6.60×10^{-17}	[14]
$N_3^+ + NO \rightarrow NO^+ + N + N_2(X^1 \Sigma_g^+, v=0)$	7.00×10^{-17}	[17]
$N_4^+ + O \rightarrow O^+ + N_2(X^1 \Sigma_g^+, v=0) + N_2(X^1 \Sigma_g^+, v=0)$	2.50×10^{-16}	[36]
$O^+ + O_3 \rightarrow O_2^+ + O_2$	1.00×10^{-16}	[36]

A. CHEMICAL SCHEMES

Reaction	Rate	Reference
$O^+ + NO \rightarrow NO^+ + O$	2.40×10^{-17}	[36]
$O^+ + NO \rightarrow O_2^+ + N$	3.00×10^{-18}	[36]
$O^+ + N_2O \rightarrow NO^+ + NO$	2.30×10^{-16}	[36]
$O^+ + N_2O \rightarrow O_2^+ + N_2(X^1 \Sigma_g^+, v=0)$	2.00×10^{-17}	[36]
$O^+ + N_2O \rightarrow N_2O^+ + O$	2.20×10^{-17}	[36]
$O^+ + NO_2 \rightarrow NO_2^+ + O$	1.60×10^{-15}	[36]
$O_2^+ + NO_2 \rightarrow NO^+ + O_3$	1.00×10^{-17}	[36]
$O_2^+ + NO_2 \rightarrow NO_2^+ + O_2$	6.60×10^{-16}	[36]
$O_4^+ + N_2(X^1 \Sigma_g^+, v=0) \rightarrow N_2O_2^+ + O_2$	2.23×10^{-23}	[36]
$NO_2^+ + NO \rightarrow NO^+ + NO_2$	2.90×10^{-16}	[36]
$N_2O^+ + NO \rightarrow NO^+ + N_2O$	2.90×10^{-16}	[36]
$N_2O_2^+ + N_2(X^1 \Sigma_g^+, v=0) \rightarrow O_2^+ + N_2^+ N_2(X^1 \Sigma_g^+, v=0)$	7.19×10^{-17}	[36]
$N_2O_2^+ + O_2 \rightarrow O_4^+ + N_2(X^1 \Sigma_g^+, v=0)$	1.00×10^{-16}	[36]
$O^- + N_2O \rightarrow NO^- + NO$	2.10×10^{-16}	[14]
$O^- + NO_2 \rightarrow NO_2^- + O$	1.20×10^{-15}	[14]
$O^- + O_2 + O_2 \rightarrow O_3^- + O_2$	7.33×10^{-43}	[14]
$O^- + CO_2 + CO_2 \rightarrow CO_3^- + CO_2$	2.53×10^{-40}	[30]
$O_2^- + NO_2 \rightarrow O_2 + NO_2^-$	8.00×10^{-16}	[14]
$O_3^- + NO \rightarrow NO_3^- + O$	1.00×10^{-17}	[14]
$O_3^- + NO_2 \rightarrow O_3 + NO_2^-$	7.00×10^{-16}	[14]
$O_3^- + NO_2 \rightarrow NO_3^- + O_2$	2.00×10^{-17}	[14]
$O_3^- + NO \rightarrow O_2 + NO_2^-$	2.60×10^{-17}	[36]
$O_3^- + O_3 \rightarrow O_2 + O_2 + O_2 + e$	1.00×10^{-16}	[41]
$NO^- + O_2 \rightarrow O_2^- + NO$	5.00×10^{-16}	[14]
$NO^- + NO_2 \rightarrow NO_2^- + NO$	7.40×10^{-22}	[14]
$NO^- + N_2O \rightarrow NO_2^- + N_2(X^1 \Sigma_g^+, v=0)$	2.80×10^{-20}	[14]
$NO_2^- + O_3 \rightarrow O_2 + NO_3^-$	1.80×10^{-17}	[14]
$NO_2^- + NO_2 \rightarrow NO_3^- + NO$	4.00×10^{-18}	[36]
$NO_2^- + NO_3 \rightarrow NO_2 + NO_3^-$	5.00×10^{-16}	[36]
$NO_3^- + NO \rightarrow NO_2^- + NO_2$	3.00×10^{-21}	[36]

Table A.6: Ionic kinetics.

Reaction	Rate	Reference
$e + O_3 \rightarrow O_2 + O + e$	$f(T_e)$	[19]

Table A.7: Electron impact dissociation processes producing ground state species.

Reaction	Rate	Reference
$N + O_2 \rightarrow NO + O$	2.87×10^{-25}	[14]
$N + O_3 \rightarrow NO + O_2$	2.00×10^{-22}	[14]
$N + NO \rightarrow N_2(X^1 \Sigma_g^+, v=0) + O$	2.74×10^{-17}	[14]
$N + NO_2 \rightarrow N_2(X^1 \Sigma_g^+, v=0) + O_2$	7.00×10^{-19}	[14]
$N + NO_2 \rightarrow N_2(X^1 \Sigma_g^+, v=0) + O + O$	9.10×10^{-19}	[14]
$N + NO_2 \rightarrow N_2O + O$	3.00×10^{-18}	[14]
$N + NO_2 \rightarrow NO + NO$	2.30×10^{-19}	[14]
$O + O_3 \rightarrow O_2 + O_2$	2.03×10^{-22}	[14]
$O + NO_3 \rightarrow O_2 + NO_2$	8.16×10^{-18}	[14]
$O + N_2O_5 \rightarrow N_2(X^1 \Sigma_g^+, v=0) + O_2 + O_2 + O_2$	2.45×10^{-22}	[14]
$NO + O_3 \rightarrow O_2 + NO_2$	1.07×10^{-21}	[14]
$NO + NO_3 \rightarrow NO_2 + NO_2$	1.11×10^{-17}	[14]
$NO_2 + O_3 \rightarrow O_2 + NO_3$	5.74×10^{-25}	[14]
$NO_3 + NO_3 \rightarrow O_2 + NO_2 + NO_2$	1.53×10^{-24}	[14]
$NO_2 + NO_3 \rightarrow NO + NO_2 + O_2$	7.72×10^{-23}	[14]
$N + N + N_2(X^1 \Sigma_g^+, v=0) \rightarrow N_2(X^1 \Sigma_g^+, v=0) + N_2(X^1 \Sigma_g^+, v=0)$	1.01×10^{-44}	[14]
$N + N + O_2 \rightarrow N_2(X^1 \Sigma_g^+, v=0) + O_2$	1.01×10^{-44}	[14]
$O + O + N_2(X^1 \Sigma_g^+, v=0) \rightarrow O_2 + N_2(X^1 \Sigma_g^+, v=0)$	3.60×10^{-49}	[14]
$O + O + O_2 \rightarrow O_2 + O_2$	4.92×10^{-45}	[14]

A.1 Kinetic model for terrestrial TLEs

Reaction	Rate	Reference
$N + O + N_2(X^1 \Sigma_g^+, v=0) \rightarrow NO + N_2(X^1 \Sigma_g^+, v=0)$	1.25×10^{-44}	[14]
$N + O + O_2 \rightarrow NO + O_2$	1.25×10^{-44}	[14]
$O + O_2 + N_2(X^1 \Sigma_g^+, v=0) \rightarrow O_3 + N_2(X^1 \Sigma_g^+, v=0)$	1.40×10^{-45}	[14]
$O + O_2 + O_2 \rightarrow O_3 + O_2$	1.15×10^{-45}	[14]
$N + N + N_2(X^1 \Sigma_g^+, v=0) \rightarrow N_2(B^3 \Pi_g, v=0) + N_2(X^1 \Sigma_g^+, v=0)$	1.96×10^{-45}	[21]
$N + N + O_2 \rightarrow N_2(B^3 \Pi_g, v=0) + O_2$	1.96×10^{-45}	[21]
$N_2(A^3 \Sigma_u^+, v=0) + O_2 \rightarrow N_2(X^1 \Sigma_g^+, v=0) + O_2$	2.00×10^{-18}	[14]
$N_2(A^3 \Sigma_u^+, v=0) + O_2 \rightarrow N_2O + O$	7.80×10^{-20}	[14]
$N_2(A^3 \Sigma_u^+, v=0) + O \rightarrow NO + N(^2D)$	7.00×10^{-18}	[14]
$N_2(A^3 \Sigma_u^+, v=0) + N_2O \rightarrow N_2(X^1 \Sigma_g^+, v=0) + N + NO$	1.00×10^{-17}	[14]
$N_2(A^3 \Sigma_u^+, v=0) + N_2(X^1 \Sigma_g^+, v=0) \rightarrow N_2(X^1 \Sigma_g^+, v=0) + N_2(X^1 \Sigma_g^+, v=0)$	3.70×10^{-22}	[14]
$N_2(A^3 \Sigma_u^+, v=0) + O_2 \rightarrow N_2(X^1 \Sigma_g^+, v=0) + O_2(a^1 \Delta_g)$	1.29×10^{-18}	[14]
$N_2(A^3 \Sigma_u^+, v=0) + O_2 \rightarrow N_2(X^1 \Sigma_g^+, v=0) + O_2(b^1 \Sigma_g^+)$	1.29×10^{-18}	[14]
$N_2(A^3 \Sigma_u^+, v=0) + O_2(a^1 \Delta_g) \rightarrow N_2(B^3 \Pi_g, v=0) + O_2$	1.00×10^{-16}	[22]
$N_2(A^3 \Sigma_u^+, v=0) + N_2(A^3 \Sigma_u^+, v=0) \rightarrow N_2(C^3 \Pi_u, v=0) + N_2(X^1 \Sigma_g^+, v=0)$	2.60×10^{-17}	[21]
$N_2(A^3 \Sigma_u^+, v=0) + N \rightarrow N_2(X^1 \Sigma_g^+, v=0) + N(^2P)$	5.00×10^{-17}	[21]
$N_2(A^3 \Sigma_u^+, v=0) + O \rightarrow N_2(X^1 \Sigma_g^+, v=0) + O(^1S)$	2.00×10^{-17}	[14]
$N_2(A^3 \Sigma_u^+, v=0) + NO \rightarrow N_2(X^1 \Sigma_g^+, v=0) + NO$	7.00×10^{-17}	[14]
$N_2(B^3 \Pi_g, v=0) \rightarrow N_2(A^3 \Sigma_u^+, v=0) + h\nu$	5.09×10^4	[14]
$N_2(B^3 \Pi_g, v=0) + NO \rightarrow N_2(A^3 \Sigma_u^+, v=0) + NO$	2.40×10^{-16}	[14]
$N_2(B^3 \Pi_g, v=0) + O_2 \rightarrow N_2(X^1 \Sigma_g^+, v=0) + O + O$	3.00×10^{-16}	[14]
$N_2(a^1 \Pi_g, v=0) + N_2(X^1 \Sigma_g^+, v=0) \rightarrow N_2(B^3 \Pi_g, v=0) + N_2(X^1 \Sigma_g^+, v=0)$	2.00×10^{-19}	[14]
$N_2(a^1 \Pi_g, v=0) + O_2 \rightarrow N_2(X^1 \Sigma_g^+, v=0) + O + O$	2.80×10^{-17}	[14]
$N_2(a^1 \Pi_g, v=0) + NO \rightarrow N_2(X^1 \Sigma_g^+, v=0) + N + O$	3.60×10^{-16}	[14]
$N_2(a^1 \Pi_g, v=0) + N_2(A^3 \Sigma_u^+, v=0) \rightarrow e + N_4^+$	1.50×10^{-17}	[21]
$N_2(a^1 \Pi_g, v=0) + N_2(a^1 \Pi_g, v=0) \rightarrow e + N_4^+$	1.00×10^{-17}	[21]
$N_2(C^3 \Pi_u, v=0) \rightarrow N_2(B^3 \Pi_g, v=0) + h\nu$	1.32×10^7	[14]
$N_2(C^3 \Pi_u, v=0) + N_2(X^1 \Sigma_g^+, v=0) \rightarrow N_2(a^1 \Pi_g, v=0) + N_2(X^1 \Sigma_g^+, v=0)$	1.00×10^{-17}	[14]
$N_2(C^3 \Pi_u, v=0) + O_2 \rightarrow N_2(X^1 \Sigma_g^+, v=0) + O(^1S) + O$	3.00×10^{-16}	[14]
$O_2(a^1 \Delta_g) + O_3 \rightarrow O_2 + O_2 + O$	3.90×10^{-22}	[14]
$O_2(a^1 \Delta_g) + N \rightarrow NO + O$	9.96×10^{-23}	[14]
$O_2(a^1 \Delta_g) + N_2(X^1 \Sigma_g^+, v=0) \rightarrow N_2(X^1 \Sigma_g^+, v=0) + O_2$	3.00×10^{-27}	[14]
$O_2(a^1 \Delta_g) + O_2 \rightarrow O_2 + O_2$	1.59×10^{-24}	[14]
$O_2(a^1 \Delta_g) + O \rightarrow O_2 + O$	7.00×10^{-22}	[14]
$O_2(a^1 \Delta_g) + NO \rightarrow O_2 + NO$	2.46×10^{-23}	[23]
$O_2(a^1 \Delta_g) + O_3 \rightarrow O_2 + O_2 + O(^1D)$	3.54×10^{-23}	[21]
$O_2(a^1 \Delta_g) + O_2(a^1 \Delta_g) + O_2 \rightarrow O_3 + O_3$	1.00×10^{-43}	[21]
$O_2(a^1 \Delta_g) \rightarrow O_2 + h\nu$	3.31×10^{-4}	[24]
$O_2(b^1 \Sigma_g^+) + O_3 \rightarrow O_2 + O_2 + O$	1.80×10^{-17}	[14]
$O_2(b^1 \Sigma_g^+) + N_2(X^1 \Sigma_g^+, v=0) \rightarrow O_2(a^1 \Delta_g) + N_2(X^1 \Sigma_g^+, v=0)$	1.38×10^{-21}	[14]
$O_2(b^1 \Sigma_g^+) + O_2 \rightarrow O_2(a^1 \Delta_g) + O_2$	4.29×10^{-23}	[14]
$O_2(b^1 \Sigma_g^+) + O \rightarrow O_2(a^1 \Delta_g) + O$	8.00×10^{-20}	[14]
$O_2(b^1 \Sigma_g^+) + NO \rightarrow O_2(a^1 \Delta_g) + NO$	4.00×10^{-20}	[14]
$O_2(b^1 \Sigma_g^+) \rightarrow O_2 + h\nu$	8.20×10^{-2}	[25]
$O_2(A^3 \Pi_u^+) + O_2 \rightarrow O_2(b^1 \Sigma_g^+) + O_2(b^1 \Sigma_g^+)$	2.90×10^{-19}	[14]
$O_2(A^3 \Pi_u^+) + N_2(X^1 \Sigma_g^+, v=0) \rightarrow O_2(b^1 \Sigma_g^+) + N_2(X^1 \Sigma_g^+, v=0)$	3.00×10^{-19}	[14]
$O_2(A^3 \Pi_u^+) + O \rightarrow O_2(b^1 \Sigma_g^+) + O(^1D)$	9.00×10^{-18}	[14]
$N(^2D) + O_2 \rightarrow NO + O$	1.22×10^{-18}	[14]
$N(^2D) + O_2 \rightarrow NO + O(^1D)$	4.90×10^{-18}	[14]
$N(^2D) + NO \rightarrow N_2O$	6.00×10^{-17}	[14]
$N(^2D) + N_2O \rightarrow NO + N_2(X^1 \Sigma_g^+, v=0)$	3.00×10^{-18}	[14]
$N(^2D) + N_2(X^1 \Sigma_g^+, v=0) \rightarrow N + N_2(X^1 \Sigma_g^+, v=0)$	6.00×10^{-21}	[14]
$N(^2D) + O \rightarrow N + O(^1D)$	4.00×10^{-19}	[21]
$N(^2P) + O_2 \rightarrow NO + O$	2.60×10^{-18}	[14]
$N(^2P) + NO \rightarrow N_2(A^3 \Sigma_u^+, v=0) + O$	3.40×10^{-17}	[14]
$N(^2P) + N_2(X^1 \Sigma_g^+, v=0) \rightarrow N(^2D) + N_2(X^1 \Sigma_g^+, v=0)$	2.00×10^{-24}	[14]
$N(^2P) + N \rightarrow N(^2D) + N$	1.80×10^{-18}	[14]
$O(^1D) + N_2(X^1 \Sigma_g^+, v=0) \rightarrow O + N_2(X^1 \Sigma_g^+, v=0)$	3.07×10^{-17}	[14]
$O(^1D) + O_2 \rightarrow O + O_2(b^1 \Sigma_g^+)$	3.58×10^{-17}	[14]
$O(^1D) + O_2 \rightarrow O + O_2$	8.95×10^{-18}	[14]
$O(^1D) + O_3 \rightarrow O + O + O_2$	1.20×10^{-16}	[14]
$O(^1D) + O_3 \rightarrow O_2 + O_2$	1.20×10^{-16}	[14]
$O(^1D) + NO \rightarrow N + O_2$	1.20×10^{-16}	[14]

A. CHEMICAL SCHEMES

Reaction	Rate	Reference
$O(^1D) + N_2O \rightarrow NO + NO$	7.20×10^{-17}	[14]
$O(^1D) + N_2O \rightarrow N_2(X^1 \Sigma_g^+, v=0) + O_2$	4.40×10^{-17}	[14]
$O(^1S) + N_2(X^1 \Sigma_g^+, v=0) \rightarrow O + N_2(X^1 \Sigma_g^+, v=0)$	5.00×10^{-23}	[14]
$O(^1S) + O_2 \rightarrow O + O_2(A^3\Pi_u^+)$	6.13×10^{-20}	[14]
$O(^1S) + O_2 \rightarrow O(^1D) + O_2$	6.13×10^{-20}	[14]
$O(^1S) + O_3 \rightarrow O(^1D) + O + O_2$	5.80×10^{-16}	[14]
$O(^1S) + O_3 \rightarrow O_2 + O_2$	5.80×10^{-16}	[14]
$O(^1S) + NO \rightarrow O + NO$	1.80×10^{-16}	[14]
$O(^1S) + NO \rightarrow O(^1D) + NO$	3.20×10^{-16}	[14]
$O(^1S) + N_2O \rightarrow O + N_2O$	6.20×10^{-18}	[14]
$O(^1S) + N_2O \rightarrow O(^1D) + N_2O$	3.10×10^{-18}	[14]
$O(^1S) + O_2(a^1 \Delta_g) \rightarrow O(^1D) + O_2(b^1 \Sigma_g^+)$	3.60×10^{-17}	[14]
$O(^1S) + O_2(a^1 \Delta_g) \rightarrow O + O + O$	3.40×10^{-17}	[14]
$O(^1S) + O_2(a^1 \Delta_g) \rightarrow O + O_2(A^3\Pi_u^+)$	1.30×10^{-16}	[14]
$O(^1S) + O \rightarrow O(^1D) + O$	1.11×10^{-17}	[14]
$O(^1D) + H_2O \rightarrow OH + OH$	1.80×10^{-16}	[30]
$H + O_2 + M \rightarrow HO_2 + M$	1.05×10^{-43}	[30]
$OH + O \rightarrow H + O_2$	3.95×10^{-17}	[30]
$OH + CO \rightarrow H + CO_2$	1.50×10^{-19}	[30]
$OH + O_3 \rightarrow HO_2 + O_2$	1.46×10^{-20}	[30]
$HO_2 + O_3 \rightarrow OH + O_2 + O_2$	7.70×10^{-22}	[30]
$HO_2 + O \rightarrow OH + O_2$	8.15×10^{-17}	[30]
$HO_2 + OH \rightarrow H_2O + O_2$	1.36×10^{-16}	[30]
$HO_2 + NO \rightarrow NO_2 + OH$	1.23×10^{-17}	[30]
$HO_2 + HO_2 \rightarrow H_2O_2 + O_2$	4.39×10^{-18}	[30]
$H_2O_2 + OH \rightarrow HO_2 + H_2O$	1.22×10^{-18}	[30]
$H_2O_2 + O \rightarrow OH + HO_2$	6.36×10^{-23}	[30]
$N(^2D) + O \rightarrow N + O$	5.51×10^{-19}	[30]
$NO_3 + NO_2 + M \rightarrow N_2O_5 + M$	4.78×10^{-41}	[30]
$NO_2 + OH + M \rightarrow HNO_3 + M$	5.87×10^{-41}	[30]
$HNO_3 + OH \rightarrow NO_3 + H_2O$	3.65×10^{-19}	[30]
$H + O_3 \rightarrow OH^* + O_2$	1.34×10^{-17}	[31]
$O + HO_2 \rightarrow OH^* + O_2$	3.67×10^{-17}	[31]
$OH^* + O \rightarrow H + O_2$	3.06×10^{-16}	[31]
$OH^* + M \rightarrow OH + M$	1.22×10^{-19}	[32]
$N(^2D) + NO \rightarrow N_2(X^1 \Sigma_g^+, v=0) + O$	1.80×10^{-16}	[36]
$N(^2P) + NO \rightarrow N_2(X^1 \Sigma_g^+, v=0) + O$	3.00×10^{-17}	[36]
$N_2(a^1 \Pi_g, v=0) + N_2(X^1 \Sigma_g^+, v=0) \rightarrow N_2(X^1 \Sigma_g^+, v=0) + N_2(X^1 \Sigma_g^+, v=0)$	1.00×10^{-17}	[14]
$N_2(a^1 \Pi_g, v=0) + NO \rightarrow N_2(X^1 \Sigma_g^+, v=0) + N + O$	3.60×10^{-16}	[14]
$N_2(a^1 \Pi_g, v=0) + O_2 \rightarrow N_2(X^1 \Sigma_g^+, v=0) + O + O(^1D)$	2.80×10^{-17}	[14]
$N_2(C^3 \Pi_u, v=0) + N_2(X^1 \Sigma_g^+, v=0) \rightarrow N_2(B^3 \Pi_g, v=0) + N_2(X^1 \Sigma_g^+, v=0)$	1.00×10^{-17}	[14]
$N_2(C^3 \Pi_u, v=0) + O_2 \rightarrow N_2(X^1 \Sigma_g^+, v=0) + O + O(^1D)$	2.50×10^{-16}	[14]
$N_2(B^3 \Pi_g, v=0) + N_2(X^1 \Sigma_g^+, v=0) \rightarrow N_2(X^1 \Sigma_g^+, v=0) + N_2(X^1 \Sigma_g^+, v=0)$	1.00×10^{-17}	[36]
$N_2(A^3 \Sigma_u^+, v=0) + O_2 \rightarrow N_2(X^1 \Sigma_g^+, v=0) + O + O$	2.54×10^{-18}	[14]
$N_2(A^3 \Sigma_u^+, v=0) + N \rightarrow N_2(X^1 \Sigma_g^+, v=0) + N$	2.20×10^{-16}	[14]
$N_2(A^3 \Sigma_u^+, v=0) + NO \rightarrow N_2(X^1 \Sigma_g^+, v=0) + NO(A^1 \Sigma^+)$	8.75×10^{-17}	[14]
$O(^1D) + N_2(X^1 \Sigma_g^+, v=0) \rightarrow O + N_2(X^1 \Sigma_g^+, v=1)$	2.40×10^{-17}	[14]
$O(^1D) + O_2 \rightarrow O + O_2(a^1 \Delta_g)$	1.00×10^{-18}	[36]
$O(^1D) + N_2O \rightarrow N_2O + O$	1.00×10^{-18}	[17]
$O(^1D) + NO_2 \rightarrow O_2 + NO$	3.00×10^{-16}	[18]
$O(^1D) + O_3 \rightarrow O + O_3$	2.41×10^{-16}	[37]
$O(^1D) + CO_2 \rightarrow O + CO_2$	1.35×10^{-16}	[37]
$O(^1D) + CO \rightarrow CO_2$	7.30×10^{-17}	[37]
$O(^1S) + O_2 \rightarrow O_2 + O$	6.13×10^{-20}	[14]
$O(^1S) + O_2(a^1 \Delta_g) \rightarrow O_2 + O(^1D)$	3.60×10^{-17}	[14]
$O(^1S) + O_2(a^1 \Delta_g) \rightarrow O + O_2(b^1 \Sigma_g^+)$	1.30×10^{-16}	[14]
$O(^1S) + O \rightarrow O(^1D) + O(^1D)$	1.11×10^{-17}	[14]
$O(^1S) + CO_2 \rightarrow O + CO_2$	3.09×10^{-19}	[37]
$O_2(a^1 \Delta_g) + NO \rightarrow O + NO_2$	4.88×10^{-24}	[37]
$O_2(b^1 \Sigma_g^+) + O \rightarrow O_2 + O$	1.88×10^{-20}	[14]
$O_2(b^1 \Sigma_g^+) + O_3 \rightarrow O_2(a^1 \Delta_g) + O_2(a^1 \Delta_g) + O$	1.80×10^{-17}	[14]
$NO(A^1 \Sigma^+) + O_2 \rightarrow NO + O_2$	1.62×10^{-16}	[38]
$NO(A^1 \Sigma^+) + N_2(X^1 \Sigma_g^+, v=0) \rightarrow NO + N_2(A^3 \Sigma_u^+, v=0)$	5.00×10^{-20}	[39]
$NO_2 + NO_3 + NO \rightarrow N_2O_5 + NO$	3.53×10^{-41}	[17]

A.1 Kinetic model for terrestrial TLEs

Reaction	Rate	Reference
$\text{NO}_2 + \text{NO}_3 + \text{N}_2\text{O}_5 \rightarrow \text{N}_2\text{O}_5 + \text{N}_2\text{O}_5$	3.53×10^{-41}	[17]
$\text{N}_2\text{O}_5 + \text{N}_2(\text{X}^1 \Sigma_g^+, v=0) \rightarrow \text{NO}_2 + \text{NO}_3 + \text{N}_2(\text{X}^1 \Sigma_g^+, v=0)$	3.07×10^{-42}	[36]
$\text{N}_2\text{O}_5 + \text{O}_2 \rightarrow \text{NO}_2 + \text{NO}_3 + \text{O}_2$	3.07×10^{-42}	[36]
$\text{O} + \text{NO}_2 + \text{N}_2(\text{X}^1 \Sigma_g^+, v=0) \rightarrow \text{NO}_3 + \text{N}_2(\text{X}^1 \Sigma_g^+, v=0)$	1.48×10^{-44}	[36]
$\text{O} + \text{NO}_2 + \text{O}_2 \rightarrow \text{NO}_3 + \text{O}_2$	1.48×10^{-44}	[36]
$\text{O} + \text{NO}_2 \rightarrow \text{O}_2 + \text{NO}$	9.78×10^{-18}	[14]
$\text{O} + \text{NO} + \text{N}_2(\text{X}^1 \Sigma_g^+, v=0) \rightarrow \text{NO}_2 + \text{N}_2(\text{X}^1 \Sigma_g^+, v=0)$	6.07×10^{-44}	[36]
$\text{O} + \text{NO} + \text{O}_2 \rightarrow \text{NO}_2 + \text{O}_2$	4.70×10^{-44}	[36]
$\text{O} + \text{NO} \rightarrow \text{O}_2 + \text{N}$	6.24×10^{-61}	[37]
$\text{N} + \text{N} + \text{N} \rightarrow \text{N}_2(\text{X}^1 \Sigma_g^+, v=0) + \text{N}$	1.80×10^{-39}	[17]
$\text{O} + \text{O} + \text{N} \rightarrow \text{O}_2 + \text{N}$	2.71×10^{-45}	[36]
$\text{O} + \text{O}_2 + \text{O}_3 \rightarrow \text{O}_3 + \text{O}_3$	3.53×10^{-48}	[17]
$\text{O} + \text{O}_2 + \text{O} \rightarrow \text{O}_3 + \text{O}$	3.83×10^{-47}	[36]
$\text{NO}_2 + \text{N}_2(\text{X}^1 \Sigma_g^+, v=0) \rightarrow \text{NO} + \text{O} + \text{N}_2(\text{X}^1 \Sigma_g^+, v=0)$	8.25×10^{-91}	[36]
$\text{NO}_2 + \text{O}_2 \rightarrow \text{NO} + \text{O} + \text{O}_2$	6.43×10^{-91}	[36]
$\text{NO}_2 + \text{NO} \rightarrow \text{NO} + \text{NO} + \text{O}$	6.43×10^{-90}	[36]
$\text{NO}_2 + \text{NO}_2 \rightarrow \text{NO} + \text{O} + \text{NO}_2$	4.85×10^{-90}	[36]
$\text{NO}_3 + \text{N}_2(\text{X}^1 \Sigma_g^+, v=0) \rightarrow \text{NO}_2 + \text{O} + \text{N}_2(\text{X}^1 \Sigma_g^+, v=0)$	7.12×10^{-66}	[36]
$\text{NO}_3 + \text{O}_2 \rightarrow \text{NO}_2 + \text{O} + \text{O}_2$	7.12×10^{-66}	[36]
$\text{NO}_3 + \text{NO} \rightarrow \text{NO}_2 + \text{O} + \text{NO}$	7.12×10^{-66}	[36]
$\text{NO}_3 + \text{N} \rightarrow \text{NO}_2 + \text{O} + \text{N}$	7.12×10^{-65}	[36]
$\text{NO}_3 + \text{O} \rightarrow \text{NO}_2 + \text{O} + \text{O}$	7.12×10^{-65}	[36]
$\text{NO}_3 + \text{N}_2(\text{X}^1 \Sigma_g^+, v=0) \rightarrow \text{NO} + \text{O}_2 + \text{N}_2(\text{X}^1 \Sigma_g^+, v=0)$	1.42×10^{-65}	[36]
$\text{NO}_3 + \text{O}_2 \rightarrow \text{NO} + \text{O}_2 + \text{O}_2$	1.42×10^{-65}	[36]
$\text{NO}_3 + \text{NO} \rightarrow \text{NO} + \text{O}_2 + \text{NO}$	1.42×10^{-65}	[36]
$\text{NO}_3 + \text{N} \rightarrow \text{NO} + \text{O}_2 + \text{N}$	1.71×10^{-64}	[36]
$\text{NO}_3 + \text{O} \rightarrow \text{NO} + \text{O}_2 + \text{O}$	1.71×10^{-64}	[36]
$\text{CO}_2 + \text{O} \rightarrow \text{CO}_2 + \text{O}_2$	9.14×10^{-75}	[37]
$\text{CO} + \text{O} + \text{N}_2(\text{X}^1 \Sigma_g^+, v=0) \rightarrow \text{CO}_2 + \text{N}_2(\text{X}^1 \Sigma_g^+, v=0)$	8.94×10^{-49}	[37]
$\text{CO} + \text{O}_2 \rightarrow \text{CO}_2 + \text{O}$	3.22×10^{-70}	[37]
$\text{CO} + \text{NO}_2 \rightarrow \text{CO}_2 + \text{NO}$	2.01×10^{-53}	[37]

Table A.8: Neutral kinetics.

A. CHEMICAL SCHEMES

Reaction	Rate	Reference
$N_2(X^1 \Sigma_g^+, v = 0, \dots, 10) + N_2(X^1 \Sigma_g^+, v = 0) \rightarrow N_2(X^1 \Sigma_g^+, v - 1) + N_2(X^1 \Sigma_g^+, v = 1, \dots, 8)$	$f(v)$	[35]
$N_2(X^1 \Sigma_g^+, v = 1, \dots, 10) + N_2(X^1 \Sigma_g^+, w - v) \rightarrow N_2(X^1 \Sigma_g^+, v - 1) + N_2(X^1 \Sigma_g^+, w)$	$f(v)$	[34]
$CO_2(001) + CO_2 \rightarrow CO_2(02^0 0) + CO_2$	1.63×10^{-21}	[44]
$CO_2(02^0 0) + CO_2 \rightarrow CO_2(001) + CO_2$	7.25×10^{-25}	[44]
$CO_2(001) + CO_2 \rightarrow CO_2(02^0 2) + CO_2$	1.63×10^{-21}	[44]
$CO_2(02^0 2) + CO_2 \rightarrow CO_2(001) + CO_2$	1.03×10^{-24}	[44]
$CO_2(001) + CO_2 \rightarrow CO_2(100) + CO_2$	2.32×10^{-22}	[44]
$CO_2(100) + CO_2 \rightarrow CO_2(001) + CO_2$	1.45×10^{-24}	[44]
$CO_2(001) + CO_2 \rightarrow CO_2(03^0 1) + CO_2$	7.42×10^{-21}	[44]
$CO_2(03^0 1) + CO_2 \rightarrow CO_2(001) + CO_2$	3.63×10^{-22}	[44]
$CO_2(001) + CO_2 \rightarrow CO_2(03^0 3) + CO_2$	7.42×10^{-21}	[44]
$CO_2(03^0 3) + CO_2 \rightarrow CO_2(001) + CO_2$	6.12×10^{-22}	[44]
$CO_2(001) + CO_2 \rightarrow CO_2(11^0 1) + CO_2$	7.42×10^{-21}	[44]
$CO_2(11^0 1) + CO_2 \rightarrow CO_2(001) + CO_2$	1.03×10^{-21}	[44]
$CO_2(010) + CO_2 \rightarrow CO_2 + CO_2$	2.72×10^{-21}	[44]
$CO_2 + CO_2 \rightarrow CO_2(010) + CO_2$	2.62×10^{-23}	[44]
$CO_2(100) + CO_2 \rightarrow CO_2(010) + CO_2$	6.80×10^{-21}	[44]
$CO_2(010) + CO_2 \rightarrow CO_2(100) + CO_2$	3.27×10^{-23}	[44]
$CO_2(100) + CO_2 \rightarrow CO_2(010) + CO_2(010)$	2.50×10^{-17}	[44]
$CO_2(010) + CO_2(010) \rightarrow CO_2(100) + CO_2$	1.25×10^{-17}	[44]
$CO_2(001) + CO_2 \rightarrow CO_2(02^0 0) + CO_2(100)$	3.60×10^{-19}	[44]
$CO_2(02^0 0) + CO_2(010) \rightarrow CO_2(001) + CO_2$	1.66×10^{-20}	[44]
$CO_2(001) + CO_2 \rightarrow CO_2(02^0 2) + CO_2(100)$	3.60×10^{-19}	[44]
$CO_2(02^0 2) + CO_2(010) \rightarrow CO_2(001) + CO_2$	2.35×10^{-20}	[44]
$CO_2(001) + CO_2 \rightarrow CO_2(100) + CO_2(010)$	3.60×10^{-19}	[44]
$CO_2(100) + CO_2(010) \rightarrow CO_2(001) + CO_2$	3.34×10^{-20}	[44]

Table A.9: Vibrational-Translational (VT) Vibrational-Vibrational (VV) processes.

Reaction	Rate	Reference
$N_2(A^3 \Sigma_u^+, v = 0, \dots, 16) + N_2(X^1 \Sigma_g^+, v = 0) \rightarrow N_2(X^1 \Sigma_g^+, v = 0) + N_2(X^1 \Sigma_g^+, v = 0)$	$f(v)$	[46]
$N_2(A^3 \Sigma_u^+, v = 0, \dots, 16) + O_2 \rightarrow N_2(X^1 \Sigma_g^+, v = 0) + O_2$	$f(v)$	[46]
$N_2(B^3 \Pi_g, v = 0, \dots, 6) + N_2(X^1 \Sigma_g^+, v = 0) \rightarrow N_2(X^1 \Sigma_g^+, v = 0) + N_2(X^1 \Sigma_g^+, v = 0)$	$f(v)$	[46]
$N_2(B^3 \Pi_g, v = 0, \dots, 6) + O_2 \rightarrow N_2(X^1 \Sigma_g^+, v = 0) + O_2$	$f(v)$	[46]
$N_2(C^3 \Pi_u, v = 0, \dots, 4) + N_2(X^1 \Sigma_g^+, v = 0) \rightarrow N_2(X^1 \Sigma_g^+, v = 0) + N_2(X^1 \Sigma_g^+, v = 0)$	$f(v)$	[47]
$N_2(C^3 \Pi_u, v = 0, \dots, 4) + O_2 \rightarrow N_2(X^1 \Sigma_g^+, v = 0) + O_2$	$f(v)$	[47]
$N_2(a^1 \Pi_g, v = 0) + N_2(a^1 \Pi_g, v = 0) \rightarrow N_2(X^1 \Sigma_g^+, v = 0) + N_2^+ + e$	2.00×10^{-16}	[17]
$N_2(W^3 \Delta_u, v = 0, \dots, 3) + N_2(X^1 \Sigma_g^+, v = 0) \rightarrow N_2(X^1 \Sigma_g^+, v = 0) + N_2(X^1 \Sigma_g^+, v = 0)$	$f(v)$	[46]
$N_2(a^1 \Pi_g, v = 0, \dots, 12) + N_2(X^1 \Sigma_g^+, v = 0) \rightarrow N_2(X^1 \Sigma_g^+, v = 0) + N_2(X^1 \Sigma_g^+, v = 0)$	$f(v)$	[49]
$N_2(a^1 \Pi_g, v = 0, \dots, 12) + O_2 \rightarrow N_2(X^1 \Sigma_g^+, v = 0) + O_2$	$f(v)$	[49]
$N_2^+(B^2 \Sigma_u^+) + N_2(X^1 \Sigma_g^+, v = 0) \rightarrow N_2^+ + N_2(X^1 \Sigma_g^+, v = 0)$	7.50×10^{-17}	[43]
$N_2^+(B^2 \Sigma_u^+) + O_2 \rightarrow N_2^+ + O_2$	6.02×10^{-16}	[43]
$N_2(B^3 \Sigma_g^+) + N_2(X^1 \Sigma_g^+, v = 0) \rightarrow N_2(X^1 \Sigma_g^+, v = 0) + N_2(X^1 \Sigma_g^+, v = 0)$	2.40×10^{-17}	Quenching of $N_2(B^3 \Pi_g)$ given in [43]
$N_2(E^3 \Sigma_g^+) + O_2 \rightarrow N_2(X^1 \Sigma_g^+, v = 0) + O_2$	7.00×10^{-18}	Quenching of $N_2(B^3 \Pi_g)$ given in [43]
$O(^5P) + O_2 \rightarrow O + O_2$	1.08×10^{-15}	[45]
$O(^5P) + N_2(X^1 \Sigma_g^+, v = 0) \rightarrow O + N_2(X^1 \Sigma_g^+, v = 0)$	1.08×10^{-15}	[45]
$O(^3P) + O_2 \rightarrow O + O_2$	7.80×10^{-16}	[45]
$O(^3P) + N_2(X^1 \Sigma_g^+, v = 0) \rightarrow O + N_2(X^1 \Sigma_g^+, v = 0)$	5.90×10^{-16}	[45]
$O(^3P) + O_2 \rightarrow O(^5P) + O_2$	6.00×10^{-17}	[45]
$O(^3P) + N_2(X^1 \Sigma_g^+, v = 0) \rightarrow O(^5P) + N_2(X^1 \Sigma_g^+, v = 0)$	2.00×10^{-17}	[45]
$N_2(C^3 \Pi_u, v = 1, \dots, 4) + N_2(X^1 \Sigma_g^+, v = 0) \rightarrow N_2(C^3 \Pi_u, v = 0, \dots, 3) + N_2(X^1 \Sigma_g^+, v = 0)$	1.00×10^{-17}	[48]

Table A.10: Electronic quenching.

A.1 Kinetic model for terrestrial TLEs

Reaction	Rate	Reference
$N_2(A^3 \Sigma_u^+, v = 2, \dots, 16) + N_2(X^1 \Sigma_g^+, v = 0) \rightarrow N_2(A^3 \Sigma_u^+, v-2) + N_2(X^1 \Sigma_g^+, v = 1)$	$f(v)$	[46]
$N_2(C^3 \Pi_u, v = 1, \dots, 4) + N_2(X^1 \Sigma_g^+, v = 0) \rightarrow N_2(C^3 \Pi_u, v-1) + N_2(X^1 \Sigma_g^+, v = 0)$	$f(v)$	[47]

Table A.11: Vibrational redistribution.

Reaction	Rate	Reference
$N_2(A^3 \Sigma_u^+, v = 0) + N_2(A^3 \Sigma_u^+, v = 0, 1) \rightarrow N_2(C^3 \Pi_u, v = 0, \dots, 4) + N_2(X^1 \Sigma_g^+, v = 0)$	$f(v)$	[49]
$N_2(A^3 \Sigma_u^+, v = 0) + N_2(A^3 \Sigma_u^+, v = 0, 1) \rightarrow N_2(B^3 \Pi_g, v = 1, \dots, 6) + N_2(X^1 \Sigma_g^+, v = 0)$	$f(v)$	[49]

Table A.12: Energy pooling reactions.

Reaction	Rate	Reference
$N_2(B^3 \Pi_g, v = 0, \dots, 6) + N_2(X^1 \Sigma_g^+, v = 0) \rightarrow N_2(A^3 \Sigma_u^+, v = 7, \dots, 16) + N_2(X^1 \Sigma_g^+, v = 0)$	$f(v)$	[46]
$N_2(A^3 \Sigma_u^+, v = 7, \dots, 16) + N_2(X^1 \Sigma_g^+, v = 0) \rightarrow N_2(B^3 \Pi_g, v = 0, \dots, 6) + N_2(X^1 \Sigma_g^+, v = 0)$	$f(v)$	[46]
$N_2(A^3 \Sigma_u^+, v = 0, \dots, 1) + N_2(X^1 \Sigma_g^+, v = 5, \dots, 10) \rightarrow N_2(B^3 \Pi_g, v = 1, \dots, 6) + N_2(X^1 \Sigma_g^+, v = 0, \dots, 5)$	$f(v)$	[50]
$N_2(B'^3 \Sigma_u^-, v = 0, 1) + N_2(X^1 \Sigma_g^+, v = 0) \rightarrow N_2(X^1 \Sigma_g^+, v = 0) + N_2(X^1 \Sigma_g^+, v = 0)$	$f(v)$	[50]
$N_2(B^3 \Pi_g, v = 0, \dots, 2) + N_2(X^1 \Sigma_g^+, v = 0) \rightarrow N_2(W^3 \Delta_u, v = 0, 1) + N_2(X^1 \Sigma_g^+, v = 0)$	$f(v)$	[50]
$N_2(W^3 \Delta_u, v = 0, \dots, 2) + N_2(X^1 \Sigma_g^+, v = 0) \rightarrow N_2(B^3 \Pi_g, v = 0, \dots, 2) + N_2(X^1 \Sigma_g^+, v = 0)$	$f(v)$	[50]
$N_2(B^3 \Pi_g, v = 4, 5) + N_2(X^1 \Sigma_g^+, v = 0) \rightarrow N_2(B'^3 \Sigma_u^-, v = 0, 1) + N_2(X^1 \Sigma_g^+, v = 0)$	$f(v)$	[50]
$N_2(B'^3 \Sigma_u^-, v = 0, 1) + N_2(X^1 \Sigma_g^+, v = 0) \rightarrow N_2(B^3 \Pi_g, v = 4, 5) + N_2(X^1 \Sigma_g^+, v = 0)$	$f(v)$	[50]

Table A.13: Intersystem collisional transfer (ICT).

Reaction	Rate	Reference
$N_2(A^3 \Sigma_u^+, v = 0) \rightarrow N_2(X^1 \Sigma_g^+, v = 0) + h\nu$	5.00×10^{-1}	[36]
$N_2(W^3 \Delta_u, v = 0) \rightarrow N_2(X^1 \Sigma_g^+, v = 0) + h\nu$	1.54×10^{-1}	[36]
$N_2(B^3 \Pi_g, v = 0, \dots, 6) \rightarrow N_2(A^3 \Sigma_u^+, v = 0, \dots, 16) + h\nu$	$f(v)$	[57]
$N_2(C^3 \Pi_u, v = 0, \dots, 4) \rightarrow N_2(B^3 \Pi_g, v = 0, \dots, 6) + h\nu$	$f(v)$	[57]
$N_2(a^1 \Pi_g, v = 0, 2, 3) \rightarrow N_2(a'^1 \Sigma_u^-) + h\nu$	$f(v)$	[57]
$N_2(a^1 \Pi_g, v = 0, \dots, 15) \rightarrow N_2(X^1 \Sigma_g^+, v = 0, \dots, 8) + h\nu$	$f(v)$	[57]
$N_2(B'^3 \Sigma_u^-, v = 0) \rightarrow N_2(B^3 \Pi_g, v = 0) + h\nu$	3.40×10^4	[36]
$N_2(B^3 \Sigma_g^+) \rightarrow N_2(A^3 \Sigma_u^+, v = 0) + h\nu$	1.20×10^3	[36]
$N_2(E^3 \Sigma_g^+) \rightarrow N_2(B^3 \Pi_g, v = 0) + h\nu$	3.46×10^2	[36]
$N_2(E^3 \Sigma_g^+) \rightarrow N_2(C^3 \Pi_u, v = 0) + h\nu$	1.73×10^3	[36]
$N_2(w^1 \Delta_u) \rightarrow N_2(a^1 \Pi_g, v = 0) + h\nu$	1.51×10^3	[36]
$N_2(a'^1 \Sigma_u^-) \rightarrow N_2(X^1 \Sigma_g^+, v = 0) + h\nu$	1.00×10^2	[36]
$N_2(a^1 \Pi_g, v = 0) \rightarrow N_2(a'^1 \Sigma_u^-) + h\nu$	9.74×10^1	[36]
$N_2(a''^1 \Sigma_g^+) \rightarrow N_2(X^1 \Sigma_g^+, v = 0) + h\nu$	2.86×10^5	[51]
$N_2(a''^1 \Sigma_g^+) \rightarrow N_2(X^1 \Sigma_g^+, v = 0) + h\nu$	2.86×10^5	[51]
$N_2^+(B^2 \Sigma_u^+) \rightarrow N_2^+ + h\nu$	1.14×10^7	[52]
$NO(A^1 \Sigma^+) \rightarrow NO + h\nu$	5.00×10^6	[55]
$O(^1S) \rightarrow O(^1D) + h\nu$	1.34	[25]
$O(^1D) \rightarrow O + h\nu$	5.10×10^{-3}	[25]
$O(^3P) \rightarrow O + h\nu$	2.98×10^{07}	[45]
$O(^5P) \rightarrow O + h\nu$	2.56×10^{07}	[45]-[58]
$O_2(A^3 \Pi_u^+) \rightarrow O_2 + h\nu$	1.10×10^1	[53]
$O_2(b^1 \Sigma_g^+) \rightarrow O_2(a^1 \Delta_g) + h\nu$	1.70×10^{-3}	[54]
$CO_2(001) \rightarrow CO_2(100) + h\nu$	3.50×10^{-1}	[56]
$CO_2(001) \rightarrow CO_2(02^0 0) + h\nu$	2.00×10^{-1}	[56]
$CO_2(001) \rightarrow CO_2 + h\nu$	4.50×10^2	[56]
$CO_2(100) \rightarrow CO_2(010) + h\nu$	2.08	[56]
$CO_2(010) \rightarrow CO_2 + h\nu$	1.56	[56]
$OH^* \rightarrow OH + h\nu$	2.18×10^2	[33]

Table A.14: Radiative decay processes.

A.2 Kinetic model for Venusian TLEs

This section collects the kinetic scheme used in the model of Venusian halos and elves (*Pérez-Invernón et al.*, 2016b). Table A.16 collects the set of chemical reactions used to obtain the equilibrium profile. The set of chemical reactions used to describe the inception and evolution of TLEs in the upper mesosphere of Venus is detailed in tables A.18 and A.19.

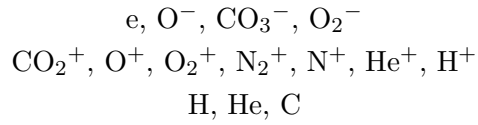


Table A.15: Species considered in the basic kinetic model providing ambient nighttime electron density profiles in Venus between 70 km and 125 km of altitude. We do not include here the species whose density remains constant in time.

Reaction No.	Reaction	Rate	Reference
1	$e + \text{CO}_2^+ \rightarrow \text{CO} + \text{O}$	$6.5 \times 10^{-7} \left(\frac{T_e}{300}\right)^{-0.8} \text{cm}^3 \text{s}^{-1}$	[1]
2	$\text{O}^- + \text{CO} \rightarrow \text{CO}_2 + e$	$6.72 \times 10^{-10} \text{cm}^3 \text{s}^{-1}$	[2]
3	$\text{O}^- + \text{CO}_2 + \text{N}_2(X^1\Sigma_g^+) \rightarrow \text{CO}_3^- + \text{N}_2(X^1\Sigma_g^+)$	$3.1 \times 10^{-28} \left(\frac{T}{300}\right)^{0.5} \text{cm}^6 \text{s}^{-1}$	[3]
4	$\text{O}^- + \text{CO}_2 + \text{CO}_2 \rightarrow \text{CO}_3^- + \text{CO}_2$	$3.1 \times 10^{-28} \left(\frac{T}{300}\right)^{0.5} \text{cm}^6 \text{s}^{-1}$	[3]
5	$\text{CO}_3^- + \text{O} \rightarrow \text{O}_2^- + \text{CO}_2$	$1.1 \times 10^{-10} \times \left(\frac{T}{300}\right)^{0.5} \text{cm}^3 \text{s}^{-1}$	[3]
6	$\text{O}_2^- + \text{O} \rightarrow \text{O}^- + \text{O}_2$	$3.3 \times 10^{-10} \text{cm}^3 \text{s}^{-1}$	[2]
7	$\text{CO}_2^+ + \text{O} \rightarrow \text{CO} + \text{O}_2^+$	$1.6 \times 10^{-10} \text{cm}^3 \text{s}^{-1}$	[4]
8	$\text{CO}_2^+ + \text{O} \rightarrow \text{CO}_2 + \text{O}^+$	$9.6 \times 10^{-11} \text{cm}^3 \text{s}^{-1}$	[4]
9	$\text{He}^+ + \text{CO}_2 \rightarrow \text{CO} + \text{O}^+ + \text{He}$	$1.0 \times 10^{-10} \text{cm}^3 \text{s}^{-1}$	[5]
10	$\text{He}^+ + \text{CO}_2 \rightarrow \text{CO}^+ + \text{O} + \text{He}$	$8.7 \times 10^{-10} \text{cm}^3 \text{s}^{-1}$	[5]
11	$\text{CO}^+ + \text{O} \rightarrow \text{CO} + \text{O}^+$	$1.4 \times 10^{-10} \text{cm}^3 \text{s}^{-1}$	[6]
12	$\text{O}^+ + \text{H} \rightarrow \text{H}^+ + \text{O}$	$2.5 \times 10^{-11} \times T^{0.5} \text{cm}^3 \text{s}^{-1}$	[6]
13	$\text{H}^+ + \text{O} \rightarrow \text{O}^+ + \text{H}$	$3.8 \times 10^{-10} \text{cm}^3 \text{s}^{-1}$	[4]
14	$\text{O}^+ + \text{CO}_2 \rightarrow \text{CO} + \text{O}_2^+$	$9.4 \times 10^{-10} \text{cm}^3 \text{s}^{-1}$	[6]
15	$\text{He}^+ + \text{O} \rightarrow \text{He} + \text{O}^+$	$5.0 \times 10^{-11} \text{cm}^3 \text{s}^{-1}$	[4]
16	$\text{O}_2^+ + e \rightarrow \text{O} + \text{O}$	$8.75 \times 10^{-6} T_e^{-2} \text{cm}^3 \text{s}^{-1}$	[4]
17	$\text{CO}^+ + e \rightarrow \text{C} + \text{O}$	$1.3 \times 10^{-5} T_e^{0.5} \text{cm}^3 \text{s}^{-1}$	[6]
18	$\text{CO}^+ + \text{CO}_2 \rightarrow \text{CO}_2^+ + \text{CO}$	$1.0 \times 10^{-9} \text{cm}^3 \text{s}^{-1}$	[6]
19	$\text{N}_2^+ + \text{CO}_2 \rightarrow \text{N}_2 + \text{CO}_2^+$	$7.7 \times 10^{-10} \text{cm}^3 \text{s}^{-1}$	[6]
20	$\text{N}_2^+ + \text{CO} \rightarrow \text{CO}^+ + \text{N}_2(X^1\Sigma_g^+)$	$7.4 \times 10^{-11} \text{cm}^3 \text{s}^{-1}$	[6]
21	$\text{N}_2^+ + \text{O} \rightarrow \text{O}^+ + \text{N}_2(X^1\Sigma_g^+)$	$3.6 \times 10^{-12} \left(\frac{T_e}{300}\right) \text{cm}^3 \text{s}^{-1}$	[6]
22	$\text{N}^+ + \text{CO} \rightarrow \text{CO}^+ + \text{N}$	$4.0 \times 10^{-10} \text{cm}^3 \text{s}^{-1}$	[6]
23	$\text{N}^+ + \text{CO}_2 \rightarrow \text{CO}_2^+ + \text{N}$	$7.5 \times 10^{-10} \text{cm}^3 \text{s}^{-1}$	[6]
24	$\text{O}^+ + e \rightarrow \text{O} + h\nu$	$3.4 \times 10^{-12} \left(\frac{T_e}{300}\right)^{0.5} \text{cm}^3 \text{s}^{-1}$	[5]
25	$\text{CO}^+ + e \rightarrow \text{CO}$	$6.5 \times 10^{-7} \left(\frac{T_e}{300}\right)^{-0.53} \text{cm}^3 \text{s}^{-1}$	[5]
26	$\text{N}^+ + e \rightarrow \text{N} + h\nu$	$3.3 \times 10^{-12} \left(\frac{T_e}{300}\right)^{-0.5} \text{cm}^3 \text{s}^{-1}$	[5]
27	$\text{N}_2^+ + e \rightarrow \text{N} + \text{N}$	$2.5 \times 10^{-7} \left(\frac{T_e}{300}\right)^{-0.5} \text{cm}^3 \text{s}^{-1}$	[5]
28	$\text{H}^+ + e \rightarrow \text{H} + h\nu$	$4.4 \times 10^{-12} \left(\frac{T_e}{300}\right)^{-0.5} \text{cm}^3 \text{s}^{-1}$	[5]
29	$\text{He}^+ + e \rightarrow \text{He} + h\nu$	$4.4 \times 10^{-12} \left(\frac{T_e}{300}\right)^{-0.5} \text{cm}^3 \text{s}^{-1}$	[5]
30	$\text{He}^+ + \text{CO}_2 \rightarrow \text{CO}^+ + \text{O} + \text{He}$	$8.7 \times 10^{-10} \text{cm}^3 \text{s}^{-1}$	[6]
31	$\text{He}^+ + \text{CO}_2 \rightarrow \text{CO}_2^+ + \text{He}$	$1.2 \times 10^{-10} \text{cm}^3 \text{s}^{-1}$	[6]
32	$\text{He}^+ + \text{CO}_2 \rightarrow \text{O}^+ + \text{CO} + \text{He}$	$1.0 \times 10^{-10} \text{cm}^3 \text{s}^{-1}$	[6]
33	$\text{He}^+ + \text{CO} \rightarrow \text{CO}^+ + \text{He}$	$1.68 \times 10^{-9} \text{cm}^3 \text{s}^{-1}$	[6]
34	$\text{He}^+ + \text{N}_2(X^1\Sigma_g^+) \rightarrow \text{N}^+ + \text{N} + \text{He}$	$9.6 \times 10^{-10} \text{cm}^3 \text{s}^{-1}$	[6]
35	$\text{He}^+ + \text{N}_2(X^1\Sigma_g^+) \rightarrow \text{N}_2^+ + \text{He}$	$6.4 \times 10^{-10} \text{cm}^3 \text{s}^{-1}$	[6]
36	$\text{CO}_2^+ + \text{H} \rightarrow \text{H}^+ + \text{CO}_2$	$1.0 \times 10^{-10} \text{cm}^3 \text{s}^{-1}$	[6]
37	$\text{CO}_2 + h\nu \rightarrow \text{CO}_2^+ + e$	$k \times \eta_1 \text{cm}^{-3} \text{s}^{-1}$	[7], [8]
38	$\text{O} + h\nu \rightarrow \text{O}^+ + e$	$k \times \eta_2 \text{cm}^{-3} \text{s}^{-1}$	[7], [8]
39	$\text{He} + h\nu \rightarrow \text{He}^+ + e$	$k \times \eta_3 \text{cm}^{-3} \text{s}^{-1}$	[7], [8]
40	$\text{H} + h\nu \rightarrow \text{H}^+ + e$	$k \times \eta_4 \text{cm}^{-3} \text{s}^{-1}$	[7], [8]

Table A.16: Basic kinetic scheme of the model providing ambient nighttime electron density profiles in Venus between 70 km and 125 km of altitude. The gas temperature (T) is in K. The electron temperature is $T_e = T$. References are as follows: [1] *Viggiano et al.* (2005); [2] *Gordillo-Vázquez* (2008); [3] *Brasseur and Solomon* (2005); [4] *Chen and Nagy* (1978); [5] *Upadhyay and Singh* (1990); [6] *Schunk and Nagy* (1980); [7] *Nordheim et al.* (2015); [8] *Chen and Nagy* (1978). Note that for photoionization mechanisms (37)-(40) reactions rates (in $\text{cm}^{-3} \text{s}^{-1}$) rather than rates ($\text{cm}^3 \text{s}^{-1}$) are shown. The values of the reaction rate k and of the nondimensional magnitudes $\eta_i = N_i/N$ (with $\eta_1 = 0.9$, $\eta_2 = 0.1$, $\eta_3 = 10^{-6}$, $\eta_4 = 10^{-6}$) are obtained from *Nordheim et al.* (2015) and *Chen and Nagy* (1978), respectively.

A. CHEMICAL SCHEMES

$e, O^-, CO_3^-, O_2^-, O^-$ CO_2^+, O_2^+, N_2^+ $O(^1S), O(^1D), O(^3P), O(^5P), C$ $N_2(A^3\Sigma_u^+), N_2(B^3\Pi_g \text{ (all } v')), N_2(W^3\Delta_u \text{ (all } v')), N_2(C^3\Pi_u \text{ (all } v'))$ $N_2(a^1\Pi_g \text{ (all } v')), N_2(a'^1\Sigma_u^- \text{ (all } v'))$ $CO_2(00^0), CO_2(10^0), CO_2(01^1), CO_2(02^0)$ $CO_2(02^2), CO_2(03^1), CO_2(03^3), CO_2(11^1)$

Table A.17: Species considered in the 2D electric discharge model between 70 km and 125 km of altitude.

Reaction No.	Reaction	Rate	Reference
1	$e + CO_2^+ \rightarrow CO + O$	$6.5 \times 10^{-7} \left(\frac{T_e}{300}\right)^{-0.8} \text{ cm}^3 \text{ s}^{-1}$	[1]
2	$O^- + CO \rightarrow CO_2 + e$	$6.72 \times 10^{-10} \text{ cm}^3 \text{ s}^{-1}$	[2]
3	$O^- + CO_2 + N_2(X^1\Sigma_g^+) \rightarrow CO_3^- + N_2(X^1\Sigma_g^+)$	$3.1 \times 10^{-28} \left(\frac{T}{300}\right)^{0.5} \text{ cm}^6 \text{ s}^{-1}$	[3]
4	$O^- + CO_2 + CO_2 \rightarrow CO_3^- + CO_2$	$3.1 \times 10^{-28} \left(\frac{T}{300}\right)^{0.5} \text{ cm}^6 \text{ s}^{-1}$	[3]
5	$CO_3^- + O \rightarrow O_2^- + CO_2$	$1.1 \times 10^{-10} \times \left(\frac{T}{300}\right)^{0.5} \text{ cm}^3 \text{ s}^{-1}$	[3]
6	$O_2^- + O \rightarrow O^- + O_2$	$3.3 \times 10^{-10} \text{ cm}^3 \text{ s}^{-1}$	[2]
7	$CO_2^+ + O \rightarrow CO + O_2^+$	$1.6 \times 10^{-10} \text{ cm}^3 \text{ s}^{-1}$	[4]
16	$O_2^+ + e \rightarrow O + O$	$8.75 \times 10^{-6} T_e^{-2/3} \text{ cm}^3 \text{ s}^{-1}$	[5]
19	$N_2^+ + CO_2 \rightarrow N_2 + CO_2^+$	$7.7 \times 10^{-10} \text{ cm}^3 \text{ s}^{-1}$	[6]
41	$e + CO_2 \rightarrow CO + O^-$	$k_1(E/N) \text{ cm}^3 \text{ s}^{-1}$	[9]
42	$e + CO_2 \rightarrow CO_2^+ + 2e$	$k_2(E/N) \text{ cm}^3 \text{ s}^{-1}$	[9]
43	$e + N_2(X^1\Sigma_g^+) \rightarrow N_2^+ + 2e$	$k_3(E/N) \text{ cm}^3 \text{ s}^{-1}$	[10]
44	$e + CO \rightarrow O^- + C$	$k_4(E/N) \text{ cm}^3 \text{ s}^{-1}$	[20]
45	$e + CO_2 \rightarrow O(^1S) + CO + e$	$k_5(E/N) \text{ cm}^3 \text{ s}^{-1}$	[9]
46	$O^- + N_2(X^1\Sigma_g^+) \rightarrow N_2O + e$	$k_6(E/N) \text{ cm}^3 \text{ s}^{-1}$	[19]
47	$e + N_2(X^1\Sigma_g^+) \rightarrow N_2(B^3\Pi_g) + e$	$k_7(E/N) \text{ cm}^3 \text{ s}^{-1}$	[10]
48	$e + N_2(X^1\Sigma_g^+) \rightarrow N_2(C^3\Pi_u) + e$	$k_8(E/N) \text{ cm}^3 \text{ s}^{-1}$	[10]
49	$e + N_2(X^1\Sigma_g^+) \rightarrow N_2(W^3\Delta_u) + e$	$k_9(E/N) \text{ cm}^3 \text{ s}^{-1}$	[10]
50	$e + N_2(X^1\Sigma_g^+) \rightarrow N_2(a^1\Pi_g) + e$	$k_{10}(E/N) \text{ cm}^3 \text{ s}^{-1}$	[10]
51	$e + CO_2 \rightarrow CO_2(00^0) + e$	$k_{11}(E/N) \text{ cm}^3 \text{ s}^{-1}$	[11]
52	$e + CO_2 \rightarrow CO_2(10^0) + e$	$k_{12}(E/N) \text{ cm}^3 \text{ s}^{-1}$	[11]
53	$e + CO_2 \rightarrow CO_2(01^1) + e$	$k_{13}(E/N) \text{ cm}^3 \text{ s}^{-1}$	[11]
54	$e + CO_2(00^0) \rightarrow CO_2 + e$	$k_{14}(E/N) \text{ cm}^3 \text{ s}^{-1}$	[11]
55	$e + CO_2(10^0) \rightarrow CO_2 + e$	$k_{15}(E/N) \text{ cm}^3 \text{ s}^{-1}$	[11]
56	$e + CO_2(01^1) \rightarrow CO_2 + e$	$k_{16}(E/N) \text{ cm}^3 \text{ s}^{-1}$	[11]
57	$e + O \rightarrow O(^3P) + e$	$k_{17}(E/N) \text{ cm}^3 \text{ s}^{-1}$	[12]
58	$e + O \rightarrow O(^5P) + e$	$k_{18}(E/N) \text{ cm}^3 \text{ s}^{-1}$	[12]
59	$e + O_2 \rightarrow O(^3P) + O + e$	$k_{19}(E/N) \text{ cm}^3 \text{ s}^{-1}$	[13]
60	$e + O_2 \rightarrow O(^5P) + O + e$	$k_{20}(E/N) \text{ cm}^3 \text{ s}^{-1}$	[14]
61	$O(^1S) + CO_2 \rightarrow \text{Products}$	$4.8 \times 10^{-14} \text{ cm}^3 \text{ s}^{-1}$	[15]
62	$O(^1S) + O_2 \rightarrow \text{Products}$	$7.4 \times 10^{-14} \text{ cm}^3 \text{ s}^{-1}$	[15]
63	$O(^1S) + N_2(X^1\Sigma_g^+) \rightarrow O(^1D) + h\nu$	$5.0 \times 10^{-17} \text{ cm}^3 \text{ s}^{-1}$	[15]
64	$O(^1S) + CO \rightarrow \text{Products}$	$4.9 \times 10^{-15} \text{ cm}^3 \text{ s}^{-1}$	[16]
65	$O(^1S) \rightarrow O(^1D) + h\nu$	1.35 s^{-1}	[2]
66	$O(^1D) \rightarrow O + h\nu$	$5.1 \times 10^{-3} \text{ s}^{-1}$	[2]
67	$O(^1D) + CO_2 \rightarrow \text{Products}$	$1.1 \times 10^{-10} \text{ cm}^3 \text{ s}^{-1}$	[2]
68	$O(^1D) + N_2(X^1\Sigma_g^+) \rightarrow \text{Products}$	$7.0 \times 10^{-11} \text{ cm}^3 \text{ s}^{-1}$	[2]
69	$O(^1D) + CO \rightarrow \text{Products}$	$8.0 \times 10^{-11} \text{ cm}^3 \text{ s}^{-1}$	[2]
70	$N_2(B^3\Pi_g \text{ (all } v')) \rightarrow N_2(A^3\Sigma_u^+ \text{ (all } v'')) + h\nu$	$1.34 \times 10^5 \text{ s}^{-1}$	[21]
71	$N_2(C^3\Pi_u \text{ (all } v')) \rightarrow N_2(B^3\Pi_g \text{ (all } v'')) + h\nu$	$2.45 \times 10^7 \text{ s}^{-1}$	[21]
72	$N_2(W^3\Delta_u \text{ (} v' = 0)) \rightarrow N_2(X^1\Sigma_g^+ \text{ (} v'' = 5)) + h\nu$	0.154 s^{-1}	[21]
73	$N_2(W^3\Delta_u \text{ (} v' = 0)) \rightarrow N_2(B^3\Pi_g \text{ (} v'' = 0)) + h\nu$	$3.1 \times 10^{-2} \text{ s}^{-1}$	[22]
74	$N_2(a^1\Pi_g \text{ (} v' = 0)) \rightarrow N_2(a'^1\Sigma_u^- \text{ (} v'' = 0)) + h\nu$	$9.74 \times 10^1 \text{ s}^{-1}$	[22]
75	$N_2(a^1\Pi_g \text{ (all } v')) \rightarrow N_2(X^1\Sigma_g^+ \text{ (all } v'')) + h\nu$	$1.0 \times 10^3 \text{ s}^{-1}$	[22]
76	$CO_2(00^0) \rightarrow CO_2(02^0) + h\nu$	0.2 s^{-1}	[17]
77	$CO_2(00^0) \rightarrow CO_2 + h\nu$	450.0 s^{-1}	[17]
78	$CO_2(10^0) \rightarrow CO_2(01^1) + h\nu$	2.08 s^{-1}	[17]
79	$CO_2(01^1) \rightarrow CO_2 + h\nu$	1.564 s^{-1}	[17]
80	$O(^5P) + O_2 \rightarrow O + O_2$	$1.08 \times 10^{-9} \text{ cm}^3 \text{ s}^{-1}$	[18]

Reaction No.	Reaction	Rate	Reference
81	$O(^5P) + N_2(X^1\Sigma_g^+) \rightarrow O + N_2(X^1\Sigma_g^+)$	$1.08 \times 10^{-9} \text{ cm}^3 \text{ s}^{-1}$	[18]
82	$O(^3P) + O_2 \rightarrow O + O_2$	$7.8 \times 10^{-10} \text{ cm}^3 \text{ s}^{-1}$	[18]
83	$O(^3P) + N_2(X^1\Sigma_g^+) \rightarrow O + N_2(X^1\Sigma_g^+)$	$5.9 \times 10^{-10} \text{ cm}^3 \text{ s}^{-1}$	[18]
84	$O(^3P) + O_2 \rightarrow O(^5P) + O_2$	$6 \times 10^{-11} \text{ cm}^3 \text{ s}^{-1}$	[18]
85	$O(^3P) + N_2(X^1\Sigma_g^+) \rightarrow O(^5P) + N_2(X^1\Sigma_g^+)$	$2 \times 10^{-11} \text{ cm}^3 \text{ s}^{-1}$	[18]
86	$O(^3P) \rightarrow O + h\nu$	$2.98 \times 10^7 \text{ s}^{-1}$	[18]
87	$O(^5P) \rightarrow O + h\nu$	$2.56 \times 10^7 \text{ s}^{-1}$	[18]

Table A.18: Basic kinetic scheme of the 2D electric discharge model between 70 km and 125 km of altitude in the mesosphere of Venus. The gas temperature (T) is in K. The electron temperature (T_e) dependence of some rates is transformed into a reduced electric field (E/N) dependence using $T_e(\text{eV}) = 2\bar{\epsilon}/3$ where the mean electron energy (ϵ) is obtained from BOLSIG+. References are as follows: [1] *Viggiano et al.* (2005); [2] *Gordillo-Vázquez* (2008); [3] *Brasseur and Solomon* (2005); [4] *Chen and Nagy* (1978); [5] *Upadhyay and Singh* (1990); [6] *Schunk and Nagy* (1980); [9] *Itikawa* (2002); [10] *Itikawa* (2006); [11] *Phelps* (2005); [12] *LaHer and Gilmore* (1990); [13] *Pagnon et al.* (1995); [14] *Erdman and Zipf* (1987); [15] *Atkinson and Welge* (1972); [16] *Filseth et al.* (1970); [17] *Parra-Rojas et al.* (2014); [18] *Dagdigian et al.* (1988); [19] *Rayment and Moruzzi* (1978); [20] *Rapp and Briglia* (1965); [21] *Capitelli et al.* (2000); [22] *Gilmore et al.* (1992). Note that reactions No. 1 through 7 together with reactions 16 and 19 are the same as in Table 2.

A. CHEMICAL SCHEMES

Reaction No.	Reaction	g	h	i	j	Reference
88-89	$\text{CO}_2(00^01) + \text{CO}_2 \rightleftharpoons \text{CO}_2(02^00) + \text{CO}_2$	0.18	7.3×10^{-14}	-850.3	86523	[23]
90-91	$\text{CO}_2(00^01) + \text{CO}_2 \rightleftharpoons \text{CO}_2(02^20) + \text{CO}_2$	0.18	7.3×10^{-14}	-850.3	86523	[23]
92-93	$\text{CO}_2(00^01) + \text{CO}_2 \rightleftharpoons \text{CO}_2(10^00) + \text{CO}_2$	0.18	7.3×10^{-14}	-850.3	86523	[23]
94-95	$\text{CO}_2(00^01) + \text{CO}_2 \rightleftharpoons \text{CO}_2(03^10) + \text{CO}_2$	0.82	7.3×10^{-14}	-850.3	86523	[23]
96-97	$\text{CO}_2(00^01) + \text{CO}_2 \rightleftharpoons \text{CO}_2(03^30) + \text{CO}_2$	0.82	7.3×10^{-14}	-850.3	86523	[23]
98-99	$\text{CO}_2(00^01) + \text{CO}_2 \rightleftharpoons \text{CO}_2(11^10) + \text{CO}_2$	0.82	7.3×10^{-14}	-850.3	86523	[23]
100-101	$\text{CO}_2(01^10) + \text{CO}_2 \rightleftharpoons \text{CO}_2 + \text{CO}_2$	1.0	4.2×10^{-12}	-2988	303930	[24]
102-103	$\text{CO}_2(10^00) + \text{CO}_2 \rightleftharpoons \text{CO}_2(01^10) + \text{CO}_2$	2.5	4.2×10^{-12}	-2988	303930	[24]
104-105	$\text{CO}_2(10^00) + \text{CO}_2 \rightleftharpoons \text{CO}_2(01^10) + \text{CO}_2(01^10)$	1.0	2.5×10^{-11}	0	0	[25]
106-107	$\text{CO}_2(00^01) + \text{CO}_2 \rightleftharpoons \text{CO}_2(02^00) + \text{CO}_2(01^10)$	1.0	3.6×10^{-13}	-1660	176948	[23]
108-109	$\text{CO}_2(00^01) + \text{CO}_2 \rightleftharpoons \text{CO}_2(02^20) + \text{CO}_2(01^10)$	1.0	3.6×10^{-13}	-1660	176948	[23]
110-111	$\text{CO}_2(00^01) + \text{CO}_2 \rightleftharpoons \text{CO}_2(10^00) + \text{CO}_2(01^10)$	1.0	3.6×10^{-13}	-1660	176948	[23]

Table A.19: Vibrational-Translational (VT) and Vibrational-Vibrational (VV) processes. The rates shown are defined as $k_{co2} = g \times h \times \exp(i/T + j/T^2)$ in cm^3s^{-1} with the gas temperature (T) in Kelvins. The rates of the return processes are calculated multiplying the direct reaction rate by $\exp(-E/\kappa_B T)$, where E is the energy emitted/absorbed during the process and κ_B stands for the Boltzmann constant. References are as follows: [23] *Lepoutre et al. (1977)*; [24] *López-Valverde (1990)*; [25] *Orr and Smith (1987)*

References

- ADACHI, T., SATO, M., USHIO, T., YAMAZAKI, A., SUZUKI, M., KIKUCHI, M., TAKAHASHI, Y., INAN, U.S., LINSKOTT, I., HOBARA, Y., FREY, H.U., MENDE, S.B., CHEN, A.B., HSU, R.R. & KUSUNOKI, K. (2016). Identifying the occurrence of lightning and transient luminous events by nadir spectrophotometric observation. *Journal of Atmospheric and Solar-Terrestrial Physics*, **145**. xxxv, 57, 112, 137
- ALBRITTON, D.L. (1978). Ion-neutral reaction-rate constants measured in flow reactors through 1977. *Atomic data and nuclear data tables*, **22**, 1–89. 236
- ASHMORE, S.E. (1950). Unusual Lightning. *Weather*, **5**, 331. 11
- ATKINSON, R. & WELGE, K.H. (1972). Temperature dependence of $O(^1S)$ deactivation by CO_2 , O_2 , N_2 , and Ar. *Journal Chemical Physics*, **57**, 3689. xxxviii, 251
- BAINES, K.H., SIMON-MILLER, A.A., ORTON, G.S., WEAVER, H.A., LUNSFORD, A., MOMARY, T.W., SPENCER, J., CHENG, A.F., REUTER, D.C., JENNINGS, D.E., GLADSTONE, G.R., MOORE, J., STERN, S.A., YOUNG, L.A., THROOP, H., YANAMANDRA-FISHER, P., FISHER, B.M., HORA, J. & RESSLER, M.E. (2007). Polar Lightning and Decadal-Scale Cloud Variability on Jupiter. *Science*, **318**, 226. xii, 20, 21, 217
- BARRINGTON-LEIGH, C.P. & INAN, U.S. (1999). Elves triggered by positive and negative lightning discharges. *Geophys. Res. Lett.*, **26**, 683. 64
- BARRINGTON-LEIGH, C.P., INAN, U.S. & STANLEY, M. (2001). Identification of sprites and elves with intensified video and broadband array photometry. *Journal of Geophysical Research*, **106**, 1741. 52
- BARTH, E.L., FARRELL, W.M. & RAFKIN, S.C.R. (2016). Electric field generation in martian dust devils. *Icarus*, **268**, 253. 26
- BATES, D.R. (1988). Transition probabilities of the bands of the oxygen systems of the nightglow. *Planetary and Space Science*, **36**, 869–873, special Issue: Atomic Oxygen Abundance in Thermosphere. 236
- BAUER, S.J., BRACE, L.M., TAYLOR, J., BREUS, T.K., KLIORÉ, A.J., KNUDSEN, W.C., NAGY, A.F., RUSSELL, C.T. & SAVICH, N.A. (1985). The Venus ionosphere. *Adv. Space Res.*, **5**, 233. xxviii, 152, 153, 166, 169, 194, 197, 208
- BENNETT, A.J. (2014). Modification of lightning quasi-electrostatic signal by mesospheric halo generation. *J. Atm. Sol.-Terr. Phys.*, **113**, 39. 56, 91, 92, 227
- BENNETT, A.J. & HARRISON, R.G. (2013). Lightning-Induced Extensive Charge Sheets Provide Long Range Electrostatic Thunderstorm Detection. *Phys Rev. Lett*, **111**, 045003. 56, 91, 96, 227
- BERING, E.A., BENBROOK, J.R., GARRETT, J.A., PAREDES, A.M., WESCOTT, E.M., MOUDRY, D.R., SENTMAN, D.D., STENBAEK-NIELSEN, H.C. & LYONS, W.A. (2002). Sprite and elve electrodynamics. *Adv. Space Res.*, **30**, 2585. 52
- BERING, E.A., BENBROOK, J.R., BHUSAL, L., GARRETT, J.A., PAREDES, A.M., WESCOTT, E.M., MOUDRY, D.R., SENTMAN, D.D., STENBAEK-NIELSEN, H.C. & LYONS, W.A. (2004a). Observations of transient luminous events (TLEs) associated with negative cloud to ground (-CG) lightning strokes. *Geophys. Res. Lett.*, **31**, L05104. 52
- BERING, I.E.A., BHUSAL, L., BENBROOK, J.R., GARRETT, J.A., JACKSON, A.P., WESCOTT, E.M., MOUDRY, D.R., SENTMAN, D.D., STENBAEK-NIELSEN, H.C. & LYONS, W.A. (2004b). The results from the 1999 sprites balloon campaign. *Adv. Space Res.*, **34**, 1782. 52
- BERK, A., ANDERSON, G.P., ACHARYA, P.K., BERNSTEIN, L.S., MURATOV, L., LEE, J., FOX, M., ADLER-GOLDEN, S.M., CHETWYND, J.H., HOKE, M.L. & OTHERS (2005). MODTRAN 5: a reformulated atmospheric band model with auxiliary species and practical multiple scattering options: update. In *Algorithms and technologies for multispectral, hyperspectral, and ultraviolet imagery XI*, vol. 5806, 662–668, International Society for Optics and Photonics. 66, 84
- BILITZA, D. & REINISCH, B.W. (2008). International reference ionosphere 2007: improvements and new parameters. *Advances in Space Research*, **42**, 599–609. 99
- BIONDI, M.A., BORTNER, M.H. & BAUER, T. (1971). *Defense Nuclear Agency Reaction Rate Handbook*. DNA 1948H (US GPO, Washington, DC, 1972). 59, 236
- BLANC, E., LEFEUVRE, F., ROUSSEL-DUPRÉ, R. & SAUVAUD, J.A. (2007). A microsatellite project dedicated to the study of impulsive transfers of energy between the Earth atmosphere, the ionosphere, and the magnetosphere. *Adv. Space Res.*, **40**, 1268. xxxv, 12, 112, 137

REFERENCES

- BOECK, W.L., VAUGHAN, O.H., BLAKESLEE, R.J., VON-NEGUT, B. & BROOK, M. (1992). Lightning induced brightening in the airglow layer. *Geophys. Res. Lett.*, **19**, 99–102. 13, 56, 111, 162
- BOLTON, S.J. & THE JUNO SCIENCE TEAM (2010). The Juno Mission. *Proceedings of the International Astronomical Union*, **6**, 92. 20
- BONAVENTURA, Z., BOURDON, A., CELESTIN, S. & PASKO, V.P. (2011). Electric field determination in streamer discharges in air at atmospheric pressure. *Plasma Sources Science and Technology*, **20**, 035012. 112
- BORST, W.L. & ZIPF, E.C. (1970). Cross Section for Electron-Impact Excitation of the (0,0) First Negative Band of N_2^+ from Threshold to 3 keV. *Phys Rev. A*, **1**, 834. 235
- BORUCKI, W.J. & MCKAY, C.P. (1987). Optical efficiencies of lightning in planetary atmospheres. *Nature*, **328**, 509. 24, 150, 213, 224
- BORUCKI, W.J., LEVIN, Z., WHITTEN, R.C., KEESSE, R.G., CAPONE, L.A., TOON, O.B. & DUBACH, J. (1982). Predicted electrical conductivity between 0 and 80 km in the venusian atmosphere. *Icarus*, **30**, 302. xxviii, 152, 153, 166, 172, 197, 208
- BORUCKI, W.J., MCKAY, C.P., JEBENS, D., LAKKARAJU, H.S. & VANAJAKSHI, C.T. (1996). Spectral Irradiance Measurements of Simulated Lightning in Planetary Atmospheres. *Icarus*, **123**, 336. 150
- BOUGHER, S.W., RAFKIN, S. & DROSSART, P. (2006). Dynamics of the Venus upper atmosphere: Outstanding problems and new constraints expected from Venus Express. *Planet. Space Sci.*, **54**, 1371. 153
- BOYS, C.V. (1926). Progressive Lightning. *Nature*, **118**, 749–750. 10
- BRASSEUR, G.P. & SOLOMON, S. (1986). *Aeronomy of the Middle Atmosphere*. Reidel, Boston, Mass, 2nd edn. 236
- BRASSEUR, G.P. & SOLOMON, S. (2005). *Aeronomy of the Middle Atmosphere*. Atmospheric and Oceanographic Sciences Library, Springer, Dordrecht, Holland, 3rd edn. xxxvii, xxxviii, 249, 251
- BIGGS, M.S., FISHMAN, G.J., CONNAUGHTON, V., BHAT, P.N., PACIASAS, W.S., PREECE, R.D., WILSON-HODGE, C., CHAPLIN, V.L., KIPPEN, R.M., VON KIENLIN, A., MEEGAN, C.A., BISSALDI, E., DWYER, J.R., SMITH, D.M., HOLZWORTH, R.H., GROVE, J.E. & CHEKHTMAN, A. (2010). First results on terrestrial gamma ray flashes from the Fermi Gamma-ray Burst Monitor. *Journal of Geophysical Research*, **115**, A07323. 64
- BUDDEN, K.G. (1985). *The Propagation of Radio Waves: The Theory of Radio Waves of Low Power in the Ionosphere and Magnetosphere*. Cambridge University Press, Cambridge. 98, 163, 167
- BURCH, D.S., SMITH, S.J. & BRANSCOMB, L.M. (1958). Photodetachment of O_2^- . *Phys. Rev.*, **112**, 171. 11
- BURTON, M.E., BURATTI, B., MATSON, D.L. & LEBRETON, J.P. (2001). The Cassini/Huygens Venus and Earth flybys: An overview of operations and results. *Journal of Geophysical Research*, **106**, 30099. 189
- CACCIATORE, M., KURNOSOV, A. & NAPARTOVICH, A. (2005). Vibrational energy transfer in N_2N_2 collisions: A new semiclassical study. *J. Chem. Phys.*, **123**, 174315. 236
- CALO, J.M., AXTMANN, R.C. & CROWDER, L. (1971). Collisional Deactivation of CO_2 and CO Luminescence. *J. Chem. Phys.*, **54**, 5428. 236
- CAPITELLI, M., FERREIRA, C.M., GORDIETS, B.F. & I., O.A. (2000). *Plasma Kinetics in Atmospheric Gases*. Atomic, Optical and Plasma Physics, Springer, Berlin, Germany. xxxviii, 236, 251
- CARDESÍN MOINELO, A., ABILDGAARD, S., GARCÍA MUÑOZ, A., PICCIONI, G. & GRASSI, D. (2016). No statistical evidence of lightning in Venus night-side atmosphere from VIRTIS-Venus Express Visible observations. *Icarus*, **277**, 395. 24, 189, 191
- CARTWRIGHT, D.C., TRAJMAR, S., CHUTJIAN, A. & WILLIAMS, W. (1977). Electron impact excitation of the electronic states of N_2 . II. Integral cross sections at incident energies from 10 to 50 eV. *Phys Rev. A*, **16**, 1041. 235
- CASTILLO, M., HERRERO, V.J., MÉNDEZ, I. & TANARRO, I. (2004). Spectrometric and kinetic study of a modulated glow air discharge. *Plasma Sources. Sci. Technol.*, **13**, 343–350. 236
- CELESTIN, S. & PASKO, V.P. (2010). Effects of spatial non-uniformity of streamer discharges on spectroscopic diagnostics of peak electric fields in transient luminous events. *Geophys. Res. Lett.*, **37**, L07804. 112
- CERISIER, J.C. (1974). Ducted and partly ducted propagation of VLF waves through the magnetosphere. *Journal of Atmospheric and Terrestrial Physics*, **36**, 1443. 163, 209
- CHANG, S.C., KUO, C.L., LEE, L.J., CHEN, A.B., SU, H.T., HSU, R.R., FREY, H.U., MENDE, S.B., TAKAHASHI, Y. & LEE, L.C. (2010). ISUAL far-ultraviolet events, elves, and lightning current. *J. Geophys. Res. (Space Phys)*, **115**, A00E46. 57

- CHANRION, O., NEUBERT, T., MOGENSEN, A., YAIR, Y., STENDEL, M., SINGH, R. & SINGH, D. (2017). Profuse activity of blue electrical discharges at the tops of thunderstorms. *Geophys. Res. Lett.*, **44**, 496. xii, 17
- CHAPMAN, S. & COWLING, T.G. (1970). *The mathematical theory of non-uniform gases: an account of the kinetic theory of viscosity, thermal conduction and diffusion in gases*. Cambridge university press. 35
- CHEN, R.H. & NAGY, A.F. (1978). A comprehensive model of the Venus ionosphere. *Journal of Geophysical Research*, **83**, 1133. xxxvii, xxxviii, 249, 251
- CHERN, J.L., HSU, R.R., SU, H.T., MENDE, S.B., FUKUNISHI, H., TAKAHASHI, Y. & LEE, L.C. (2003). Global survey of upper atmospheric transient luminous events on the ROCSAT-2 satellite. *J. Atm. Sol.-Terr. Phys.*, **65**, 647. xxxv, 112, 137
- CHERN, J.L., WU, A.M. & LIN, S.F. (2014). Globalization extension of transient luminous events from FORMOSAT-2 observation. *Acta Astronautica*, **98**, 64. xi, 11, 12, 14, 15, 17, 57, 64, 77
- CHRISTIAN, H.J., BLAKESLEE, R.J., BOCCIPPIO, D.J., BOECK, W.L., BUECHLER, D.E., DRISCOLL, K.T., GOODMAN, S.J., HALL, J.M., KOSHAK, J.M., MACH, D.M. & STEWART, M.F. (2003). Global frequency and distribution of lightning as observed from space by the Optical Transient Detector. *Journal of Geophysical Research*, **108**, ACL 4-1. xi, 7, 8
- CLEMMOW, P.C. & HEADING, J. (1954). Coupled forms of the differential equations governing radio propagation in the ionosphere. In *Mathematical Proceedings of the Cambridge Philosophical Society*, vol. 50, 319-333, Cambridge University Press. 98
- COHEN, I.B. (1941). *Benjamin Franklin's Experiments: A New Edition of Franklin's Experiments and Observations on Electricity*. Springer, Dordrecht, Holland. 1
- COLE, K.D. & HOEGY, W.R. (1997). Nonlinear whistlers: Implications for 100 Hz electric fields observed in the Venus ionosphere. *Journal of Geophysical Research*, **102**, 14615. 23, 149
- COLIN, L. (1980). The Pioneer Venus Program. *Journal of Geophysical Research*, **85**, 7575. 199
- COOK, A.F., DUXBURY, T.C. & HUNT, G.E. (1979). First results on Jovian lightning. *Nature*, **280**, 794. 19, 211
- CUMMER, S.A., BRIGGS, M.S., DWYER, J.R., XIONG, S., CONNAUGHTON, V., FISHMAN, G.J., LU, G., LYU, F. & SOLANKI, R. (2014). The source altitude, electric current, and intrinsic brightness of terrestrial gamma ray flashes. *Geophys. Res. Lett.*, **41**, 8586. 9, 57, 64
- DAGDIGIAN, P.J., FORCH, B.E. & MIZIOLEK, W. (1988). Collisional transfer between and quenching of the 3p 3P and 5P states of the oxygen atom. *Chem. Phys. Lett.*, **148**, 299. xxxviii, 236, 251
- DORMAND, J.R. & PRINCE, P.J. (1980). A family of Runge-Kutta formulae. *Journal of Computational and Applied Mathematics*, **6**, 19. 35, 37
- DUBROVIN, D., NIJDAM, S., VAN VELDHUIZEN, E.M., EBERT, U., YAIR, Y. & PRICE, C. (2010). Sprite discharges on Venus and Jupiter-like planets: A laboratory investigation. *J. Geophys. Res. (Space Phys)*, **115**, A00E34. 150, 212
- DUBROVIN, D., LUQUE, A., GORDILLO-VÁZQUEZ, F.J., YAIR, Y., PARRA-ROJAS, F.C., EBERT, U. & PRICE, C. (2014a). Impact of lightning on the lower ionosphere of Saturn and possible generation of halos and sprites. *Icarus*, **241**, 313-328. 159
- DUBROVIN, D., LUQUE, A., GORDILLO-VÁZQUEZ, F.J., YAIR, Y., PARRA-ROJAS, F.C., EBERT, U. & PRICE, C. (2014b). Impact of lightning on the lower ionosphere of Saturn and possible generation of halos and sprites. *Icarus*, **241**, 313. 212, 214
- DWYER, J.R., RASSOUL, H.K., SALEH, Z., UMAN, M.A., JERGAULD, J. & PLUMER, J.A. (2005). X-ray bursts produced by laboratory sparks in air. *Geophys. Res. Lett.*, **32**, L20809. 4
- DYUDINA, U.A., DEL GENIO, A., INGERSOLL, A.P., PORCO, C.C., WEST, R.A., VASAVADA, A.R. & BARBARA, J.M. (2004). Lightning on Jupiter observed in the H α line by the Cassini imaging science subsystem. *Icarus*, **172**, 24. 20, 224
- DYUDINA, U.A., INGERSOLL, A.P., EWALD, S.P., PORCO, C.C., FISCHER, G., KURTH, W.S. & WEST, R.A. (2010). Detection of visible lightning on Saturn. *Geophys. Res. Lett.*, **37**, L09205. 20, 211, 213, 216, 217, 224
- DYUDINA, U.A., INGERSOLL, A.P., EWALD, S.P., PORCO, C.C., FISCHER, G. & YAIR, Y. (2013). Saturn's visible lightning, its radio emissions, and the structure of the 2009-2011 lightning storms. *Icarus*, **226**, 1020. 20, 211, 213, 216, 217, 224
- ERDMAN, P.W. & ZIPP, E.C. (1987). Excitation of the OI (3s 5 S 0-3p 5 P; 7774 Å) multiplet by electron impact on CO $_2$. *Journal Chemical Physics*, **87**, 4540. xxxviii, 235, 251
- EVERETT, W.H. (1903). Rocket Lightning. *Nature*, **68**, 599. 10
- FAHR, H. & MÜLLER, K.G. (1967). Ionenbewegung unter dem Einfluß von Umladungsstößen. *Zeitschrift für Physik A Hadrons and Nuclei*, **200**, 343. 34
- FILSETH, S.V., STUHL, F. & WELGE, K.H. (1970). Collisional deactivation of O (1 S). *Journal Chemical Physics*, **52**, 239. xxxviii, 251

REFERENCES

- FISCHER, G., KURTH, W.S., DYUDINA, U.A., KAISER, M.L., ZARKA, P., LECACHEUX, A., INGERSOLL, A.P. & GURNETT, D.A. (2007). Analysis of a giant lightning storm on Saturn. *Icarus*, **190**, 528. 213
- FISCHER, G., GURNETT, D.A., KURTH, A.F., ZARKA, P., DYUDINA, U.A., FARRELL, W.M. & KAISER, M.L. (2008). Atmospheric Electricity at Saturn. *Space Science Reviews*, **137**, 271. xii, 20, 23, 213
- FISHMAN, G.J., BHAT, P.N., MALLOZZI, R., HORACK, J.M., KOSHUT, T., KOUVELIOTOU, C., PENDLETON, G.N., MEEGAN, C.A., WILSON, R.B., PACIESAS, W.S., GOODMAN, S.J. & CHRISTIAN, H.J. (1994). Discovery of Intense Gamma-Ray Flashes of Atmospheric Origin. *Science*, **264**, 1313. 9
- FRANZ, R.C., NEMZEK, R.J. & WINCKLER, J.R. (1990). Television Image of a Large Upward Electrical Discharge Above a Thunderstorm System. *Science*, **249**, 48. xi, 11, 12
- FREY, H.U., MENDE, S.B., CUMMER, S.A., LI, J., ADACHI, T., FUKUNISHI, H., TAKAHASHI, Y., CHEN, A.B., HSU, R.R., SU, H.T. & CHANG, Y.S. (2007). Halos generated by negative cloud-to-ground lightning. *Geophys. Res. Lett.*, **34**, L18801. 52
- FUKUNISHI, H., TAKAHASHI, Y., KUBOTA, M., SAKANOI, K., INAN, U.S. & LYONS, W.A. (1996). Elves: Lightning-induced transient luminous events in the lower ionosphere. *Geophys. Res. Lett.*, **23**, 2157. 162
- GALAND, L., MOORE, L., CHARNAY, B., MUELLER-WODARG, I. & MENDILLO, M. (2009). Solar primary and secondary ionization at Saturn. *Journal of Geophysical Research*, **114**, A06313. 215
- GAOPENG, L., BLAKESLEE, R.J., JINGBO, L., SMITH, D.M., SHAO, X.M., MCCAUL, E.W., BUECHLER, D.E., CHRISTIAN, H.J., HALL, J.M. & CUMMER, S.A. (2010). Lightning mapping observation of a terrestrial gamma-ray flash. *Geophys. Res. Lett.*, **37**, L11806. 160
- GARCÍA MUÑOZ, A.L., HUESO, R., SÁNCHEZ-LAVEGA, A., MARKIEWICZ, W.J., TITOV, D.V., WITASSE, O. & OPITZ, A. (2013). Limb imaging of the Venus O_2 visible nightglow with the Venus Monitoring Camera. *Geophys. Res. Lett.*, **40**, 2539. 23
- GIBNEY, E. (2016). Rescued Japanese spacecraft delivers first results from Venus. *Nature*, **532**, 157. 191
- GILLI, G., LÓPEZ-VALVERVE, M.A., FUNKE, B., LÓPEZ-PUERTAS, M., DROSSART, P., PICCIONI, G. & FORMISANO, V. (2011). Non-LTE CO limb emission at 4.7 μm in the upper atmosphere of Venus, Mars and Earth: Observations and modeling. *Planet. Space Sci.*, **59**, 1010. 153
- GILMORE, F.R., LAHER, R.R. & ESPY, P.J. (1992). Franck-Condon Factors, r-Centroids, Electronic Transition Moments, and Einstein Coefficients for Many Nitrogen and Oxygen Band Systems. *J. Phys. Chem. Ref. Data*, **21**, 1005. xxxviii, 236, 251
- GOODMAN, S.J., BLAKESLEE, R.J., KOSHAK, J.M., MACH, D., BAILEY, J., BUECHLER, D., CAREY, L., SCHULTZ, C., BATEMAN, M., MCCAUL, E. & OTHERS (2013). The GOES-R geostationary lightning mapper (GLM). *Atmospheric research*, **125**, 34–49. 8
- GORDIETS, B.F., FERREIRA, C.M., GUERRA, V.L., LOUREIRO, J.M.A.H., NAHORNY, J., PAGNON, D., TOUZEAU, M. & VIALLE, M. (1995). Kinetic model of a low-pressure N_2 - O_2 flowing glow discharge. *IEEE Trans. Plasma Sci.*, **23**, 750. 236
- GORDILLO-VÁZQUEZ, F.J. (2008). Air plasma kinetics under the influence of sprites. *J. Phys. D*, **41**, 234016. xxxvii, xxxviii, 11, 56, 58, 59, 60, 249, 251
- GORDILLO-VÁZQUEZ, F.J. (2010). Vibrational kinetics of air plasmas induced by sprites. *J. Geophys. Res - Space Phys.*, **115**, A00E25. 56, 60, 235, 236
- GORDILLO-VÁZQUEZ, F.J., LUQUE, A. & SIMEK, M. (2011). Spectrum of sprite halos. *J. Geophys. Res. (Space Phys)*, **116**, A09319. 55, 56, 88, 89
- GORDILLO-VÁZQUEZ, F.J., LUQUE, A. & SIMEK, M. (2012). Near infrared and ultraviolet spectra of TLEs. *J. Geophys. Res. (Space Phys)*, **117**, A05329. 56, 66, 88, 89
- GORDILLO-VÁZQUEZ, F.J., LUQUE, A. & HALDOUPIS, C. (2016). Upper D region chemical kinetic modeling of LORE relaxation times. *Journal of Geophysical Research: Space Physics*, **121**, 3525–3544. 57
- GRAY, C.L., CHANOVER, N.J., SLANGER, T.G. & MOLAVERDIKHANI, K. (2014). The effect of solar flares, coronal mass ejections, and solar wind streams on Venus' 5577 Å oxygen green line. *Icarus*, **233**, 342. 171, 176, 192
- GUDMUNDSSON, J.T., KOUZNETSOV, I.G., PATEL, K.K. & LIEBERMAN, M.A. (2001a). Electronegativity of low-pressure high-density oxygen discharges. *Journal of Physics D: Applied Physics*, **34**, 1100. 236
- GUDMUNDSSON, J.T., KOUZNETSOV, I.G., PATEL, K.K. & LIEBERMAN, M.A. (2001b). Electronegativity of low-pressure high-density oxygen discharges. *Journal of Physics D: Applied Physics*, **34**, 1100. 236
- GUERRA, V. & LOUREIRO, J. (1999). Kinetic model of a low-pressure microwave discharge in O_2 - H_2 including the effects of O^- ions on the characteristics for plasma maintenance. *Plasma Sour. Sci. Technol.*, **8**, 110. 236
- GUREVICH, A.V. & ZYBIN, K.P. (2001). Runaway breakdown and electric discharges in thunderstorms. *Physics Uspekhi*, **44**, 1119. 4
- GUREVICH, A.V., MILIKH, G.M. & ROUSSEL-DUPRE, R. (1992). Runaway electron mechanism of air breakdown and preconditioning during a thunderstorm. *Phys. Lett. A*, **165**, 463. 4

- GURNETT, D.A., SHAW, R.R., ANDERSON, R.R., KURTH, W.S. & SCARF, F.L. (1979). Whistlers observed by Voyager 1: Detection of lightning on Jupiter. *Geophys. Res. Lett.*, **6**, 511. 19, 211
- GURNETT, D.A., KURTH, W.S., CAIRNS, I.H. & GRANROTH, L.J. (1990). Whistlers in Neptune's magnetosphere: Evidence of atmospheric lightning. *Journal of Geophysical Research*, **95**, 20967. 19, 212
- GURNETT, D.A., KURTH, W.S., ROUX, A., GENDRIN, R., KENNEL, C.F. & BOLTON, S.J. (1991). Lightning and plasma wave observations from the Galileo flyby of Venus. *Science*, **253**, 1522. 23
- GURNETT, D.A., ZARKA, P., MANNING, R., KURTH, W.S., HOSPODARSKY, G.B., AVERKAMP, T.F., KAISER, M.L. & FARRELL, W.M. (2001). Non-detection at Venus of high-frequency radio signals characteristic of terrestrial lightning. *Nature*, **409**, 313. 23
- HAGELAAR, G.J.M. & PITCHFORD, L.C. (2005). Solving the Boltzmann equation to obtain electron transport coefficients and rate coefficients for fluid models. *Plasma Sour. Sci. Technol.*, **14**, 722. xiii, xxiv, xxx, 53, 60, 114, 155, 156, 163, 215
- HAMPTON, D.L., HEAVNER, M.J., WESCOTT, E.M. & SENTMAN, D.D. (1996). Optical spectral characteristics of sprites. *Geophys. Res. Lett.*, **23**, 89. 56
- HANSELL, S.A., WELLS, W.K. & HUNTEN, D.M. (1995). Optical detection of lightning on Venus. *Icarus*, **117**, 345. 23
- HANSON, R.J. (1971). A numerical method for solving Fredholm integral equations of the first kind using singular values. *SIAM Journal on Numerical Analysis*, **8**. 122, 123
- HELLING, C., JARDINE, M., STARK, C. & DIVER, D. (2013). Ionization in atmospheres of brown dwarfs and extrasolar planets. III. Breakdown conditions for mineral clouds. *The Astrophysical Journal*, **767**, 136. 26
- HELLIWELL, R.A. (1965). *Whistlers and related ionospheric phenomena*, vol. 50. Stanford University Press, Stanford. 9, 97, 163, 209
- HERRON, J.T. & GREEN, D.S. (2001). Chemical Kinetics Database and Predictive Schemes for Nonthermal Humid Air Plasma Chemistry. Part II. Neutral Species Reactions. *Plasma Chemistry and Plasma Processing*, **21**, 459–481. 236
- HINSON, D.P., FLASAR, F.M., KLIORÉ, A.J., SCHINDER, P.J., TWICKEN, J.D. & HERRERA, R.G. (1997). Jupiter's ionosphere: Results from the first Galileo radio occultation experiment. *Geophys. Res. Lett.*, **24**, 2107. 215
- HO, C.M., STRANGWAY, R.J. & RUSSELL, C.T. (1991). Occurrence Characteristics of VLF bursts in the nightside ionosphere of Venus. *Journal of Geophysical Research*, **96**, 21,361. 208
- HOLDER, T., SIMEK, M., BONAVENTURA, Z., PRUKNER, V. & GORDILLO-VÁZQUEZ, F.J. (2016). Radially and temporally resolved electric field of positive streamers in air and modelling of the induced plasma chemistry. *Plasma Sources Science and Technology*, **25**, 045021. 113
- HU, W., CUMMER, S.A. & LYONS, W.A. (2007). Testing sprite initiation theory using lightning measurements and modeled electromagnetic fields. *J. Geophys. Res. (Atmos.)*, **112**, D13115. 61
- HUBA, J.D. (1992). Theory of small scale density and electric field fluctuations in the nightside Venus ionosphere. *Journal of Geophysical Research*, **97**, 149, 163
- HUBA, J.D. & ROWLAND, H.L. (1993). Propagation of electromagnetic waves parallel to the magnetic field in the nightside Venus ionosphere. *Journal of Geophysical Research*, **98**, 149, 163, 208
- HUNTEN, D.M., ROACH, F.E. & CHAMBERLAIN, J.W. (1956). A photometric unit for the airglow and aurora. *Journal of Atmospheric and Terrestrial Physics*, **8**, 345. 176
- INAN, U. & MARSHALL, R.A. (2011). *Numerical Electromagnetics: The FDTD Method*. Cambridge Univ. Press, New York. xii, xiii, 32, 37, 38, 39, 40, 42, 43, 45, 46
- INAN, U.S., BELL, T.F. & RODRIGUEZ, J.V. (1991). Heating and ionization of the lower ionosphere by lightning. *Geophys. Res. Lett.*, **18**, 705. 32, 37, 57
- INAN, U.S., BARRINGTON-LEIGH, C., HANSEN, S., GLUKHOV, V.S., BELL, T.F. & RAIKIDEN, R. (1997). Rapid lateral expansion of optical luminosity in lightning-induced ionospheric flashes referred to as 'elves'. *Geophys. Res. Lett.*, **24**, 583. 56
- ISRAELEVICH, P.L., YAIR, Y., DEVIR, A.D., JOSEPH, J.H., LEVIN, Z., MAYO, I., MOALEM, M., PRICE, C., ZIV, B. & STERNLIEB, A. (2004). Transient airglow enhancements observed from the space shuttle Columbia during the MEIDEX sprite campaign. *Geophys. Res. Lett.*, **31**, L06124. 162
- ITIKAWA, Y. (2002). Cross sections for electron collisions with carbon dioxide. *Journal of Physical and Chemical Reference Data*, **31**, 749. xxxviii, 251
- ITIKAWA, Y. (2006). Cross sections for electron collisions with nitrogen molecules. *Journal of Physical and Chemical Reference Data*, **35**, 31. xxxviii, 251
- JACKSON, J.D. (1962). *Classical Electrodynamics*. John Wiley & Sons, Ltd. 51
- JACKSON, T.L. & FARRELL, W.M. (2006). Electrostatic fields in dust devils: an analog to Mars. *IEEE Transactions on Geoscience and Remote Sensing*, **44**, 2942. 26

REFERENCES

- KAISER, M.L., DESCH, M.D., FARRELL, W.M. & ZARKA, P. (1991). Restrictions on the characteristics of Neptunian lightning. *Journal of Geophysical Research*, **96**, 19043. 19, 212
- KAM, A.W. & PIPKIN, F.M. (1991). Measurement of the lifetime of the metastable $a^1\Sigma_g^+$ state of N_2 . *Phys. Rev. A*, **43**, 3279. 236
- KAMARATOS, E. (2006). Active nitrogen and oxygen: Enhanced emissions and chemical reactions. *Chem. Phys.*, **323**, 271. 236
- KANMAE, T., STENBAEK-NIELSEN, H.C. & MCHARG, M.G. (2007). Altitude resolved sprite spectra with 3 ms temporal resolution. *Geophys. Res. Lett.*, **34**, L07810. xviii, 11, 56, 89, 90
- KASEMIR, H.W. (1959). The thunderstorm as a generator in the global electric circuit. *Z. Geophys.*, **25**, 1
- KAZIL, J., KOPP, E., CHABRILLAT, S. & BISHOP, J. (2003). The University of Bern Atmospheric Ion Model: Time-dependent modeling of the ions in the mesosphere and lower thermosphere. *Journal of Geophysical Research: Atmospheres*, **108**. 236
- KOSSYL, I.A., KOSTINSKY, A.Y., MATVEYEV, A.A. & SILAKOV, V.P. (1992). Kinetic scheme of the non-equilibrium discharge in nitrogen-oxygen mixtures. *Plasma Sour. Sci. Technol.*, **1**, 207. 59, 236
- KOVACS, I. (1969). *Rotational Structure in the Spectra of Diatomic Molecules*. American Elsevier, New York, USA. 66
- KRASNOPOLSKY, V.A. (1980). On Lightnings in the Venus Atmosphere According to the Venera 9 and 10 data. *Cosmic Res.*, **18**, 556. 22, 150, 159, 171, 172, 208
- KRASNOPOLSKY, V.A. (2006). A sensitive search for nitric oxide in the lower atmospheres of Venus and Mars: Detection on Venus and upper limit for Mars. *Icarus*, **182**, 80. 23
- KRASNOPOLSKY, V.A. (2010). Venus night airglow: Ground-based detection of OH, observations of O_2 emissions, and photochemical model. *Icarus*, **207**, 17. 153
- KRAUS, J.D. (1956). Impulsive radio signals from the planet Venus. *Nature*, **178**, 33. 22
- KREHBIEL, P. (1986). *The electrical structure of thunderstorms*. Studies in Geophysics, National Academic Press, 2101 Constitution Avenue, N.W. xi, 3
- KREHBIEL, P.R., RIOUSSET, J.A., PASKO, V.P., THOMAS, R.J., RISON, W., STANLEY, M.A. & EDENS, H.E. (2008). Upward electrical discharges from thunderstorms. *Nature Geoscience*, **1**, 233. 16
- KREMNEV, R.S. & THE VEGA BALLOON SCIENCE TEAM (1987). Vega balloon system and instrumentation. *Adv. Space Res.*, **7**, (12)307. 189
- KRUPENIE, P.H. (1972). The spectrum of Molecular Oxygen. *J. Phys. Chem. Ref. Data.*, **1**. 236
- KSANFOMALITI, L.V. (1980). Discovery of frequent lightning discharges in clouds on Venus. *Nature*, **284**, 244. 22
- KSANFOMALITI, L.V., VASILCHIKOV, N.M., GANPANTSEROVA, O.F., PETROVA, E.V. & SUVOROV, A.P. (1979). Electrical discharges in the atmosphere of Venus. *Soviet Astronomy Letters*, **5**, 122. 22
- KUO, C.L., CHEN, A.B., LEE, Y.J., TSAI, L.Y., CHOU, R.K., HSU, R.R., SU, H.T., LEE, L.C., CUMMER, S.A., FREY, H.U., MENDE, S.B., TAKAHASHI, Y. & FUKUNISHI, H. (2007). Modeling elves observed by FORMOSAT-2 satellite. *J. Geophys. Res. (Space Phys)*, **112**, A11312. 32, 37, 56, 57, 64, 77, 147
- KUO, C.L., WILLIAMS, E., BÓR, J., LIN, Y.H., LEE, L.J., HUANG, S.M., CHOU, J.K., CHEN, A.B., SU, H.T., HSU, R.R., SÁTORI, G., FREY, H.U., MENDE, S.B., TAKAHASHI, Y. & LEE, L.C. (2013). Ionization emissions associated with $N_2^+ 1N$ band in halos without visible sprite streamers. *Journal of Geophysical Research*, **118**, 5317. 52, 74, 75
- KURNOSOV, A., NAPARTOVICH, A., SHNYREV, S. & CACCIA-TORE, M. (2007). Vibrational energy exchanges in nitrogen: Application of new rate constants for kinetic modeling. *J. Phys. Chem. A*, **111**, 7057–7065. 236
- KURTH, W.S., HOSPODARSKY, G.B., GURNETT, D.A., KAISER, M.L., WAHLUND, J.E., ROUX, A., CANU, P., ZARKA, P. & TOKAREV, Y. (2001). An overview of observations by the Cassini radio and plasma wave investigation at Earth. *Journal of Geophysical Research*, **106**, 30239. 9
- LAHER, R.R. & GILMORE, F.R. (1990). Updated excitation and ionization cross sections for electron impact on atomic oxygen. *Journal of Physical and Chemical Reference Data*, **19**, 277. xxxviii, 236, 251
- LAWTON, S.A. & PHELPS, A.V. (1978). Excitation of the $b^1\Sigma_g^+$ state of O_2 by low energy electrons. *J. Chem. Phys.*, **69**, 1055. 235
- LEE, J.H. & KALLURI, D.K. (1999). Three-dimensional FDTD simulation of electromagnetic wave transformation in a dynamic inhomogeneous magnetized plasma. *IEEE Transactions on Antennas and Propagation*, **47**, 1146. xiii, 37, 38, 40, 41, 42, 43, 44, 45, 46, 47
- LEHTINEN, N.G. & INAN, U.S. (2008). Radiation of ELF/VLF waves by harmonically varying currents into a stratified ionosphere with application to radiation by a modulated electrojet. *J. Geophys. Res - Space Phys.*, **113**, A06301. 27, 28, 97, 98, 151, 193, 196, 229

- LEHTINEN, N.G. & INAN, U.S. (2009). Full-wave modeling of transionospheric propagation of VLF waves. *Geophys. Res. Lett.*, **115**, A00E40. 98, 193, 196
- LEHTINEN, N.G., MARSHALL, R.A. & INAN, U.S. (2010). Full-wave modeling of early VLF perturbations caused by lightning electromagnetic pulses. *J. Geophys. Res. (Space Phys)*, **115**, A00E40. 98, 193, 196
- LELLOUCH, E., CLANCY, T., CRISP, D., KLIORE, A.J., TITOV, D. & BOUGHER, S.W. (1997). *Monitoring of Mesospheric Structure and Dynamics. In: Venus-II*, vol. 142. University of Arizona Press, Tucson, AZ. 153
- LEPOUTRE, F., LOUIS, G. & MANCEAU, H. (1977). Collisional relaxation in CO₂ between 180 K and 400 K measured by the spectrophone method. *Chem. Phys. Lett.*, **48**, 509. xxxviii, 236, 252
- LINSTROM, P.J. & MALLARD, W.G. (2015). NIST chemistry webbook. NIST standard reference database 69. National Institute of Standards and Technology. 236
- LITTLE, B., ANGER, C.D., INGERSOLL, A.P., VASAVADA, A.R., SENSKE, D.A., BRENNEMAN, H.H., BORUCKI, W.J. & THE GALILEO SSI TEAM (1999). Galileo Images of Lightning on Jupiter. *Icarus*, **142**, 306. xii, 19, 20, 224
- LIU, N., DWYER, J.R., STENBAEK-NIELSEN, H.C. & MCHARG, M.G. (2015). Sprite streamer initiation from natural mesospheric structures. *Nature Communications*, **6**, 7540. 31
- LIU, N., DWYER, J.R. & CUMMER, S.A. (2017). Elves Accompanying Terrestrial Gamma Ray Flashes. *Journal of Geophysical Research: Space Physics*, **122**, 10,563–10,576, 2017JA024344. 9, 32, 37, 57, 64, 69, 70, 84
- LOI, S.T., MURPHY, T., CAIRNS, I.H., MENK, F.W., WATERS, C.L., ERICKSON, P.J., TROTT, C.M., HURLEY-WALKER, N., MORGAN, J., LENC, E., OFFRINGA, A.R., BELL, M.E., EKBERS, R.D., GAENSLER, B.M., LONSDALE, C.J., FENG, L., HANCOCK, P.J., KAPLAN, D.L., BERNARDI, G., BOWMAN, J.D., BRIGGS, F., CAPPALLO, R.J., DESHPANDE, A.A., GREENHILL, L.J., HAZELTON, B.J., JOHNSTON-HOLLITT, M., McWHIRTER, S.R., MITCHELL, D.A., MORALES, M.F., MORGAN, E., OBEROI, D., ORD, S.M., PRABU, T., SHANKAR, N.U., SRIVANI, K.S., SUBRAHMANYAN, R., TINGAY, S.J., WAYTH, R.B., WEBSTER, R.L., WILLIAMS, A. & WILLIAMS, C.L. (2015). Real-time imaging of density ducts between the plasmasphere and ionosphere. *Journal of Atmospheric and Terrestrial Physics*, **42**, 3707. 163, 209
- LÓPEZ-VALVERDE, M.A. (1990). *Emisiones infrarrojas en la atmósfera de Marte*. Ph.D. thesis, Universidad de Granada. xxxviii, 252
- LOPEZ-VALVERDE, M.A., DROSSART, P., CARLSON, R., MEHLMAN, R. & ROSS-SEROTE, M. (2007). Non-LTE infrared observations at Venus: From NIMS/Galileo to VIRTIS/Venus Express. *Planet. Space Sci.*, **55**, 1757. 153, 171, 193
- LUQUE, A. & EBERT, U. (2009). Emergence of sprite streamers from screening-ionization waves in the lower ionosphere. *Nature Geoscience*, **2**, 757. 31, 55, 56
- LUQUE, A. & GORDILLO-VÁZQUEZ, F.J. (2011). Mesospheric electric breakdown and delayed sprite ignition caused by electron detachment. *Nature Geoscience*, **4**, 52, 59
- LUQUE, A., DUBROVIN, D., GORDILLO-VÁZQUEZ, F.J., EBERT, U., PARRA-ROJAS, F.C., YAIR, Y. & PRICE, C. (2014). Coupling between atmospheric layers in gaseous giant planets due to lightning-generated electromagnetic pulses. *J. Geophys. Res. (Space Phys)*, **119**, 8705. xxxi, 32, 37, 38, 41, 212, 214, 216, 219, 223, 224, 229
- LUQUE, A., GORDILLO-VÁZQUEZ, F.J. & PAYÉ, E. (2015). Ground-based search for lightning in Jupiter with GTC/OSIRIS fast photometry and tunable filters. *Astronomy and Astrophysics*, **577**, A92. 20
- LYU, F., CUMMER, S.A. & McTAGUE, L. (2015). Insights into high peak current in-cloud lightning events during thunderstorms. *Geophys. Res. Lett.*, **42**, 6836. 9, 57, 64
- MACKENZIE, T. & TOYNBEE, H. (1886). Meteorological Phenomena. *Nature*, **33**, 245. 10
- MAGGIO, C.R., MARSHALL, T.C. & STOLZENBURG, M. (2009). Estimations of charge transferred and energy released by lightning flashes. *J. Geophys. Res.*, **114**, D14203. 62, 159, 172
- MAKHLouF, U.B., PICARD, R.H. & WINICK, J.R. (1995). Photochemical-dynamical modeling of the measured response of airglow to gravity waves 1. Basic model for OH airglow. *J. Geophys. Res.*, **100**, 11289. 236
- MALAN, D.J. (1937). Sur les Décharges Orageuses dans la Haute Atmosphère. *C. R. Acad. Sci.*, **205**, 812–813. 10
- MARKIEWICZ, W.J., TITOV, D.V., LIMAYE, S.S., KELLER, H.U., IGNATIEV, N., JAUMANN, R., THOMAS, N., MICHALIK, H., MOISSL, R. & RUSSO, P. (2007). Morphology and dynamics of the upper cloud layer of Venus. *Nature*, **450**, 633. 156
- MARSHALL, R.A., INAN, U.S. & GLUKHOV, V.S. (2010). Elves and associated electron density changes due to cloud-to-ground and in-cloud lightning discharges. *J. Geophys. Res. (Space Phys)*, **115**, A00E17. 32, 37, 57, 187, 222
- MARSHALL, R.A., DA SILVA, C.L. & PASKO, V.P. (2015). Elve doublets and compact intracloud discharges. *Geophys. Res. Lett.*, **42**, 6112. 32, 37, 69, 84

REFERENCES

- MARUBASHI, K., GREBOWSKY, J.M. & TAYLOR, H.A. (1985). Magnetic field in the wake of Venus and the formation of ionospheric holes. *Journal of Geophysical Research*, **90**, 1385. 163, 194, 208
- MCDANIEL, E.W. & MASON, E.A. (1973). *The mobility and diffusion of ions in gases*. 166
- MENDE, S.B., FREY, H.U., HSU, R.R., SU, H.T., CHEN, A.B., LEE, L.C., SENTMAN, D.D., TAKAHASHI, Y. & FUKUNISHI, H. (2005). D region ionization by lightning-induced electromagnetic pulses. *J. Geophys. Res. (Space Phys)*, **110**, A11312. 137
- MEZENTSEV, A., LEHTINEN, N., ØSTGAARD, N., PÉREZ-INVERNÓN, F.J. & CUMMER, S.A. (2018). Spectral Characteristics of VLF Sferics Associated With RHESSI TGFs. *Journal of Geophysical Research: Atmospheres*, n/a–n/a, 2017JD027624. 29, 110, 230
- MICHAEL, M., TRIPATHI, S.N., BORUCKI, W.J. & WHITTEN, R.C. (2009). Highly charged cloud particles in the atmosphere of Venus. *Journal of Geophysical Research*, **114**, E04008. 152, 153, 156, 166, 208
- MONTIJN, C., HUNSDORFER, W. & EBERT, U. (2006). An adaptive grid refinement strategy for the simulation of negative streamers. *J. Comput. Phys.*, **219**, 801. 35, 62
- MOORE, L., MENDILLO, M., MÜLLER-WODARG, I.C.F. & MURR, D.L. (2004). Modeling of global variations and ring shadowing in Saturn's ionosphere. *Icarus*, **172**, 503. 215
- MORRILL, J.S. & BENESCH, W.M. (1996). Auroral N₂ emissions and the effect of collisional processes on N₂ triplet state vibrational populations. *J. Geophys. Res.*, **101**, 261. 236
- MORRILL, W.L. (2000). Electron collision data for plasma chemistry modeling. *Advances In Atomic, Molecular, and Optical Physics*, **43**, 7935. 235
- MORUZZI, J.L., EKIN JR, J.W. & PHELPS, A.V. (1968). Electron Production by Associative Detachment of O⁻ Ions with NO, CO, and H₂. *The Journal of Chemical Physics*, **48**, 3070. 59, 78
- MOUDRY, D., STENBAEK-NIELSEN, H., SENTMAN, D. & WESCOTT, E. (2003). Imaging of elves, halos and sprite initiation at 1ms time resolution. *J. Atm. Sol.-Terr. Phys.*, **65**, 509. 52, 56
- NAG, A., MURPHY, M.J., SCHULZ, W. & CUMMINS, K.L. (2015). Lightning locating systems: Insights on characteristics and validation techniques. *Earth and Space Science*, **2**, 65–93, 2014EA000051. 8, 9, 97
- NAULT, B.A., LAUGHNER, J.L., WOOLDRIDGE, P.J., CROUNSE, J.D., DIBB, J., DISKIN, G., PEISCHL, J., PODOLSKIE, J.R., POLLACK, I.B., RYERSON, T.B., SCHEUER, E., WENNBERG, P.O. & COHEN, R.C. (2017). Lightning NO_x Emissions: Reconciling Measured and Modeled Estimates With Updated NO_x Chemistry. *Geophysical Research Letters*, **44**, 9479–9488, 2017GL074436. 77, 78
- NEUBERT, T., KUVVETLI, I., BUDTZ-JØRGENSEN, C., ØSTGAARD, N., REGLERO, V. & ARNOLD, N. (2006). The atmosphere-space interactions monitor (ASIM) for the international space station. *xxxv*, **12**, 112, 137
- NEUBERT, T., CHANRION, O., ARNONE, E., ZANOTTI, F., CUMMER, S., LI, J., FÜLLERKRUG, M., SOULA, S. & VAN DER VELDE, O. (2011). The properties of a gigantic jet reflected in a simultaneous sprite: Observations interpreted by a model. *J. Geophys. Res. (Space Phys)*, **116**, A12329. 31
- NICKOLAENKO, A.P. & HAYAKAWA, M. (2002). *Resonances in the Earth-ionosphere cavity*, vol. 19. Springer Science & Business Media. xi, 10, 97
- NORDHEIM, T.A., DARTNELL, L.R., DESORGHIER, L., COATES, A.J. & JONES, G.H. (2015). Ionization of the venusian atmosphere from solar and galactic cosmic rays. *Icarus*, **245**, 80. xxxvii, 153, 155, 249
- ORR, B.J. & SMITH, I.M. (1987). Collision-induced vibrational energy transfer in small polyatomic molecules. *J. Phys. Chem.*, **91**, 6106. xxxviii, 252
- PAGNON, D., AMORIN, J., NAHORNY, J., TOUZEAU, M. & VIALLE, M. (1995). On the use of actinometry to measure the dissociation in O₂ DC glow discharges: determination of the wall recombination probability. *Journal of Physics D: Applied Physics*, **28**, 1856. xxxviii, 235, 251
- PANCHESHNYI, S. (2013). Effective ionization rate in nitrogen-oxygen mixtures. *J. Appl. Phys. D*, **46**, 155201. 34, 59, 236
- PARIS, P., AINTS, M., VALK, F., PLANK, T., HALJASTE, A., KOZLOV, K.V. & WAGNER, H.E. (2005). Intensity ratio of spectral bands of nitrogen as a measure of electric field strength in plasmas. *J. Phys. D*, **38**, 3894. 112
- PARRA-ROJAS, F.C., LUQUE, A. & GORDILLO-VÁZQUEZ, F.J. (2013a). Chemical and electrical impact of lightning on the Earth mesosphere: The case of sprite halos. *J. Geophys. Res - Space Phys.*, **118**, 1–25. 56, 58, 59, 60
- PARRA-ROJAS, F.C., PASSAS, M., CARRASCO, E., LUQUE, A., TANARRO, I., SIMEK, M. & GORDILLO-VÁZQUEZ, F.J. (2013b). Spectroscopic diagnostics of laboratory air plasmas as a benchmark for spectral rotational (gas) temperature determination in TLEs. *J. Geophys. Res - Space Phys.*, **118**, 4649. 66
- PARRA-ROJAS, F.C., LUQUE, A. & GORDILLO-VÁZQUEZ, F.J. (2014). Chemical and thermal impacts of sprite streamers in the Earth's mesosphere. *Journal of Geophysical Research*, **120**, 8899. xxxviii, 251

- PARRA-ROJAS, F.C., LUQUE, A. & GORDILLO-VÁZQUEZ, F.J. (2015). Chemical and thermal impact of sprite streamers in the Earth mesosphere. *J. Geophys. Res - Space Phys.*, **56**, 58, 59, 60, 236
- PASKO, V.P., INAN, U.S. & BELL, T.F. (1996). Sprites as luminous columns of ionization produced by quasi-electrostatic thundercloud fields. *Geophys. Res. Lett.*, **23**, 649, 51
- PASKO, V.P., STANLEY, M.A., MATHEWS, J.D., INAN, U.S. & WOOD, T.G. (2002). Electrical discharge from a thundercloud top to the lower ionosphere. *Nature*, **416**, 152–154. xii, 17, 18
- PASKO, V.P., YAIR, Y. & KUO, C.L. (2012). Lightning related transient luminous events at high altitude in the Earth's atmosphere: Phenomenology, mechanisms and effects. *Space Science Reviews*, **168**, 475–516. xiii, 11, 50, 51
- PASSAS, M., SÁNCHEZ, J., LUQUE, A. & GORDILLO-VÁZQUEZ, F.J. (2014). Transient Upper Atmospheric Plasmas: Sprites and Halos. *IEEE Transactions on Plasma Science*, **42**. xii, 15
- PASSAS, M., SÁNCHEZ, J., SÁNCHEZ-BLANCO, E., LUQUE, A. & GORDILLO-VÁZQUEZ, F.J. (2016). GRASSP: a spectrograph for the study of transient luminous events. *Applied Optics*, **55**, 6436. 66
- PERALTA, J., LEE, Y.J., MCGOULDRIK, K., SAGAWA, H., SÁNCHEZ-LAVEGA, A., IMAMURA, T., WIDEMANN, T. & NAKAMURA, M. (2016). Overview of useful spectral regions for Venus: An update to encourage observations complementary to the Akatsuki mission. *Icarus*, **288**, 235. 24, 151
- PÉREZ-INVERNÓN, F.J., GORDILLO-VÁZQUEZ, F.J. & LUQUE, A. (2016a). On the electrostatic field created at ground level by a halo. *Geophys. Res. Lett.*, **43**, 7015. xviii, xix, 29, 91, 94, 96, 228
- PÉREZ-INVERNÓN, F.J., LUQUE, A. & GORDILLO-VÁZQUEZ, F.J. (2016b). Mesospheric optical signatures of possible lightning on Venus. *J. Geophys. Res. (Space Phys)*, **121**, 7026. xxiv, xxvi, xxvii, xxviii, xxxv, 29, 151, 154, 157, 158, 166, 174, 175, 176, 177, 178, 179, 180, 181, 183, 197, 208, 229, 248
- PÉREZ-INVERNÓN, F.J., LEHTINEN, N.G., GORDILLO-VÁZQUEZ, F.J. & LUQUE, A. (2017a). Whistler Wave Propagation Through the Ionosphere of Venus. *Journal of Geophysical Research: Space Physics*, **122**, 11,633–11,644. xxviii, xxix, xxx, 29, 151, 197, 200, 202, 203, 205, 207, 230
- PÉREZ-INVERNÓN, F.J., LUQUE, A. & GORDILLO-VÁZQUEZ, F.J. (2017b). Three-dimensional modeling of lightning-induced electromagnetic pulses on Venus, Jupiter, and Saturn. *Journal of Geophysical Research: Space Physics*, **122**, 7636–7653, 2017JA023989. xxvii, xxviii, xxxi, xxxii, xxxiii, xxxv, xxxvi, 29, 151, 185, 186, 187, 188, 190, 218, 220, 221, 222, 223, 225, 226, 229
- PEVERALL, R., ROSÉN, S., PETERSON, J.R., LARSSON, M., AL-KHALILI, A., VIKOR, L., SEMANIAC, J., BOBBENKAMP, R., LE PADELLEC, A., MAURELLIS, A.N. & VAN DER ZANDE, W.J. (2001). Dissociative recombination and excitation of O_2^+ : Cross sections, product yields and implications for studies of ionospheric airglows. *J. Chem. Phys.*, **114**, 6679, 236
- PHELPS, A.V. (1991). Cross Sections and Swarm Coefficients for Nitrogen Ions and Neutrals in N_2 and Argon Ions and Neutrals in Ar for Energies from 0.1 eV to 10 keV. *J. Phys. Chem. Ref. Data*, **20**, 557. 235
- PHELPS, A.V. (2005). A compilation of atomic and molecular data: <http://jila.colorado.edu/~avp/>. xxxviii, 236, 251
- PHELPS, V. (1969). NO electron cross sections: <http://jilawww.colorado.edu>. 236
- PHILLIPS, J.L., LUHMANN, J.G. & RUSSELL, C.T. (1986). Magnetic configuration of the Venus magnetosheath. *Journal of Geophysical Research: Space Physics*, **91**, 7931–7938. xxv, 165
- PICCIONI, G., DROSSART, P. & SUETTA, E.E.A. (2007). VIR-TIS: The Visible and Infrared Thermal Imaging Spectrometer. *ESA special publication*, **1295**, 1. 189
- PIERCE, E.T. (1974). Atmospheric electricity-some themes. *Bulletin of the American Meteorological Society*, **55**, 1186. xi, 2
- PIPER, L.G. (1988). State-to-state $N_2(A^3\Sigma^+_u)$ energy pooling reactions. II. The formation and quenching of $N_2(B^3\Pi_g, v=1-12)$. *J. Chem. Phys.*, **88**, 6911. 236
- PIPER, L.G. (1989). The excitation of $N_2(B^3\Pi_g, v=1-12)$ in the reaction between $N_2(A^3\Sigma^+_u)$ and $N_2(X, v \geq 5)$. *J. Chem. Phys.*, **91**, 864. 236
- PIPER, L.G. (1992). Energy transfer studies on $N_2(X^1\Sigma^+_g, v)$ and $N_2(B^3\Pi_g)$. *J. Chem. Phys.*, **97**, 270. 236
- PIPER, L.G., GREEN, B.D., BLUMBERG, W.A.M. & WOLNIK, S.J. (1985). N_2^+ Meinel band quenching. *J. Chem. Phys.*, **82**, 3139. 236
- PITCHFORD, L.C., MCKOY, B.V., CHUTJIAN, A. & TRAJMAR, A. (2012). Swarm Studies and Inelastic Electron-Molecule collisions. Swarm Studies and Inelastic Electron-Molecule Collisions: Proceedings of the Meeting of the Fourth International Swarm Seminar and the Inelastic Electron-Molecule Collisions Symposium, July 19–23, 1985, Tahoe City, California, USA. 236
- PORCO, C.C., WEST, R.A. & SQUYRES, S.E.A. (2004). Cassini Imaging Science: Instrument Characteristics And Anticipated Scientific Investigations At Saturn. *Space Science Reviews*, **115**, 363. 189

REFERENCES

- PRICE, C. & RIND, D. (1992). A simple lightning parameterization for calculating global lightning distributions. *Journal of Geophysical Research*, **97**, 9919. 7
- PRICE, C., PENNER, J. & PRATHER, M. (1997). NO_x from lightning: 1. Global distribution based on lightning physics. *Journal of Geophysical Research*, **102**, 5929. 77
- QIN, J., PASKO, V.P., MCHARG, M.G. & STENBAEK-NIELSEN, H.C. (2014). Plasma irregularities in the D-region ionosphere in association with sprite streamer initiation. *Nature Communications*, **5**, 3740. 31
- RADZIG, A.A. & SMIRNOV, B.M. (2012). *Reference data on atoms, molecules, and ions*, vol. 31. Springer Science & Business Media. 236
- RAKOV, V.A. & UMAN, M.A. (2003). *Lightning Physics and Effects*. Cambridge University Press, Cambridge. xi, 2, 3, 5, 52, 62, 63, 160
- RAPP, D. & BRIGLIA, D.D. (1965). Total cross sections for ionization and attachment in gases by electron impact. II. Negative-ion formation. *International Journal of Mass Spectrometry and Ion Physics*, **43**, 1480. xxxviii, 251
- RAYMENT, S.W. & MORUZZI, J.L. (1978). Electron detachment studies between O^- ions and nitrogen. *International Journal of Mass Spectrometry and Ion Physics*, **26**, 321. xxxviii, 351
- RISON, W., KREHBIEL, P.R., STOCK, M.G., EDENS, H.E., SHAO, X.M., THOMAS, R.J., STANLEY, M.A. & ZHANG, Y. (2016). Observations of narrow bipolar events reveal how lightning is initiated in thunderstorms. *Nature Communications*. 4, 9
- RODRÍGUEZ, A.E., MORGAN, W.L., TOURYAN, K.J., MOENY, W.M. & MARTIN, T.H. (1991). An air breakdown kinetic model. *Journal of Applied Physics*, **70**, 2015–2022. 236
- ROMPS, D.M., SEELEY, J.T., VOLLARO, D. & MOLINARI, J. (2014). Projected increase in lightning strikes in the United States due to global warming. *Science*, **346**, 851. 7
- RUSSELL, C.T. & DOUGHERTY, M.K. (2010). Magnetic Fields of the Outer Planets. *Space Science Reviews*, **152**, 251. 215
- RUSSELL, C.T. & SCARF, F.L. (1990). Evidence for lightning on Venus. *Adv. Space Res.*, **10**, (5)125. 199
- RUSSELL, C.T., VON DORNUM, M. & STRANGEWAY, R.J. (1989). VLF bursts in the night ionosphere of Venus: Estimates of the Poynting flux. *Geophys. Res. Lett.*, **16**, 579. 191, 198, 208
- RUSSELL, C.T., LEINWEBER, H., HART, R.A., WEI, H.Y., STRANGEWAY, R.J. & ZHANG, T.L. (2013). Venus Express observations of ULF and ELF waves in the Venus ionosphere: Wave properties and sources. *Icarus*, **226**, 1527. xxx, 24, 149, 167, 196, 199, 204, 205, 206, 208
- RYCROFT, M.J., ISRAELSSON, S. & PRICE, C. (2000). The global atmospheric electric circuit, solar activity and climate change. *J. Atm. Sol.-Terr. Phys.*, **62**, 1563. 92
- SAGDEEV, R.Z., LINKIN, V.M., KERZHANOVICH, V.V., LIPATOV, A.N., SHURUPOV, A.A., BLAMONT, J.E., CRISP, D., INGERSOLL, A.P., ELSON, L.S., PRESTON, R.A., HILDEBRAND, C., RAGENT, B., SEIFF, A., YOUNG, R.E., PETTIT, G., BOLOH, L., ALEXANDROV, Y.N., ARMAND, N.A., BAKITKO, R.V. & SELIVANOV, A.S. (1986). Overview of VEGA Venus balloon in situ meteorological measurements. *Science*, **231**, 1411. 189
- SATO, M., USHIO, T., MORIMOTO, T., KIKUCHI, M., KIKUCHI, H., ADACHI, T., SUZUKI, M., YAMAZAKI, A., TAKAHASHI, Y., INAN, U. *et al.* (2015). Overview and early results of the Global Lightning and Sprite Measurements mission. *Journal of Geophysical Research: Atmospheres*, **120**, 3822–3851. xxxv, 112, 137
- SCARF, F.L., TAYLOR, W.W.L., RUSSELL, C.T. & BRACE, L.H. (1980). Lightning on Venus: Orbiter Detection of Whistler Signals. *Journal of Geophysical Research*, **85**, 8158. 22, 149, 196, 199, 201, 208
- SCHUMANN, U. & HUNTRESER, H. (2007). The global lightning-induced nitrogen oxides source. *Atmospheric Chemistry and Physics*, **7**, 3823. 7, 77, 78
- SCHUMANN, W.O. (1952). Über die Dämpfung der elektromagnetischen Eigenschwingungen des Systems Erde — Luft — Ionosphäre. *Zeitschrift für Naturforschung A*, **7**, 250. 9
- SCHUNK, R.W. & NAGY, A.F. (1980). Ionospheres of the terrestrial planets. *Reviews of Geophysics*, **18**, 813. xxxvii, xxxviii, 249, 251
- SENTMAN, D.D., STENBAEK-NIELSEN, H.C., MCHARG, M.G. & MORRILL, J.S. (2008). Plasma chemistry of sprite streamers. *J. Geophys. Res - Atmos.*, **113**, D11112. 11, 56, 58, 59, 60, 236
- SIMÕES, F., HAMELIN, M., GRARD, R., APLIN, K.L., BÉGHIN, C., BERTHELIER, J.J., BESSER, B.P., LEBRETON, J.P., LÓPEZ-MORENO, J.J., MOLINA-CUBEROS, G.J., SCHWINGENSCHUH, K. & TOKANO, T. (2008). Electromagnetic wave propagation in the surface-ionosphere cavity of Venus. *Journal of Geophysical Research*, **113**, E07007. 195
- SIMEK, M. (2002). The modelling of streamer-induced emission in atmospheric pressure, pulsed positive corona discharge: N_2 second positive and $\text{NO}-\gamma$ systems. *J. Phys. D*, **35**, 1967. 235, 236

- SIMEK, M. (2003). Determination of $N_2(A^3\Sigma_u^+)$ metastable density produced by nitrogen streamers at atmospheric pressure: 2. Experimental verification. *Plasma Sour. Sci. Technol.*, **12**, 454. 236
- SKALNI, J.D., MATEJCIK, S., KIENDLER, A., STAMATOVIC, A. & MÄRK, T.D. (1996). Dissociative electron attachment to ozone using a high-resolution crossed beams technique. *Märk*, **255**, 112. 235
- SLANGER, T.G. & COPELAND, R.A. (2003). Energetic Oxygen in the Upper Atmosphere and the Laboratory. *Chemical Reviews*, **103**, 4731–4766, PMID: 14664631. 236
- SLANGER, T.G., HUESTIS, D.L., COSBY, P.C., CHANOVER, N.J. & BIDA, T.A. (2006). The Venus nightglow: Ground-based observations and chemical mechanisms. *Icarus*, **182**, 1. 171, 176, 191
- SMIRNOV, B.M. & MASSEY, H.S.W. (1982). *Negative ions*. McGraw-Hill Companies. 236
- STARIKOVSKAIA, S.M., STARIKOVSKII, A.Y. & ZATSEPIN, D.V. (2001). Hydrogen oxidation in a stoichiometric hydrogen-air mixture in the fast ionization wave. *Combustion Theory Modelling*, **5**, 97. 236
- STIX, T.H. (1992). *Waves in Plasmas*. American Institute of Physics, 1992nd edn. xxv, 167, 168, 169
- STOREY, L.R.O. (1953). An investigation of whistling atmospherics. *Phil. Trans. R. Soc. Lond. A*, **246**, 113–141. 163
- STRANGEWAY, R.J. (1995). Plasma wave evidence for lightning on Venus. *Journal of Atmospheric and Terrestrial Physics*, **57**, 537. 22, 149
- STRANGEWAY, R.J. (1996). Collisional Joule dissipation in the ionosphere of Venus: The importance of electron heat conduction. *J. Geophys. Res - Space Phys.*, **101**, 2279. 166
- STRANGEWAY, R.J. (2003). Plasma waves and electromagnetic radiation at Venus and Mars. *Adv. Space Res.*, **33**, 1956. 22, 149, 167, 196, 199, 201, 208
- STRANGEWAY, R.J., RUSSELL, C.T. & HO, C.M. (1993). Observation of intense wave bursts at very low altitudes within the Venus nightside ionosphere. *Geophys. Res. Lett.*, **20**, 2771. 22, 149
- SWEET, R.A. (1977). A Cyclic Reduction Algorithm for Solving Block Tridiagonal Systems of Arbitrary Dimension Read More: <http://epubs.siam.org/doi/abs/10.1137/0714048>. *SIAM J. Numer. Anal.*, **14**, 706. 33, 37, 62
- TAKAHASHI, Y., YOSHIDA, J., YAIR, Y., IMAMURA, T. & NAKAMURA, M. (2008). Lightning Detection by LAC Onboard the Japanese Venus Climate Orbiter, Planet-C. *Space Science Reviews*, **137**, 317. 24, 151, 191, 192
- TARANENKO, Y.N., INAN, U.S. & BELL, T.F. (1993). The interaction with lower ionosphere of electromagnetic pulses from lightning: Excitation of optical emissions. *Geophys. Res. Lett.*, **20**, 2675–2678. 32, 37, 57
- TAYLOR, H.A., BRINTON, H.C., BAUER, S.J., HARTLE, R.E., CLOUTIER, P.A., DANIELL, R.E. & DONAHUE, T.M. (1979). Ionosphere of Venus: First observations of day-night variations of the ion composition. *Science*, **205**, 96. 152, 166, 167, 208
- THÉBAULT, E., FINLAY, C.C., BEGGAN, C.D., ALKEN, P., AUBERT, J., BARROIS, O., BERTRAND, F., BONDAR, T., BONESS, A., BROCCO, L. & OTHERS (2015). International geomagnetic reference field: the 12th generation. *Earth, Planets and Space*, **67**, 79. 101
- THOMAN, J.J.W., GRAY, J.A., DURANT, J.J.L. & PAUL, P.H. (1992). Collisional electronic quenching of $NO(A^2\Sigma^+)$ by N_2 from 300 to 4500 K. *J. Chem. Phys.*, **97**, 8156. 236
- THOMAS, L. (1974). Recent developments and outstanding problems in the theory of the D region. *Radio Science*, **9**, 121. 61, 235
- TITOV, D.V., SVEDHEM, H., MCCOY, D., LEBRETON, J.P., BARABASH, S., BERTAUX, J.L., DROSSART, P., FORMISANO, V., HAEUSLER, B., KORABLEV, O.I., MARKIEWICZ, W., NEVEANCE, D., PETZOLD, M., PICCIONI, G., ZHANG, T.L., TAYLOR, F.W., LELLOUCH, E., KOSCHNY, D., WITASSE, O., WARHAUT, M., ACOMAZZO, A., RODRIGUES-CANNABAL, J., FABREGA, J., SCHIRMANN, T., CLOCHET, A. & CORADINI, M. (2006). Venus Express: Scientific Goals, Instrumentation, and Scenario of the Mission. *Cosmic Res.*, **44**, 334. 199
- TOST, H., JÖCKEL, P. & LELIEVELD, J. (2007). Lightning and convection parameterisations – uncertainties in global modelling. *Atmospheric Chemistry and Physics*, **7**, 4568. 8
- TSANG, S.E., COATES, A.J., JONES, G.H., FRAHM, R.A., WINNINGHAM, J.D. & BARABASH, S. (2015). Ionospheric photoelectrons at Venus: Case studies and first observation in the tail. *Planet. Space Sci.*, **113**, 385. 153
- TURNBULL, D.N. & LOWE, R.P. (1991). Temporal variations in the hydroxyl nightglow observed during ALOHA-90. *Geophys. Res. Lett.*, **18**, 1345. 236
- UNITED STATES COMMITTEE ON EXTENSION TO THE STANDARD ATMOSPHERE (1976). *U.S. standard atmosphere, 1976*. National Oceanic and Atmospheric Administration : for sale by the Supt. of Docs., U.S. Govt. Print. Off. 61
- UPADHYAY, H.O. & SINGH, R.N. (1990). Dynamical features of Venus ionosphere from comparative study of theoretical and in-situ measured electron density profiles. *Adv. Space Res.*, **10**, (5)41. xxxvii, xxxviii, 249, 251

REFERENCES

- VALLANCE JONES, A. (1974). *Aurora*. D. Reidel Publishing Co., Dordrecht, Holland. 236
- VAN DER VELDE, O.A. & MONTANYÀ, J. (2016a). Statistics and variability of the altitude of elves. *Geophysical Research Letters*, **43**, 5467–5474, 2016GL068719. 13, 32
- VAN DER VELDE, O.A. & MONTANYÀ, J. (2016b). Statistics and variability of the altitude of elves. *Geophys. Res. Lett.*, **43**, 27
- VAN DER VELDE, O.A., MONTANYÀ, J., FULLEKRUG, M. & SOULA, S. (2011). Gravity waves, meteor trails, and asymmetries in elves. In *XIV International Conference on Atmospheric Electricity*. 57
- VAUGHAN JR., O.H. & VONNEGUT, B. (1989). Recent observations of lightning discharges from the top of a thundercloud into the air above. *J. Geophys. Res.*, **94 D11**, 13,179–13,182. 11
- VIGGIANO, A.A. (2006). Much Improved Upper Limit for the Rate Constant for the Reaction of O_2^+ with N_2 . *The Journal of Physical Chemistry A*, **110**, 11599–11601, pMID: 17034151. 236
- VIGGIANO, A.A., A., E., HELLBERG, F., THOMAS, R.D., ZHAUNERCHYK, V., GEPPERT, W.D., MONTAIGNE, H., LARSSON, M., KAMINSKA, M. & ÖSTERDAHL, F. (2005). Rate constants and branching ratios for the dissociative recombination of CO_2^+ . *J. Chem. Phys.*, **122**, 226101. xxxvii, xxxviii, 249, 251
- VONNEGUT, B., VAUGHAN JR., O.H. & BROOK, M. (1989). Nocturnal photographs taken from a U-2 airplane looking down on top of clouds illuminated by lightning. *Bull. Amer. Meteor. Soc.*, **70**, **10**, 1263–1271. 11
- VORGUL, I. & HELLING, C. (2016). Flash ionization signature in coherent cyclotron emission from brown dwarfs. *Monthly Notices of the Royal Astronomical Society*, **458**, 1041. 26
- WARWICK, J.W., PEARCE, J.B., EVANS, D.R., CARR, T.D., SCHAUBLE, J.J., ALEXANDER, J.K., KAISER, M.L., DESH, M.D., PEDERSEN, M., LECACHEUX, A. *et al.* (1981). Planetary radio astronomy observations from Voyager 1 near Saturn. *Science*, **212**, 239. 19, 211
- WATSON, S.S. & MARSHALL, T.C. (2007). Current propagation model for a narrow bipolar pulse. *Geophys. Res. Lett.*, **34**, L04816. 9, 64, 70
- WESCOTT, E.M., SENTMAN, D.D., HEAVNER, M.J., HAMPTON, D.L., OSBORNE, D.L. & VAUGHAN, O.H. (1996). Blue starters: Brief upward discharges from an intense Arkansas thunderstorm. *Geophys. Res. Lett.*, **23**, 2153. 16
- WESCOTT, E.M., STENBAEK-NIELSEN, H.C., SENTMAN, D.D., HEAVNER, M.J., MOUDRY, D.R. & SABBAS, F.T.S. (2001). Triangulation of sprites, associated halos and their possible relation to causative lightning and micrometeors. *Journal of Geophysical Research*, **106**, 10467. 52, 55, 89
- WHITAKER, M., BIONDI, M.A. & JOHNSEN, R. (1981). Electron-temperature dependence of dissociative recombination of electrons with N_2^+ - N_2 dimer ions. *Phys. Rev. A*, **24**, 743–745. 236
- WILLIAMS, M.A., KRIDER, E.P. & HUNTEN, D.M. (1983). Planetary lightning - Earth, Jupiter, and Venus. *Reviews of Geophysics and Space Physics*, **21**, 892. 213
- WILSON, C.T.R. (1916). On Some Determinations of the Sign and Magnitude of Electric Discharges in Lightning Flashes. *Proceedings of the Royal Society of London. Series A, Containing Papers of a Mathematical and Physical Character*, **92**, 555. 1
- WILSON, C.T.R. (1921). Investigations on Lightning Discharges and on the Electric Field of Thunderstorms. *Royal Society of London Philosophical Transactions Series A*, **221**, 73. 1
- WILSON, C.T.R. (1925). The electric field of a thundercloud and some of its effects. *Proc. Phys. Soc. London*, **37**, 32D. 11
- WINKLER, H. & NOTHOLD, J. (2014). The chemistry of daytime sprite streamers - a model study. *Atmospheric Chemistry and Physics*, **14**, 3545–3556. 56
- WINKLER, H. & NOTHOLD, J. (2015). A model study of the plasma chemistry of stratospheric Blue Jets. *J. Atm. Sol.-Terr. Phys.*, **122**, 75. 15
- YAIR, Y. (2012). New results on planetary lightning. *Adv. Space Res.*, **50**(3), 293–310. 17
- YAIR, Y., LEVIN, Z. & TZIVION, S. (1995). Microphysical processes and dynamics of a Jovian thundercloud. *Icarus*, **114**, 278. 213
- YAIR, Y., FISCHER, G., SIMÕES, F., RENNO, N. & ZARKA, P. (2008). Updated Review of Planetary Atmospheric Electricity. *Space Sci. Rev.*, **137**, 29. 17, 150
- YAIR, Y., TAKAHASHI, Y., YANIV, R., EBERT, U. & GOTO, Y. (2009). A study of the possibility of sprites in the atmospheres of other planets. *J. Geophys. Res. (Planets)*, **114**, E09002. 150, 152, 157, 170, 212, 214, 228
- YARON, M., VON ENGEL, A. & VIDAUD, P.H. (1976). The collisional quenching of $O_2^*(^1\Delta_g)$ by NO and CO_2 . *Chemical Physics Letters*, **37**, 159–161. 236
- YEE, K.S. (1966). Numerical Solution of Initial Boundary Value Problems Involving Maxwell's Equations in Isotropic Media. *IEEE Transactions on Antennas and Propagation*, **14**, 302. 39, 63

- ZARKA, P. & PEDERSEN, B.M. (1986). Radio detection of uranian lightning by Voyager 2. *Nature*, **323**, 605. 19, 212
- ZARKA, P., CECCONI, B. & KURTH, W.S. (2004). Jupiter's low-frequency radio spectrum from Cassini/Radio and Plasma Wave Science (RPWS) absolute flux density measurements. *Journal of Geophysical Research*, **109**, A09S15. 20
- ZINN, J., SUTHERLAND, C.D. & GANGULY, S. (1990). The solar flare of August 18, 1979 - Incoherent scatter radar data and photochemical model comparisons. *J. Geophys. Res.*, **95**, 16705. 236

Declaration

I herewith declare that I have produced this thesis without the prohibited assistance of third parties and without making use of aids other than those specified; notions taken over directly or indirectly from other sources have been identified as such. This thesis has not previously been presented in identical or similar form to any other Spanish or foreign examination board. The thesis work was conducted from 2014 to 2018 under the supervision of Dr. Francisco J. Gordillo Vázquez and Dr. Alejandro Luque Estepa.

Granada, January 26, 2018

Curriculum Vitae

Personal information

Date of birth: 25th September 1989

Place of birth: Málaga, Spain

Education and employment

2014-2018: PhD Studies at the Instituto de Astrofísica de Andalucía (IAA- CSIC) and University of Granada, Granada, Spain
Dissertation: “Modelling of atmospheric electricity phenomena in the atmospheres of Venus, Earth, Jupiter and Saturn”

2013-2014: M. Sc. degree in Physics of Complex Systems at the National Distance Education University (UNED), Madrid, Spain
Dissertation: “Generación de un aerosol mediante la atomización de un líquido conductor. Análisis teórico y aplicaciones tecnológicas.”

2008-2013: B.S. in Physics at the University of Granada, Granada, Spain.

Short stays

Aug. 2017 - Oct. 2017: National Center for Atmospheric Research (NCAR), University Corporation for Atmospheric Research (UCAR), Boulder, Colorado, United States of America

Project: “Modelling the global chemical impact of lightning and Blue Jets”

Aug. 2016 - Oct. 2016: Birkeland Centre for Space Science, University of Bergen, Bergen, Norway Project: “Modelling lightning-produced VLF wave propagation through the atmospheres of Venus and the Earth”

Participation in publicly funded R&D projects

Mar. 2017 - Feb. 2021: Instituto de Astrofísica de Andalucía (IAA- CSIC), Granada, Spain

Title: “Science and Innovation with Thunderstorms (SAINT)”

Funding Entity: “H2020-MSCA-ITN-2016 (Marie Curie Innovation Training Networks - ITN)”

Jan. 2018 - Dec. 2019: Instituto de Astrofísica de Andalucía (IAA- CSIC), Granada, Spain

Title: “Contribución del IAA a la explotación científica de ASIM: Observaciones desde el suelo y análisis de datos” Funding Entity:

“ESP2017-86263-C4-4-R”

Jan. 2016 - Dec. 2018: Instituto de Astrofísica de Andalucía (IAA- CSIC), Granada, Spain

Title: “Contribución del IAA a la explotación científica de ASIM”

Funding Entity: “ESP2015-69909-C5-2-MINECO”

Jan. 2014 - Dec. 2017: Instituto de Astrofísica de Andalucía (IAA- CSIC), Granada, Spain

Title: “La propagación de rayos como un problema de formación de patrones” Funding Entity: “FIS2014-61774-EXP”

Jan. 2014 - Dec. 2016: Instituto de Astrofísica de Andalucía (IAA- CSIC), Granada, Spain

Title: “Atmospheric Space Interactions Monitor (ASIM). FM

Manufacturing and Scientific Return: The IAA contribution”

Funding Entity: “ESP2013-48032-C5-5-R”

Mar. 2011 - Mar. 2016: Instituto de Astrofísica de Andalucía
(IAA- CSIC), Granada, Spain

Title: “Thunderstorm Effects on the Atmosphere-ionosphere
System (TEA-IS) network” Funding Entity: “09-RNP-101 (LESC)
(European Networking Foundation - Research Networking Pro-
grammes)”

Publications

Journal papers

- **Pérez-Invernón, F. J.**, Gordillo-Vázquez, F. J. and Luque, A., *Modeling the chemical impact and the optical emissions produced by lightning-induced electromagnetic fields in the upper atmosphere: the case of halos and elves triggered by different lightning discharges*, Journal of Geophysical Research: Atmospheres (submitted)
- Mezentsev, A., Lehtinen, N., Østgaard, N., **Pérez-Invernón, F. J.** and Cummer, S. A. (2018). *Spectral characteristics of VLF sferics associated with RHESSI TGFs*, Journal of Geophysical Research: Atmospheres, 123, doi.org/10.1002/2017JD027624
- **Pérez-Invernón, F. J.**, Lehtinen, N. G., Gordillo-Vázquez, F. J., and Luque, A. (2017), *Whistler wave propagation through the ionosphere of Venus. Journal of Geophysics and Engineering Space Physics*, 122, 11, 63311,644, doi.org/10.1002/2017JA024504
- **Pérez-Invernón, F. J.**, A. Luque, and F. J. Gordillo-Vázquez (2017), *Three-dimensional modeling of lightning-induced electromagnetic pulses on Venus, Jupiter, and Saturn*, J. Geophys. Res. Space Physics, 122, 76367653, doi:10.1002/2017JA023989.
- **Pérez-Invernón, F. J.**, A. Luque, and F. J. Gordillo-Vázquez (2016), *Mesospheric optical signatures of possible*

lightning on Venus, J. Geophys. Res. Space Physics, 121, 70267048, doi:10.1002/2016JA022886.

- **Pérez-Invernón, F. J.**, F. J. Gordillo-Vázquez, and A. Luque (2016), *On the electrostatic field created at ground level by a halo*, Geophys. Res. Lett., 43, 72157222, doi:10.1002/2016GL069590.

Conference proceedings

- **Pérez-Invernón, F. J.**, A. Luque, and F. J. Gordillo-Vázquez. *Modeling of transient luminous events produced by cloud to ground lightning and narrow bipolar pulses: detailed spectra and chemical impact*, American Geophysical Union fall meeting 2017 (AGU), New Orleans, United States of America, 2017.
- **Pérez-Invernón, F. J.**, F. J. Gordillo-Vázquez and A. Luque. *Study of transient lightning-driven discharges in the upper atmosphere of the Earth, Venus and giant gaseous planets*, XXXVI Biennial Meeting of the Real Sociedad Española de Física, Santiago de Compostela, Spain, 2017.
- **Pérez-Invernón, F. J.**, F. J. Gordillo-Vázquez and A. Luque. *Modelling the chemical and electrical impact of lightning in the upper atmospheric plasma of planetary atmospheres*, XXXIII Int. Conf. Phenomena in ionized gases (ICPIG), Lisboa, Estoril, Portugal, 2017.
- **Pérez-Invernón, F. J.**, A. Luque and F. J. Gordillo-Vázquez. *Lightning-driven discharges in Venus and giant gaseous planets: chemical impact and possible optical emissions on the upper atmospheres*, 1st IUGG Symposium on Planetary Science (IUGG-PS), Berlin, Germany, 2017.
- **Pérez-Invernón, F. J.**, A. Luque and F. J. Gordillo-Vázquez. *Modeling lightning impact on the upper atmospheres of Venus and giant gaseous planets*, V Reunión

de Ciencias Planetarias y Exploración del Sistema Solar (CPESS), Madrid, Spain, 2017.

- **Pérez-Invernón, F. J.**, A. Luque and F. J. Gordillo-Vázquez. *3D modeling of lightning-induced electromagnetic pulses on Venus, Jupiter and Saturn*, European Geosciences Union General Assembly 2017 (EGU), Vienna, Austria, 2017.
- Gordillo-Vázquez, F. J., M. Passas, Sánchez, M., **F. J., Pérez-Invernón**, A. Luque, O. van der Velde and J., Montayà. *High-resolution spectra of sprites and halos with GRASSP*, European Geosciences Union General Assembly 2017 (EGU), Vienna, Austria, 2017.
- Mezentsev, A., Lehtinen, N., Østgaard, N., **F. J., Pérez-Invernón**, and Cummer, S. *Spectral characteristics of VLF sferics associated with TGFs*, European Geosciences Union General Assembly 2017 (EGU), Vienna, Austria, 2017.
- **Pérez-Invernón, F. J.**, A. Luque and F. J. Gordillo-Vázquez. *Mesospheric optical signature of possible lightning on Venus*, Final TEA-IS international conference, Copenhagen, Denmark, 2016.
- **Pérez-Invernón, F. J.**, F. J. Gordillo-Vázquez and A. Luque. *Electrodynamical model of lightning-produced upper atmospheric glow discharges*, 23rd Europhysics Conference on Atomic and Molecular Physics of Ionized Gases (ES-CAMPIG), Bratislava, Slovakia, 2016.
- **Pérez-Invernón, F. J.**, A. Luque and F. J. Gordillo-Vázquez. *Preliminary modeling studies of lightning in Venus*, IV Reunión de Ciencias Planetarias y Exploración del Sistema Solar (CPESS), Alicante, Spain, 2015.
- **Pérez-Invernón, F. J.**, A. Luque and F. J. Gordillo-Vázquez. *Preliminary modeling studies of lightning in Venus*, TEA-IS international conference, Vienna, Austria, 2015.

Works highlighted in the media

- **Pérez-Invernón, F. J.**, A. Luque, and F. J. Gordillo-Vázquez (2016), *Mesospheric optical signatures of possible lightning on Venus*, J. Geophys. Res. Space Physics, 121, 70267048, doi:10.1002/2016JA022886.

Highlighted by: Hall, S. (2016), *Searching for lightnings signature on Venus*, Eos, 97,

<https://doi.org/10.1029/2016EO057293>. Published on 10 August 2016.

Others

- **Pérez-Invernón, F. J.**, M. Passas-Varo, A. Luque and F. J. Gordillo-Vázquez, *Rayos en el Sistema Solar*, Información y actualidad astronómica (IAA), núm 48, número de febrero de 2016, pp. 3-6

Presentations

2017

- **Pérez-Invernón, F. J.**, A. Luque, and F. J. Gordillo-Vázquez. *Modeling of transient luminous events produced by cloud to ground lightning and narrow bipolar pulses: detailed spectra and chemical impact*, American Geophysical Union fall meeting 2017 (AGU), New Orleans, United States of America, 2017 [Oral + conference proceedings].
- **Pérez-Invernón, F. J.**, and F. J. Gordillo-Vázquez. *Parameterization of Blue Jets and lightnings in WACCM: frequency and chemical impact of atmospheric electricity phenomena*, Seminar, National Center for Atmospheric Research, Boulder, Colorado, United States of America, 2017 [Oral].
- **Pérez-Invernón, F. J.**, F. J. Gordillo-Vázquez and A. Luque. *Study of transient lightning-driven discharges in the upper atmosphere of the Earth, Venus and giant gaseous planets*, XXXVI Biennial Meeting of the Real Sociedad Española de Física, Santiago de Compostela, Spain, 2017 [Oral + conference proceedings].
- **Pérez-Invernón, F. J.**, F. J. Gordillo-Vázquez and A. Luque. *Modelling the chemical and electrical impact of lightning in the upper atmospheric plasma of planetary atmospheres*, XXXIII Int. Conf. Phenomena in ionized gases (ICPIG), Lisboa, Estoril, Portugal, 2017 [Oral + conference proceedings].

- **Pérez-Invernón, F. J.**, A. Luque and F. J. Gordillo-Vázquez. *Lightning-driven discharges in Venus and giant gaseous planets: chemical impact and possible optical emissions on the upper atmospheres*, 1st IUGG Symposium on Planetary Science (IUGG-PS), Berlin, Germany, 2017 [Oral + conference proceedings].
- **Pérez-Invernón, F. J.**, A. Luque and F. J. Gordillo-Vázquez. *Modeling lightning impact on the upper atmospheres of Venus and giant gaseous planets*, V Reunión de Ciencias Planetarias y Exploración del Sistema Solar (CPESS), Madrid, Spain, 2017 [Oral + conference proceedings].
- **Pérez-Invernón, F. J.**, A. Luque and F. J. Gordillo-Vázquez. *3D modeling of lightning-induced electromagnetic pulses on Venus, Jupiter and Saturn*, European Geosciences Union General Assembly 2017 (EGU), Vienna, Austria, 2017 [Oral + conference proceedings].

2016

- **Pérez-Invernón, F. J.**, A. Luque and F. J. Gordillo-Vázquez. *Mesospheric optical signature of possible lightning on Venus*, Final TEA-IS international conference, Copenhagen, Denmark, 2016 [Poster presentation + conference proceedings].
- **Pérez-Invernón, F. J.**, F. J. Gordillo-Vázquez and A. Luque. *Electrodynamical model of lightning-produced upper atmospheric glow discharges*, 23rd Europhysics Conference on Atomic and Molecular Physics of Ionized Gases (ES-CAMPIG), Bratislava, Slovakia, 2016 [Poster presentation + conference proceedings].

2015

- **Pérez-Invernón, F. J.**, A. Luque and F. J. Gordillo-Vázquez. *Preliminary modeling studies of lightning in Venus*, IV Reunión de Ciencias Planetarias y Exploración del Sistema Solar (CPESS), Alicante, Spain, 2015 [Oral + conference proceedings].
- **Pérez-Invernón, F. J.**, A. Luque and F. J. Gordillo-Vázquez. *Preliminary studies of lightning in Venus*, Jornada de Doctorandos del Programa de Doctorado “Física y Ciencias del Espacio”, Granada, Spain, 2015 [Poster presentation].
- **Pérez-Invernón, F. J.**, A. Luque and F. J. Gordillo-Vázquez. *Preliminary modeling studies of lightning in Venus*, TEA-IS international conference, Vienna, Austria, 2015 [Oral].